Investigating Post-Task Responses using MEG and 7T fMRI

Sebastian C. Coleman MSci



Thesis presented to

The University of Nottingham

For the degree of

Doctor of Philosophy

February 2024

Abstract

Electrophysiology and haemodynamics related to human brain function can be measured using several modern imaging techniques. Magnetoencephalography (MEG) enables direct measurement of neuromagnetic fields created by signal transmission in neuronal ensembles, with high temporal resolution but limited spatial resolution and depth sensitivity. Functional magnetic resonance imaging (fMRI) enables the indirect measurement of neuronal activity through changes in blood oxygenation, with lower temporal resolution but high spatial specificity throughout the entire brain. These techniques can be used to investigate the spatial origin and dynamics of brain activity, in response to tasks or during resting state. This thesis uses MEG and fMRI to study responses that occur in the transition period between task cessation and rest, which we term *post-task responses* (PTRs).

The most well-known PTR in electrophysiology is the *beta rebound*, a rise in motor cortex oscillatory power following movement cessation, lasting up to 10 seconds. The haemodynamic PTR often manifests as a *post-stimulus undershoot* in the blood oxygenation level dependent (BOLD) signal, lasting up to a minute. Both of these responses have displayed characteristics that warrant neuroscientific and clinical investigation, including reliable amplitude modulations with task conditions and reduction in clinical populations. Despite this, current research into electrophysiological PTRs outside of the motor cortex, following non-motor activities, is severely lacking. In addition, the relationship between electrophysiological and haemodynamic PTRs is poorly understood. This thesis details three experiments aiming to establish PTRs as an important brain-wide phenomenon that enables regulation of functional network activity during the transition to rest.

The first experimental chapter, “Post-Task Responses in Oscillatory Activity follow Cessation of Working Memory Processes”, used MEG to measure PTRs following an n-back working memory task. PTRs were measured across the brain in regions associated with higher cognition, increasing in amplitude with working memory load and showing promising relationships with reaction times. This chapter establishes PTRs in electrophysiology as a more general property of the cortex than previously thought, induced by non-motor activity and spanning multiple frequency bands and regions.

The next experimental chapter, “Characterising Post-Task Responses using Hidden Markov Models”, compares PTRs in electrophysiology following working memory and

movement by examining *burst* characteristics of these responses, using a hidden Markov model (HMM) to infer burst timing in a data-driven manner. The analysis revealed stark similarities between region-wise burst properties across two different tasks and showed that PTRs are supported by coincidence of these bursts in widespread cortical networks. This chapter provides further evidence that PTRs are a fundamental property of the cortex, underpinned by long-range cortical interactions.

The final experiment, “Spatial and Dynamic Dissociation of Primary and Post-Stimulus BOLD Responses”, used ultra-high field fMRI to study the post-stimulus BOLD response following working memory. Results showed similarities between post-stimulus BOLD responses and the electrophysiological PTR, with modulations that are spatially and dynamically decoupled from responses that occurred during the preceding task. Using the high spatial resolution and depth sensitivity of fMRI, this chapter reveals the influence of the PTR on several distinct functional networks, including interactions with deep grey matter regions that are difficult to study with MEG.

Contents

Abstract i

1 Introduction 1

1.1 Functional Brain Imaging 2

1.1.1 Direct Measures of Brain Function 2

1.1.2 Indirect Measures of Brain Function 4

1.2 Thesis Aims 5

1.3 Thesis Layout 8

1.4 Impact Statement 9

2 Brain Function 11

2.1 Cellular Origins of Brain Function 11

2.1.1 The Neuron 11

2.1.2 Signal Generation 12

2.1.3 Synaptic Transmission 14

2.2 Brain Anatomy and Functional Segregation 16

2.2.1 Grey and White Matter 16

2.2.2 Functional Segregation of the Cortex 17

2.2.3 Subcortical Structures 18

2.2.4 Hierarchical Neuronal Processing 19

2.3 Measurable Brain Activity 21

2.3.1 Neural Contributions to MEG Signal 21

2.3.2 Types of Electrophysiological Response 22

2.3.3 Evoked Responses 23

2.3.4 Induced Responses 24

2.3.5 Haemodynamic Signals 30

2.3.6 Negative BOLD Responses 33

2.3.7 Resting State Functional Networks 34

2.3.8 Relationship between MEG and fMRI Signal 35

2.4 Summary 38
3 Magnetoencephalography 39
3.1 MEG Data Acquisition 39
3.1.1 SQUID Operation 39
3.1.2 Magnetometers and Gradiometers 43
3.1.3 Synthetic Gradiometry 44
3.1.4 Magnetic Shielding 44
3.1.5 Experimental Setup 45
3.1.6 Anatomical Co-Registration 46
3.2 MEG Data Analysis 48
3.2.1 Forward Modelling 49
3.2.2 The Inverse Problem 54
3.2.3 Beamforming 55
3.2.4 Event-Related Analysis 57
3.2.5 Functional Connectivity 60
3.3 Summary 61
4 Functional MRI 62
4.1 fMRI Data Acquisition 62
4.1.1 Nuclear Spin 62
4.1.2 Spin Precession 64
4.1.3 Bulk Magnetisation 64
4.1.4 Spin Excitation 66
4.1.5 Longitudinal Relaxation 68
4.1.6 Transverse Relaxation 69
4.1.7 Slice Selection 70
4.1.8 Frequency and Phase Encoding 71
4.1.9 Echo Planar Imaging 72
4.1.10 Accelerated Imaging 74
4.1.11 Anatomical Imaging 75

4.1.12 Susceptibility-Induced Distortions 76
4.1.13 Noise in Functional Data 77
4.1.14 MRI System 78
4.1.15 Origin of Contrast in Functional MRI 80
4.2 fMRI Data Analysis 83
4.2.1 Typical Pre-Processing Steps 83
4.2.2 General Linear Modelling 84
4.2.3 Group Level Analysis 88
4.2.4 Independent Component Analysis 90
4.3 Summary 90
5 Post-Task Responses in Oscillatory Activity follow Cessation of Working Memory Processes 91
5.1 Abstract 91
5.2 Publication and Contribution Note 91
5.3 Introduction 92
5.4 Methods 94
5.4.1 Paradigm 94
5.4.2 Acquisition 95
5.4.3 Behavioural Analysis 96
5.4.4 MEG Pre-Processing 96
5.4.5 Beamforming 96
5.4.6 Standard Brain Normalisation 97
5.4.7 Time-Frequency Responses 98
5.4.8 Residual Post-Task Response Modulation 99
5.4.9 Post-Movement Beta Rebound 99
5.4.10 Oscillatory Stimulus Response 99
5.5 Results 100
5.5.1 Behaviour 100
5.5.2 Activation Maps 101

5.5.3 Time-Frequency Responses 103
5.5.4 Attention Network 106
5.5.5 Post-Movement Beta Rebound 107
5.5.6 Residual PTR Modulation 108
5.5.7 Neural-Behaviour Correlations 109
5.5.8 Oscillatory Stimulus Response 110
5.6 Discussion 112
5.6.1 Beta Rebound in Attention and Motor Networks 112
5.6.2 The Role of Alpha Rebounds in Working Memory 114
5.6.3 Post-Task Theta Undershoots May Modulate Default Network Activity 114
5.6.4 Post-Task Responses are Modulated by Behavioural Markers of Task Difficulty 115
5.6.5 Limitations and Future Work 116
5.7 Conclusion 117
5.8 APPENDIX A 118
5.8.1 Peak Modulation Timecourses 118
5.8.2 Task vs Rest Contrast 119
6 Characterising Post-Task Responses using Hidden Markov Models 121
6.1 Abstract 121
6.2 Publication and Contribution Note 121
6.3 Introduction 122
6.4 Hidden Markov Modelling 124
6.4.1 Markov Chains 124
6.4.2 The Joint Posterior Probability 125
6.4.3 Free Parameter Optimisation 126
6.4.4 Model Configuration 128
6.5 Methods 129
6.5.1 Paradigms 129
6.5.2 Data Acquisition 131

6.5.3 Pre-Processing 132
6.5.4 Parcellation Beamformer 132
6.5.5 Hidden Markov Modelling 133
6.5.6 The PTR State 133
6.5.7 State Grouping with K-Means Clustering 134
6.5.8 Temporal K-Means Clustering Simulation 134
6.5.9 State Probability 137
6.5.10 Burst Characteristics 137
6.5.11 Burst Connectivity 138
6.5.12 Correlating State Probability with Behaviour 139
6.6 Results 139
6.6.1 PTR State Grouping 139
6.6.2 PTR State Probability 142
6.6.3 Single-Trial State Activity 143
6.6.4 Burst Characteristics 143
6.6.5 Connectivity 145
6.6.6 Relating PTRs to Behaviour 149
6.7 Discussion 150
6.7.1 The PTR State Captures Transient Oscillatory Bursts 150
6.7.2 Grouping Whole-Brain Bursting States 151
6.7.3 Burst Events across Visuomotor and Working Memory Tasks have Similar Region-Wise Characteristics 152
6.7.4 The Role of Bursts in Cortical Network Formation 153
6.7.5 HMMs Isolate Functionally Relevant Features in MEG Data 156
6.7.6 Limitations and Future Work 156
6.8 Conclusion 157
6.9 Appendix 158
7 Spatial and Dynamic Dissociation of Primary and Post-Stimulus BOLD Responses 160
7.1 Abstract 160

7.2 Publication and Contribution Note 160
7.3 Introduction 161
7.4 Methods 164
7.4.1 Paradigm 164
7.4.2 Acquisition 165
7.4.3 Pre-Processing 166
7.4.4 General Linear Model Analysis 166
7.4.5 Pseudo T-Statistic Analysis 167
7.4.6 Functional Network Responses 169
7.4.7 Normalised Post-Stimulus Response 170
7.4.8 Primary and Post-Stimulus Response Regression 170
7.5 Results 171
7.5.1 General Linear Model 171
7.5.2 Pseudo T-Statistic 174
7.5.3 Peak Pseudo T-Stat in Deep Brain Regions 180
7.6 Discussion 182
7.6.1 Spatial Dissociation of Primary and Post-Stimulus BOLD Responses 183
7.6.2 Dynamic Decoupling of Primary and Post-Stimulus BOLD Responses 184
7.6.3 Vascular Interpretation 184
7.6.4 Relationships Between MEG and fMRI Post-Stimulus Responses 185
7.6.5 Post-Stimulus Responses in Deep Grey Matter 187
7.6.6 Limitations and Future Work 188
7.7 Conclusions 190
7.8 APPENDIX A 191
7.8.1 Other Pseudo T-Stat Contrasts 191
7.9 Appendix B 193
7.9.1 Signal to Noise of Different Contrasts 193
8 Conclusion 197

8.1 Overview of Findings 197
8.2 Future Work 198
8.3 Closing Remarks 201
References 202

1 Introduction

Study of the brain has been conducted for *at least* several thousand years, with the earliest recorded reference to the brain dating back to 17th century BC (Feldman and Goodrich, 1999), although this was purportedly copied from an even older manuscript. A section of the manuscript is shown below in Figure 1.1, taken from (Feldman and Goodrich, 1999).

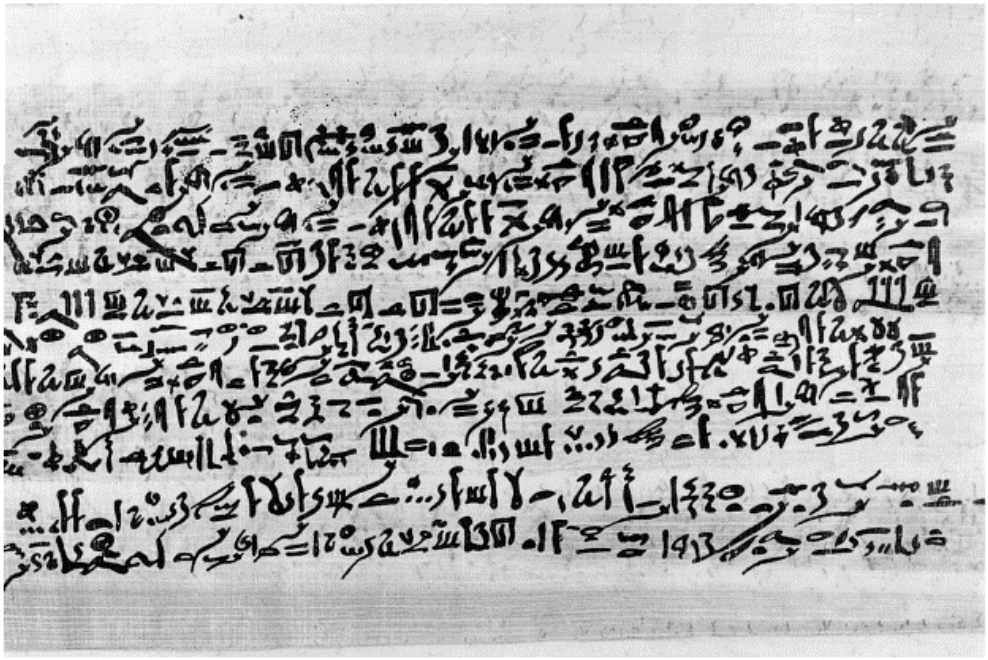


***Figure 1.1**: A section of the Edwin Smith Surgical Papyrus (Feldman and Goodrich 1999), the earliest known reference to the human brain, detailing a host of head injuries and surgical procedures.*

Early study of the brain was necessarily structural in nature, as no techniques existed that could measure the neuroelectric currents that constitute brain function. However, the past century has seen many sophisticated techniques emerge that have revolutionised our understanding of the brain. These advances have allowed us to investigate not only brain structure, including physical damage or degradation to tissues, but also brain function, allowing us to gain insight into illnesses that are not easily understood using structure alone, such as epilepsy and schizophrenia. The following introduction will outline these advancements in functional neuroimaging and the aims of this thesis, which uses cutting edge non-invasive imaging techniques to investigate electrophysiological and haemodynamic signals in the healthy human brain.

1.1 Functional Brain Imaging

1.1.1 Direct Measures of Brain Function

In the 19th Century, Carlo Matteucci performed a series of experiments that demonstrated that human physiology is underpinned by electrical currents (Moruzzi, 1996). Perhaps most notably, in 1843, he provided evidence that electric currents produce reflexive muscle switches. Later in the century, Richard Caton measured electrical impulses on the surface of living brains, directly demonstrating the electrical nature of brain activity (Caton, 1875).

It was not until the 20th century that neuroelectric signals were measured *in vivo* in the human brain by Hans Berger (Berger, 1929). This recording, which used electrodes placed upon the scalp surface to measure currents conducted through the scalp, was termed the **Electroencephalogram (EEG)**. EEG has developed notably since its conception, with relatively cheap, whole-head systems available commercially and used widely in both research and clinical settings (Soufineyestani et al., 2020). In research settings, these systems are typically formed of flexible caps containing an array of electrodes which detect neuroelectric signals originating from the brain. EEG is able to sample at high temporal resolution (> 100 Hz), allowing the direct measurement of rapidly changing signals that arise due to the synchronous firing of neurons in the brain. To improve the electrical connection between electrodes and the scalp, the skin is prepared with alcohol and gentle abrasion to remove dead skin, and a conductive gel is used to physically connect the electrodes to the scalp surface. This preparation process can make performing whole-head EEG time-consuming and sometimes uncomfortable for the participant. In addition, EEG is sensitive to volume conduction effects, causing spatial blurring of signals and high sensitivity to muscle artefacts. This makes scalp EEG impractical for pinpointing precise sources of brain activity.

EEG can also be performed invasively, termed **intracranial EEG (iEEG)** (Parvizi and Kastner, 2018). This category includes **electrocorticography (ECoG)**, where a grid of electrodes are placed directly on the cortical surface following a craniotomy (surgical removal of a section of skull), and **stereo EEG (sEEG)** (Stricsek et al., 2018), where a set of depth electrodes, each with up to 16 electrical contacts, are placed inside the brain tissue in various locations through small holes in the skull. ECoG is very effective at pinpointing superficial sources of activity under the electrode grid, as the removal of the skull means there is less spatial blurring and higher signal to noise ratio (SNR) than scalp EEG, however, sensitivity to sources elsewhere in the brain is low due to signal

decay with distance. On the other hand, sEEG recordings are often taken in close proximity to both superficial and deep sources of activity, and data can be taken from many locations in the brain simultaneously. It can therefore be argued that sEEG provides the most direct information about human brain electrophysiology. Both ECoG and sEEG are often used to identify epileptogenic networks in preparation for surgery (Bartolomei et al., 2017, Yang et al., 2014). The limitation of all iEEG techniques is their highly invasive nature, meaning recordings are almost always limited to patients with severe illnesses, limiting the comparisons that can be made with healthy brains. In addition, the placement of electrodes is biased towards areas affected by the illness, often temporal regions in the case of epilepsy (Iasemidis et al., 1988, Dührsen et al., 2020), rather than a homogenous distribution around the brain.

Magnetoencephalography (MEG) (Cohen, 1972) provides a potential non-invasive middle-ground between the accessibility of EEG and the signal quality of iEEG. MEG measures the magnetic field produced by (mostly) the same neuronal activity that is measured with EEG. Unlike EEG, MEG does not suffer from spatial blurring due to conductivity effects, as the fields pass through the various tissues and skull largely undistorted. This means that MEG signals are more spatially specific than EEG signals and less prone to muscle artefacts, with similar high temporal resolution across both modalities. MEG sensors typically operate at cryogenic temperatures, meaning the array of sensors must remain in a fixed helmet-shaped configuration in a dewar of liquid helium, limiting head movement during scanning. This also makes MEG more expensive. Despite these limitations, the high data quality and minimal preparation time make MEG an ideal research tool (Baillet, 2017). MEG acquisition and analysis is explained further in Chapter 3, and used in Chapters 5 and 6. To overcome some of the issues with cryogenic MEG, new MEG systems are being developed with a different type of sensor that operates at room temperature, with a wearable helmet design to allow for a greater range of movement (Schofield et al., 2022).

In addition to direct electrophysiological measurement of brain function, it is also possible to detect chemicals known as neurotransmitters, involved in the transmission of neuronal signals, using an application of nuclear magnetic resonance (NMR) known as **functional magnetic resonance spectroscopy (fMRS)** (Pasanta et al., 2023). Two important neurotransmitters measured with fMRS are glutamate and gamma aminobutyric acid (GABA). Glutamate is involved in neuronal excitation, supporting the firing of neurons, while GABA is involved in neuronal inhibition, preventing the firing of neurons. Concentrations of each of these chemicals can serve as a direct measure of neurochemical brain function. The temporal resolution of this technique is low, close

to a minute per datapoint at best (Stanley and Raz, 2018), limiting its application as an independent measure of brain function. However, fMRS can provide unique neurochemical insight when used in conjunction with other functional imaging techniques.

1.1.2 Indirect Measures of Brain Function

The ongoing firing of neurons requires a near-constant supply of oxygen and glucose, transported to neuronal assemblies by the blood. If the rate of firing increases in a particular brain region, metabolic demands rise, which is reflected by increased blood flow to the region. Several techniques exist that can measure this metabolic process, acting as indirect measures of brain function.

The first of these is **positron emission tomography (PET)** (Ter-Pogossian et al., 1975). In PET scanning, a radioactive tracer chemical such as fluorodeoxyglucose is injected into the participant, flowing quickly to the brain. The tracer chemical is unstable, rapidly decaying into a more stable isotope and emitting a positron. The positron annihilates with a nearby electron, releasing two gamma photons travelling exactly 180° apart. After many of these events, the location of the tracer, and therefore the metabolic blood supply, can be inferred. This technique is generally avoided in healthy participants as it produces ionising radiation, but is commonly used to detect tumours in cancer patients (Schöder and Gönen, 2007, Flanagan et al., 1998).

Another technique that provides an indirect measure of brain function is **functional near-infrared spectroscopy (fNIRS)** (Jöbsis, 1977). This technique shines near-infrared light through the scalp and skull in optodes that are mounted in a cap configuration on the head. Oxygenated and deoxygenated blood have different absorption spectra, meaning that the reflected light provides information about the ratio of oxygenated and deoxygenated blood in the underlying tissues, acting as a proxy of brain function. This technique has poor spatial resolution and the underlying signals are sluggish in comparison to direct electrophysiological measures. However, fNIRS is non-invasive, wearable (allowing movement) and relatively cheap.

Perhaps the most popular method to indirectly measure brain activity is **functional magnetic resonance imaging (fMRI)** (Ogawa et al., 1990). Magnetic resonance imaging (MRI) is most well-known as a technique for studying the structure of the body and brain, however, it can also be used to track changes in blood oxygenation in the brain which act as a proxy of brain function. This technique exploits the fact that oxygenated and deoxygenated blood have different magnetic properties, meaning the MRI signal in a location will depend on the local ratio of the two. This is known as the

blood oxygenation level dependent (BOLD) signal. If many MRI images are taken in quick enough succession (usually 1 – 5 s), the BOLD signal can be measured at relatively high spatial resolution (usually 1 – 4mm), with good sensitivity to both deep and superficial sources of activity. Greater magnetic field strengths increase the signal measured with fMRI, allowing for greater spatial and temporal resolutions. Functional MRI is explained in greater depth in Chapter 4 and used in Chapter 7.

1.2 Thesis Aims

In this thesis, we explore the electrophysiological and haemodynamic signals following stimulus or task cessation, termed *post-stimulus* or *post-task responses* (PTRs)[1]. Specifically, these responses occur at the start of a *rest period*, rather than a period of continued attention to a task. A schematic of these responses is shown in Figure 1.2.

[1] In this thesis we have used the term 'post-task response' when referring to the MEG response in between task periods and rest due to the additional (faster) MEG responses that occur following individual stimuli presentation within a task period. The relatively slow fMRI response does not require this differentiation, and so the conventional terminology of post-stimulus response has been used.

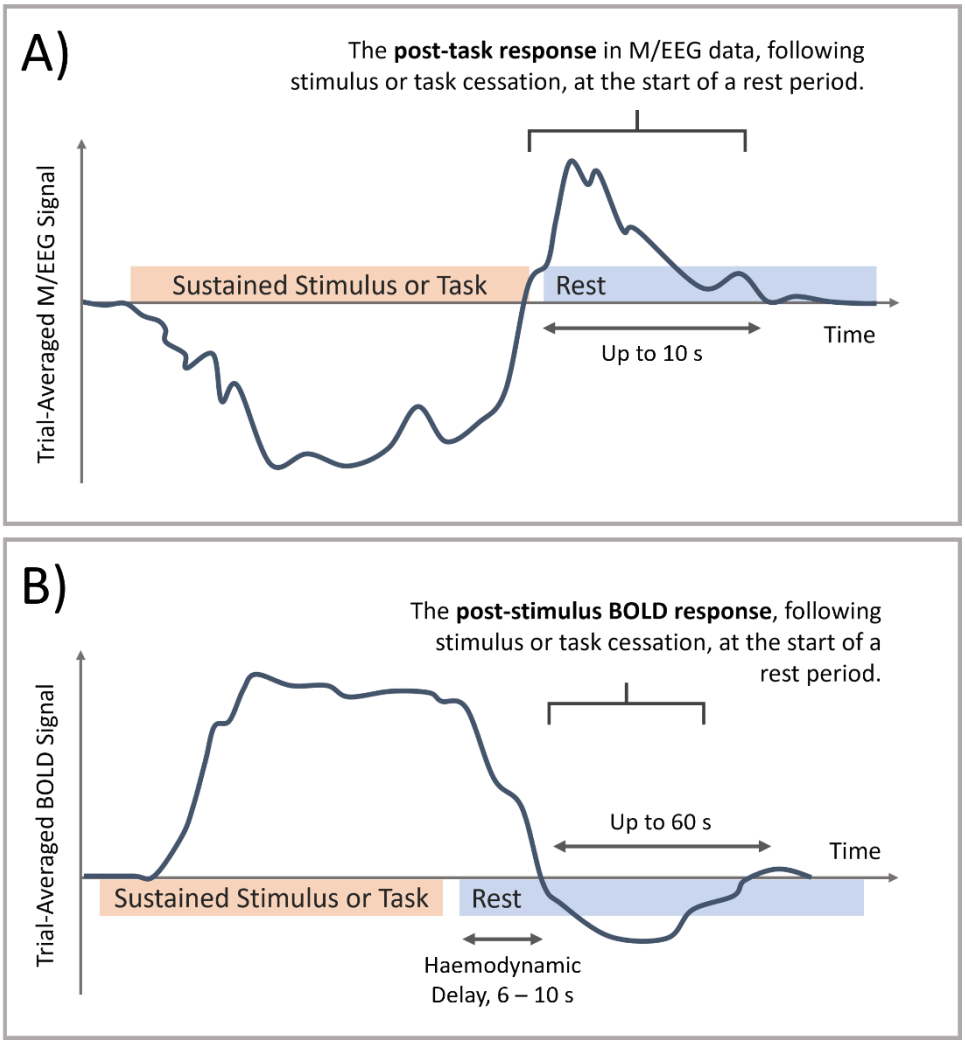


***Figure 1.2**: A schematic showing the timing of the post-task M/EEG response (A), as well as the post-stimulus BOLD fMRI response (B), which are the subject of this thesis. These responses occur following a sustained stimulus or task period, at the start of a rest period.*

The most well established electrophysiological PTR is the post-movement beta rebound (PMBR), a response characterised by an increase in beta (13 – 30 Hz) oscillatory power following movement cessation, lasting for up to 10 s before returning to resting levels (Pfurtscheller et al., 1996b). This response has been shown to have neuroscientific and clinical relevance, modulating with features of the prior movement, including movement force (Fry et al., 2016) and duration (Pakenham et al., 2020), and with neurological conditions such as schizophrenia (Hunt et al., 2019, Gascoyne et al., 2021), autism (Gaetz et al., 2020) and multiple sclerosis (Barratt et al., 2017a). The relationship between the MEG PTR and schizophrenia is particularly interesting, as the response is shown to scale with disease severity. These features make the PTR a promising candidate as a diagnostic or prognostic biomarker of neurological illness,

with potential to guide future treatment strategies. Existing evidence suggests that the PMBR is reflective of increased top-down inhibition in motor networks, preventing further movement or sensory perception from taking place after a stimulus or task has ended (Pfurtscheller et al., 1996b, Solis-Escalante et al., 2012, Zhang et al., 2008). In turn, this suggests that reduced PMBR in patient populations is a marker of reduced inhibitory control, which may be driven by impaired connectivity in top-down control circuitry. This is expanded upon in Chapter 2.3.4.

Although the PMBR in M/EEG has been well-studied and characterised, research into PTRs outside of the motor cortex following non-movement tasks is severely lacking. One reason for this is experiment design, with most studies opting for very minimal rest periods in between sequential stimuli or task periods, making the study of PTRs virtually impossible. In this thesis, we aim to uncover whether PTRs are a general property of the cortex and cognition, occurring outside of the motor cortex following non-movement activity.

Several traditional practices in M/EEG analysis have prevented the study of PTRs as a brain-wide phenomenon. The first is frequency banding, which is typically set a priori, often limiting the reported sources of activity, e.g., only studying the location of peak beta-band activity in motor paradigms. In addition, traditional M/EEG analysis considers only the average response over many trials, ignoring the trial-level features of the response. Recent years have seen a rise in an alternative description of oscillatory activity through *bursting* models (Jones, 2016, Quinn et al., 2019, Seedat et al., 2020, Little et al., 2019, Lundqvist et al., 2024), which describe the transient, high amplitude oscillatory events that form smooth responses, such as PTRs, after trial-averaging. Bursts have been shown to relate to behavioural outcomes in a task (Little et al., 2019), functional connectivity (Seedat et al., 2020, Vidaurre et al., 2016) and neurological condition (Rier et al., 2021, Gascoyne et al., 2021). A technique that is becoming popular for identifying bursts, without a priori knowledge of frequency response or task timings, is hidden Markov modelling (HMM) (Woolrich et al., 2013, Vidaurre et al., 2016, Quinn et al., 2018, Seedat et al., 2020), an unsupervised machine learning technique that infers a set of mutually exclusive states that describe the data at each timepoint. We aim to use this approach to explore PTR characteristics without the constraints of frequency banding or trial-averaging.

Finally, the relationship between electrophysiological PTRs and the post-stimulus BOLD response is poorly understood, especially in subcortical regions which are difficult to study with M/EEG. A robust feature of the BOLD fMRI response is the post-

stimulus undershoot (Frahm et al., 1996). This feature was previously thought to be a vascular consequence of the primary (during-stimulus) BOLD response, but there is mounting evidence that the post-stimulus undershoot has a neuronal origin which is distinct from that of the primary response (Chen and Pike, 2009, Mullinger et al., 2013, Sadaghiani et al., 2009, Shmuel et al., 2006). Post-stimulus undershoots, like the PMBR in MEG, have been associated with increased neuronal inhibition, suggesting a relationship between the responses measured with each modality. In addition, the post-stimulus BOLD response, like the PMBR measured with M/EEG, has shown promise as a clinical tool, with reported reductions in magnitude in patients with schizophrenia (Hanlon et al., 2016) and autism (Murray et al., 2020). Direct links between electrophysiological and haemodynamic responses that occur in the post-task period are difficult to make, given the difference in spatial and temporal resolutions between the two modalities and the respective neuronal generators of each signal. We aim to contribute to the evidence that the post-stimulus BOLD response is neuronal in origin, providing a potential counterpart to the electrophysiological PTR that can be studied with greater spatial specificity and depth sensitivity.

We use the best available technologies to study PTRs in electrophysiology and haemodynamics. To study electrophysiological PTRs, we use MEG, which has superior spatial resolution to EEG, allowing us to study regions and networks that are activated immediately post-task, in theta (4 – 8 Hz), alpha (8 – 13 Hz) and beta (13 – 30 Hz) bands, following non-motor tasks. We use HMMs to characterise the transient single-trial events which constitute these responses, comparing these events across the brain in motor and non-motor tasks. Finally, we use 7T fMRI to study the post-stimulus BOLD response in both superficial and deep brain networks, as a potential haemodynamic correlate of the electrophysiological PTR. We utilise the high spatial and temporal resolutions enabled by 7T MRI as well as long rest periods to allow haemodynamic activity to properly return to baseline before subsequent trials.

1.3 Thesis Layout

This thesis starts by outlining basic neuroscientific theory in Chapter 2, both cellular and cognitive, required to understand the interpretations of MEG and fMRI signals that are discussed in the experimental chapters. This includes the origin and transmission of neuronal signals, structural and functional organisation of the brain, and the macroscopic signals produced by large ensembles of neurons.

The next two chapters outline the acquisition and analysis techniques applied in the experimental chapters. This includes the theory of MEG in Chapter 3, describing the

sensors, magnetic shielding and a typical experiment setup. We also outline the traditional analysis techniques used to interrogate the data. This is followed by the equivalent for fMRI in Chapter 4, describing the physics of MRI, various pulse sequences used in the experimental chapters, and standard analysis procedures.

Chapter 5, the first experimental chapter, uses MEG to uncover whether PTRs follow working memory processes, an example of higher cognitive function. Importantly, we use long rest periods in between task blocks to allow MEG activity to fully come to baseline after any persistent PTR activity. Using traditional analysis techniques, we find that PTRs occur in multiple brain regions and frequency bands, are modulated by working memory load, and show promising relationships with behavioural measures of task difficulty.

Following our discovery of PTRs in a working memory task, Chapter 6 uses HMMs to characterise the transient single-trial events that drive these responses, comparing our working memory dataset with a visuomotor dataset containing the well-studied PMBR. We find that intrinsic burst characteristics driving PTRs are consistent on a region-wise basis across tasks. We also find that PTRs are supported by coincidence of bursts across the entire cortex as well as in task-specific networks.

Chapter 7, the final experimental chapter, studies 7T fMRI responses with a similar working memory task to the previous experimental chapters, allowing us to study the post-stimulus BOLD response as a potential correlate of electrophysiological PTRs following working memory. We find condition-dependent modulation of post-stimulus BOLD responses in three distinct networks, as well as in subcortical structures, which are challenging to image using M/EEG. We find that the post-stimulus BOLD response has spatial and dynamic components that are modulated independently of the primary response.

Finally, in Chapter 8 we make a set of reflections and conclusions based on all of the work presented, including directions that future research may take in further study of the post-task period of brain activity.

1.4 Impact Statement

Overall, this thesis provides valuable insight into network control mechanisms that are essential for healthy brain function. The findings presented corroborate existing evidence showing that the post-task period of activity reveals functionally relevant information about the brain that does not seem to be contained within responses that occur *during* stimulation.

As described earlier, the PMBR, measured with M/EEG, has shown a range of clinical interactions in previous studies, showing promise as a clinical biomarker for neurological illness. Specifically, responses such as this could be used to diagnose or prognose illnesses before sufficient behavioural symptoms have emerged. However, this research has only focussed on motor paradigms, limiting understanding of these effects in higher-order networks and illnesses that affect these networks. In addition, the PMBR differs similarly across a range of seemingly different disorders, highlighting the need for a more complete mechanistic understanding of how these disorders affect brain function. The work presented in this thesis provides evidence that PTRs are a general phenomenon exhibited by a range of cortical networks, following higher cognitive activity as well as movement, and seemingly performing a common function in networks that are recruited for a task. The addition of PTRs following working memory in clinical studies would provide a powerful addition to the well-established PMBR, giving insight into control mechanisms in non-motor networks that may be implicated in clinical populations. The study of a range of PTRs in varied networks may enable the delineation of different types and severities of neurological illness, which in turn could guide drug development and bespoke treatment strategies. Finally, this thesis provides another step towards a better understanding of the relationship between PTRs in M/EEG and fMRI, which should allow the non-invasive study of dysfunction in deep grey matter regions in the future, again providing a more complete understanding of cognitive control mechanisms and malfunction of these systems. Based on this work, future clinical protocols could utilise PTRs taken with both M/EEG and fMRI, acquired over several standardised paradigms, to form a thorough assessment of cognitive control mechanisms in a range of essential brain networks.

2 Brain Function

The following chapter provides a description of the mechanisms that underly brain function, including transmission of signals between individual cells, structural and functional segregation of the brain, and macro-scale properties such as haemodynamics and neural oscillations that are measured with fMRI and MEG.

2.1 Cellular Origins of Brain Function

2.1.1 The Neuron

Neurons are cells in the brain that form the basis of cognitive function (Kandel et al., 2000). These cells allow us to respond to stimuli in our environment, such as photons of light, odorous molecules and vibrations in air. Broadly speaking, neurons are split into three categories: *sensory neurons*, receiving information (e.g. heat on the skin) and transmitting to the central nervous system (brain and spinal cord); *motor neurons*, sending information from the central nervous system to the body to control movement; *inter-neurons*, receiving and transmitting information between other neurons. Inter-neurons make up most of the neuronal population in the brain. Neurons are formed primarily of the soma, or cell body, an axon and dendrites, see Figure 2.1. Signals are sent via axon terminals and received via dendrites. The structure of neurons can differ, broadly categorised as: *unipolar*, making up all sensory neurons, containing only a cell body and axon; *bipolar*, with a cell body, axon and a single set of dendrites; *multipolar*, with a cell body, axon and multiple sets of dendrites. Multipolar neurons can be further differentiated based on their geometry, as either stellate, meaning dendrites spread out in all directions in a star-like formation, or pyramidal, where dendrites spread out in one direction from a roughly pyramidal-shaped cell body (see Fig. 2.1). The arrangement of dendrites determines the contribution of neurons to brain imaging techniques such as EEG and MEG (see section 2.3.1).

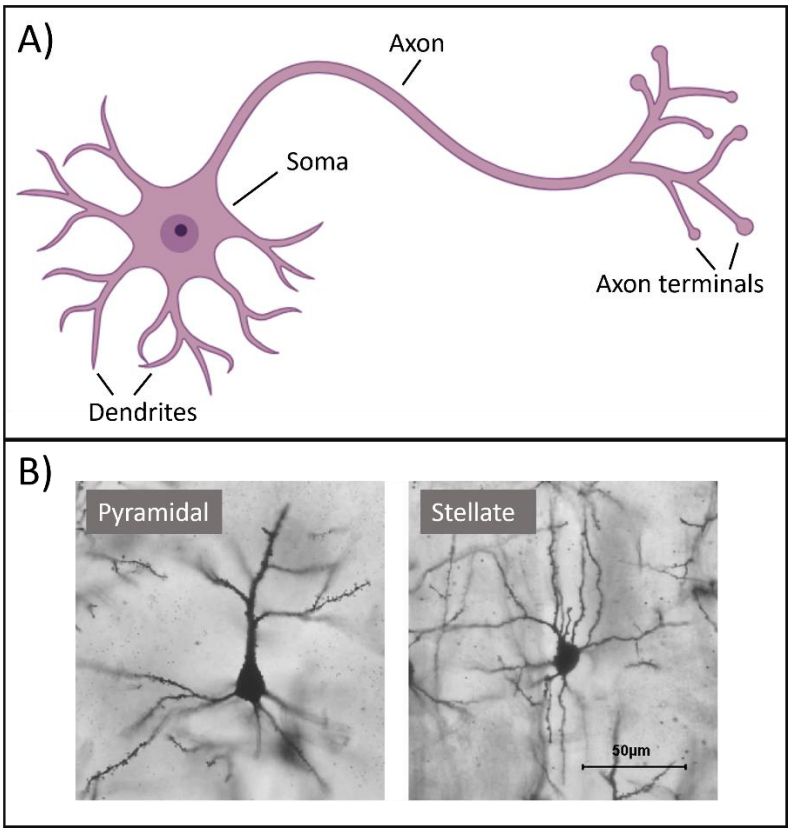


***Figure 2.1**: Panel A shows a diagram of a typical multipolar neuron, showing the axon terminals, axon, soma, and dendrites. Chemical and electrical inputs from other cells are received through the dendrites, and outputs are transmitted from the axon terminals to other cells. Panel B shows the two primary ways in which dendrites are arranged, either pyramidal or stellate, adapted from (Churchill et al. 2004).*

2.1.2 Signal Generation

The primary electrical signal produced by a neuron is known as the *action potential (Kandel et al., 2000)*. A key component of action potentials in neurons is the cell membrane. The electrical potential across this membrane is known as the *membrane potential*. At rest, the membrane maintains a *resting membrane potential*, which is typically around -70 mV inside the cell, occurring due to unequal distribution of ions on either side of the membrane, predominantly sodium (Na^+) and potassium (K^+).

Transport of ions across the cell membrane is facilitated largely by *channels*, and *pumps*. Channels allow passive transport of ions via diffusion, although some types of channels will allow certain ions to diffuse through more readily. Pumps use active transport, requiring energy to move specific ions through the membrane. Pumps maintain the concentration gradient between the inside and outside of the cell. For example, sodium-potassium pumps keep the concentration of sodium inside the cell around one tenth of its concentration outside the cell, whilst potassium is kept 20 times

higher inside the cell than its concentration outside. At rest, the cell channels are more permeable to potassium than sodium, allowing potassium to diffuse out of the cell due to the concentration gradient, leaving the inside of the cell more negatively charged.

In order to produce an action potential, a neuron must first enter an excitable state. Inputs from other neurons arrive through the dendrites, creating a change in resting membrane potential at the *axon hillock*, a region near the cell body, before the axon. If the resting membrane potential at the axon hillock reaches a particular threshold voltage, typically around -55 mV, a series of events is triggered, causing production of an action potential. The change in resting membrane potential from around -70 mV to -55 mV causes voltage-gated sodium channels to open, allowing a rapid influx of Na^+ across the membrane into the cell down the concentration gradient. This results in an overall positive membrane potential, a process known as *depolarisation*. Once the membrane potential reaches a peak of around +40 mV, voltage-gated potassium channels open, allowing K^+ ions to diffuse out of the cell down the concentration gradient, a process known as *repolarisation*. Importantly, the repolarisation phase overshoots, creating a short period of *hyperpolarisation*. Hyperpolarisation ensures directionality of the signal, and also creates a *refractory* period where the cell is less excitable for a short time, limiting the time between consecutive action potentials. The process of action potential production is shown schematically in Figure 2.2, as well as a plot of the changes in membrane potential. Following production at the axon hillock, the action potential travels down the length of the axon to be transmitted to other cells. Action potentials are always the same amplitude, meaning higher initial depolarisation does not increase the amplitude of the action potential, instead contributing to the frequency of subsequent action potentials.

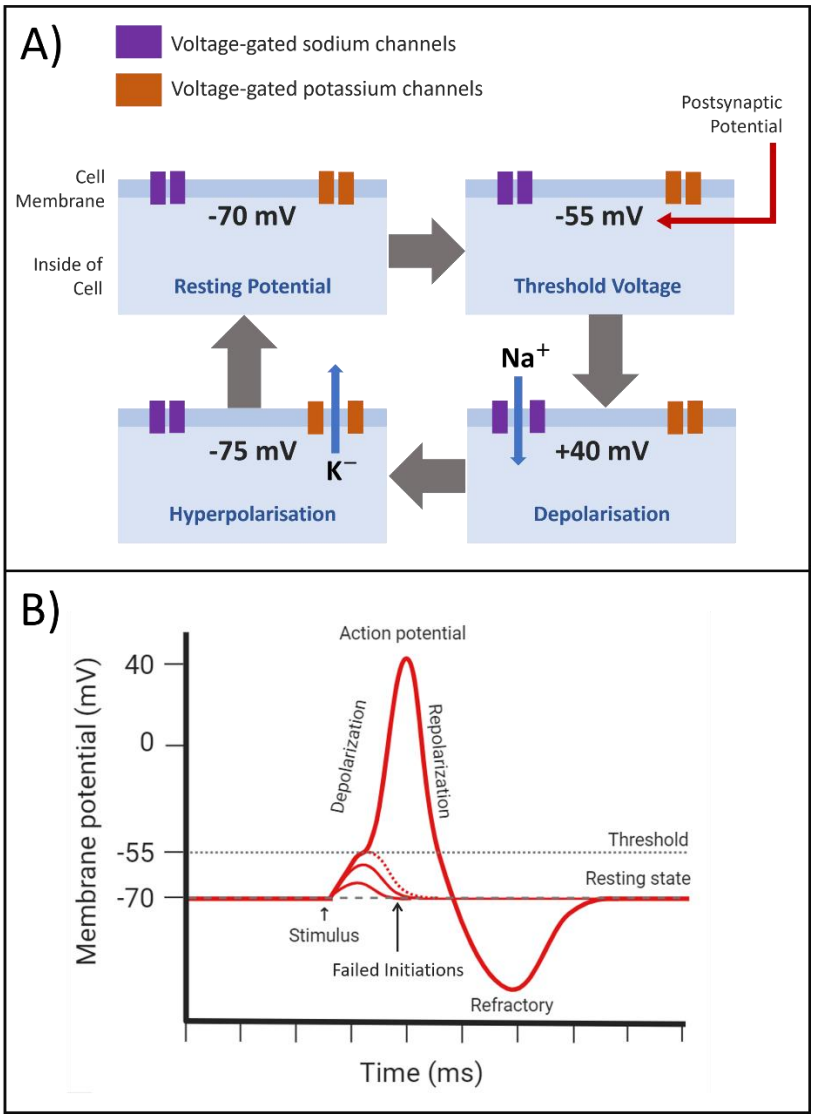


***Figure 2.2**: Panel A contains a simplified schematic showing the processes that occur at the axon hillock to create an action potential. Changes in resting membrane potential cause the opening and closing of voltage-gated channels, allowing specific ions to pass through the membrane following concentration gradients. The movement of ions across the membrane causes the membrane potential to change, according to the plot in panel B, going through phases of depolarisation, repolarisation and hyperpolarisation before returning to resting state. Hyperpolarisation creates a refractory period, temporarily reducing neuron excitability.*

2.1.3 Synaptic Transmission

The action of a single neuron is not very useful alone. In order to achieve complex behaviours in humans and animals, neurons must communicate with other neurons using synaptic transmission. A *synapse* is the point at which the axon terminals of one neuron meet the dendrites of another. A single neuron can receive signals from several thousand other neurons and send signals to a similar number of other neurons. We

call the neuron producing the signal the *presynaptic* cell, and the one receiving the signal the *postsynaptic* cell. Synapses allow signals to propagate using either electrical or chemical processes (Kandel et al., 2000). In the case of electrical synapses, the presynaptic and postsynaptic cell are physically connected by a set of *gap junction channels*, which allow signals to propagate directly through shared cytoplasm. Chemical synapses consist of a small gap, or *cleft*, which a particular set of chemicals, known as *neurotransmitters*, diffuse across, binding to proteins on the postsynaptic receptor site. Chemical synapses allow for a greater range of behaviours than electrical synapses, as there are numerous types of neurotransmitters and receptor sites that lead to different outcomes in postsynaptic cells.

In chemical synaptic transmission, neurotransmitters are released into the cleft when an action potential propagates down the axon to the axon terminals (a schematic is shown in Fig. 2.3). Once neurotransmitters bind to the postsynaptic membrane, ion-specific channels are opened in the postsynaptic cell, leading to a flow of ions across the membrane, causing a *postsynaptic potential*, which is a shift in the postsynaptic membrane potential away from resting levels. The effect of postsynaptic potentials can either be *excitatory* or *inhibitory*. Excitatory neurotransmitters will trigger a slight depolarisation by opening sodium channels, causing an influx of sodium ions into the cell, increasing the chance of an action potential. Inhibitory neurotransmitters will trigger a slight hyperpolarisation by opening potassium channels, causing potassium ions to leave the cell, decreasing the chance of an action potential. A single neuron can have many excitatory and inhibitory inputs which travel down the dendrites and sum at the axon hillock. The balance of excitatory and inhibitory inputs at the axon hillock at any point in time determines whether the postsynaptic cell produces an action potential. While neurons can have both excitatory and inhibitory inputs, it should be noted that the output from a neuron is usually either excitatory or inhibitory. For example, pyramidal neurons are the primary excitatory neuron in mammals.

The current created due to chemical synaptic transmission has two components: *Primary* current, and *volume* current. The primary current is created by the influx of ions from the extracellular to the intracellular space, through channels in the dendritic cell membrane – in the case of sodium ions, the influx creates an intracellular source (increase in potential), creating a flow of ions down the dendrite towards the cell body. A side-effect of the influx of sodium ions is the creation of a local extracellular *sink* (reduction) in potential, which must be balanced by a volume current which flows in the extracellular medium.

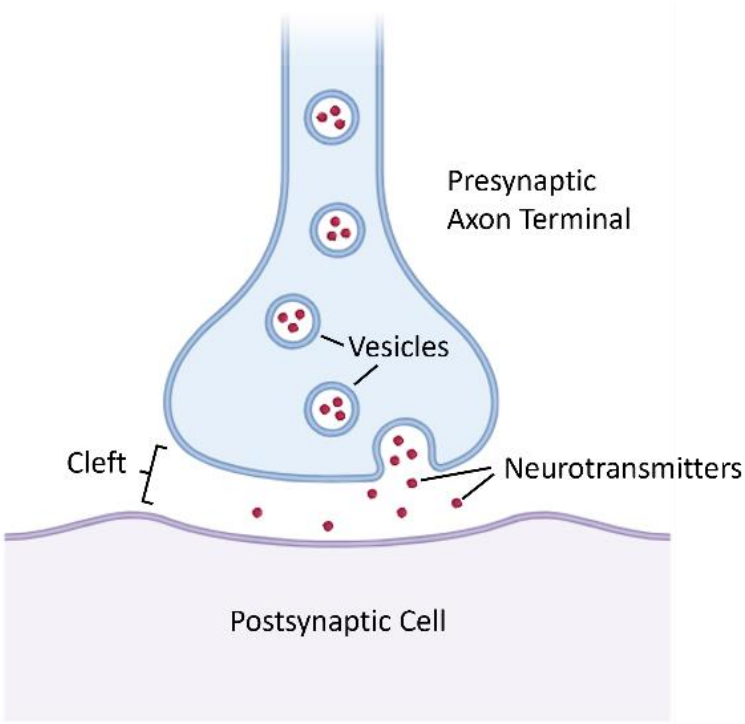


***Figure 2.3**: A schematic showing the process of chemical synaptic transmission. An action potential in the presynaptic cell triggers the production of neurotransmitter chemicals, which are transported to the axon terminal in vesicles. The neurotransmitters are released into a small gap, or cleft, where they diffuse to receptor sites on the postsynaptic cell membrane, causing changes in the postsynaptic membrane potential.*

2.2 Brain Anatomy and Functional Segregation

2.2.1 Grey and White Matter

The brain can be divided into white and grey matter (Mercadante and Tadi, 2023). White matter consists mostly of axons, getting its name from the layer of *myelin* surrounding the axons, which is pale in colour and speeds up the rate of signal transmission. Axons in the white matter form so-called neuronal tracts which physically connect different regions of the brain, allowing for long range neuronal communication. Grey matter is formed mostly of cell bodies and dendrites, with the high abundance of cell bodies giving it its darker colour. Grey matter is essential to almost all cognitive functions performed by humans due to the sheer number of connections that are made within it, allowing complex neural networks to form. An MRI of a brain is shown in Figure 2.4, with white and grey matter labelled.

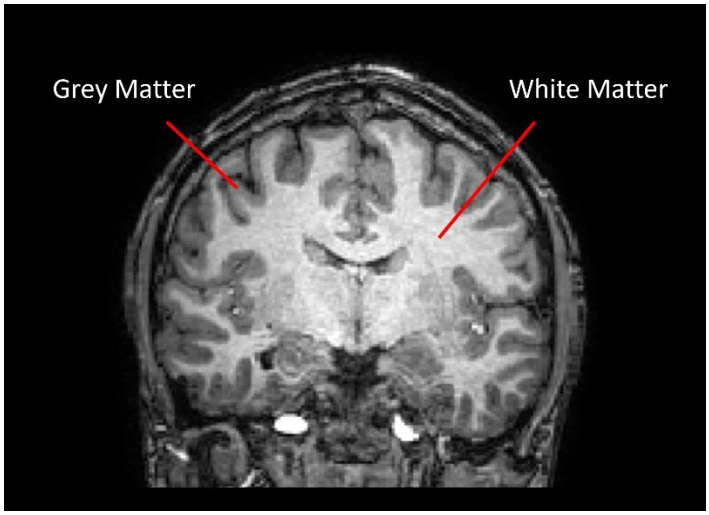


***Figure 2.4**: An MRI of a brain, showing white and grey matter. White matter mostly occupies the deeper parts of the brain, while grey matter occupies the superficial layer of the brain as well as subcortical structures (see section 2.2.3).*

Cortical grey matter is split into a set of cortical layers (Shipp, 2007), each performing a distinct function. For example, layer IV receives input from sensory neuronal pathways, while layer I, the outermost layer, plays a role in integrating inputs from other cortical regions. In addition to layers, neurons in grey matter tend to arrange themselves into cortical columns, which are clusters of neurons, mostly pyramidal neurons, with similar functionality (e.g., dealing the same aspect of sensory inputs), oriented perpendicular to the cortical surface. We can think of a cortical column as a single processing unit, with the ability to take sensory information, process it, and produce outputs which are sent to other cortical columns and regions of the brain.

2.2.2 Functional Segregation of the Cortex

As discussed above, neurons within a cortical column tend to share functional properties, such as responding to the same type of stimuli. In turn, groups of columns amass to form broader functional domains which deal with a more general aspect of cognition, e.g., visual processing. A coarse set of functional domains is shown in Figure 2.5, including frontal, parietal, occipital and temporal lobes (Kandel et al., 2000, Casillo et al., 2020). Generally speaking, the occipital lobe is associated with visual processing, the parietal lobe is associated with higher order visual and sensory processing, including attention and spatial awareness, the temporal lobe is associated with auditory processing and memory, and the frontal lobe is associated with executive functions as well as motor planning and execution. It should be noted that this is perhaps the most coarse functional segregation of the cortex; each of these lobes can

be subdivided into more specific functional domains. For example, the occipital (visual) lobe can be split into several sub-regions, starting with v1, related to early stages of visual processing, followed by v2, v3 and v4 which deal with later, more complex stages of visual processing (Roland and Zilles, 1998). Importantly, these large functionally segregated regions, as well as those within each lobe, are connected to one another in a complex network, meaning that the information processed in one region can be combined with information from other regions to form a more complete picture of the world around us.

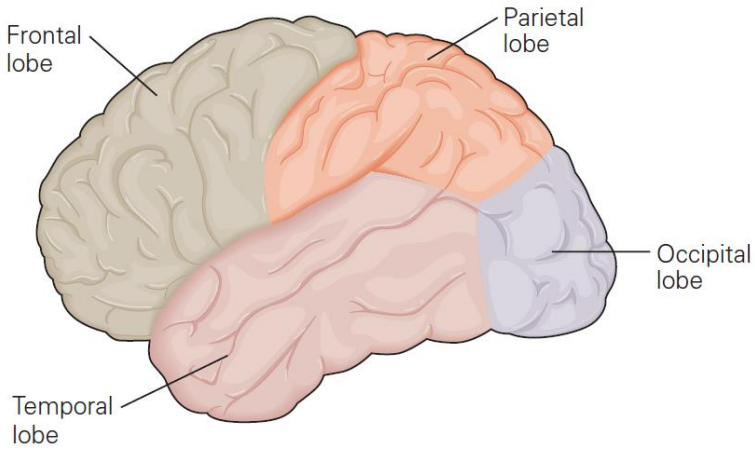


***Figure 2.5**: The lobes of the brain, representing broad functional domains in the cortex, each dealing with a particular aspect of cognition. Taken from (Kandel et al. 2000).*

2.2.3 Subcortical Structures

Beneath the cortex lies a set of structures, known as subcortical structures, which far predate the cortex in evolutionary terms, being shared by much simpler vertebrates. Generally speaking, these structures deal with early stages of information processing, receiving information from the body and sensory systems and guiding the flow of information to higher order cortical structures. For example, the amygdala, sat deep under the temporal lobe, is involved in immediate threat detection (Öhman, 2005), creating a fear response to natural threats such as snakes or spiders that is far faster than our higher cognitive response to the same stimuli, allowing us to react before we have consciously attended to the stimulus. The thalamus, the largest subcortical structure, sitting centrally beneath the cortex, is heavily involved in sensory processing (Sommer and Wurtz, 2006, Yen and Lu, 2013), receiving information from our sensory systems, including visual information from the retina, or pain signals from receptors in the skin, and relaying (and sometimes, limiting) the information to various other regions of the brain for further processing. The hippocampus, located under the medial temporal lobe (Eichenbaum et al., 1999), controls whether information becomes

embedded in long-term memory based on information from other systems. Although these subcortical structures, as well as those not mentioned here, are particularly implicated in certain processes, it should be noted that subcortical structures are essential to nearly all human behaviour. A diagram of the position of these structures in the brain is shown in Figure 2.6 (Raju, 2020).

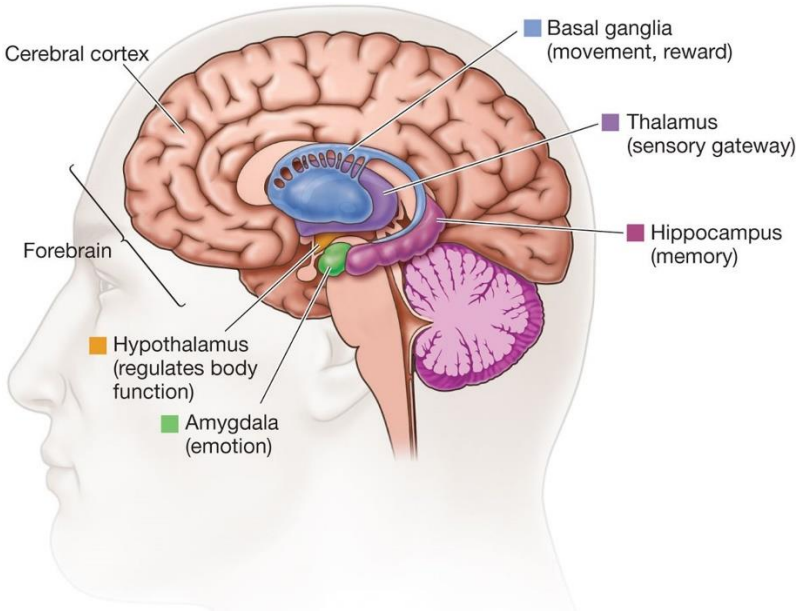


***Figure 2.6**: A labelled diagram of subcortical structures in the brain, taken from (Raju, 2020). These structures are evolutionarily older than the cortex, being shared with more simple vertebrates, and are involved in early stages of information processing.*

2.2.4 Hierarchical Neuronal Processing

As described in the above sub-sections, different regions of the brain, both cortical and subcortical, deal with specific aspects of information processing. Connectivity of these regions, in so-called neural pathways and circuits, allows for efficient transmission between hierarchical processing units.

The way that information is transmitted through neural pathways can be described as bottom-up and top-down, based on the direction in which information travels through the hierarchy of processing units. The terms feedforward and feedback are also commonly used to describe these processes. Bottom-up processes are those which are data-driven, where sensory information is used to guide a response in higher cognitive brain regions. Bottom-up processes (Ward, 2013) generally begin at sensory neurons, travelling to the thalamus, where the information is relayed to regions involved in early sensory processing (e.g., v1). An example of a bottom-up process is the recognition of pain after touching a hot object or seeing a flashing light.

Top-down processes (Gilbert and Li, 2013) are guided by perception rather than data, meaning higher cognitive constructs, such as attention and perception, as well as a priori knowledge, are used to inform the response to external information. For example, information about a non-attended visual stimulus is prevented from reaching higher order visual brain regions for further processing. Top-down circuitry minimises the amount of information that must be actively processed from the environment to form a useful model of our surroundings, in turn reducing the energy expenditure of ongoing cognition.

Both bottom-up and top-down processes are involved in any given neural pathway. For example, in the visual pathway (Wurtz and Kandel, 2000): sensory neurons in the retina pick up visual information; visual information is converted to neural signals which are transmitted to the thalamus; the thalamus then transmits signals to v1 in the occipital cortex via thalamo-cortical connections to begin processing; processed signals are then transmitted to higher-order visual regions such as v2, v3 etc via cortico-cortical connections to be processed and integrated with information from other brain regions. So far, this process has been purely bottom-up, however, thalamo-cortical and cortico-cortical *loops* allow information to be fed back down the hierarchy of processing units to modulate signals which are fed upwards (top-down information flow), based on existing models, e.g., knowledge that a particular type of visual stimulus is irrelevant to the task at hand. A schematic of simplified neural circuitry is shown in Figure 2.7.

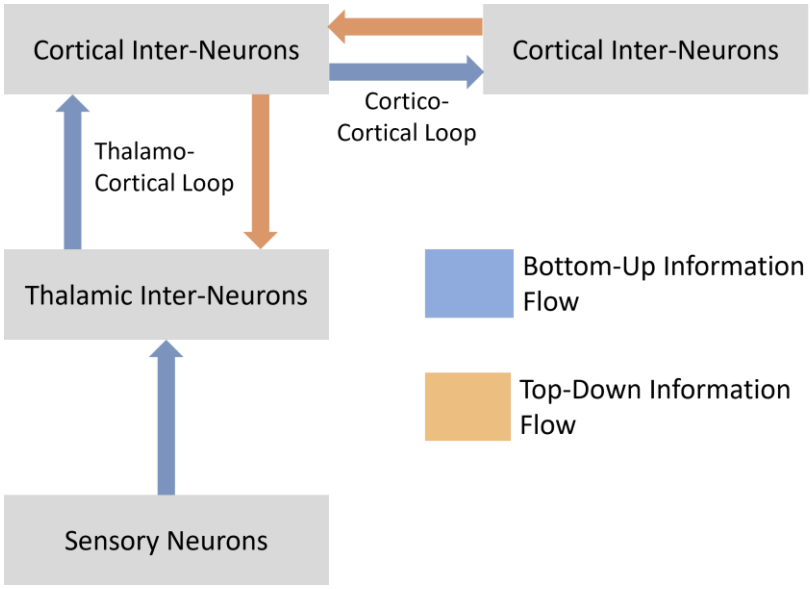


***Figure 2.7**: A simplified schematic demonstrating the principle of bottom-up and top-down information flow, in the context of neural pathways. Sensory information flows upwards through the hierarchy of processing units, from sensory neurons, to the thalamus, to cortical regions which deal with early sensory processing. These cortical regions then often transmit this information to other cortical regions that deal with higher-level sensory processing. Thalamo-cortical and cortico-cortical loops allow for higher order brain regions to modulate the transmission of bottom-up signals through the pathway, transmitting information down the hierarchy of processing units. In reality, connections between brain regions are much more complex than this schematic, but the same principles are applied.*

2.3 Measurable Brain Activity

We now understand how signals are produced in neurons, how these propagate into a vast network via synapses and dendrites, and how the brain operates in functional domains to process these signals. Several non-invasive imaging techniques such as MEG and fMRI (see Chapters 1, 3 and 4) are able to measure macro-scale properties of brain function, arising due to the action of large ensembles of neurons. This sub-section will outline the signals commonly measured by non-invasive techniques such as EEG, MEG and fMRI.

2.3.1 Neural Contributions to MEG Signal

The first human electroencephalogram was taken by Hans Berger in 1924 (Berger, 1929), marking the beginning of a vast field of study into electrophysiological brain signals that could be taken non-invasively in humans using techniques such as EEG or MEG. These signals arise directly due to neuronal activity, or more specifically, the synchronous activity of large ensembles of neurons.

As explained in section 2.1.2, the action potential is the output of a neuron, while the postsynaptic potential is the input (Ullsperger and Debener, 2010). The different properties of these signals determine how they contribute to measurable signals. Action potentials are higher in amplitude, but they only last around 1 ms. Postsynaptic potentials are lower in amplitude, but lasts around 10 ms. In addition, action potentials act as a quadrupolar current, meaning the magnetic field decays as $1/r^3$, while postsynaptic potentials act as a current dipole, with a corresponding field decay of $1/r^2$. The properties of these signals mean that postsynaptic potentials are more likely to temporally overlap and produce a large enough field to be measured extracranially using MEG. A single postsynaptic current is typically around 20 fAm (Hämäläinen et al., 1993), meaning that around 100,000 – 1000,000 of these must coincide to produce a measurable MEG signal. Dendrites occupy the grey matter of the brain, meaning postsynaptic potentials only originate in grey matter, constraining the locations of MEG contributors in the brain.

The geometry of neurons further constrains the source of extracranial measurable signals. The dendrites of stellate neurons (section 2.1.1) point in all directions, meaning the fields measured far from the cell sum to zero. The dendrites of pyramidal neurons are approximately parallel to each other, with an overall net direction, meaning they create a measurable field at a distance from the cell. Pyramidal neurons are the primary excitatory cells in mammals, but the postsynaptic potentials (the signals primarily measured by EEG and MEG), which act as the input to these cells, can be both inhibitory and excitatory.

2.3.2 Types of Electrophysiological Response

Extracranial responses are commonly split into two categories: induced and evoked responses. Evoked potentials are changes in electrical potential specifically related to stimuli. These are time-locked and phase-locked to stimulus timings, meaning that responses occur with the same phase and latency relative to stimulus presentation. Induced responses are changes in the power of spontaneous rhythms, which are ongoing rhythms in the cortex, related to changes in cognitive states. Induced responses are time-locked to tasks and stimuli, but not phase locked, meaning that there will be between-trial variation in amplitude and phase of the signal. Different brain regions and tasks are associated with particular induced frequency responses, leading to a set of canonical frequency bands that can be used to characterise a response. A simple schematic of evoked and induced responses is shown in Figure 2.8. The following sections will describe these categories of electrophysiological response, both

evoked and induced, in greater detail, including the neuroscientific and clinical relevance of both.

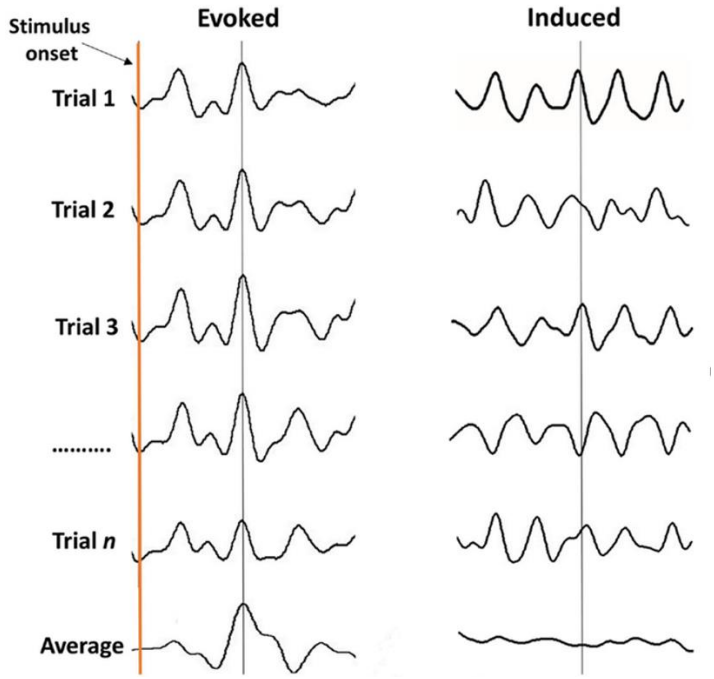


***Figure 2.8**: A simplified schematic showing evoked and induced responses in electrophysiological recordings. Evoked potentials occur with the same phase and latency following stimulus onset, meaning that simply averaging over trials will reduce the effect of random noise. Induced responses are changes in the power of ongoing spontaneous rhythms, related to a stimulus or task. Induced responses do not occur with the same phase between trials, meaning that simple averaging cannot be used to reduce the effects of noise.*

2.3.3 Evoked Responses

Evoked potentials are phase-locked responses relating to processing of stimuli, occurring with the same shape and latency following sensory input. These were reported in humans shortly after Berger's initial demonstrations of spontaneous rhythms, in response to light flickering at a specific frequency (Adrian and Matthews, 1934). These responses are related to the transmission of information through neural pathways which occurs upon sensory stimulation, occurring at a particular latency and location depending on the neural pathway (e.g., visual, auditory) that is activated. An example of an evoked response is the P100 (Shigeto et al., 1998, Spehlmann, 1965), a visual evoked response which can be measured in the primary visual cortex (v1), relating to early visual processing. Further evoked responses often follow this, such as the P300 (Machado et al., 2014), occurring in higher cognitive regions (such as the parietal cortex), relating to the integration of visual information with higher cognitive processes such as attention and working memory. It is debated whether measured evoked responses are created by neural activation in discrete, functionally defined

domains (e.g., v1), superimposed on other neuronal signals and noise, or a stimulus-induced phase-resetting of ongoing neural synchrony (Makeig et al., 2002).

Both bottom-up and top-down processes contribute to the measured evoked potentials. For example, different types of stimulus (e.g., visual, auditory, sensory) will create different spatiotemporal evoked potentials due to differences in the type and location of sensory neurons which receive the stimulation, e.g., sensory neurons in the eyes or ears, reflecting a bottom-up flow of information. However, evoked potentials can also be modulated by higher order processes such as attention (Hillyard and Anllo-Vento, 1998), reflecting top-down flow of information through neural pathways.

Due to the phase locking of evoked potentials, they can be analysed quite simply by averaging over trials, reducing the effects of random noise (see Chapter 3). Due to the relationship between evoked potentials and stimulus processing in the brain's sensory systems, they can be used clinically to detect malfunction in such systems (Halliday et al., 1973), manifesting as changes in waveform morphology. They can also be used in neuroscientific study, often in conjunction with induced and behavioural measures, as a marker of stimulus perception (Sutton et al., 1965, Du et al., 2017, Morgan et al., 1996).

2.3.4 Induced Responses

Spontaneous rhythms were first measured in humans by Hans Berger in 1924 (Berger, 1929), measuring what we now call the *alpha* rhythm, which was initially coined the *Berger* rhythm (Adrian and Matthews, 1934). In his experiments, approximately ten of these waves occurred per second while the subject was at rest with closed eyes, disappearing when the subject was fully attended to their environment. This was the first example of an induced EEG response in humans, i.e., a change in oscillatory power during a particular cognitive state, relative to a baseline cognitive state which is often a rest (no changing stimuli or task demands). To measure induced responses, the potentials must be squared and averaged over trials (see Chapter 3) as the waxing and waning pattern of spontaneous rhythms varies both within and between subjects (Pfurtscheller and Lopes da Silva, 1999, Adrian and Matthews, 1934), with no phase locking relative to stimulus presentation. In the case of the beta rhythm, the oscillations are often explicitly described as *bursts* (see Chapter 6) due to the extreme fluctuations that can be seen on the single trial level (Pfurtscheller, 1981, Pfurtscheller et al., 1996b), as seen in Figure 2.9.

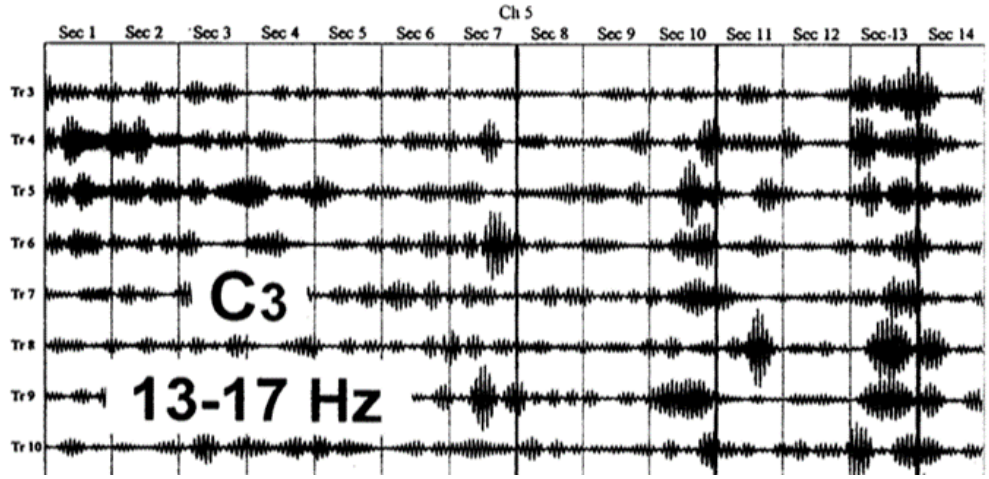


***Figure 2.9**: A figure taken from (Pfurtscheller, Stancak, and Neuper 1996b) showing bursting behaviour of induced brain activity in the low beta band.*

Induced responses come in the form of event-related synchronisation (ERS) and event-related desynchronisation (ERD) (Pfurtscheller and Lopes da Silva, 1999), corresponding to increases and decreases in oscillatory power, respectively, relative to baseline. Changes of these types are often split into a set of canonical frequency bands (Ullsperger and Debener, 2010), including delta (2 – 4 Hz), theta (4 – 8 Hz), alpha (8 – 13 Hz), beta (13 – 30 Hz) and gamma (30 – 100 Hz), which tend to be localised to particular regions of the brain, in response to a particular type of stimulus or task. These rhythms will be explained further in the subsections below. It must be noted that these descriptions aim only to provide a basis to understand the methodologies presented in later chapters, as research surrounding oscillatory rhythms is expansive and there are many distinct interpretations of the described effects that cannot be easily reconciled.

The Alpha Rhythm

The alpha rhythm, in the 8 – 13 Hz range, was the first spontaneous rhythm to be measured, nearly 100 years ago (Berger, 1929). These were found to be the strongest over the occipital cortex during a relaxed wakeful state with closed eyes and were interrupted by opening the eyes. Although the exact neurophysiological mechanisms underlying alpha oscillations are uncertain, experimental evidence and mathematical models have shown that alpha oscillations depends on the resonance properties of thalamo-cortical loops (see section 2.2.4) (Hindriks and van Putten, 2013, Da Silva et al., 1974, Steriade et al., 1990). Other studies have shown that both thalamic and pyramidal cortical neurons can have intrinsic “pacemaker” properties which encourage rhythmicity in the firing of connected circuits, leading to alpha oscillations (Da Silva and

Van Leeuwen, 1977, Andersen and Andersson, 1968). In addition, studies using iEEG in monkeys and humans have found convincing relationships between alpha oscillations and feedback (top-down) information flow (see section 2.2.4) in cortical circuits, showing directionality of alpha oscillations from higher order to lower order regions (Halgren et al., 2019, Van Kerkoerle et al., 2014).

Alpha oscillations were long associated with an idling brain (Pfurtscheller et al., 1996a), such that the oscillation represents a default state for the visual network. Testing over more complex paradigms showed that alpha oscillations were reliably modulated by working memory load, and were directly related to task performance, leading to the hypothesis that alpha oscillations are related to active suppression of external/distracting information to prioritise task-relevant neural processes (Jensen et al., 2002, Tuladhar et al., 2007). In keeping with the putative models of alpha generation discussed above, it is likely that increases in alpha relate to increases in feedback inhibition in thalamo-cortical circuits (see section 2.2.4), essential in managing sensory information flow throughout cortex (Klimesch et al., 2007, Jensen and Mazaheri, 2010).

The Beta Rhythm

The beta rhythm was the second spontaneous rhythm to be reported by Hans Berger (Berger, 1930). These were smaller and faster (13-30 Hz) oscillations that seemed to replace the alpha rhythm upon opening of the eyes. These were later found to relate more closely to sensorimotor activity, with higher spontaneous power during rest, and reduction due to movement of one or more body parts (Neuper and Pfurtscheller, 2001, Pfurtscheller, 1981). Beta activity was also found to modulate with passive motor stimuli, i.e., touch, or imagined movements (Pfurtscheller et al., 2005, Pfurtscheller and Neuper, 2001).

Given the fact that beta oscillations were strongest during inactivity (Pfurtscheller, 1981, Pfurtscheller et al., 1996b, Stancak and Pfurtscheller, 1995), this rhythm was initially considered a correlate of an idling sensorimotor system. Similar to alpha, later studies showed that beta may relate to active inhibition in the sensorimotor network, with effects such as slowing of voluntary movements made during periods of high beta oscillatory power (Chen et al., 1998, Jensen et al., 2005, Gilbertson et al., 2005, Pogosyan et al., 2009). Other lines of evidence have related beta oscillations to inter-regional connectivity, showing increased beta coherence (phase relationship) during known co-activity of brain regions (Roelfsema et al., 1997, Classen et al., 1998). In addition, forming another parallel with alpha, beta oscillations have been specifically

linked to top-down neuronal processes, with increased beta coherence in higher cognitive networks during periods of top-down attention-shifting processes (Buschman and Miller, 2007). As with alpha, the evidence relating beta oscillations to both behavioural inhibition and inter-regional connectivity suggests that these oscillations may be closely related to top-down inhibition in neural circuits, essential in managing information flow through neural pathways to higher cognitive regions (see section 2.2.4).

The Theta Rhythm

Theta oscillations are defined as approximately 4 – 8 Hz, and are known to modulate with a variety of cognitive tasks, particularly those involving working memory (Klimesch, 1999, Sauseng et al., 2010). Theta rhythms are commonly measured across frontal midline electrodes/sources (Inanaga, 1998), although studies also report parietal theta activity related to working memory (Sauseng et al., 2005, Wolinski et al., 2018). In addition, hippocampal theta is a well-studied phenomenon in animal brains (Nuñez and Buño, 2021), with phase-locking effects demonstrated between prefrontal and hippocampal theta in the rat brain (Siapas et al., 2005) and putative roles in navigational learning (Foster and Wilson, 2007) and working memory (Vertes, 2005). Experiments have shown that pacemaker properties in the medial septum (subcortical structure separating the two brain hemispheres, closely involved with the hippocampus) are likely to generate hippocampal theta (Gogolak et al., 1968), and relationships between frontal and hippocampal theta suggest a common generator (Mitchell et al., 2008, Soltani Zangbar et al., 2020). However, other studies have suggested a separate generator of frontal theta in the anterior cingulate (Asada et al., 1999).

Interestingly, during cognitive tasks, theta is usually shown to increase (ERS) during the attentive state, which is the opposite behaviour to alpha and beta, which reliably decrease (ERD) during increased attention. Some studies show relationships between theta rhythms and the default mode network (DMN) (Scheeringa et al., 2008, Tyvaert et al., 2008), an example of a *functional network* (see section 2.3.7) whose activity often *negatively* tracks attentiveness (Anticevic et al., 2012, Ceko et al., 2015). This relationship may explain the opposing behaviour of theta compared to alpha and beta, as periods of high amplitude theta may correspond to *inactivity* of the DMN to facilitate attention, just as periods of high amplitude alpha and beta correspond to *inactivity* of the visual and sensorimotor systems. As with alpha networks, this is likely achieved by top-down information flow in recursive neural circuits (Mitchell et al., 2008) which link

the hippocampus with the DMN through fronto-hippocampal pathways (Soltani Zangbar et al., 2020).

Other Spontaneous Rhythms

The delta and gamma rhythms will be described here for completeness, albeit in less detail as they are not the focus of this thesis.

Gamma activity ranges from 30 – 100 Hz (Ullsperger and Debener, 2010) and is often associated with a state of cortical excitability. Evidence from animal experiments suggests that visual gamma, observed reliably with multiple modalities in primary visual regions, is related to bottom-up (feedforward) information flow in the visual pathway (Michalareas et al., 2016, Van Kerkoerle et al., 2014), reflecting the opposite process to alpha oscillations in the same system. Increases in gamma activity are often seen during ERD of the lower frequency bands, specifically theta and alpha, suggesting functional coupling, posited as a mechanism for guiding the flow of information in functional networks (Jensen and Mazaheri, 2010). This is supported by evidence relating gamma to synchronisation of spike timings in neural networks (Singer, 1993). Interestingly, gamma oscillations measured with stereo EEG (sEEG) are found to be spatially coupled to haemodynamic (blood flow) changes measured with fMRI (see section 2.3.5) (Lachaux et al., 2007), although the amplitudes of the signals are not directly coupled (Muthukumaraswamy and Singh, 2009, Butler et al., 2017).

Delta waves are those with frequencies below 4 Hz (Ullsperger and Debener, 2010), and are typically associated with sleep, particularly so-called *slow-wave* sleep, and are more prominent in children. Elevated delta power during wakeful states in adults has been associated with pathology.

Post-Stimulus Induced Responses

The sections above described how spontaneous rhythms may vary in power due to changes in cognitive state. Another group of induced responses are those that occur shortly *after* a change in cognitive state, more specifically, during a transition between an engaged state and rest, i.e., a *post-stimulus response*. These have long been studied in the beta band following movement (Pfurtscheller, 1981, Pfurtscheller et al., 1996b), and are often referred to as post-movement beta rebounds (PMBR). The PMBR is defined as a post-movement ERS in beta power, usually occurring in contralateral motor regions, lasting 6 – 10 s (Neuper and Pfurtscheller, 2001). This effect has been described as a temporary increase in the number of *beta burst* events (Pfurtscheller, 1981, Pfurtscheller et al., 1996b), i.e., moments of high amplitude beta

activity that sum over trials to form a smooth ERS (see Chapter 6), as shown in Figure 2.10. A similar post-stimulus ERS effect is seen in the alpha band too, spanning central, parietal and occipital regions (Neuper and Pfurtscheller, 2001, Mullinger et al., 2013, Mullinger et al., 2017), following both movement and visual stimulation. Although these are usually termed post-stimulus responses, it should be noted that we refer to these in later chapters as *post-task responses* (PTRs) as we find that responses of this type follow cognitive tasks as well as sustained sensorimotor or visual stimuli (see Chapter 5).

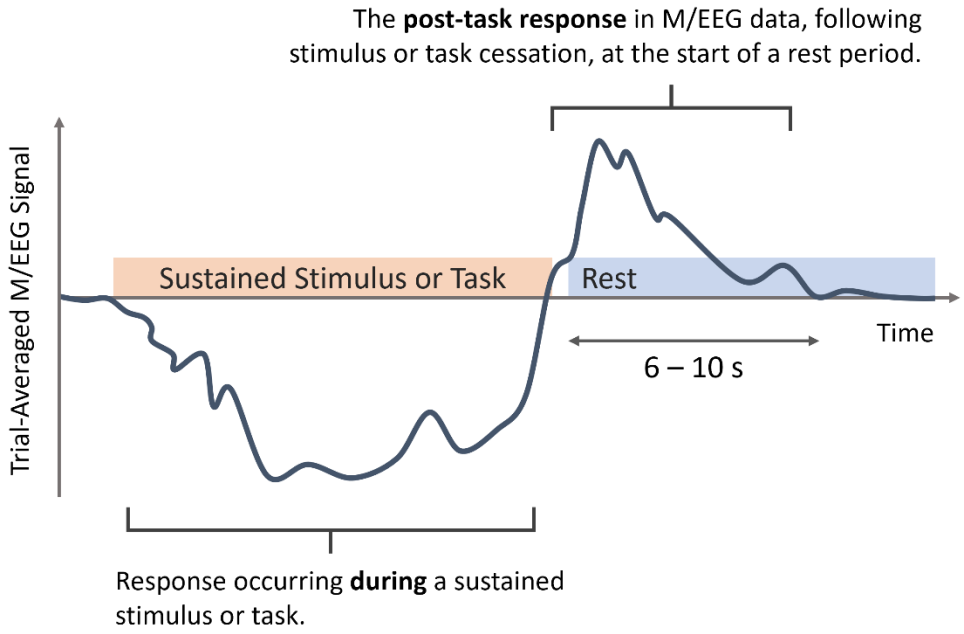


***Figure 2.10**: A schematic of the post-task induced response, measured with MEG or EEG following stimulus or task cessation and lasting for up to 10 s. This response must occur at the start of a rest period, not during a period of continued engagement. See Figure 2.11 for the equivalent response in BOLD fMRI data.*

The precise neural mechanisms that produce post-stimulus responses in EEG and MEG are not fully understood, but there is a wealth of evidence that relates post-stimulus ERS in alpha and beta to inhibition of cortical networks (Neuper and Pfurtscheller, 2001, Chen et al., 1998, Mullinger et al., 2013, Mullinger et al., 2017, Pakenham et al., 2020, Pfurtscheller et al., 2005, Fry et al., 2016). Evidence includes, but is not limited to: the fact that these rhythmic increases occur during *inactivity* rather than activity, or during periods of behavioural inhibition (Pfurtscheller et al., 1996b, Pfurtscheller et al., 2005); these responses scale in magnitude in seemingly more demanding task conditions (Fry et al., 2016, Pakenham et al., 2020); these responses are greater after termination of real vs imagined movements (Solis-Escalante et al., 2012). In keeping with established evidence surrounding neural oscillations in the

alpha and beta bands (see section 2.3.4), these responses may be generated by top-down information flow in circuits which link the thalamus to cortical sensory networks, limiting the sensory information flowing to higher cortical regions following cessation of task-related processes.

This group of responses is made particularly interesting by the many reported links with pathology, including patients with schizophrenia (Gascoyne et al., 2021, Hunt et al., 2019), autism spectrum disorder (ASD) (Gaetz et al., 2020) and multiple sclerosis (MS) (Barratt et al., 2017b). In the case of schizophrenia, the PMBR was shown to scale with symptom severity (Gascoyne et al., 2021), with recent onset and established patients showing progressive reduction in PMBR amplitude compared to healthy controls, giving the PMBR potential as a prognostic marker of neurological illness. Given the putative role of beta oscillations in inter-regional connectivity (discussed earlier in this section), enabling top-down control of neural circuits, the reduced PMBR in schizophrenic patients may relate to disrupted network integrity, an effect which has been documented with multiple modalities (Wheeler and Voineskos, 2014, Friston, 2002). In the case of ASD, the PMBR is again shown to be reduced in patients compared to controls (Gaetz et al., 2020), which may reflect impaired inhibitory mechanisms in neural circuits involved with motor planning and control, a well-documented effect in ASD patients (Kana et al., 2007, Yuk et al., 2020). In MS patients, the PMBR is delayed, with a longer time-to-peak compared to controls, which is consistent with reduction in processing speed (Strober et al., 2009), likely caused by structural degradation (Schoonheim et al., 2015), particularly in white matter (see section 2.2.1).

2.3.5 Haemodynamic Signals

MRI primarily images Hydrogen nuclei (protons) in the body (see Chapter 4), and therefore cannot directly image brain activity, which largely takes the form of electrical impulses. However, several scanning techniques exist in MRI which, when performed at a high enough temporal resolution (several seconds), are able to take measures which can be used as proxies of brain function. These measures include cerebral blood flow (CBF), cerebral blood volume (CBV), and the blood oxygenation level dependent (BOLD) signal. CBV is a measure of how much volume is occupied in a given space by blood vessels, while CBF is a measure of the rate of flow through these blood vessels. In addition, metabolic rate of oxygen consumption ($CMRO_2$), which describes the rate of energy consumption in a particular region, can be estimated using models that relate the BOLD signal to the CBF signal (Xu et al., 2009). The term functional MRI (fMRI) can be used to describe any measurements of these types, although it is

usually used to describe the BOLD signal, which arises due to a combination of CBF, CBV and $CMRO_2$. How the BOLD signal, which is the subject of Chapter 7, is believed to be generated due to different underlying neuronal activity will be explained in detail in this section, linking to the changes in CBF, CBV and $CMRO_2$ that have been either been reported or modelled.

The Primary BOLD Response

When activity in an ensemble of neurons increases, there is a local increase in $CMRO_2$, reflecting the increased demand for oxygen (Logothetis and Wandell, 2004). The increase in neuronal activity triggers relaxing of smooth muscle surrounding blood vessels, causing an increase in both CBF and CBV, supplying oxygenated blood to tissues surrounding the neurons. Oxygenated blood contains oxyhaemoglobin, which is diamagnetic, whereas deoxygenated blood contains deoxyhaemoglobin, which is paramagnetic. Paramagnetic deoxyhaemoglobin distorts local magnetic fields, creating a relative drop in MR signal (see Chapter 4). When the brain is at rest the average amount of neuronal activity remains relatively stable, reflected in a consistent ratio of oxy/deoxyhaemoglobin. However, when the brain is performing a task, neuronal activity in recruited regions significantly increases. The subsequent increase in CBF and CBV following activation overcompensates for the rise in $CMRO_2$, thus shifting the composition of blood towards diamagnetic oxyhaemoglobin, primarily in the capillaries and venules (Ogawa et al., 1993a). As a result, the local MRI signal (see Chapter 4) increases, peaking around 6 s after stimulation (see Fig. 2.11). This is known as the primary peak and is the most well-understood part of the BOLD response.

The Post-Stimulus BOLD Response

The post-stimulus undershoot is a second robust feature of the BOLD response, consisting of a drop in signal below baseline around 6 s after stimulus cessation, taking up to a minute to recover to baseline (Frahm et al., 1996). The origin of this part of the response with respect to CBF, CBV and $CMRO_2$ is highly debated (van Zijl et al., 2012). The earliest model proposed that CBF and CBV were tightly coupled, and dropped after stimulus cessation, while $CMRO_2$ recovered more slowly, as excess energy is required to supply ionic pumps in neuron cell membranes which bring membrane potentials back to rest (see section 2.1.2), leaving an excess demand for oxygen which would temporarily deplete oxyhaemoglobin and create a drop in signal below baseline (Kruger et al., 1996, Frahm et al., 1996). This model implies a post-stimulus BOLD response that is proportional to the amount of local neuronal activity that has occurred

during a stimulus or task, reflected in the energy required to rebalance the local ionic gradients. An alternative model instead proposed that it was CBV that recovered more slowly than CBF and $CMRO_2$ due to venous *ballooning* (Buxton et al., 1998). In this model, the vasculature surrounding an ensemble of neurons is modelled as a balloon with elastic properties, where the balloon inflates following stimulation due to relaxing of the smooth muscle and the subsequent increase in CBV and CBF. Following stimulus cessation, CBF drops, but CBV cannot fall as fast due to the elastic properties of blood vessel walls, creating a temporary reduction in relative oxygenated blood concentration. This model also implies a post-stimulus BOLD response that is proportional to the primary peak, as a greater primary peak implies greater CBV, which should translate to a proportional ballooning effect. The balloon model was a particularly popular interpretation of the BOLD response, leading many to believe that the post-stimulus undershoot was merely a vascular consequence of the primary peak, holding no excess information about neuronal processes. However, later studies have provided evidence that the post-stimulus undershoot may be driven in part by an undershoot in CBF (Chen and Pike, 2009, Mullinger et al., 2013, Sadaghiani et al., 2009), which is thought to relate to a local shift towards neuronal inhibition (see section 2.1.3). This will be explored further in Chapter 7. This forms an interesting parallel with existing theories of the post-stimulus M/EEG response (beta/alpha rebound), which has been posited as a mechanism for inhibitory control (Pfurtscheller et al., 2005, Pakenham et al., 2020, Mullinger et al., 2017).

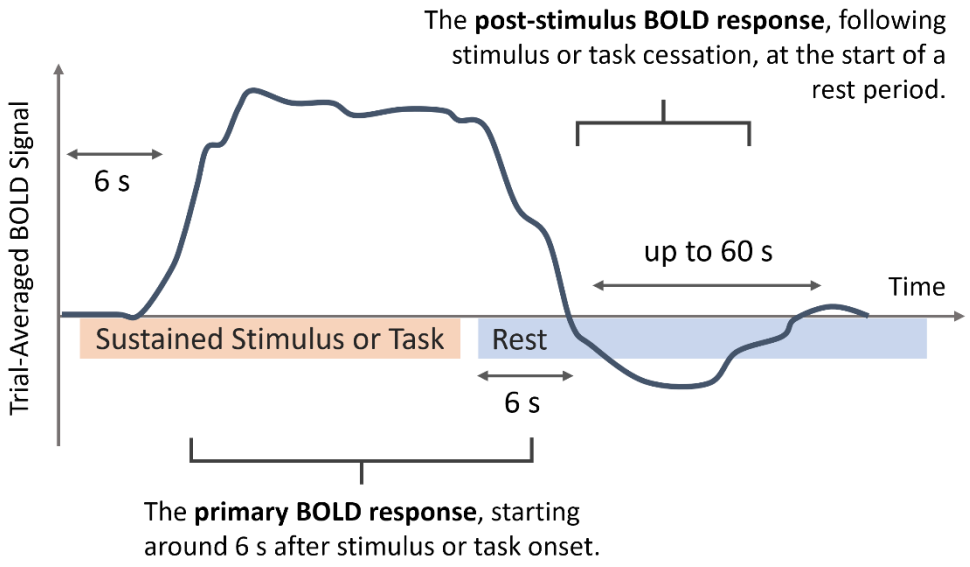


***Figure 2.11**: A schematic of the BOLD response to a stimulus or task. The peak of the response occurs around 5 – 6 s after stimulus onset. Following stimulus withdrawal, the response "undershoots" before returning to baseline. This response can be flipped (negative peak and poststimulus overshoot) in task-negative brain regions. The equivalent response for M/EEG data can be seen in Figure 2.10.*

Like the PMBR in electrophysiology, the post-stimulus BOLD response has also been shown to modulate in clinical populations compared to controls. In patients with schizophrenia, the post-stimulus BOLD response was reduced in amplitude (less negative undershoot) (Hanlon et al., 2016). Importantly, there was no effect on the primary response, suggesting that the post-stimulus phase of the response may have a distinct neuronal origin. This forms a parallel with the studies mentioned in section 2.3.4, which showed that the PMBR was reduced in patients with schizophrenia, while the during-stimulus response was not (Gascoyne et al., 2021, Hunt et al., 2019). In addition, patients with ASD also showed reduced post-stimulus BOLD response, with no reduction of the primary response (Murray et al., 2020), forming another parallel with the PMBR (Gaetz et al., 2020). Similar to the electrophysiological cases, the studies discussed here speculated that the reduced post-stimulus BOLD response was related to reduced inhibitory processing.

2.3.6 Negative BOLD Responses

As well as the haemodynamic response shown in Figure 2.11, where a positive primary peak is followed by a negative undershoot. There are many reported instances of the opposite behaviour – negative primary peak, sometimes followed by a positive overshoot. These can occur in regions surrounding a positive BOLD response, thought to be at least partially caused by a "stealing" of blood flow due to nearby activation (Devor et al., 2005, Harel et al., 2002). However, negative BOLD responses have also

been reported in ipsilateral regions where the contralateral equivalent region is activated (Hamzei et al., 2002, Mayhew et al., 2022), thought to relate to increased inhibition, leading to decreased neuronal firing, in the ipsilateral part of a bilateral network. In addition, negative BOLD responses are reported in task-negative networks (see section 2.3.7), which are shown to be neuronal in origin, and become more negative with more challenging task conditions, likely reflecting inhibitory processes (Lin et al., 2011). Positive post-stimulus BOLD responses (overshoots) have been reported in some studies (Sten et al., 2017, Anticevic et al., 2012, Grimm et al., 2009), but are less pronounced than post-stimulus undershoots and are not properly accounted for in models of the post-stimulus response involving sustained $CMRO_2$ or CBV.

2.3.7 Resting State Functional Networks

The discussion so far has been concerned with task-based changes in haemodynamic activity. However, one of the major discoveries made using fMRI was the identification of *functional networks*, i.e., groups of regions with correlated dynamics, that became active during *resting state* (Biswal, 2012). The novelty in this discovery was the fact that the nodes within these networks, which were already known to co-activate during relevant tasks, became spontaneously co-activated while the brain was not engaged in any particular activity, suggesting that these regions are closely connected in neuronal circuitry (see section 2.2.4). Since this discovery, there is a vast field of study into how the network organisation of the brain is perturbed by different activities, pathologies, and demographics (Fox and Greicius, 2010). More recently, studies have achieved similar results using MEG, identifying a range of networks whose activity spontaneously becomes synchronised during rest (Brookes et al., 2011a). Despite the fundamental differences in the generators of MEG and fMRI signal, similarities in resting state network connectivity suggest that meaningful comparisons can be made between the two modalities.

Commonly identified functional networks include the visual and sensorimotor networks, consisting of bilateral visual and sensorimotor regions, respectively. Other networks, such as the dorsal attention network (DAN), default mode network (DMN) and salience network (SN), are comprised of both superficial and deep brain regions which are spatially dispersed over the brain. The DAN, as the name suggests, has long been associated with increased attention, particularly in tasks that involve executive function such as working memory (Szczepanski et al., 2013). This is not surprising given that the superficial component of the DAN is formed of the frontal eye fields, known to be involved in the planning and execution of saccadic eye movement

(Schall, 2004) required for spatial sampling of the environment, as well as regions in the parietal cortex, known to be involved in maintaining and manipulating information in working memory (Koenigs et al., 2009, Curtis, 2006). The DMN is often shown to negatively track attention, forming a counterpart to the DAN in many cases (Raichle, 2015). The DMN is formed of bilateral prefrontal, parietal, and temporal nodes, as well as the posterior cingulate. This network is often associated with mind-wandering and rest, previously referred to as the task-negative network. The SN is formed of the bilateral insula, anterior cingulate and dorsolateral prefrontal cortex, and is often co-modulated with either the DAN or DMN. This network has been linked to addressing homeostatic demands (Seeley, 2019), as well as switching between the DAN and DMN (Goulden et al., 2014).

2.3.8 Relationship between MEG and fMRI Signal

As described in section 2.3.1, EEG and MEG measure synchronous postsynaptic potentials to pyramidal neurons, which primarily exist in the grey matter, with sensitivity that decreases with depth. The BOLD signal reflects the delivery of oxygen to these same neurons, meaning there is some correspondence between the two signals. However, BOLD signal, as well as being much slower, is not limited to particular types of neuron, does not decrease in sensitivity with depth, and does not require synchronicity of firing. Although the origin of the BOLD signal is complex, the primary mechanism by which it is linked to neuronal activity is energy consumption. Attwell and Lauglin estimated that around three quarters of the energy consumption of the neuron is associated with the repolarisation phase of neuronal activity (Attwell and Laughlin, 2001). This energy is required to supply active transport through pumps to rebalance ionic gradients across the cell membrane. As the majority of ion movement across the cell membrane occurs due to neuronal *input* at the dendrites, we can infer that most of the energy, and therefore oxygen consumption, of the neuron occurs due to postsynaptic activity rather than the action potential itself. This has been demonstrated in many animal studies that compared the BOLD response to both spiking (action potential) activity and local field potentials (LFPs, i.e., synchronous postsynaptic activity), showing consistently stronger relationships between BOLD and LFPs than spiking activity (Logothetis et al., 2001, Shmuel et al., 2006, Goense and Logothetis, 2008). Although difficult to replicate non-invasively in humans, these studies provide support for the relationship between BOLD and extracranial neuronal measures such as EEG and MEG, which are thought to be primarily driven by LFPs.

Many studies have tried to uncover the neurovascular coupling between fMRI and M/EEG measures in Humans, but the topic remains challenging. A commonly reported

effect in concurrent recording of EEG and BOLD is an inverse relationship between changes in alpha/beta oscillatory power and BOLD signal (Ritter et al., 2009, Yuan et al., 2010, Pang and Robinson, 2018). It may seem at odds that high amplitude oscillations are measured in the EEG while the metabolic oxygen consumption is reduced in the same regions and time windows. However, following on from the discussions so far on the origins of electrophysiological oscillations (see section 2.3.4) and the BOLD signal (see section 2.3.5): EEG oscillations are a measure of synchronous postsynaptic currents in neurons, which, in the case of alpha and beta oscillations, are thought to relate to feedback processes in neural circuits (Halgren et al., 2019, Van Kerkoerle et al., 2014), predominantly relating to inhibitory neuronal signalling (Jensen et al., 2002, Tuladhar et al., 2007, Chen et al., 1998). This has the overall effect of reducing neuronal firing, leading to lower metabolic demands and thus a reduction in BOLD signal. Conversely, a reduction of alpha/beta oscillations is likely reflective of increased feedforward processes relating to the propagation of sensory information through thalamo-cortical and intra-cortical pathways, which has the effect of increasing overall neuronal firing, increasing the metabolic demand. This inverse relationship between neural oscillations and BOLD is supported by invasive recordings in humans, showing negative relationships between beta oscillations and BOLD (Conner et al., 2011).

Two components of the EEG signal that are known to relate more directly to the BOLD signal than oscillations in the alpha/beta range are gamma oscillations (Lachaux et al., 2007, Conner et al., 2011) and ultra-low frequency components (< 0.2 Hz) (Zarahn et al., 1997, Robinson et al., 2006, He et al., 2008, Pang and Robinson, 2018). Gamma oscillations have already been discussed briefly in section 2.3.4, and may relate to BOLD more closely than alpha/beta as they are thought to relate to feedforward (states of excitation) processes rather than feedback (Michalareas et al., 2016, Van Kerkoerle et al., 2014). However, the two signals have been shown to dissociate in visual paradigms, such that BOLD signal responds to total visual input while gamma band activity responds to the degree of relationship between the inputs (Butler et al., 2017). This finding highlights the role of neural oscillations in the integration of information across both focal and widespread functional domains, an effect that is thought to relate directly to oscillatory phase relationships (Fries, 2015). Gamma also modulates with features of visual stimuli such as shape, position and movement speed, demonstrating sensitivity to the *type* of information that is being processed by visual networks (Muthukumaraswamy and Singh, 2013). The BOLD signal, although clearly a marker of brain activity, is unlikely to be sensitive to fast interactions between functional

domains, and thus responds more closely to overall energy consumption in a region rather than specific features of the information being processed. The relationship between BOLD and ultra-low frequency components in EEG is particularly interesting as these components are nearly always filtered out in pre-processing using a highpass filter set at around 1 Hz. Mathematical models using neural field theory have shown that alpha oscillations and BOLD may be related to high and low frequency components of the same underlying neural activity, both being generated by variations in cortico-thalamic and intra-thalamic feedback (Pang and Robinson, 2018).

Given the discussion so far, a question arises as to how these relationships between BOLD and M/EEG signal continue, or dissociate, during the post-stimulus response. We have already established that a rise above baseline in the MEG signal is often associated with increased inhibition, particularly related to feedback neuronal signalling. Conversely, increases above baseline in BOLD are associated with increased excitation. The most well-studied post-stimulus MEG response is the PMBR, characterised by a post-stimulus increase in beta band power in the contralateral motor cortex following movement, with strong evidence supporting an inhibitory role in the motor network. Multimodal work has shown that positive BOLD responses (i.e., positive primary peak and post-stimulus undershoot) coincide spatially with the PMBR (Stevenson et al., 2011) as well as alpha band responses in contralateral motor regions (Mullinger et al., 2013). Spatial correspondence, as well as trial-wise amplitude correspondence, has also been reported between visual alpha post-stimulus responses and the BOLD post-stimulus undershoot (Mullinger et al., 2017). Given these relationships, it is reasonable to assume that a positive primary peak in BOLD is driven by the rise in neuronal excitation related to a decrease in M/EEG oscillatory power, and a post-stimulus undershoot in BOLD is driven by the rise in neuronal inhibition, and thus a decrease in energy consumption, related to an increase in M/EEG oscillatory power. However, these results remain untested in post-stimulus responses outside of primary sensory regions, primarily due to the lack of existing work on post-stimulus M/EEG responses in a wider range of cortical networks. Another question that arises is why post-stimulus overshoots (above baseline) in BOLD seem to have no obvious neuronal counterpart in M/EEG data. According to current understanding, overshoots in BOLD should have a correlate in M/EEG data that relates to a state of increased excitation. Based on the discussion so far, this could manifest as increased gamma band activity, or a post-stimulus *dip* in lower frequency (theta, alpha, beta) oscillatory power, although neither of these effects, to our knowledge, have been demonstrated.

2.4 Summary

This chapter has described how brain function arises due to activity of single neurons, and how this activity scales up to the macroscopic signals that are measured with techniques such as MEG and fMRI. The following chapters will describe how these macroscopic signals are acquired and analysed.

3 Magnetoencephalography

3.1 MEG Data Acquisition

The first MEG recording was performed in 1968 by David Cohen using a copper induction coil as a sensor within a magnetically shielded room (MSR) (Cohen, 1968). Such sensors resulted in poor quality recordings with lots of noise. Cohen later demonstrated the use of superconducting quantum interference devices (SQUIDs) to record MEG, along with a better MSR, resulting in much greater signal quality (Cohen, 1972). He performed a similar experiment to Hans Berger's initial EEG experiment, showing an increase in spontaneous alpha oscillations with eyes closed, compared to open (see Chapter 2). Although MEG has undergone much development since this initial demonstration, with commercial systems now housing several hundred SQUID sensors, the same underlying principles remain. The following sections will describe the principles of MEG acquisition using SQUIDs, which are used in the experimental work presented in Chapters 5 and 6.

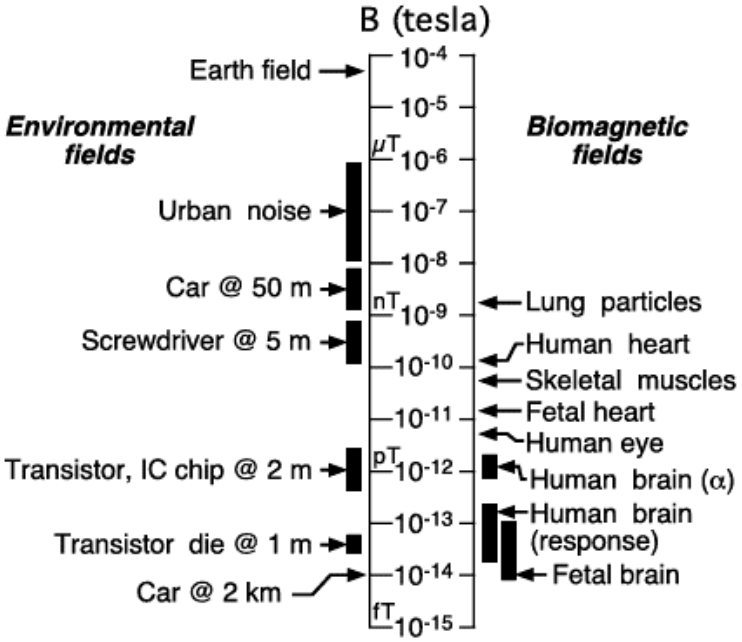


***Figure 3.1**: An image taken from (Vrba 2002) comparing the magnetic fields measured from the brain with those measured from external sources and other biomagnetic sources.*

3.1.1 SQUID Operation

Magnetic fields originating from synchronous action of neurons (see Chapter 2) are extremely small, occupying a range of tens to several hundred femtoTesla (fT) at the scalp surface, which is many orders of magnitude smaller than magnetic fields created

by nearby objects such as cars or electrical appliances (Vrba, 2002), as shown in Figure 3.1. This section will describe how *superconductivity* and *Josephson junctions* are used in superconducting quantum interference devices (SQUIDs) to measure these incredibly small magnetic fields.

Superconductivity describes a state at which there is no electrical resistance below a particular critical temperature, T_c. This state is described using the theory proposed by Bardeen, Cooper and Schrieffer in 1957, known as BCS theory (Bardeen et al., 1957). Conductors can be described as a positively charged lattice formed of cations (positively charged ions) containing a "sea" of negatively charged electrons that can flow through the material. BCS theory states that when an electron travels through a lattice, the positive ions in the lattice are attracted to the electron via the electromagnetic force, bringing them closer towards the electron. This creates a slight increase in the positive charge density around the position of the electron, causing nearby electrons to be attracted towards this area. This process binds electrons into *Cooper pairs*. In a regular conductor, the Pauli exclusion principle forbids electrons (and all fermions) from occupying the same quantum state, meaning each electron is described by a distinct wavefunction that interacts with the surrounding lattice, causing electrical resistance. However, Cooper pairs are bosons, meaning that all electrons in the conductor can occupy the same quantum state, described by the same macroscopic wavefunction (Bardeen, 1950). The macroscopic wavefunction forms a lower energy, and thus favourable state for the electrons. Importantly, the macroscopic wavefunction is not sensitive to lattice interactions that cause the scattering of individual electrons in a regular conductor. As a result of this, current flows in a superconductor with zero resistance. This state is easily broken by thermal energy, meaning T_c is often only a few degrees above absolute zero.

A consequence of the macroscopic wavefunction in a superconductor is quantization of magnetic flux. In a classically conducting loop, magnetic flux, which is the magnetic field that passes through the loop, induces a current in the loop via electromagnetic induction. In a superconducting loop, magnetic flux causes the wavefunction to acquire phase. However, as the wavefunction must be continuous (single-valued) at any given point around the entire loop, phase changes caused by flux must change the phase of the wavefunction enough to bring it back to its original phase. In other words, flux is quantized, where a single *flux quantum* has value $\Phi_0 = \frac{2\hbar}{e}$ (around 20 fT/m^2). Flux quantization is essential to the operation of SQUIDs (Clarke, 1989), enabling reliable measurement of field changes on the order of a single flux quantum.

Josephson junctions (Josephson, 1962) are superconductors separated by a thin insulator, often oxide layers. As long as the barrier is thin enough, Cooper pairs are able to tunnel through, meaning the wavefunction remains coherent on both sides of the junction. With no current applied to the system, there is no bias in tunnelling direction, thus the phase of the wavefunction at each side of the junction remains the same. A voltage applied to the system creates a phase difference in the wavefunction either side of the junction, relating to the tunnelling current,

$$I = I_0 \sin(\delta), \tag{3.1}$$

where I_0 is the maximum supercurrent in the junction, and δ is the difference in phase between the superconductors either side of the junction. This relationship between phase and current is critical in the operation of SQUIDs.

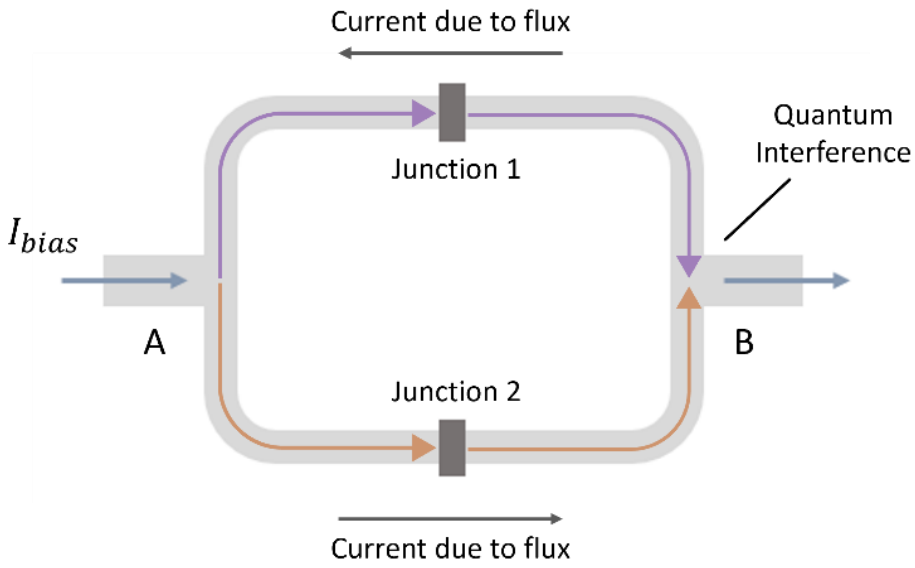


***Figure 3.2**: A superconducting loop with a pair of Josephson junctions in parallel, forming the basis of a SQUID magnetometer. A bias current flows from A to B, splitting equally between junctions 1 and 2. With no applied magnetic flux, the phase of the wavefunctions at each side should be the same. An applied flux adds an additional current which flows in a single direction around the loop, creating a phase difference at each junction based on the adjusted tunnelling current. This produces a quantum interference pattern at side B which produces a measurable voltage.*

SQUIDs exploit the relationship between phase and current by connecting two Josephson junctions in parallel. A biasing current is applied to the loop from side A to side B (see Fig. 3.2). The supercurrent splits between junctions 1 and 2, tunnelling through each with the same resultant phase at both junctions. The wavefunctions then interact at side B via quantum interference.

The magnetic flux is the field that passes through a given area (the area formed by the superconducting loop in our case). Magnetic flux through a conducting loop induces a current in the loop via electromagnetic induction. In a superconducting loop, flux is quantized, suc With no magnetic flux through the loop, the phase difference between junctions 1 and 2 will be the same. However, magnetic flux will induce a further current in the loop *that flows in a single direction*, i.e., it will reduce the tunnelling current at one junction and increase the tunnelling current at the other. This results in a phase difference in the wavefunction at the two junctions, Φ, creating a change in the voltage measured between points A and B,

$$V \propto \cos\left(\frac{2e}{\hbar}\Phi\right), \tag{3.2}$$

thus allowing the SQUID to infer the amount of magnetic flux through the loop. This expression is periodic, with period equal to the flux quantum, Φ_0, meaning many flux values will give the same voltage (voltage vs flux plotted in Fig. 3.3). This issue is solved by using a separate circuit, inductively linked to the SQUID, that provides an equal and opposite field to the flux through the SQUID. This means the voltage across the SQUID is kept constant (at a so-called “lock point”), allowing measurement of the voltage (and therefore the magnetic flux) using the separate circuit. While the SQUIDs allow the calculation of magnetic flux, the fields read by the MEG system are initially received by an arrangement of pickup coils, also made of superconducting material, with corresponding circuits which inductively pass the measured fields to the SQUID loop (Wierenga, 1993). This is shown in the simplified schematic in Figure 3.3. To remain superconductive, SQUIDs must remain submerged in a dewar filled with liquid helium. The SQUIDs themselves are kept high up in the dewar, while the pickup coils are arranged in a helmet configuration around the head. An insulating layer protects the participant from the extremely cold temperature, meaning the pickup coils are always several centimetres away from the scalp.

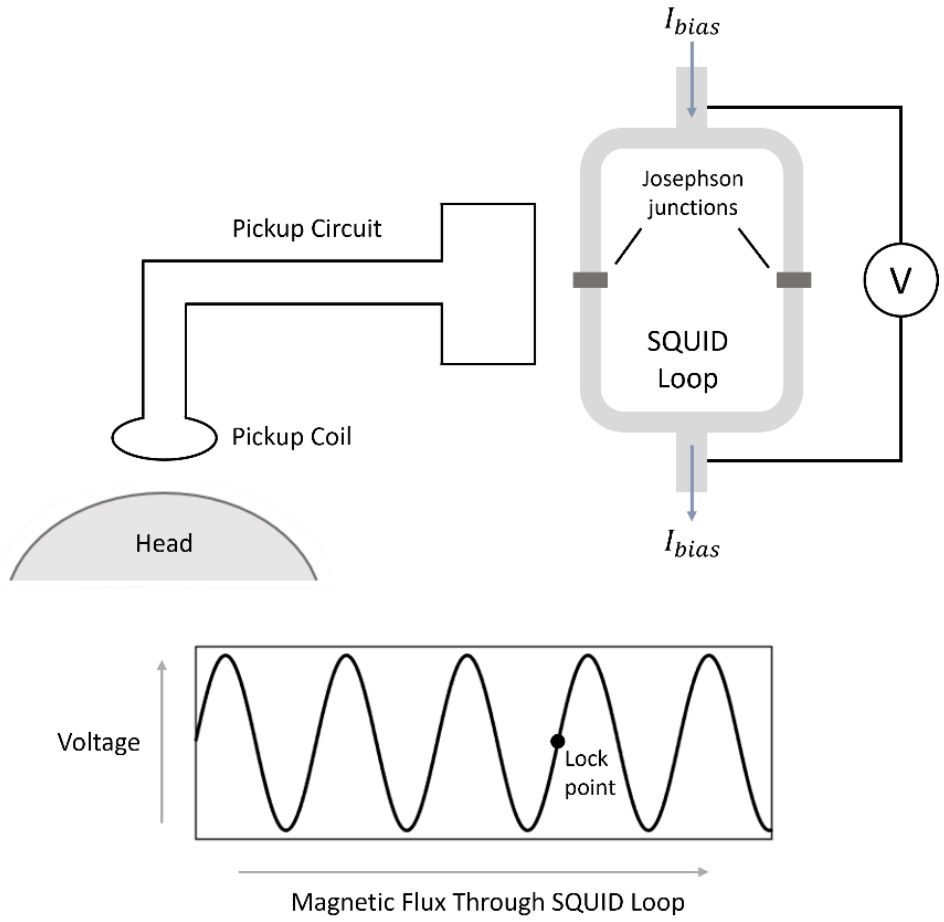


***Figure 3.3**: A schematic showing operation of a SQUID magnetometer, which can be used to take a MEG recording. The SQUID consists of a loop of superconductive material, with two Josephson junctions in parallel. The phase of the superconductive wavefunction at each junction is dependent on the tunnelling current. Magnetic flux through the loop creates a difference in the phase between the two opposing junctions, which creates a measurable voltage. A separate pickup circuit picks up the magnetic fields from the subject's brain, which are inductively passed to the SQUID.*

3.1.2 Magnetometers and Gradiometers

The measured flux at the pickup coils of a MEG system will be a sum of neurophysiological signals from all parts of the brain, as well as physiological artefacts from the rest of the body and external noise. The design of pickup coils can affect the sensitivity of MEG measurements to these different signals. The simplest pickup coil design is a single loop, where the SQUID acts as a magnetometer (Vrba and Robinson, 2001). In this configuration, magnetic flux induces a current in the pickup coil, which is inductively passed to the SQUID. An issue with magnetometers is that they are particularly sensitive to unwanted signal from the rest of the body and environment.

Hardware gradiometers (Vrba and Robinson, 2001) employ two oppositely wound pickup coils separated by a short distance. Here, the *difference* in magnetic field between the two coils is measured by the SQUID rather than the absolute magnetic

flux. Because magnetic fields from a current dipole decay with the cube of distance, the change in flux between the two coils will be much greater for nearby sources, making gradiometers particularly sensitive to more superficial sources. In turn, this makes gradiometers less sensitive to deep sources, but also environmental noise, making them preferrable over magnetometers in most cases. The type of gradiometry described here is referred to as first order gradiometry.

3.1.3 Synthetic Gradiometry

Modern MEG systems have the ability to achieve higher order gradiometry using combinations of coils in different positions (Vrba and Robinson, 2001). These are often referred to as synthetic gradiometers as they are applied post-hoc, with the raw signal still being read by hardware first order gradiometers or magnetometers. Second order gradiometry is often achieved by comparing the signal at a first order gradiometer with a set of reference coils which sit much higher than the pickup coils in the dewar. Third order gradiometers (and even higher orders), available exclusively in CTF MEG systems (as used in this thesis), are created using combinations of first order gradiometers as well as the reference coils. Synthetic gradiometry allows for superior noise reduction compared to magnetometers, as can be seen in Figure 3.4.

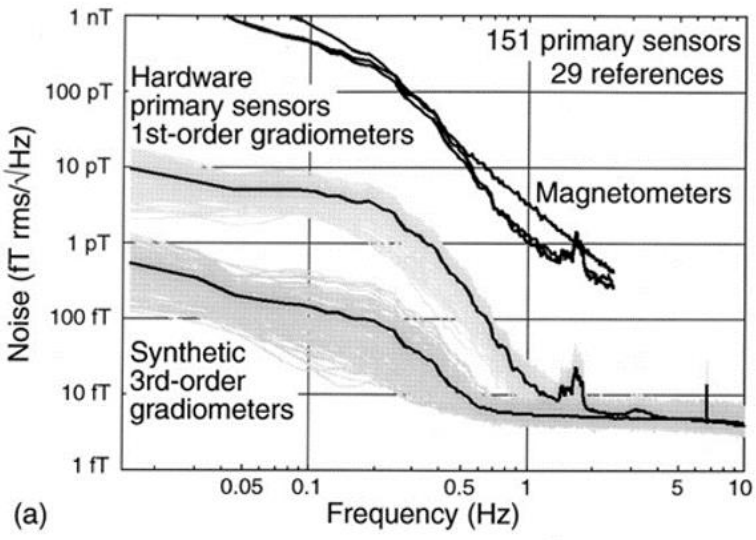


***Figure 3.4**: A comparison of the noise profile for magnetometers, hardware first order gradiometers and synthetic higher order gradiometers, taken from (Vrba and Robinson 2001). These were measured using a 151-channel MEG system with 29 reference coils, within a magnetically shielded room.*

3.1.4 Magnetic Shielding

Even with the use of gradiometers, the time-varying fields that will be induced in the SQUIDs due to activity outside of the lab will make it impractical to record MEG signal. This is demonstrated by the magnitude comparison in Figure 3.1. To create a

magnetically quiet environment for brain signals to be recorded, SQUID systems are placed in MSRs. In typical MSRs, quasi-static external fields (varying at <10 Hz) are largely removed by an effect known as flux shunting (Hoburg, 1995). This phenomenon relies on the high magnetic permeability of materials such as mu-metal, which provide a low magnetic reluctance route for external fields, causing them to be guided through the material rather than permeating the room. Higher frequency external fields are mitigated using eddy current cancellation (Celozzi et al., 2008). Conductors exposed to time-varying magnetic fields will produce a current, known as an eddy current, which produces a flux which opposes the applied magnetic field. This means higher frequency external fields are repelled. Layers of highly conductive materials such as copper or aluminium are used for MSRs to maximise this effect. A standard MSR for MEG is cuboidal in shape, consisting of several layers of mu-metal as well as layers of either copper or aluminium.

3.1.5 Experimental Setup

The experimental setup for MEG recording is relatively standard across MEG vendors and sites. The steps that must be taken are as follows:

- **Connecting hardware**: Any hardware required for the task, such as button boxes, must be connected to a stimulus computer outside the MSR that controls the presentation of stimuli. Parts that are inside the MSR must be connected to other electronics via waveguides, which are thin bores in the MSR wall. Most electronics must be kept outside of the MSR to maintain a magnetically quiet environment. Visual stimuli are presented to the participant via a projector, which projects through a waveguide onto a mirror setup, allowing the participant to view images on a screen.
- **Stimulation/trigger setup**: Programs must be set up on a stimulation computer which present stimuli and tasks to the participant. These programs control the timing of different stimuli, whilst also sending *triggers* that encode the timing of each stimulus within the dataset. Triggers in MEG are often 8-bit digital signals sent via parallel ports, meaning multiple triggers can be sent simultaneously as long as only mutually exclusive 8-bit values are chosen.
- **Participant setup**: Even though MSRs and gradiometers are used to reduce noise in MEG scanning, there are still residual fields in the MSR, meaning that any metal on the participant can create considerable noise, either due to ferromagnetic impurities or movement of the metal through the residual field. For these reasons, participants must remove all metal before scanning, and participants with non-removable metal (e.g., dental implants) may be

unsuitable for scanning entirely. Once in the scanner, it is easy to identify whether there is residual metal present on the participant as there will be large artifacts in the MEG data during small movements like blinking and breathing.

- **Fiducial markers and head digitisation**: Before entering the scanner, a set of fiducial markers (usually 3) must be fixed to the participant's head. These are electrodes that are energised during the scan, providing landmarks which can be located by the MEG scanner. In conjunction with this, it is common to create a head digitisation, giving a set of points in 3D space that trace the surface of the head relative to the fiducial points. The digitisation is used later for *co-registration* (see section 3.1.6) with an anatomical MRI.

A schematic of a standard MEG experimental setup is shown in Figure 3.5.

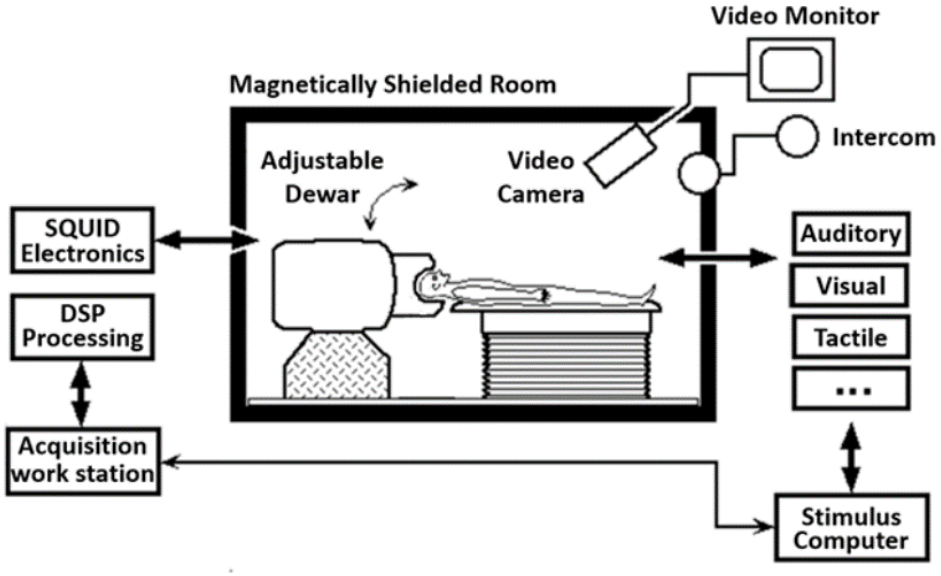


***Figure 3.5**: A schematic of a standard MEG lab, taken from (Vrba 2000). The MEG dewar is positioned inside a magnetically shielded room (MSR) to mitigate the effect of external fields. Most electronics remain outside the MSR to prevent noise, with key components such as button boxes (or other stimulation/response equipment) being fed through waveguides, which are thin bores in the MSR wall.*

3.1.6 Anatomical Co-Registration

For many applications of MEG, it is critical to know the precise locations of activity in the brain (see section 3.2.1). This can be achieved using anatomical co-registration, which is the process of mapping an anatomical MRI to the fiducial markers and digitised head surface collected during the scanning session. We therefore need an MRI of the whole head with good contrast and high resolution (see Chapter 4), which must be transformed to the same coordinate space as the MEG sensors. The position of the fiducial markers is known relative to the MEG, so once the MRI is moved to the same coordinates as the fiducials and corresponding head digitisation, we can discern

the position of the brain relative to each of the MEG sensors. This process is illustrated in Figure 3.6.

Digitisations can be created in several ways. The two methods used for the data presented in this thesis will be described here. The grip-force data in Chapter 6 used digitisations from a Polhemus FASTRACK digitiser (Polhemus, Colchester, VT, USA). This system consists of a transmitter box which faces the participant, a receiver which is placed on top of the head, and a stylus whose position is known relative to the receiver. The stylus can then be traced around the head surface to create a 3D digitisation. The n-back data presented in Chapters 5 and 6 used a Structure Sensor (Occipital Inc., San Francisco, CA, USA) which uses a combination of infrared laser light and visible light to create a 3D colour model of the head. Here, green stickers can be placed on top of the fiducial markers so these positions can be located and marked in the digitisation points.

Because the MRI is a volume image and the digitisation is a point cloud representing only the outer surface, we must first convert the outer surface of the head in the MRI to a 3D cloud of points. Then, an algorithm such as iterative closest point (ICP) can be applied (Rusinkiewicz and Levoy, 2001), which minimises the distance between two point clouds representing the same object.

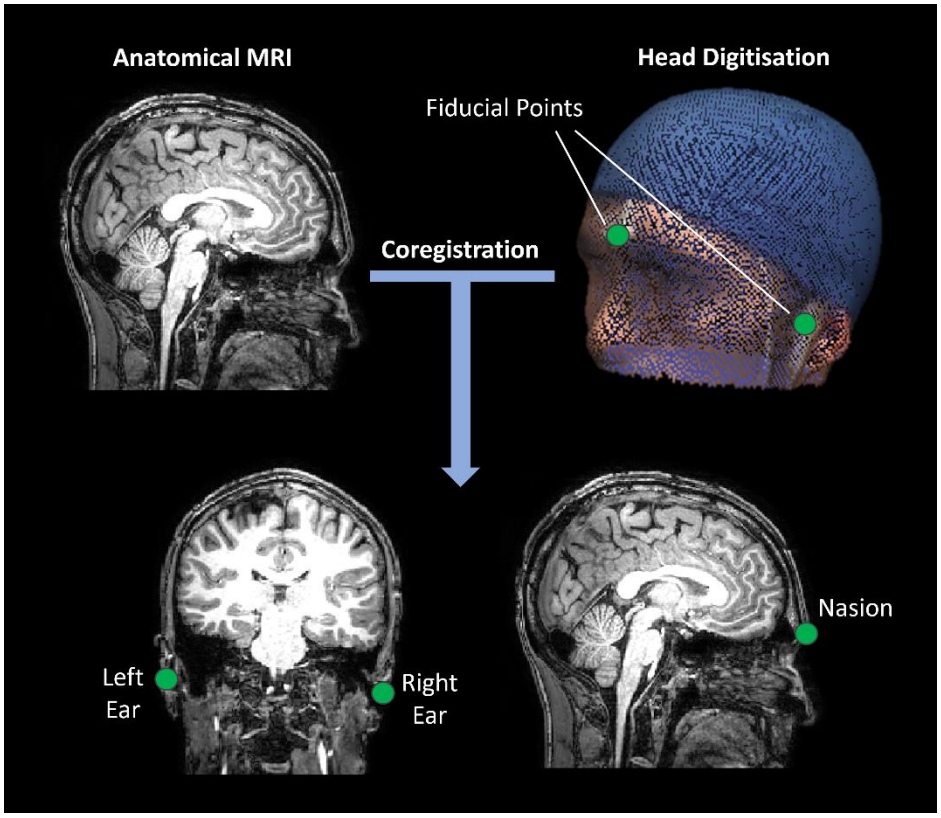


***Figure 3.6**: A schematic of the process of MEG coregistration, which transforms an anatomical MRI (top left) of the participant to the position of the participant's head during the MEG scan. A digitisation is required of the participant's head (top right), including headshape points and fiducial markers, which are often the nasion (between eyebrows), along with left and right preauricular points (ears). Importantly, the position of the fiducial points is known relative to the MEG sensors. A distance minimisation algorithm transforms the MRI to fit optimally within the digitisation. The fiducial points are then mapped onto the MRI (bottom row), so that the position of the MRI (and therefore the brain) is known within the array of MEG sensors.*

3.2 MEG Data Analysis

In its raw format, a continuous set of channel timecourses, MEG data provides little insight into the workings of the human brain. Many of the interesting effects reported with MEG (see Chapter 2), such as oscillatory modulations due to task condition and pathology, phase-locked evoked responses and functional connectivity, require tailored analyses to be observed and interpreted. In addition, further inference can be made about these effects when projected into source-space, i.e., from sensors outside of the brain to the emitting locations inside the brain. This section deals with standard techniques used to localise sources of activity in the brain, namely forward and inverse modelling, as well as techniques used to further analyse source-space data, such as time-frequency analysis and connectivity.

3.2.1 Forward Modelling

The first step to localising sources of MEG activity in the brain is *forward modelling*. The goal of the forward model is to estimate the magnetic field that would be measured at the array of sensors from an arrangement of sources in the brain with unitary amplitude. These unitary sources are placed in predetermined locations, forming a *source-space*, which is usually a regularly spaced grid covering the entire brain, but can also be based on the cortical surface of the participant. Using the transformation derived through co-registration (described in the section 3.1.6), the location of the source space with respect to the MEG sensors can be known. From here, the field that would be produced at the sensors by each unitary source can be calculated, forming the forward solution.

As MEG sources can be approximated as dipolar (see Chapter 2), we can calculate a forward solution by considering a field produced by a source with current density, $\boldsymbol{J}$, travelling through a conductive volume, G, contained by surface, S (Sarvas, 1987). Underpinning these calculations are Maxwell's equations:

$$\nabla \cdot \boldsymbol{E} = \frac{\rho}{\varepsilon} \tag{3.3}$$

$$\nabla \cdot \boldsymbol{B} = 0 \tag{3.4}$$

$$\nabla \times \boldsymbol{E} = -\frac{\partial \boldsymbol{B}}{\partial t} \tag{3.5}$$

$$\nabla \times \boldsymbol{B} = \mu_0 \left(\boldsymbol{J} + \frac{\partial \boldsymbol{E}}{\partial t} \right) \tag{3.6}$$

where $\boldsymbol{E}$ and $\boldsymbol{B}$ are electrical and magnetic fields, respectively, μ_0 and ε are the magnetic permeability and electrical permittivity in a vacuum, and ρ is charge density. The fields measured by MEG vary at relatively low frequencies (< 100 Hz), thus, the partial derivatives with time can be set to zero (Hämäläinen et al., 1993), simplifying equations 3.5 and 3.6 to

$$\nabla \times \boldsymbol{E} = 0 \tag{3.7}$$

$$\nabla \times \boldsymbol{B} = \mu_0 \boldsymbol{J}. \tag{3.8}$$

The field $\boldsymbol{B}$ at a location $\boldsymbol{r}$ away from any current source can be calculated using the continuous counterpart of the Biot-Savart law,

$$\boldsymbol{B}(\boldsymbol{r}) = \frac{\mu_0}{4\pi} \int_{\boldsymbol{G}} \boldsymbol{J}(\boldsymbol{r}') \times \frac{\boldsymbol{r} - \boldsymbol{r}'}{|\boldsymbol{r} - \boldsymbol{r}'|^3} \, dv \tag{3.9}$$

where $\boldsymbol{r}'$ is a position inside the volume G and dv is an element of the same volume. As described in Chapter 2, post-synaptic potentials are the summation of primary currents, $\boldsymbol{J}_P$, and volume currents, $\boldsymbol{J}_v$. We assume that volume currents, which are produced in the extracellular space, are uniformly conducted through the volume G. We can therefore rewrite, using Ohm's law, the volume current as a product of the conductivity of tissue, σ, and the electric field, $\boldsymbol{E} = -\nabla V$, giving

$$\boldsymbol{J}(\boldsymbol{r}') = \boldsymbol{J}_P(\boldsymbol{r}') + \boldsymbol{J}_v(\boldsymbol{r}') = \boldsymbol{J}_P(\boldsymbol{r}') - \sigma\nabla V(\boldsymbol{r}'). \tag{3.10}$$

Combining this expression with equation 3.9, and setting $\boldsymbol{a} = \boldsymbol{r} - \boldsymbol{r}'$ gives

$$\boldsymbol{B}(\boldsymbol{r}) = \frac{\mu_0}{4\pi}\left[\int_G \boldsymbol{J}_P(\boldsymbol{r}') \times \frac{\boldsymbol{a}}{|\boldsymbol{a}|^3}\,dv - \sigma\int_G \nabla V(\boldsymbol{r}') \times \frac{\boldsymbol{a}}{|\boldsymbol{a}|^3}\,dv\right], \tag{3.11}$$

where the first integral term is driven by the primary current, and the second is driven by the volume current. The term relating to volume current can be re-written as

$$\boldsymbol{B}_v(\boldsymbol{r}) = -\frac{\mu_0\sigma}{4\pi}\int_G \nabla \times V(\boldsymbol{r}')\frac{\boldsymbol{a}}{|\boldsymbol{a}|^3}\,dv \tag{3.12}$$

using the vector identity $\nabla a \times \nabla b = \nabla \times (a\nabla b)$. This is a volume integral, but it can be converted to a surface integral

$$\boldsymbol{B}_v(\boldsymbol{r}) = -\frac{\mu_0\sigma}{4\pi}\int_s \boldsymbol{n} \times V(\boldsymbol{r}')\frac{\boldsymbol{a}}{|\boldsymbol{a}|^3}\,ds \tag{3.13}$$

using Stokes' theorem, where $\boldsymbol{n}$ is a unit vector, normal to the surface, pointing outward from the element ds. Now, substituting this back into equation 3.11 gives

$$\boldsymbol{B}(\boldsymbol{r}) = \frac{\mu_0}{4\pi}\left[\int_G \boldsymbol{J}_P(\boldsymbol{r}') \times \frac{\boldsymbol{a}}{|\boldsymbol{a}|^3}\,dv - \sigma\int_s \boldsymbol{n} \times V(\boldsymbol{r}')\frac{\boldsymbol{a}}{|\boldsymbol{a}|^3}\,ds\right], \tag{3.14}$$

which is a simplified form of the Geselowitz formula (Geselowitz, 1970), assuming uniform conduction through the volume. This formula shows that the volume current (second term) can be represented as a set of fictitious currents on the surface of the conductor.

Spherical Head Model

The simplest approximation of a human head is a homogeneous sphere. This sphere (Fig. 3.7) has volume, V, and outer surface, S, and we assume a uniform conductivity, σ, throughout the entire volume. Typically, MEG sensors are oriented radially to the surface of the head (Fig. 3.7), so we can assume that only radial components of the magnetic field are detected by a sensor outside of the volume.

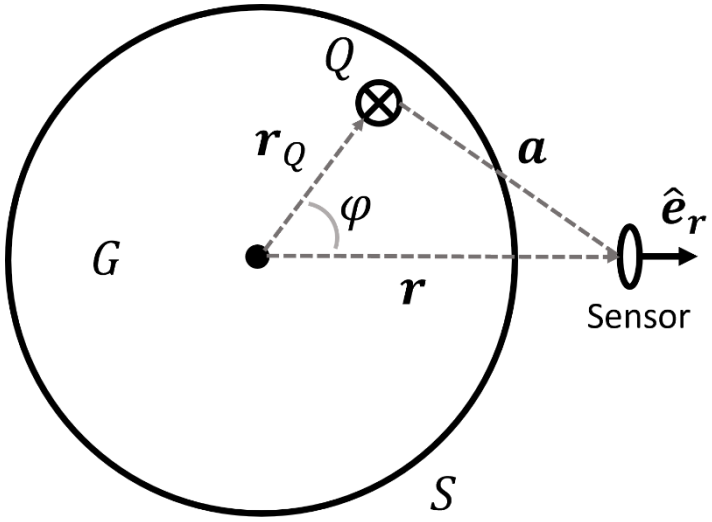


***Figure 3.7**: The simplest way to construct the MEG forward solution is using a simple spherical conductor model. Here, the head is modelled as a spherical conductor of volume G, encased by surface S. A dipole q points into the page here, at position r_q from the centre. A MEG sensor sits at position r, a distance a away from the dipole.*

We can write the radial component of the magnetic field as

$$B_r(\boldsymbol{r}) = \boldsymbol{B}(\boldsymbol{r}) \cdot \boldsymbol{e_r} \tag{3.15}$$

where $\boldsymbol{e_r}$ is a radial unit vector at the position of the sensor, which, when substituted into equation 3.14, gives

$$\boldsymbol{B}(\boldsymbol{r}) = \frac{\mu_0}{4\pi}\left[\int_{\boldsymbol{G}} \boldsymbol{J}_P(\boldsymbol{r}') \times \frac{\boldsymbol{a}}{|\boldsymbol{a}|^3} \cdot \boldsymbol{e_r} dv - \sigma \int_{\boldsymbol{s}} \hat{\boldsymbol{n}} \times V(\boldsymbol{r}') \frac{\boldsymbol{a}}{|\boldsymbol{a}|^3} \cdot \boldsymbol{e_r}\, ds\right]. \tag{3.16}$$

Now, just taking the volume current term, and expanding out $\boldsymbol{a} = \boldsymbol{r} - \boldsymbol{r}'$, we get

$$\boldsymbol{n}(\boldsymbol{r}') \times (\boldsymbol{r} - \boldsymbol{r}') \cdot \boldsymbol{e_r} = (\boldsymbol{n}(\boldsymbol{r}') \times \boldsymbol{r} - \boldsymbol{n}(\boldsymbol{r}') \times \boldsymbol{r}') \cdot \boldsymbol{e_r} = \boldsymbol{0} \tag{3.17}$$

as the cross product of parallel vectors $(\boldsymbol{n}(\boldsymbol{r}') \times \boldsymbol{r})$, as well as the dot product of perpendicular vectors $((\boldsymbol{n}(\boldsymbol{r}') \times \boldsymbol{r}) \cdot \boldsymbol{e_r})$, are both zero. In other words, the contribution of volume currents in a spherical head model is zero. Therefore,

$$\boldsymbol{B_r}(\boldsymbol{r}) = \frac{\mu_0}{4\pi} \int_{\boldsymbol{G}} \boldsymbol{J}_P(\boldsymbol{r}') \times \frac{\boldsymbol{a}}{|\boldsymbol{a}|^3} \cdot \boldsymbol{e_r} dv \tag{3.18}$$

meaning that the solution is independent of tissue conductivity when using a spherical head model. This expression assumes that the current, $\boldsymbol{J}_P(\boldsymbol{r}')$, is distributed evenly over a surface with radius r'. We can also model the current as a single dipole, $\boldsymbol{Q}$, at position $\boldsymbol{r}_Q$,

$$\boldsymbol{J}_P(\boldsymbol{r}') = \boldsymbol{Q}\delta(\boldsymbol{r}' - \boldsymbol{r}_Q) \tag{3.19}$$

where $\delta(\boldsymbol{r}' - \boldsymbol{r}_Q)$ is a Dirac-delta function at position $\boldsymbol{r}_Q$. Equation 3.18 then becomes

$$\boldsymbol{B}_{\boldsymbol{r}}(\boldsymbol{r}) = \frac{\mu_0}{4\pi}\int_{\boldsymbol{G}} \boldsymbol{Q}\delta\left(\boldsymbol{r}' - \boldsymbol{r}_Q\right) \times \frac{\boldsymbol{a}}{|\boldsymbol{a}|^3} \cdot \boldsymbol{e}_{\boldsymbol{r}} dv = \frac{\mu_0}{4\pi}\boldsymbol{Q}(\boldsymbol{r}_Q) \times \frac{\boldsymbol{a}}{|\boldsymbol{a}|^3} \cdot \boldsymbol{e}_{\boldsymbol{r}} \tag{3.20}$$

as the integral of a Dirac-delta function is simply the rest of the integral evaluated at the point where the function is non-zero. In reality, dipoles will have a non-radial field component at the sensors, so we must consider the entire field, $\boldsymbol{B}(\boldsymbol{r})$. We can assume that there is no current density, $\boldsymbol{J}$, outside of the volume G, and that the curl (rotation) of the field is zero. These assumptions simplify equation 3.8 to become

$$\boldsymbol{B}(\boldsymbol{r}) = -\mu_0 \nabla U(\boldsymbol{r}), \tag{3.21}$$

where $U(\boldsymbol{r})$ is the scalar potential. Scalar potentials, f, of a conservative vector field, $\boldsymbol{F}$, can be expressed in terms of a line integral, such that

$$f(b) - f(a) = \int_L \boldsymbol{F} \cdot d\boldsymbol{l}, \tag{3.22}$$

where b and a are two positions in the vector field, creating L. In other words, if a field is conservative, a line integral between two points within the field is the difference of the scalar potentials at each end of the line. Therefore, taking a line integral between positions $\boldsymbol{r}$ and ∞, and recognising that the field reduces to zero at infinity, we can write

$$U(\boldsymbol{r}) = -\int_0^\infty \nabla U(\boldsymbol{r} + l\boldsymbol{e}_{\boldsymbol{r}}) \cdot \boldsymbol{e}_{\boldsymbol{r}} dl = \frac{1}{\mu_0}\int_0^\infty B_{\boldsymbol{r}}(\boldsymbol{r} + l\boldsymbol{e}_{\boldsymbol{r}}) \cdot \boldsymbol{e}_{\boldsymbol{r}} dl, \tag{3.23}$$

which then becomes

$$U(\boldsymbol{r}) = \frac{1}{4\pi}\,\boldsymbol{Q}(\boldsymbol{r}_Q) \times \left(\boldsymbol{r}' - \boldsymbol{r}_Q\right) \cdot \boldsymbol{e}_{\boldsymbol{r}} \int_0^\infty \frac{dl}{\left|\boldsymbol{r} + l\hat{\boldsymbol{e}}_{\boldsymbol{r}} - \boldsymbol{r}_Q\right|^3}. \tag{3.24}$$

The solution to this equation is

$$U(\boldsymbol{r}) = -\frac{1}{4\pi}\frac{\boldsymbol{Q} \times \boldsymbol{r}_Q \cdot \boldsymbol{r}}{F} \tag{3.25}$$

where $F = |\boldsymbol{a}|(|\boldsymbol{r}||\boldsymbol{a}| + |\boldsymbol{r}|^2 - \boldsymbol{r}_Q \cdot \boldsymbol{r})$ and $\boldsymbol{a} = \boldsymbol{r} - \boldsymbol{r}_{\boldsymbol{Q}}$. This can now be combined with equation 3.21, giving the Sarvas equation (Sarvas, 1987):

$$\boldsymbol{B}(\boldsymbol{r}) = \frac{\mu_0}{4\pi F^2}\left(F\boldsymbol{Q} \times \boldsymbol{r}_{\boldsymbol{Q}} - \boldsymbol{Q} \times \boldsymbol{r}_{\boldsymbol{Q}} \cdot \boldsymbol{r}\nabla F\right) \tag{3.26}$$

where $\nabla F = \left(\frac{|a|^2}{|\boldsymbol{r}|} + \frac{a}{|a|} \cdot \boldsymbol{r} + 2|\boldsymbol{a}| + 2|\boldsymbol{r}|\right)\boldsymbol{r} - (|\boldsymbol{a}| + 2|\boldsymbol{r}| + \frac{\boldsymbol{a}}{|\boldsymbol{a}|} \cdot \boldsymbol{r})\boldsymbol{r_Q}$. This is the general solution for the field originating inside a uniform sphere. Of course, this is far simpler than the reality, given that a human head is formed of multiple layers with different geometries and conductivities. However, the single sphere model provides a good mathematical basis for understanding how more complex forward solutions arise.

Alternative Head Models

The most accurate head model used for solving the forward problem in M/EEG is the three-layer boundary element model (BEM), which takes into account the separate brain, skull and scalp geometries and conductivities (Fuchs et al., 1998). This method provides clear advantages over the single-sphere head model, but requires advanced segmentation techniques, in turn requiring a high-quality anatomical MRI, and is more computationally expensive. Inclusion of all three layers is more important for EEG, where the forward model is particularly dependent on layer conductivities compared to MEG. An alternative solution that provides balance between accuracy and computational expense (speed) involves using multiple overlapping spheres to model the head (Huang et al., 1999). For each sensor, a “local” sphere is fit within the head geometry, occupying the section of the head closest to the sensor. The combination of these spheres then provides a fairly accurate model of brain geometry (see Fig. 3.8), at a fraction of the computational expense. This was the method used for all forward modelling in this thesis.

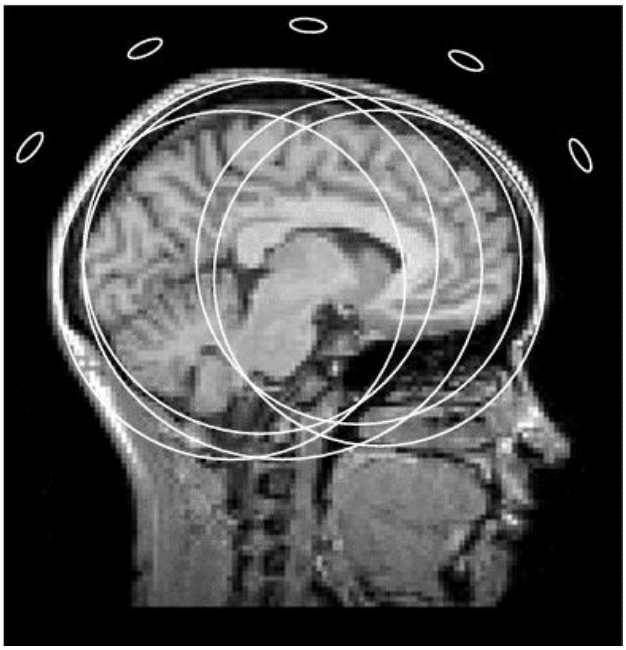


***Figure 3.8**: Multiple-spheres head model for MEG forward modelling. This approach is superior to the single-sphere head model, where rather than one sphere representing the entire head shape, one sphere is fitted to a section of the head closest to each sensor. The sum of all spheres then forms a relatively accurate model of the head.*

3.2.2 The Inverse Problem

The MEG signal measured at sensor i as a function of time, $b_i(t)$, can be thought of in terms of cumulative effects of dipole strengths from all locations in the source space,

$$b_i(t) = \sum_{j=1}^{M} L_{i,j} \cdot q_j(t)\,, \tag{3.27}$$

where $L_{i,j}$ is the field that would be measured at sensor i given a source with unit strength at source-space location j, $q_j(t)$ is the actual source strength at source-space location j, and M is the total number of source-space locations. This can be written more concisely as

$$\hat{b}(t) = \boldsymbol{L}\hat{q}(t), \tag{3.28}$$

where $\hat{b}$ is the measured field across all sensors, $\boldsymbol{L}$ is the *lead field* matrix, with dimensions $N \times M$, where N is the number of channels, and $\hat{q}$ is a vector of all source strengths. Solving this equation to find $\hat{q}(t)$ from a set of measured fields, $\hat{b}(t)$, is known as the *inverse problem*. As there are usually many more source-space locations than sensors, $\boldsymbol{L}$ is both non-square and singular, and thus cannot simply be inverted

to find a solution for $\hat{q}(t)$. However, several techniques exist to construct an approximation of the most likely source arrangements by applying constraints to the system.

3.2.3 Beamforming

The method applied in this thesis to solve the inverse problem is known as beamforming, a technique originating in communication technologies (Van Veen and Buckley, 1988, Litva and Lo, 1996) to unmix signals coming from different sources. This technique acts as a spatial filter, suppressing signal originating from all locations apart from the region of interest. To construct the beamformer, a set of weights are derived from the data for each location of interest (voxel in the brain). These weights are then applied to the sensor level signals to produce an estimate of the source-level signal. The source estimate at position *and location* θ can be written as

$$q_{\boldsymbol{\theta}}(t) = w_{\theta 0}\boldsymbol{b_0}(t) + w_{\theta 1}\boldsymbol{b_1}(t) + \cdots + w_{\theta N}\boldsymbol{b_N}(t) = \widehat{w}_{\boldsymbol{\theta}}^{T}\hat{b}(t) \qquad (3.29)$$

where $\widehat{w_\theta}$ is the vector of weights for θ. This is shown in Figure 3.9 as a schematic. Note that both the position and direction of the dipole are contained within θ – how the direction is determined will be explained later in the section.

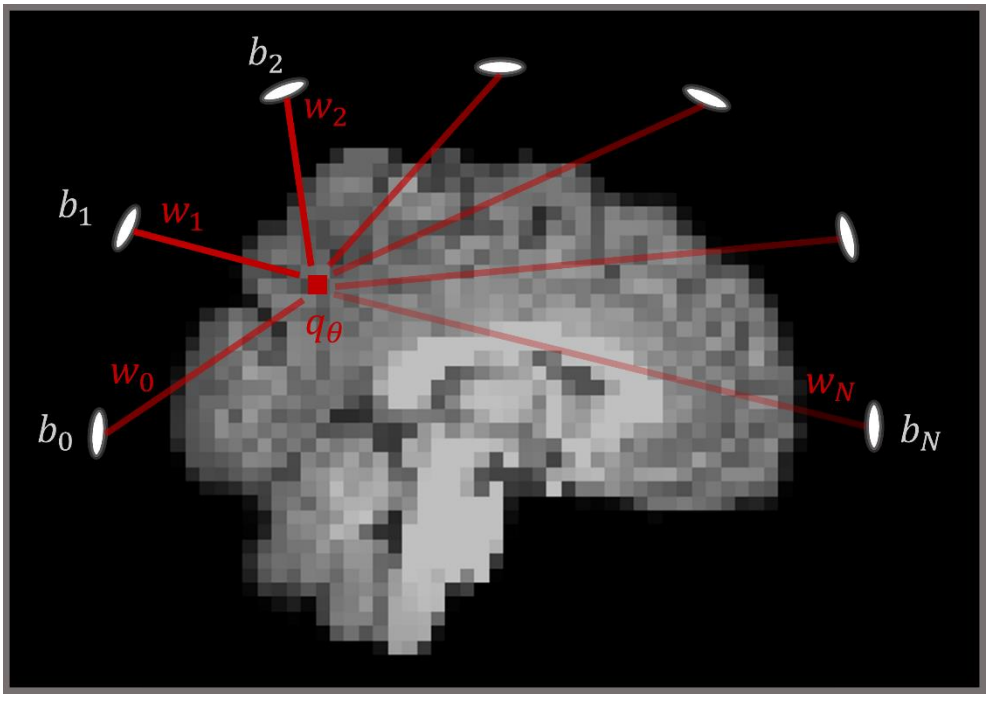


Figure 3.9: A beamformer acts as a spatial filter, suppressing signals from all locations other than the region of interest. A set of weights, $\widehat{w}_{\boldsymbol{\theta}}$, are derived, specific to each location, θ, in the brain, which are then applied to the sensor level data, $\hat{b}(t)$, to reconstruct source activity, $q_{\boldsymbol{\theta}}(t)$.

The weights are calculated by minimising the variance of the set of source signals whilst imposing a linear (unit gain) constraint at the source of interest, i.e., the projected variance at the source of interest must remain constant whilst being minimised everywhere else. Due to these conditions, beamformers of this type are described as *linearly constrained minimum variance* (LCMV) beamformers. Mathematically, the constrained minimisation can be written as

$$\min_{\boldsymbol{w}_\theta}(\sigma^2), \text{ subject to } \widehat{w}_\theta^T \hat{L}_\theta = 1 \tag{3.30}$$

Where σ^2 is the variance of the estimated source, $\langle q_{\boldsymbol{\theta}}{}^{\boldsymbol{2}}(t)\rangle$. The solution to this minimisation gives

$$\widehat{w}_\theta^T = \frac{\hat{L}_{\boldsymbol{\theta}}^T \boldsymbol{C^{-1}}}{\hat{L}_{\boldsymbol{\theta}}^T \boldsymbol{C^{-1}} \hat{L}_\theta} \tag{3.31}$$

(Van Veen and Buckley, 1988) where $\boldsymbol{C}$ is the covariance matrix of the data, equal to $\langle \hat{b}(t)\hat{b}(t)^T \rangle$. Therefore, the beamformer derives weights based on the data itself, contained in the covariance matrix, and the position of dipoles with respect to the sensors, contained in the forward solution.

The discussion so far has considered a fixed, known dipole orientation, contained in θ. In practice, the optimal orientation of the dipole at each position needs to be calculated. Vector beamformers calculate the dipole strength in all three cartesian directions, meaning the weights for a particular location in the brain will be an $N \times 3$ matrix. Scalar beamformers, on the other hand, assume a single fixed dipole orientation, meaning the weights for a particular location will be a vector of length N. The dipole orientation in a scalar beamformer may be determined by cortical geometry, using a direction that is normal to the cortical surface. This approach is in concordance with the idea that pyramidal neurons, which are the main drivers of MEG signal, are arranged along cortical columns that run normal to the cortical surface (see Chapter 2). It should be noted here that MEG is most sensitive to dipoles that are tangential to the scalp surface, meaning MEG will be intrinsically less sensitive to gyri peaks and sulci troughs in the grey matter, although experiments have shown that MEG is still sensitive to most of the cortical surface (Hillebrand and Barnes, 2002). Another approach to optimising dipole orientation, and the one applied in Chapters 5 and 6 of this thesis, is to choose the orientation that maximises the beamformer power output (Westner et al., 2022). This orientation can be found by considering the covariance of the vector beamformer output for a location j, given by $cov\big(q_{\boldsymbol{j}}(t)\big) = (\hat{L}_{\boldsymbol{j}}^T \boldsymbol{C^{-1}} \hat{L}_j)^{-1}$. The orientation that maximises beamformer power output is the eigenvector corresponding

to the largest eigenvalue of $cov(q_j(t))$. Using this orientation, a single source estimate can be calculated at each source-space location in the brain.

As well as being able to reconstruct the timecourse of activity from a voxel in the brain, it is often useful to form a static map of activation to a particular task. This can be calculated using a pseudo T-statistic (~~T~~-stat), which, for a source space location and orientation, θ, can be written as

$$~~T~~ = \frac{\hat{w}_\theta^T \boldsymbol{C}_a \hat{w}_\theta - \hat{w}_\theta^T \boldsymbol{C}_c \hat{w}_\theta}{2\hat{w}_\theta^T \boldsymbol{C}_c \hat{w}_\theta}, \tag{3.32}$$

where C_a and C_c are the active and control covariance matrices, taken during time-windows representing activity, and inactivity, respectively. It should be noted that the active and control covariance matrices are usually bandpass filtered to highlight sources of activity in different frequency bands, which often correspond to different regions and processes in the brain (see Chapter 2).

3.2.4 Event-Related Analysis

The measured MEG signal for an event-related paradigm, either at a particular channel or reconstructed source location, comprises induced responses (changes in spontaneous rhythms), and evoked potentials (see Chapter 2), along with other environmental and physiological signals. Researchers often wish to isolate and amplify the signals that are modulated by task-based activity, whilst suppressing all other signals. This is achieved in a slightly different way depending on whether the signal of interest is evoked or induced (Pfurtscheller and Lopes da Silva, 1999).

Evoked Responses

Evoked responses are time-locked and phase-locked to a particular event. Because of this, a channel or source timecourse can simply be averaged around event timings, such that the relative amplitude of the evoked response is enhanced relative to noise, and any other events that occur in a different phase, e.g. blinking, spontaneous rhythms, movement artifacts, are averaged out. This process is demonstrated in the simple simulation shown in Figure 3.10 where a Gaussian phase-locked signal of interest is trial-averaged to reduce the effects of random noise. Before averaging evoked responses, the data is often frequency filtered to a more restricted frequency, such as 1 – 48 Hz, to eliminate higher frequency noise (including noise from mains electricity, at 50 Hz) and low frequency drifting whilst maintaining signals of interest.

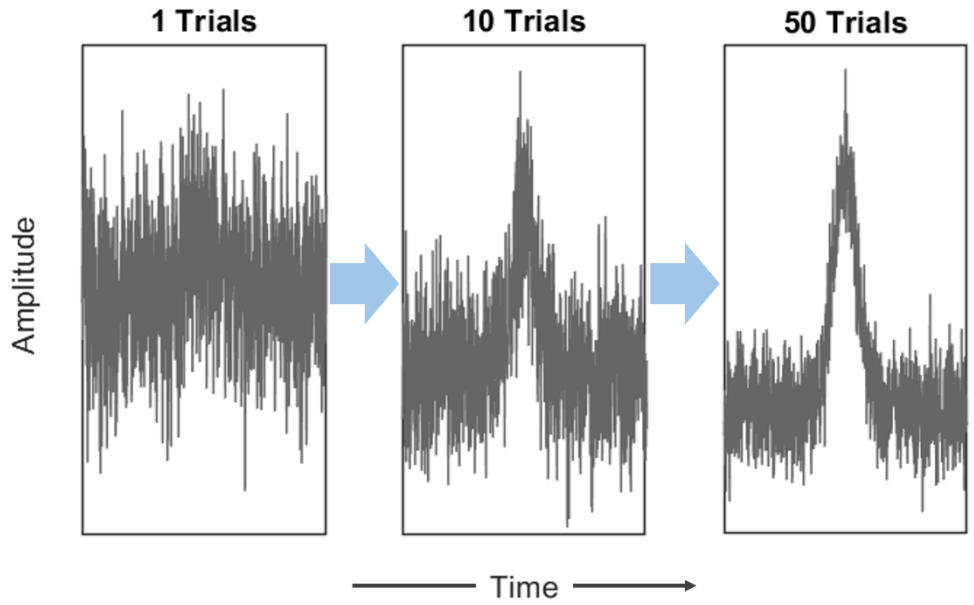


***Figure 3.10**: A simulation of a Gaussian shaped signal, added to random noise, acting as a simulation of an evoked response in MEG or EEG data. Averaging over more trials increases the amplitude of the signal relative to surrounding noise. This approach works due to phase-locking of the signal to a particular timepoint.*

Induced Responses

Induced responses are time-locked to events, but not phase-locked. Because of this, there are several extra steps involved to evaluate the trial-averaged response. The first step is bandpass filtering. As described in the Chapter 2, induced responses are segregated into a set of frequency bands which relate to both the emitting brain regions and cognitive state. Bandpass filtering allows the contribution of a specific frequency range to the overall signal to be calculated. It should be noted that this step also removes a great deal of noise (including unwanted brain signals) from the signal, as this is often of a higher frequency than the induced responses. Next, given that spontaneous rhythms are not phase-locked, meaning that peaks and troughs in the wave may occur at different times in different trials, the envelope of the signal must be used rather than the absolute amplitude. This can be achieved by simply squaring the signal, or alternatively, taking the Hilbert transform, which allows the signal to be separated into instantaneous amplitude and frequency components (Liu, 2012). The absolute value of the Hilbert transform of a narrowband filtered signal is equal to the envelope of the signal. Taking the envelope of the signal allows induced responses to remain after trial-averaging. This is demonstrated below in Fig 3.11 with simulated data, containing spontaneous alpha (10 Hz) fluctuations as well as random noise. Averaging without taking the Hilbert envelope (left) only acts to decrease the signal, whereas averaging after taking the Hilbert transform produces a clear difference between the high-signal and low-signal periods. If combining average timecourses

across multiple subjects, a baseline, which is often the mean value during an “off” period, is subtracted from the timecourse, to remove the effect of between-subject variability in baseline oscillatory amplitude.

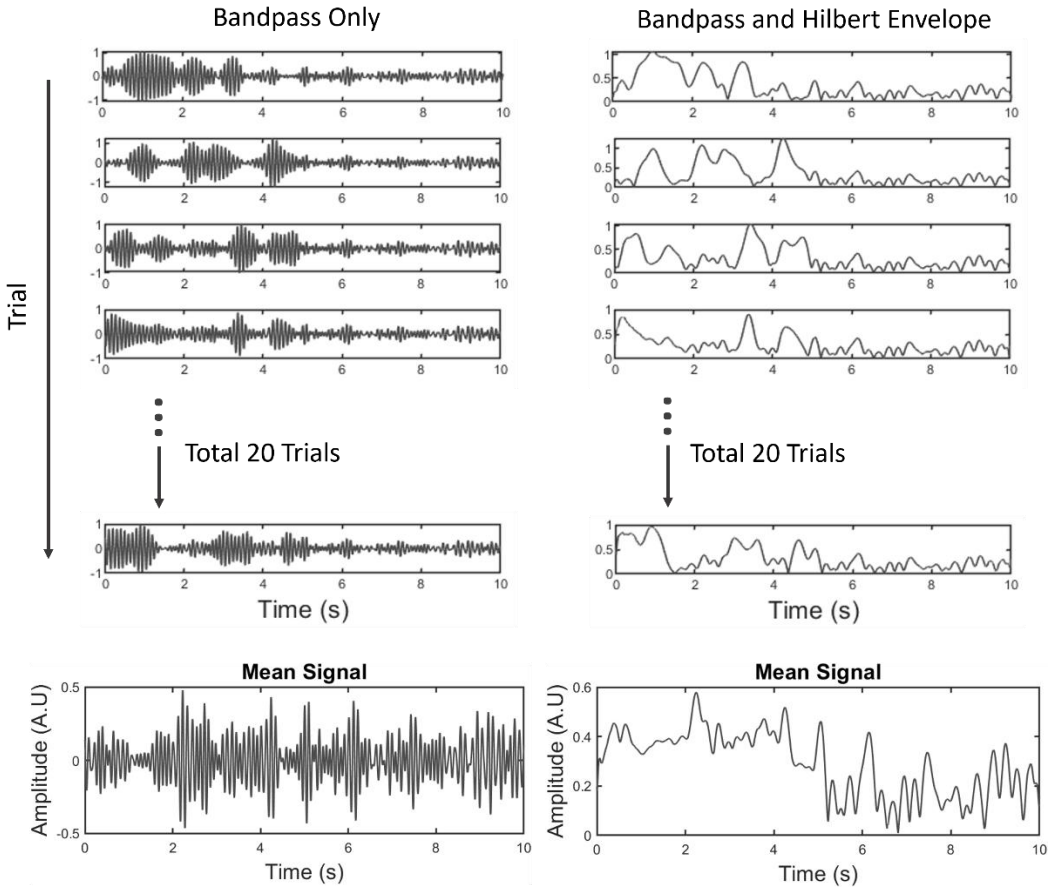


***Figure 3.11**: A simulation of an induced 10 Hz response. The 10 Hz spontaneous rhythm randomly “bursts” during the first 5 seconds, with varied timing and phase, and stops during the second half. The 10 Hz bursting is added to random noise. The simulated signal is bandpass filtered to the alpha band (8 – 12 Hz), and the envelope of the signal is the calculated using a Hilbert transform (shown on the right-hand side). Averaging the signal that has only been bandpass filtered reduces the difference between “on” and “off” periods as the oscillations are often out of phase, while averaging the signal envelopes allows the trials to summate (Note different y-axis for mean signal plots to individual trial plots).*

In practice, researchers may not know the specific frequency band that will be modulated by a task, and in some cases, multiple bands may be affected. To view the entire time-frequency response to a task at a particular channel or source location, it is common to average power envelopes after filtering over a range of frequencies, presenting them as a matrix where the colour represents the frequency density at a

given time-point. This is known as a time-frequency spectrogram (TFS). This can either represent *absolute* change, or *relative* change, in a given frequency range. If the goal is to show absolute change, a baseline, often taken as the mean during an “off” period, is subtracted from each row separately. If the goal is showing relative change, the rows must also be divided by the baseline value. Relative change removes any bias towards frequency ranges with higher intrinsic amplitude, such as the alpha band. A simulated TFS, constructed using a scenario akin to Figure 3.11, is shown below in Figure 3.12, showing increased alpha/beta spontaneous rhythms during the first 5 s.

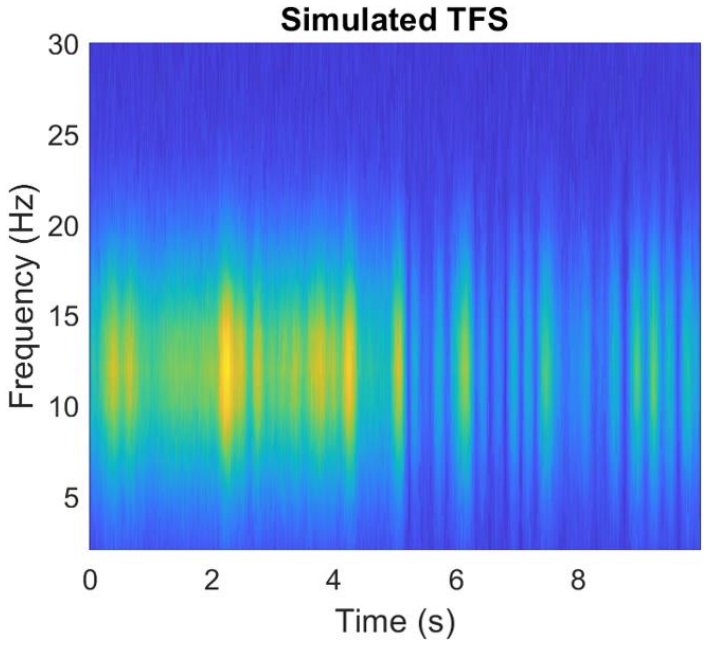


***Figure 3.12**: A time-frequency spectrogram of simulated alpha/low-beta induced activity, similar to the activity shown in Figure 3.11, where the first 5 seconds of each simulated trial contain random oscillatory bursts. The colours represent the strength of oscillations within each y (frequency) value, at each x (time) value.*

The methods discussed so far provide a means to assess the average induced response for a given task. Using a TFS or average timecourse, researchers may take parameters such as mean amplitude or peak height during time windows of interest, such as during stimulus presentation. Using these values, the effects of factors such as task condition, pathology, and behaviour on the MEG signal can be deduced. This is a powerful approach that underpins the bulk of neuroscientific studies using MEG.

3.2.5 Functional Connectivity

As well as analysing the timecourses and power spectra for single channels or brain regions, MEG is able to measure statistical relationships between groups of channels or regions, often referred to as functional connectivity. Functional connectivity has given insight into the network properties of the brain (Brookes et al., 2011a, Quinn et

al., 2018) and provides a promising biomarker for several clinical populations (Dubbelink et al., 2013, Hinkley et al., 2010). Measures of MEG functional connectivity can be grouped as follows:

- **Amplitude**: Signals from different locations are filtered into a frequency band of interest and power envelopes of these signals are correlated as a measure of functional connectivity (Brookes et al., 2011a, O'Neill et al., 2015).
- **Phase**: Signals from different locations are filtered into a frequency band of interest and the phase coherence between signals is used as a measure of functional connectivity. Several variations of phase-based connectivity metrics exist (Colclough et al., 2016).

An issue with all connectivity metrics is cross-talk, or source-leakage. With MEG, this arises primarily due to the ill-posed nature of the inverse problem (Schoffelen and Gross, 2009), causing a blurring of the responses across nearby voxels, which has been shown to lead to spurious connectivity results (Colclough et al., 2016). A way to mitigate this is through techniques such as *symmetric orthogonalization* (Colclough et al., 2015). Prior to orthogonalization, the columns in the data matrix, each representing activity from a single region, may contain a degree of linear dependency. To orthogonalize the data, the matrix is firstly *whitened*, finding the closest matrix of uncorrelated vectors (with identity covariance). The length of these vectors is then adjusted to minimise the Euclidian distance between the new matrix and the original data, thus finding an orthonormal set of vectors that best represent the data.

3.3 Summary

This chapter has introduced the basic concepts that underpin data acquisition and analysis with MEG, allowing us to detect and model sources of extremely small neuromagnetic fields from the brain. In Chapters 5 and 6 we use these techniques to investigate aspects of neuronal activity discussed in Chapter 2.

4 Functional MRI

4.1 fMRI Data Acquisition

Functional MRI using blood oxygenation level dependent (BOLD) signal was first demonstrated in 1992, showing clear activation of the human visual cortex during a visual stimulus paradigm (Kwong et al., 1992). Since then, fMRI has become one of the most popular techniques for functional neuroimaging, with a range of demonstrated clinical and research applications (Lee et al., 2013, Matthews et al., 2006). This thesis applies functional magnetic resonance imaging (fMRI) techniques to investigate post-stimulus haemodynamic changes which may provide a functional correlate to those measured using MEG. The following chapter will provide a brief theoretical basis for understanding how fMRI data is acquired, including the concept of nuclear magnetic resonance (NMR) signal, and how this signal is exploited to produce an image with varying contrast between tissues.

4.1.1 Nuclear Spin

Underpinning all of NMR is the concept of *spin*. Spin is a form of angular momentum that is intrinsic to a particle, taking the same value irrespective of the particle's history (e.g., energetic collisions) or the temperature of the system, even at absolute zero, where there is no classical angular momentum. Unlike classical angular momentum, spin angular momentum is quantized, characterised by the spin quantum number, s, which takes integer values for bosons (e.g. 0, 1, 2…) and half-integer values for fermions (e.g. 1/2, 3/2, 5/2…). The direction of spin is also quantized, characterised by the magnetic quantum number, m_s, which has $2s + 1$ possible values in integer steps from $-s$ to $+s$ and represents the z component of the spin angular momentum. The spin angular momentum vector, $\boldsymbol{J}$, has magnitude equal to $m\hbar$ along the z axis, where $\hbar$ is the reduced Planck's constant ($h/2\pi$).

Spin is closely related to magnetism. A charged particle with non-zero spin can be thought of as a rotating charged sphere, giving rise to a magnetic moment, $\boldsymbol{\mu}$, aligned with the angular momentum vector. The magnetic moment is related to the spin angular momentum via the *gyromagnetic ratio*, γ, such that

$$\boldsymbol{\mu} = \gamma \boldsymbol{J}. \tag{4.1}$$

The gyromagnetic ratio is property of the nucleus and is specific for each type of nucleus – for hydrogen nuclei, i.e., single protons, often used for imaging the body/brain, this is $\gamma = 42.58\ \mathrm{MHz\,T^{-1}}$.

In the presence of an external magnetic field, $\boldsymbol{B}$, the energy of the nuclear magnetic moment is

$$E = -\boldsymbol{\mu} \cdot \boldsymbol{B}. \tag{4.2}$$

The negative sign indicates that the energy of a nuclear magnetic moment is lowest when positively aligned with the external magnetic field. For a field with magnitude, B_0, applied in the z direction, such that $\boldsymbol{B} = B_0\boldsymbol{k}$ (where $\boldsymbol{i}, \boldsymbol{j}, \boldsymbol{k}$ are cartesian unit vectors), the only non-zero component of energy will be $-\mu_z B_0$. Using the fact that the magnitude of $\boldsymbol{J}$ is equal to $m_s\hbar\boldsymbol{k}$, along with equation 4.1, we can re-write the energy of a hydrogen ($s = 1/2$) nuclear magnetic moment as

$$E = -\gamma m_s \hbar B_0 = \pm\frac{\gamma\hbar B_0}{2}, \tag{4.3}$$

where two distinct energy levels arise due to the $2s + 1$ possible values of m_s. This process is known as *Zeeman splitting.* Naturally, more energy states would arise if considering a different nucleus with greater spin (e.g., $s = 3/2$). The two spin-states that arise in hydrogen nuclei are often referred to as *spin-up* and *spin-down*, when the magnetic moment is parallel or anti-parallel to the magnetic field, respectively. The difference in these two energy levels is $\Delta E = \gamma\hbar B_0$. Due to the quantization of spin states, a photon of exactly this energy is required to promote a spin from the lower energy to the higher energy state. The corresponding frequency of this photon,

$$\omega_0 = \gamma B_0, \tag{4.4}$$

is known as the Larmor frequency.

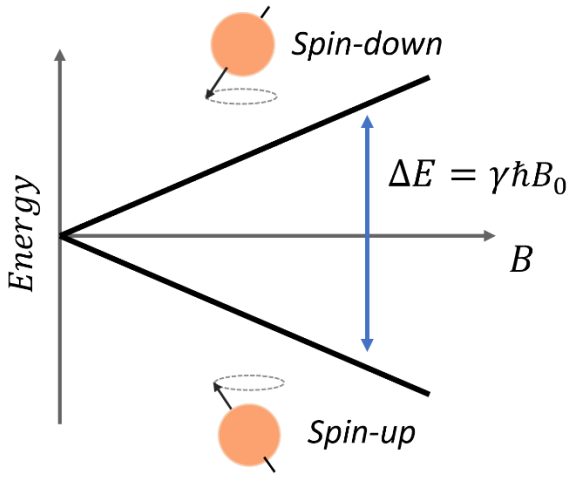


Figure 4.1*: In an applied magnetic field pointing in the z-direction, the spin-states for nuclear magnetic moments separate into two distinct energy levels, spin-up (aligned with magnetic field) and spin-down (anti-aligned with magnetic field). This process is known as Zeeman splitting.*

4.1.2 Spin Precession

As described in the above section, an applied magnetic field in the z direction causes nuclear magnetic moments to tend towards the lower energy spin-up state, aligned with the applied field. In classical terms, we can think of the magnetic field as applying a torque, τ, on the magnetic moments. Torque is defined as the rate of change of angular momentum, giving

$$\tau = \frac{d\boldsymbol{J}}{dt} = \boldsymbol{\mu} \times \boldsymbol{B}, \tag{4.5}$$

which, by substituting in Equation 4.1, becomes

$$\frac{d\boldsymbol{\mu}}{dt} = \gamma \boldsymbol{\mu} \times \boldsymbol{B}. \tag{4.6}$$

As we are considering a magnetic field in the z direction, and the cross product of parallel vectors is zero, the magnetic moment will have zero motion in the z direction. Equation 4.6 can be re-written in terms of each cartesian component as

$$\frac{d\mu_x}{dt} = \gamma \mu_{\boldsymbol{y}} B_{\boldsymbol{0}}, \quad \frac{d\mu_y}{dt} = \gamma \mu_{\boldsymbol{x}} B_{\boldsymbol{0}}, \quad \frac{d\mu_z}{dt} = 0. \tag{4.7}$$

The solutions to these equations are:

$$\begin{aligned} \mu_x(t) &= \mu_x(0)\cos(\gamma B_0 t) + \mu_y(0)\sin(\gamma B_0 t), \\ \mu_x(t) &= -\mu_x(0)\sin(\gamma B_0 t) + \mu_y(0)\cos(\gamma B_0 t), \\ \mu_z(t) &= \mu_z(0). \end{aligned} \tag{4.8}$$

These equations correspond to *precession* around the z axis with constant frequency equal to γB_0, i.e., the Larmor frequency (Eq. 4.4).

4.1.3 Bulk Magnetisation

In a system at absolute zero (no thermal energy) and a perfectly uniform B_0 field, we would expect a “pure” spin-up state in the z direction for an ensemble of nuclear magnetic moments, as all moments would take the lowest possible energy level, i.e., aligned parallel with the magnetic field. However, in realistic conditions, magnetic moments will be promoted to higher energy levels due to thermal interactions, resulting in a distribution of spin states. In a system with temperature, T, the distribution of spin states can be estimated using a Boltzmann distribution, such that

$$\frac{n_{up}}{n_{down}} = e^{\frac{-\Delta E}{k_b T}} = e^{\frac{-\gamma \hbar B_0}{k_b T}}, \tag{4.9}$$

where n_{up} and n_{down} are the number of spins in the spin-up and spin-down states, ΔE is the difference in energy between the two spin states, and k_b is the Boltzmann constant. The bias towards the lower energy spin-up state creates a net bulk magnetisation in the direction of the applied field, $\boldsymbol{M} = M_0\boldsymbol{k}$, which, for hydrogen nuclei ($s = 1/2$), has magnitude given by

$$M_0 = \frac{N(\gamma\hbar)^2 B_0}{4k_b T}, \tag{4.10}$$

where N is the number of spins. This magnetisation forms the basis of NMR signal. From Equation 4.10 we can see that net magnetisation, and thus NMR signal, can be increased by using higher field strengths, using nuclei with higher gyromagnetic ratio, or decreasing the temperature (although this is often not practical in human imaging). The equation of motion for the bulk magnetisation is similar to that of a single nuclear magnetic moment, given by

$$\frac{d\boldsymbol{M}}{dt} = \gamma\boldsymbol{M} \times \boldsymbol{B}, \tag{4.11}$$

indicating that the magnetisation vector, although initially aligned statically with the applied field, exhibits precessional motion when knocked out of alignment.

Figure 4.2 illustrates the origin of net magnetisation for an ensemble of nuclear magnetic moments in an applied field. It is important to note here that in practice, due to energetic interactions in the system and non-uniform external fields, the nuclear moments are still mostly oriented randomly, with only a small bias towards positive alignment in the z direction.

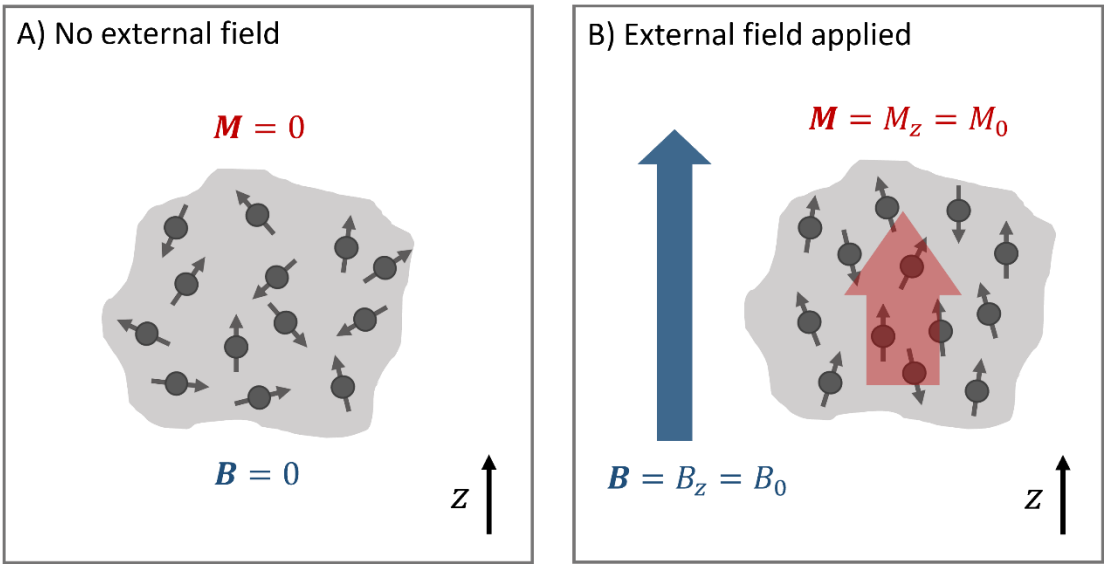


***Figure 4.2**: With no external field applied (panel A), an ensemble of nuclear magnetic moments will have no net direction. Applying an external field in the z-direction (panel B) causes the magnetic moments to align either parallel or anti-parallel to the direction of the field, corresponding to the spin-up (lower energy) and spin-down (higher energy) states, respectively. This creates a net magnetisation (red arrow) in the direction of the applied field, related to the strength of the applied field, the number of magnetic moments, the type of nucleus, and the temperature.*

4.1.4 Spin Excitation

To measure an NMR signal, the net magnetisation must be perturbed out of alignment with the B_0 field. This is achieved using a time-varying magnetic field, which we can write as

$$\boldsymbol{B}(t) = 2B_1 \cos(\omega t)\boldsymbol{i} \tag{4.12}$$

where B_1 is generally much lower than B_0, and ω is the oscillation frequency. The equation of motion for the bulk magnetisation (Eq. 4.10) now becomes

$$\frac{d\boldsymbol{M}}{dt} = \gamma(\boldsymbol{M} \times (B_0\boldsymbol{k} + 2B_1 \cos(\omega t)\boldsymbol{i})). \tag{4.13}$$

This expression is difficult to solve due to the time dependence, but can be simplified by introducing a *rotating frame of reference*, where the cartesian axes are rotating clockwise around the z direction at frequency ω. In the laboratory frame of reference, Equation 4.12 can be re-written in terms of two fields, with one rotating clockwise at ω and the other rotating anti-clockwise at the same frequency:

$$\boldsymbol{B}(t) = B_1(\cos(\omega t)\boldsymbol{i} - \sin(\omega t)\boldsymbol{j}) + B_1(\cos(\omega t)\boldsymbol{i} + \sin(\omega t)\boldsymbol{j}). \tag{4.14}$$

If we now transform to the rotating frame of reference, the clockwise rotating field (first term) appears static, while the anti-clockwise rotating field (second term) appears to

rotate anti-clockwise at 2ω. The rapid variation of this anti-clockwise field means we can assume it has no significant effect on the time-evolution of the bulk magnetisation (it is off-resonance) and can therefore be ignored. We can write the relationship between the time evolution of magnetisation in the laboratory and rotating reference frames as

$$\frac{d\boldsymbol{M}}{dt} = \frac{d\boldsymbol{M'}}{dt} - \omega\boldsymbol{k} \times \boldsymbol{M'}. \tag{4.15}$$

where $\boldsymbol{M'}$ is the magnetisation in the rotating frame. Using Equations 4.13 and 4.15, we can now write the time evolution of the bulk magnetisation in the rotating frame as

$$\frac{d\boldsymbol{M'}}{dt} = \boldsymbol{M'} \times \left((\gamma B_0 - \omega)\boldsymbol{k} - \gamma B_1 \boldsymbol{i'}\right), \tag{4.16}$$

where $\boldsymbol{i'}$ is the x direction unit vector in the rotating frame. Here, we can see that when the time-varying applied field oscillates at the Larmor frequency, $\omega_0 = \gamma B_0$, i.e., on-resonance, the equation simplifies to

$$\frac{d\boldsymbol{M'}}{dt} = \gamma B_1 \boldsymbol{M'} \times \boldsymbol{i'}, \tag{4.17}$$

which corresponds to rotation about the x axis (in the rotating frame) at frequency γB_1. After a time, τ, the magnetisation will have moved through an angle, α, often called the *flip-angle:*

$$\alpha = \gamma B_1 \tau. \tag{4.18}$$

In summary, when a time-varying field is applied perpendicular to the static field (and the direction of bulk magnetisation) at the Larmor frequency, i.e., on-resonance, the magnetisation will be rotated through an angle α according to Equation 4.18 in the rotating frame of reference, as shown in Figure 4.3. In the laboratory frame of reference, this corresponds to an increasing of the precession angle of the magnetisation vector. The time varying field is often named using the characteristic field amplitude, B_1, or referred to as a radiofrequency (RF) pulse, as the required frequency falls in the radiowave range. Using the gyromagnetic ratio of hydrogen nuclei, which is 42.58 MHz/T, we can calculate that for a 3T B_0 field, the frequency of the B_1 field must be 127.73 MHz, while for a 7T B_0 field, the frequency must be 298.06 MHz. Often, RF pulses are also referred to in terms of the specific flip angle, e.g. a 90° RF pulse has a flip angle of 90°, transferring all of the magnetisation from the longitudinal (z) direction to the transverse (xy) plane.

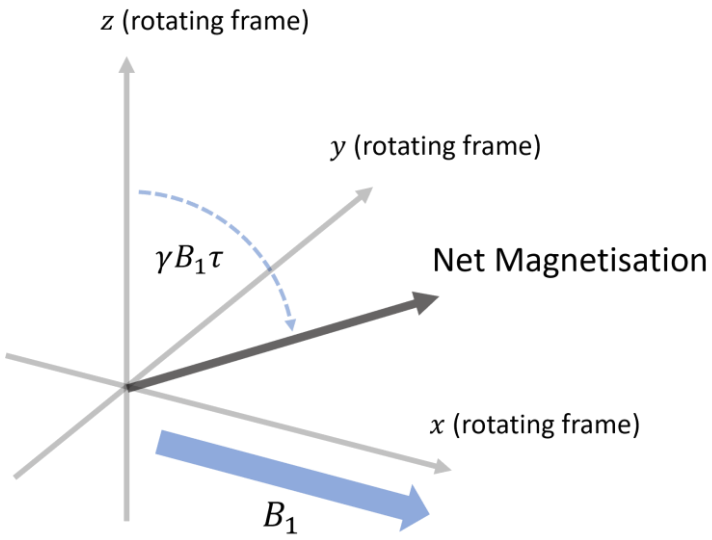


***Figure 4.3**: An applied field in the x direction, oscillating at the Larmor frequency, causes the bulk magnetisation to be rotated from alignment with the longitudinal (z) axis, towards the transverse (xy) plane. In a frame of reference that rotates at the Larmor frequency, this is a simple rotation of the magnetisation vector by the flip angle, $\alpha = \gamma B_1 \tau$, however, in the lab frame of reference, the magnetisation follows precessional motion, introducing a rotating transverse magnetisation.*

4.1.5 Longitudinal Relaxation

Following an RF pulse, the net longitudinal (z direction) magnetisation will be altered depending on the flip angle. For example, following a 90° pulse, the net magnetisation will be rotated entirely into the transverse (xy) plane. Molecular motion, which arises due to thermal energy in the system, will cause state transitions in nuclear spins due to local changes in the magnetic environment. This can be understood in a similar way to RF pulses, in that the local magnetic field changes must oscillate at the Larmor frequency for energy to be transferred from the nuclear spin to the surrounding molecules, causing relaxation of the nuclear spin to lower energy states and eventual recovery of the initial net magnetisation, M_0, at thermal equilibrium. This process is known as longitudinal relaxation. The recovery of longitudinal relaxation over time, t, following application of a 90° RF pulse can be written as

$$M_z(t) = M_0\left(1 - e^{-t/T_1}\right). \tag{4.19}$$

In this equation, T_1 is the time taken to recover around 63% $(1 - 1/e)$ of the initial magnetisation. As this process relies on molecular motion creating magnetic field fluctuations close to the Larmor frequency, the value of T_1 changes based on the molecular environment. Generally speaking, media with restricted motion such as tissues will have shorter T_1 values than freely moving media such as water due to the characteristic timescales of molecular motion in each case. Importantly, different

tissues in the body will have different T_1 values. These tissues will therefore have different brightnesses in the image, depending on the time that the image is taken during the relaxation process. How an image is taken will be described in later sections.

4.1.6 Transverse Relaxation

As described in Section 4.1.4, the RF pulse also introduces a transverse component of net magnetisation that rotates at the Larmor frequency. However, the spins constituting the net magnetisation gradually lose phase coherence due to inhomogeneities in the local field and interactions between neighbouring spins. Inhomogeneities in the local field that cause spin dephasing can be split into two categories: static inhomogeneities caused by, for example, inhomogeneities in the static B_0 field, and time-varying inhomogeneities caused by slow motion of molecules. Dephasing due to static inhomogeneities has an associated time constant, T_2', and can be undone, or *refocussed*, using 180° RF pulses. Refocussing pulses work by rotating spins 180° around a direction in the transverse plane, meaning the spins that precess the fastest are now behind in phase and those that precess the slowest are in front, such that the difference in precession speed now moves the spins back into phase rather than further apart. Spins can be continually refocussed, forming *echoes* that occur in intervals of the *echo time* (TE). Dephasing due to time varying field inhomogeneities has an associated time constant, T_2, and is irreversible, i.e., the phase coherence cannot be recovered. Thus, each spin echo will be reduced in amplitude according to T_2. The measured decay of transverse signal due to these two effects after a single RF pulse is often called a *free induction decay* (FID), and has associated time constant T_2^*, where

$$\frac{1}{T_2^*} = \frac{1}{T_2'} + \frac{1}{T_2}. \tag{4.20}$$

The decay of the signal envelope with time, t, for any of the transverse time constants, can be written as

$$M_{xy} = -M_0 e^{\frac{-t}{T_2}} \tag{4.21}$$

and is known as transverse relaxation. This process is displayed in Fig 4.4. As with T_1, different tissues in the body will have different T_2 and T_2^* values, creating contrast in an image taken at different times during the signal decay process. For both T_1 and T_2 weighted images, the FID (in the transverse plane) is the signal that constitutes an image.

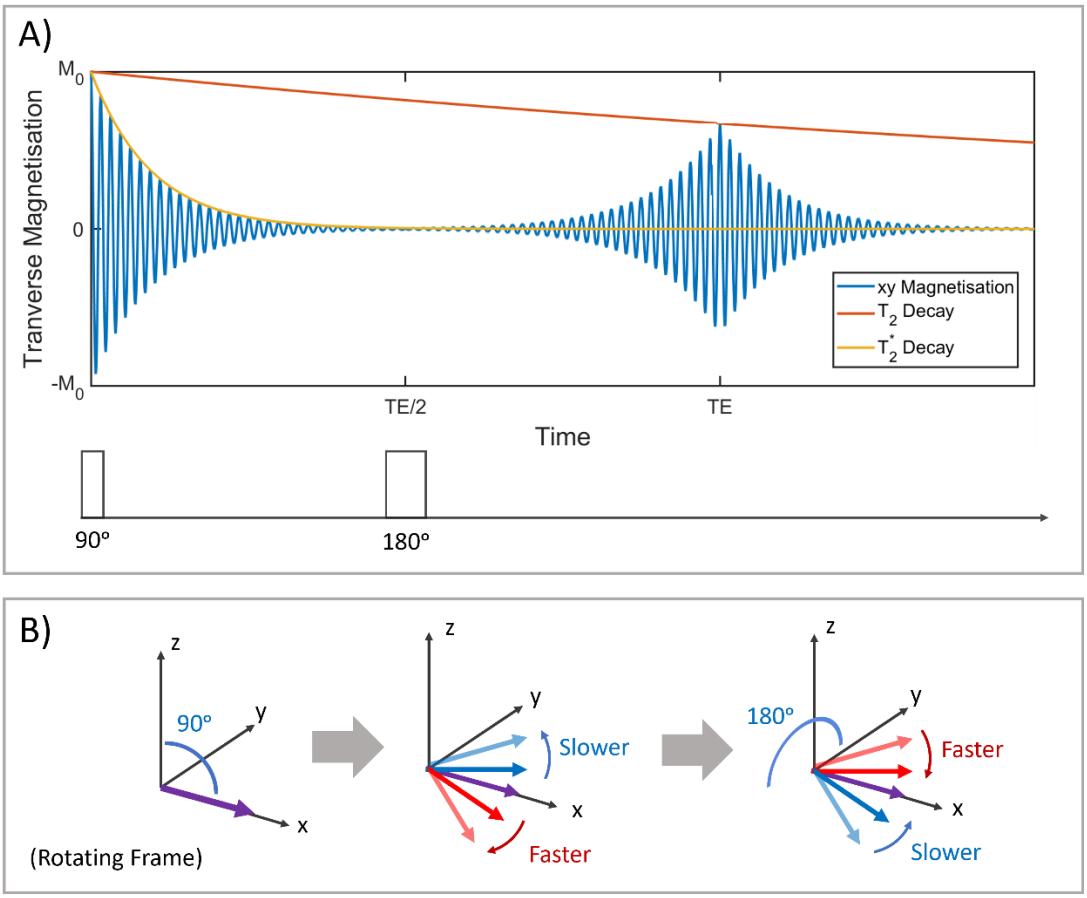


***Figure 4.4**: A) Simulated transverse magnetisation, showing the NMR signal in the transverse plane after a 90° pulse at time 0, followed by a 180° pulse at time TE/2. The magnetisation decays after the 90° pulse with time constant T_2^*. The spins are brought back into phase by the 180° pulse, forming an echo at time TE, which is reduced in amplitude from the initial amplitude according to time constant T_2. B) A schematic of the effect of the 90° and 180° pulse on the bulk magnetisation, showing rotation of bulk magnetisation (left), spin dephasing due to T_2^* effects, and refocussing of $T_2^{'}$ effects. Note that in panel B, there will be some additional irreversible phase offset caused by T_2 effects.*

4.1.7 Slice Selection

To create an image in a particular plane, we must create a spatial dependency in the signal. This is accomplished using magnetic field *gradients*. As the Larmor frequency depends on the applied magnetic field strength, if we apply a further magnetic field which varies linearly in a particular direction, the Larmor frequency will depend on the position of the spins in the same direction.

Applying a gradient in the longitudinal (z) direction, G_{slice}, enables excitation of a thin *slice* of spins in the transverse (xy) direction, as the bandwidth of the RF pulse, $\Delta\omega$, can be tailored to the Larmor frequencies of the corresponding slice. The thickness of the slice can be written as

$$\Delta z = \frac{\Delta\omega}{\gamma G_z}. \tag{4.22}$$

It should be noted that for the RF pulse to contain a range of frequencies, a sinc shaped pulse should be used, as the Fourier transform (frequency content) of a sinc function is rectangular with width that can be tailored to equal $\Delta\omega$, as shown in Figure 4.5.

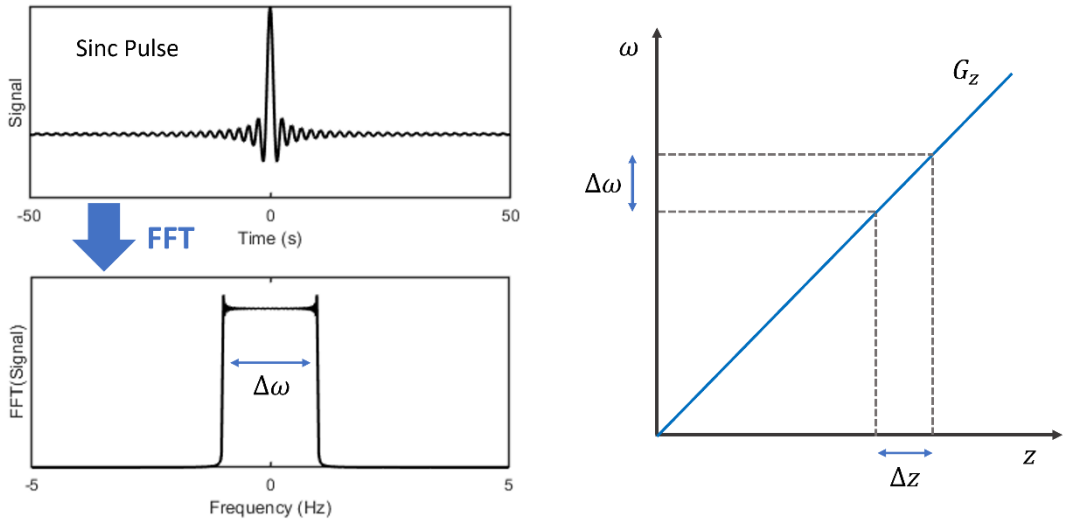


***Figure 4.5**: The plots on the left show how a sinc pulse contains a band of frequencies, $\Delta\omega$, demonstrated using a fast fourier transform (FFT). The diagram on the right shows a slice of thickness, Δz, is excited using a sinc pulse of bandwidth, $\Delta\omega$, when a magnetic field gradient, G_z, is applied.*

4.1.8 Frequency and Phase Encoding

Once a slice in the z direction has been excited, gradients are applied in the x and y directions, known as frequency-encoding (G_{freq}), and phase-encoding (G_{phase}) gradients, respectively. Phase-encoding gradients create a linear shift in the Larmor precession frequency based on position of spins in the y direction. Applying a phase-encoding gradient for a short time will therefore create a phase offset in precessional motion of the spins that varies linearly across the y direction.

Following phase-encoding, a frequency-encoding gradient is applied in the x direction, shifting the Larmor precession frequency based on position of the spins in the x axis. This gradient pulse is applied during sampling, or *readout*, of the image, and is therefore applied for longer than the phase-encoding gradients to allow the signal to evolve (enough time for an echo to form). During readout, the frequencies contained in the signal encode spin positions in the x direction, while the phase encodes positions in the y direction.

In order to better conceptualise the sampling of image data using frequency and phase-encoding gradients, it is useful to consider the effect in *k-space.* Coordinates in k-space (k_x, k_y) correspond to accumulated phase due to applied gradients, such that the origin corresponds to accumulated phase with no gradients applied. The brightness of a pixel in k-space represents the contribution of a particular spatial frequency to the NMR signal. Features that are near the origin in k-space correspond to low spatial frequencies features in the real image, i.e., low resolution features, while finer details in the real image correspond to features near the outside of the k-space image. K-space must therefore be properly sampled to produce a high quality image. Assuming k-space sampling begins at the origin, a line can be sampled in either the phase-encoding (k_y) or frequency-encoding (k_x) direction, which will finish at $k = \gamma G t$, after applying a gradient, G, for a time, t. Once k-space has been properly sampled, a 2D real-space image can be calculated using a 2D Fourier transform (Nussbaumer and Nussbaumer, 1982). The process of converting between real space and frequency space is shown in Fig. 4.6 using a simple binary image of a square.

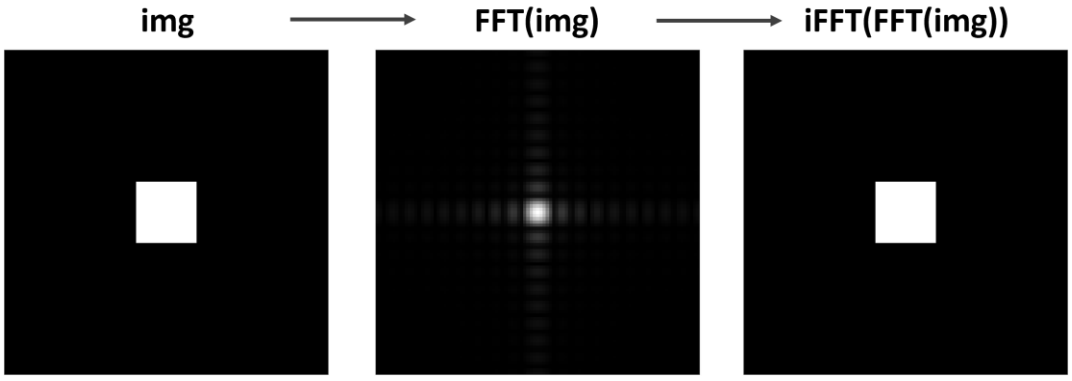


***Figure 4.6**: A demonstration of the conversion between real space (x, y) and frequency (k_x, k_y) space, using a simple binary image of a square. In the image on the left, labelled "img", each pixel simply represents the value at a spatial coordinate, whereas in the middle image, which is the fast Fourier transform (FFT) of "img", each pixel represents the contribution of a spatial frequency to the data in "img". Taking the inverse fast Fourier transform (iFFT), converts back from frequency space to real space, recovering the original image.*

4.1.9 Echo Planar Imaging

The way that k-space is sampled plays an important role in the resulting image. Applying a single frequency encoding gradient following an RF pulse allows for a single straight line to be sampled in k-space, with k_y position determined by the preceding phase encoding. Sampling the entirety of k-space in this way can lead to long acquisition times. For functional imaging, where data must be acquired quickly, the most commonly used sequence is echo planar imaging (EPI) (Mansfield, 1977,

Stehling et al., 1991). EPI uses rapidly switched gradients to traverse an entire k-space plane following a single excitation, typically acquiring a 2D image in less than 100 ms. This process begins with RF excitation, tuned to a particular slice (see Fig. 4.5), followed by a combination of frequency and phase encoding gradients which are used to encode an initial position in k-space to begin sampling. Next, sequential frequency encoding gradients sample lines in k-space, each in the opposite direction, separated by small phase encoding gradients, often called "blips". A schematic of a single slice acquisition using EPI is shown in Figure 4.7. Sequential slices are acquired by repeating this process, although the RF pulse at the start of each sequential acquisition with EPI is often not a 90° pulse, as longitudinal magnetisation has usually not fully recovered by the time an image has been sampled. The appropriate pulse duration can be determined using the Ernst angle, $\alpha_e = \cos^{-1}(e^{-TR/T_1})$, where TR is the repetition time – the time between successive excitations.

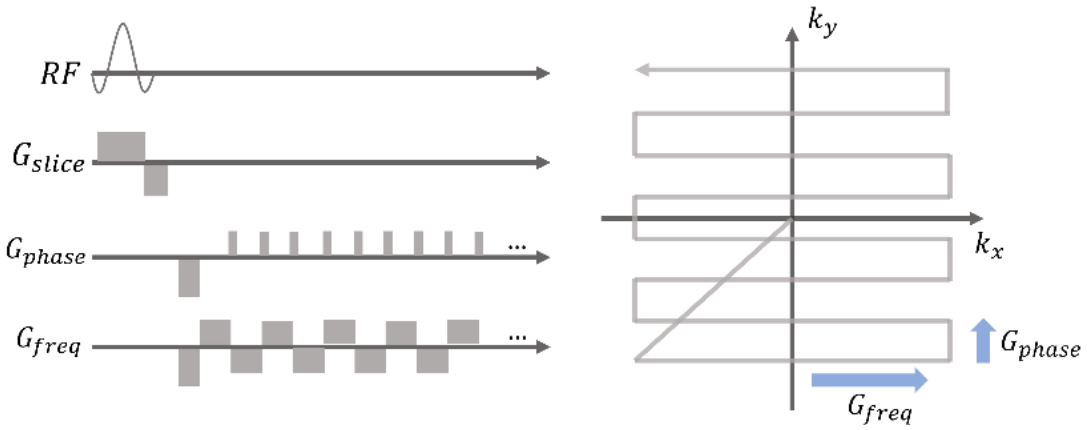


***Figure 4.7**: A schematic showing how k-space is sampled in a gradient echo EPI sequence of a single slice in the transverse plane. Rapidly switched frequency-encoding gradients produce a string of gradient echoes, with short phase-encoding "blips" as the frequency encoding gradients change polarity. This allows an entire 2D image to be formed following a single RF pulse.*

The sequence described so far is usually called gradient-echo EPI, as the switching of frequency-encoding gradient direction creates a string of echoes by continually dephasing and refocussing spins. Given that the switching of gradients is only able to reverse the dephasing caused by the previous gradient, this sequence is sensitive to T_2^* effects, i.e., both static and time-varying field inhomogeneities. However, EPI can also be performed using sequential RF pulses to refocus the spins, known as spin-echo EPI. Refocussing pulses are able to reverse the dephasing caused by static field inhomogeneities, making spin echo EPI more sensitive to T_2 effects, i.e., time-varying field inhomogeneities, which cannot be reversed. In general, gradient-echo EPI can be acquired faster, as echoes can be achieved in shorter times, but the added sensitivity

to field inhomogeneities makes this sequence more prone to susceptibility-induced distortions (see section 4.1.12). It should also be noted that gradient-echo has increased sensitivity to drainage of deoxygenated blood in veins compared to spin-echo (Frahm et al., 1994), which is mostly sensitive to oxygenation changes in capillaries (more local to neurons). Gradient-echo EPI is applied in Chapter 7 to investigate functional changes in BOLD response.

Furthermore, it is possible to sample an entire volume simultaneously in a modification of EPI known as echo volumar imaging (EVI). This is achieved by exciting a thick slab rather than a single slice and using additional phase-encoding gradients in the slice-selection (z) axis to spatially encode in 3D. The same slab is excited repeatedly with lower flip-angle RF pulses, and slices of k_{xy} are sampled in between G_z phase-encoding blips. Compared to 2D EPI, 3D EPI has intrinsically higher SNR, by a factor of $\sqrt{N_{slices}}$, as spins from all voxels within the excited slab contribute to the acquired signal. In addition, the extra phase-encoding direction increases the degree of undersampling that can be performed in accelerated imaging techniques (described in the next section), allowing for reduced TR.

In all EPI acquisition, there is a rough trade-off between TR, voxel size and SNR. When taking functional measures such as BOLD, it is important to keep TR short to capture haemodynamics related to brain activity, which occur in the timescale of several seconds. For a given volume (e.g., an entire brain), using smaller voxels will increase TR and also reduce SNR as there are fewer spins in each voxel. It is therefore common to use larger voxels in functional sequences compared to structural, to maximise SNR and keep TR relatively short, although it should be noted that larger voxel sizes also increase sensitivity to physiological noise (see section 4.1.13).

4.1.10 Accelerated Imaging

Several techniques can be employed to reduce TR in sequences such as EPI whilst maintaining sufficient SNR. The first is parallel imaging (Pruessmann et al., 1999), known as SENSE (sensitivity encoding) in Philips MRI systems. This technique uses multiple receive coils (see section 4.1.14) in different positions, each with different sensitivity profiles to the volume being scanned, i.e., voxels in closer proximity to each coil will produce a greater signal. The extra information from the sensitivity variation in the coils means that images from each coil can be undersampled, i.e., less lines taken in a k-space plane, and later combined to produce a full image, reducing the time taken to acquire an entire volume. This technique is characterised by a SENSE factor, which corresponds to the amount of undersampling performed with each coil, e.g. a SENSE

factor of 2 means only half of the phase encoding steps are required. Parallel imaging intrinsically reduces SNR because less data is acquired when k-space is undersampled, while other effects, such as errors in estimation of coil sensitivities, also tend to reduce SNR. However, this is often outweighed by the benefit of faster acquisition.

Another technique used to speed up acquisition is simultaneous multi-slice, or multi-band (MB) imaging. In MB imaging, multiple slices are excited simultaneously using a combination of multiple RF pulse, each offset at a different frequency (Blaimer et al., 2013, Larkman et al., 2001). Using a multi-coil receiver setup, the slices can then be delineated due to the additional spatial encoding information provided by the coils. Although multiband does not undersample k-space, SNR is still reduced according to a geometry factor, or g-factor, relating to the geometry of the array of receiver coils relative to the object being measured (Blaimer et al. 2013). The multiband factor, which is typically 2 – 4 for Philips MRI systems (as used in this Thesis), describes the number of slices that are acquired simultaneously, and therefore the reduction in the time taken to acquire a volume image.

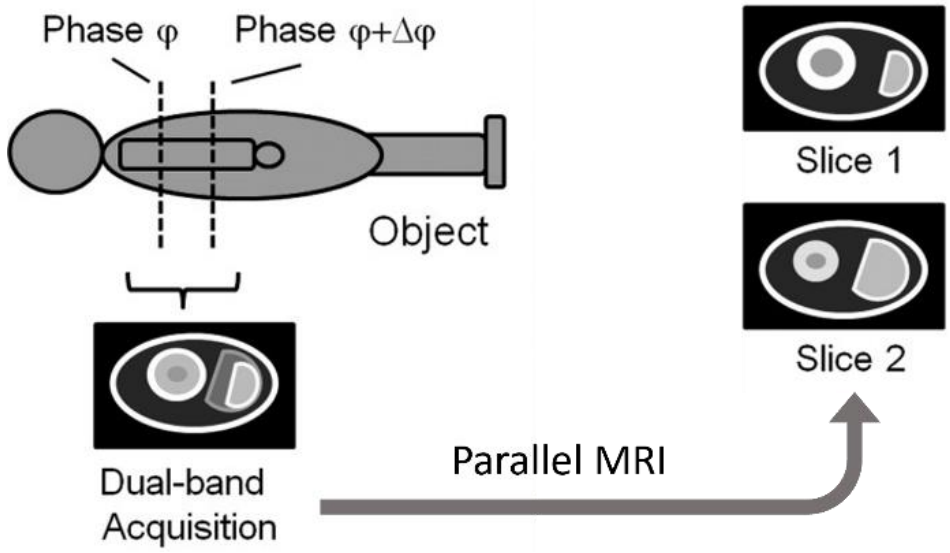


***Figure 4.8**: A schematic, adapted from (Blaimer et al. 2013), showing multi-slice MRI. Two separate slices are excited simultaneously, creating an image which contains information from both slices. The slices can then be delineated using spatial encoding information from parallel receive coils.*

4.1.11 Anatomical Imaging

Functional imaging is performed using sequences with fast acquisition and lower image quality. In many cases, a high-quality anatomical image of the brain is required, for applications in fMRI and also M/EEG. In the case of fMRI, anatomical images aid with visualisation, and allow for *co-registration* to a standard brain for the purpose of

group averaging. The most common MRI sequence used for anatomical images is magnetisation-prepared rapid acquisition gradient echo (MPRAGE) (Mugler III and Brookeman, 1990).

MPRAGE is a sequence that produces high resolution images with good contrast between different tissues in the brain. The sequence is an example of an inversion recovery sequence. MPRAGE starts with a $180°$ inversion pulse that rotates the net magnetisation vector such that it opposes the static field. The spins are allowed to relax for a chosen time, known as the inversion time (TI), before an image is taken using a 3D gradient echo readout. Because tissues will be at different points of the longitudinal relaxation process during k-space sampling, this sequence is T_1 weighted. TI must therefore be chosen to give maximum contrast between tissues of interest. MPRAGE is used to take T1-weighted anatomical images in Chapter 5 to allow for co-registration and source reconstruction with MEG data.

Another popular sequence used for anatomical imaging is phase sensitive inversion recovery (PSIR) (Hou et al., 2005). In a regular inversion recovery sequence, the MR signal (corresponding to voxel brightness) only depends on the magnitude of the bulk magnetisation at the point when image readout begins. This would mean that two tissues with equal and opposite magnetisation at TI would have zero contrast in the image. In a PSIR sequence, TI is chosen such that an image is taken in the middle of the *null points* (point of zero signal) of white and grey matter. This image is then phase-corrected, recovering the sign as well as the magnitude of each voxel to maximise contrast between white and grey matter. This thesis uses a modified PSIR sequence (Mougin et al., 2016) in Chapter 7, which takes a second image after the null points of grey matter, white matter and cerebrospinal fluid. The second image is used to retrieve the sign of the magnetisation in the first image, as well as correct the bias field (Van de Moortele et al., 2009).

4.1.12 Susceptibility-Induced Distortions

For all types of imaging using MRI, inhomogeneities in the static B_0 field can create distortions in the image. This is because spatial information in the image is encoded using the accumulated phase due to magnetic field gradients, so any additional phase offset that occurs due to B_0 field inhomogeneities will create spatial distortions as the accumulated phase will not match the voxel position. Although some inhomogeneities arise due to hardware, they are also caused by differences in *magnetic susceptibility* of different tissues (Graham et al., 2017). Magnetic susceptibility is a measure of how magnetised a material becomes in the presence of a magnetic field. Thus, at

boundaries between tissues with different magnetic susceptibility, there will be a shift in local precession phase which will lead to spatial distortions in the image. These can be partially corrected by informing active shimming coils (see section 4.1.14) with a B_0 map taken prior to running the main scanning sequences, although further post-processing is often required with sequences which are particularly prone to these artefacts. It should be noted that inhomogeneities due to magnetic susceptibility become greater as the strength of the B_0 field is increased. This is because precession frequency increases with the applied field (Eq. 4.4), meaning differences in phase due to inhomogeneities will be greater. In addition, sequences such as gradient-echo EPI (section 4.1.9) are more prone to susceptibility-induced distortions as they are sensitive to both static and time-varying field inhomogeneities due to the use of gradient echoes to perform fast acquisition.

4.1.13 Noise in Functional Data

Noise in functional imaging is generally estimated by temporal signal to noise ratio (tSNR), found by dividing the mean of a voxel timecourse by its standard deviation. The two primary sources of noise in fMRI data are thermal and physiological noise. Thermal noise is created by thermal agitation of charge carriers in both the scanner electronics and the participant (Bodurka et al., 2007, Liu, 2016). Thermal noise has been shown to become the dominant source of noise at high resolutions (Triantafyllou et al., 2005), making high field strengths such as 7T preferrable in this regime as the tSNR will scale will the SNR, which in turn scales with field strength.

Physiological noise is entirely driven by the participant and dominates (compared to thermal noise) when using larger voxel sizes (Triantafyllou et al., 2005). There are several persistent sources of physiological noise that are mostly unavoidable, even in particularly motivated participants (Murphy et al., 2013). Firstly, the cardiac and respiratory cycles both create periodic movement in the scanner, causing time-varying inhomogeneities in the static field which can induce additional phase offset, and thus distortions in the image (Murphy et al., 2013, Brosch et al., 2002). Additionally, head movement caused by breathing can lead to periodic shifting in the location of spins according to breathing phase (Friston et al., 1996). Given that cardiac and respiratory cycles occur in a frequency range that is similar to BOLD changes (Akselrod et al., 1981, Wise et al., 2004, Birn et al., 2006), these physiological noise sources can cause spurious results. As well as periodic activity, it has also been shown that changes in breathing rate can drive changes in BOLD due to fluctuations in arterial CO_2 concentration (Wise et al., 2004). Measures can be put in place during the scan, such as head padding and active shimming, to partially mitigate effects caused by

respiratory and cardiac cycles. However, post-processing techniques are usually still required to remove these noise sources from the data. One approach to removing periodic physiological noise from the data is retrospective image correction [RETROICOR] (Glover et al., 2000), which is the method applied in Chapter 7. This method assumes that the data are corrupted by separate periodic functions representing the cardiac and breathing cycles. Data is taken during the scan to measure each of these cycles, using equipment such as a respiratory bellows and a pulse oximeter. The phase timecourse of cardiac and breathing data are then calculated and transformed into low-order Fourier series (trigonometric functions). These are then fit to the EPI data using linear regressions, and subsequently removed.

4.1.14 MRI System

As discussed in the previous sections, to form an image using MRI we need a static B_0 field, an oscillating B_1 field, and magnetic field gradients, G_{slice}, G_{freq} and G_{phase}. It is beneficial for B_0 to be as high as possible as the MRI signal strength is based on the bulk magnetisation (Eq. 4.19, 4.21), which in turn is related to the strength of the applied field (Eq. 4.10). Typical values of B_0 include 1.5T, 3T and 7T (around 100,000 times stronger than Earth's magnetic field at the surface). As well as overall strength, the B_0 field must also be stable across time. To achieve fields with the required strength and temporal stability, MRI magnets are made of solenoids of superconductive material (see description of superconductivity in Chapter 3). The field is then proportional to the number of coils in the solenoid per unit length, as well as the current through the coil. Using superconducting material allows for extremely strong and stable magnetic fields to be produced, as current flows without the effects of electrical resistance which would usually cause energy loss over an extended period of use. A downside of using superconductive coils is that they must remain cryogenically cooled using liquid helium, as is the case with MEG scanners (see Chapter 3).

Another requirement of the B_0 field is uniformity, specifically within the space where the brain (or any body-part being scanned) will occupy. As described in section 4.1.12, additional phase offset due to field inhomogeneities will create spatial distortions in the image. These inhomogeneities can be mostly corrected using *shims*. Passive shims are fixed pieces of ferromagnetic material, creating fixed alterations to the field. Active shims are coils which must be energised to produce corrective fields, providing a more flexible solution to field inhomogeneities. As with susceptibility-induced distortions, inhomogeneities due to intrinsic magnet properties become greater as the strength of

the B_0 field is increased (Eq. 4.4), meaning field correction is particularly important at high field strengths such as 7T.

To create gradients, G_{slice}, G_{freq} and G_{phase} which are usually applied in the z, x and y directions, respectively, a set of three gradient coils are required (Carpenter and Williams, 1999). Gradients in the z direction (aligned with the bore) are usually created by circular wire coils, whereas gradients in the x and y directions are created using coils in a saddle orientation (see Fig. 4.9). The current passed through each of these coils following an RF pulse determines the spatial encoding of precessional motion. Gradient coils are usually a fixed part of the MRI system which do not need to be changed based on the scanning sequence.

RF coils are used to transmit the B_1 field as well as receive the transverse MRI signal (the FID). These two functions may be handled by the same coil, or in separate transmit and receive coils (Carpenter and Williams, 1999). Transmit coils produce oscillating B_1 fields which are able to excite spins over large spans of tissue, while receive coils pick up transverse magnetisation through electromagnetic induction, before it is amplified, digitised and filtered to extract frequency and phase information. Transmit coils should be placed close to the tissue of interest to maximise the strength of the MR signal measured (see Fig. 4.9).

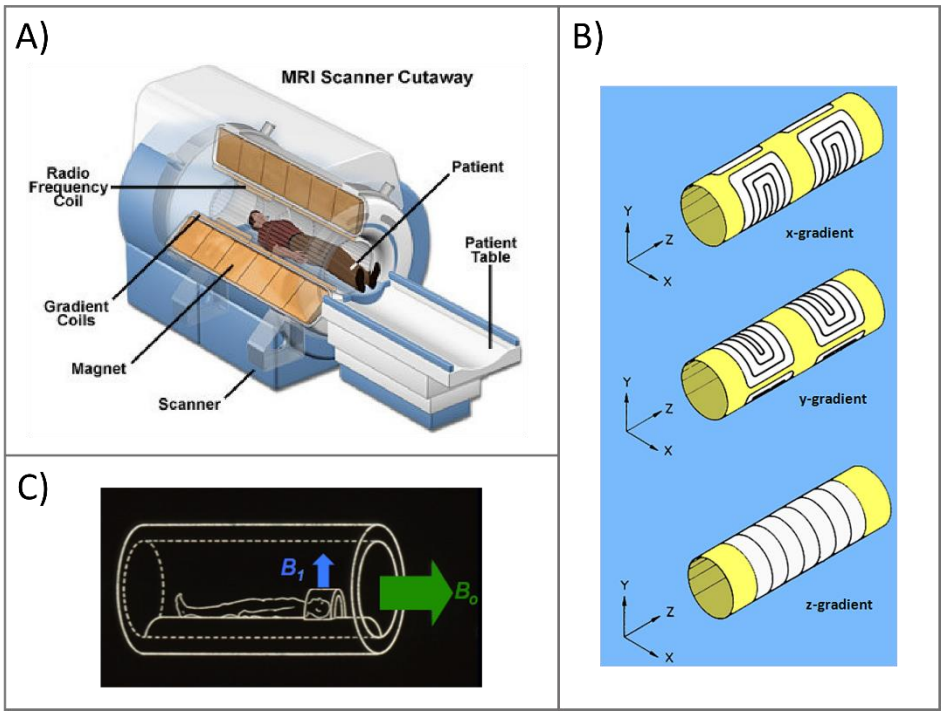


***Figure 4.9**: Panel A shows a cutaway of a typical MRI scanner (taken from https://www.analogictips.com, access date 15/02/2024), showing a patient in the MRI magnet bore, as well as the positions of gradient and RF coils. Panel B shows typical coil geometries for gradients in the x, y and z directions (taken from https://mriquestions.com, access date 15/02/2024), which are usually integrated to the scanner bore. Panel C shows a RF coil, producing the B_1 field perpendicular to the static B_0 field (taken from https://mriquestions.com, access date 15/02/2024). The RF coil in panel C is specifically designed for head scanning, allowing the receive component to be much closer to the tissues of interest.*

4.1.15 Origin of Contrast in Functional MRI

Oxygen is a fundamental requirement for brain function. The brain has no storage capacity for oxygen, thus requiring a constant supply to meet ongoing demands. Oxygen is delivered to the brain in red blood cells, bound to a protein called haemoglobin that has four *haem* (iron containing) groups, each of which can bind to an oxygen molecule. Haemoglobin that is saturated with oxygen is known as oxyhaemoglobin. Following dissociation of oxygen from the haem groups, this becomes deoxyhaemoglobin. Importantly, deoxyhaemoglobin is *paramagnetic,* meaning it becomes weakly magnetised when exposed to a magnetic field, while oxyhaemoglobin is *diamagnetic,* meaning it does not become magnetised when exposed to a magnetic field. Therefore, the presence of deoxyhaemoglobin creates local field inhomogeneities that encourage transverse magnetisation decay. Upon

activation, the ratio of oxyhaemoglobin to deoxyhaemoglobin increases due to the fact that blood flow overcompensates for the increase in metabolic demand (see Chapter 2). This occurs primarily in the venules and veins after oxygen has been transferred to the tissue in the capillary bed (Ogawa et al., 1993b). The increased ratio of oxyhaemoglobin to deoxyhaemoglobin following activation causes a relative decrease in the local magnetic susceptibility, and therefore a decrease in the field inhomogeneity felt by nearby hydrogen nuclei. This process increases T_2 and T_2^*, i.e., increasing the relative BOLD signal from baseline levels. This is the primary contributor to contrast in functional MRI (Ogawa et al., 1990).

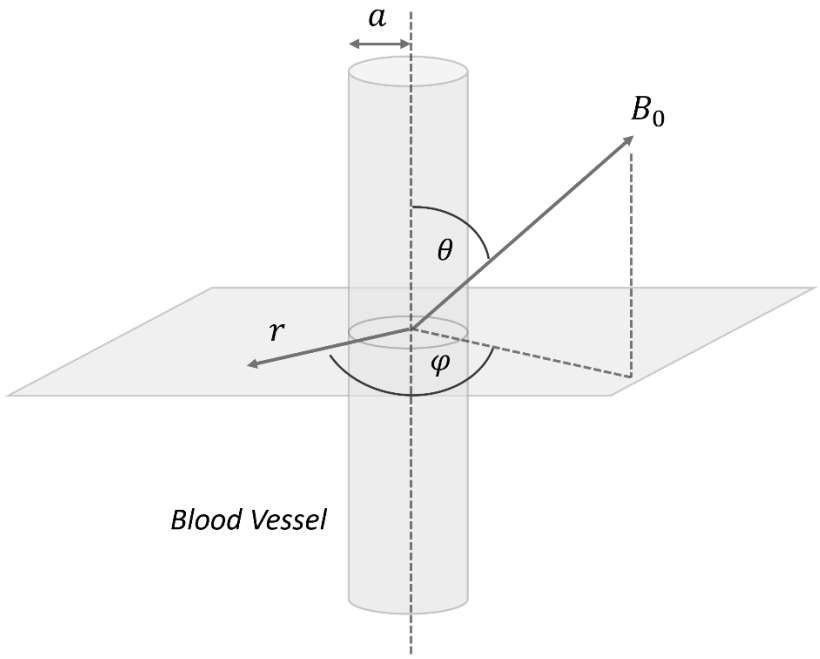


***Figure 4.10**: A schematic of a blood vessel, modelled as an infinite cylinder with radius a, at angle θ from the static B_0 field. This model is used to derive the dephasing effect of field inhomogeneities at a distance r from the vessel, at angle φ from the field.*

The susceptibility effects of deoxyhaemoglobin have effects both within the blood vessels, as well as in the space surrounding the vessels. Ogawa *et al* modelled the intravascular and extravascular effects on magnetic susceptibility by considering blood vessels in the brain as infinite cylinders, oriented randomly at angle θ with respect to the static B_0 field, as shown in Figure 4.10 (Ogawa et al., 1993b). Using this model, the following equations can be derived for the change in precessional frequency both within and outside the vessel:

$$\Delta\omega_{outside} = 2\pi\Delta\chi(1-Y)\omega_0({}^{a}/_{r})^2 \sin^2(\theta)\cos(2\varphi)\,, \tag{4.23}$$

$$\Delta\omega_{inside} = 2\pi\Delta\chi(1-Y)\omega_0\left(\cos^2\theta - {}^{1}/_{3}\right).$$

In these equations, Y is the fraction of oxygenated blood within a vessel of radius a, and $\Delta\chi$ is the susceptibility difference between oxygenated and deoxygenated blood. A consequence of these equations is that both the intravascular and extravascular dephasing effects will increase with applied field strength, as the Larmor frequency increases linearly with field strength (Eq. 4.4). It should also be noted that due to the dependence on trigonometric functions of θ and φ, the BOLD contrast could be dramatically reduced based on the orientation of the blood vessel. Gagnon *et al* quantified this variation in BOLD sensitivity across the cortex using two-photon microscopy of the rodent brain to map realistic microvasculature (Gagnon et al., 2015).

The effect of blood oxygenation on T_2 and T_2^* contrast can be understood using *static dephasing* and *dynamic averaging* (Ogawa and Lee, 1990, Yablonskiy and Haacke, 1994, Ogawa et al., 1993a). Water follows a random diffusion pathway in the extravascular space, characterised by the *diffusion length*, i.e., the net distance diffused in a given time. Static dephasing occurs when a field inhomogeneity varies on a scale that is large compared to the diffusion length of water. In this regime, the dephasing can be refocussed, thus having a greater effect on T_2^* contrast. Dynamic averaging occurs when a field inhomogeneity varies on a scale that is comparable to the diffusion length of water. These time-varying inhomogeneity effects cannot be refocussed, and therefore have a greater effect on T_2 contrast. Inhomogeneities around blood vessels vary on a scale that is proportional to their radius. Consequently, for large vessels, e.g., draining veins, the diffusion length of water in the extravascular space is small compared to the gradient of the inhomogeneity, meaning static dephasing, and thus T_2^* contrast, dominates in this regime. Conversely, for small vessels, e.g. capillaries, the diffusion length of water is comparable to the gradient of the extravascular inhomogeneity, meaning dynamic averaging, and thus T_2 contrast, dominates here. It is important to note, from Equation 4.23, that dephasing is proportional to the applied field strength, via the Larmor frequency. This means that at higher fields, due to decreased T_2^* the TE required for optimal contrast is reduced, along with the relevant diffusion length of water. Consequently, at higher fields, the contribution of smaller blood vessels to the BOLD signal is increased.

Dynamic averaging also plays a role in the intravascular signal. Within the blood vessels, the source of field inhomogeneity is the individual red blood cells, rather than the bulk effect of the blood vessel, meaning the fields vary according to the size of the blood cells. As the size of red blood cells is small compared to the diffusion length of water within a blood vessel, the presence of deoxyhaemoglobin decreases the T_2 due to dynamic averaging. From Equation 4.23, we can see that this effect is independent

of vessel size. Another factor to consider for intravascular BOLD signal is the difference between the T_2 of blood compared to surrounding tissue. In Chapter 2, we discussed how neuronal activation causes an increase in CBV. If blood has a longer T_2 than surrounding tissue then an increase in CBV will cause an increase in BOLD signal intensity. However, if the T_2 of blood is shorter than surrounding tissue, an increase in CBV will cause a decrease in BOLD signal. At 3T, the T_2 of oxygenated blood is comparable to that of grey matter, but the T_2 of deoxygenated blood is slightly lower, meaning an increase in CBV following activation, and thus an increase in the fraction of oxygenated blood, will cause a relative increase in the intravascular BOLD signal. However, at 7T, the T_2 of blood is much lower than grey matter, meaning the intravascular BOLD signal is mostly lost at the TE values typically used.

Based on the discussion above, it becomes apparent that GE and SE EPI sequences will differ in sensitivity to different parts of the vasculature. As GE EPI is sensitive to T_2^* contrast, this sequence will be more sensitive to signal around large blood vessels. On the other hand, SE EPI, due to T_2 sensitivity, will measure greater contribution from smaller blood vessels along with intravascular signal at lower field strengths. Because of this, signal in SE EPI is thought to relate more closely to neuronal activity than GE EPI, as the small blood vessels (capillaries) are in closer proximity to the neurons being activated.

4.2 fMRI Data Analysis

4.2.1 Typical Pre-Processing Steps

Following acquisition of EPI data, several pre-processing steps are applied before any analysis of task-driven effects. Typical pre-processing steps include:

- **Motion Correction:** The EPI data are separated in the time dimension, forming a series of 3D volume images. A rigid body matrix (6 degrees of freedom, 3 each for translation and rotation) is calculated between each volume and a nominated fixed volume to align the images across all timepoints.
- **Spatial Smoothing:** The EPI data are convolved with a smoothing kernel, which, for a 3D volume image, is a cube containing a 3D Gaussian function with full-width-half-maximum of ~ 2 voxel widths. This reduces the effect of any noise with high spatial frequency but can also diminish fine detail in the image.
- **Highpass Filtering:** Scanner components can heat up over time due to repeated gradient switching, causing drifting of the signal baseline. This can be

removed using a highpass filter, removing very low frequency effects in the data (typically < 0.01 Hz).

4.2.2 General Linear Modelling

A common method to analyse fMRI data is using a general linear model [GLM] (Friston et al., 1995). This approach models the effect of stimuli, tasks, and other factors such as behaviour and demographic information, on the BOLD signal. We start with a simple linear equation,

$$\boldsymbol{Y} = \boldsymbol{X}\beta + \varepsilon \tag{4.24}$$

relating variable $\boldsymbol{Y}$ to variable $\boldsymbol{X}$ via the linear transformation contained in β, with error ε. This is the same equation used to relate any two variables via linear regression, no matter the dimensionality of the independent variable (i.e., this is also the equation for *multiple regression*). In the case of BOLD data, $\boldsymbol{Y}$ is the measured data, $\boldsymbol{X}$ is a *design matrix* where each row contains an independent variable, or *regressor*, relating to the experimental paradigm, β is the vector of weights corresponding to contributions of each column in $\boldsymbol{X}$**,** and ε is the error between the model and the measured data.

Take the simplest example – an experiment containing only two conditions, e.g. eyes-open and eyes-closed. This can be represented as a simple binary timecourse, often called a *boxcar* model, where a value of 1 represents eyes-open and a value of zero represents eyes-closed. In a sense, the boxcar model represents the near-instantaneous changes in cognitive state that occur when moving from one task condition to another. However, haemodynamics are not modulated in such a fast binary manner, despite being related to neuronal activity. To better reflect haemodynamic activity, we must first calculate the convolution of the boxcar with a *haemodynamic response function* (HRF), which represents the haemodynamic response to a unitary stimulus. The most commonly accepted HRF is shown in Figure 4.11, which is formed from the sum of two gamma functions (Glover, 1999), containing a primary peak, and post-stimulus undershoot (the origins of these parts of the response have already been discussed in Chapter 2).

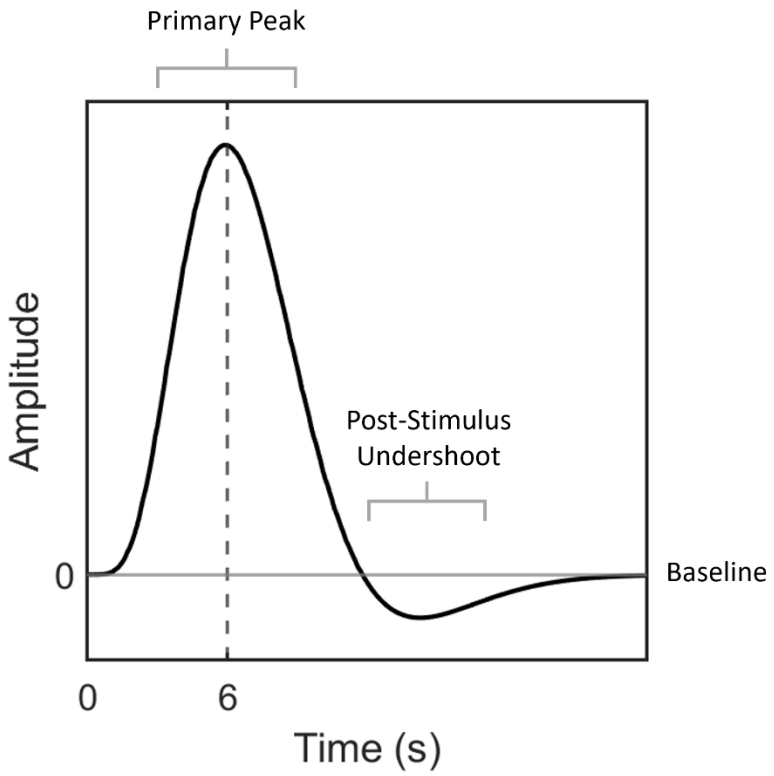


***Figure 4.11**: The commonly accepted form of the haemodynamic response function (Glover 1999), which is the BOLD fMRI response to a unitary stimulus. The response consists of an initial peak, followed by an undershoot below baseline following stimulus withdrawal.*

As such, each column of the design matrix relating to a task variable can be written as

$$\boldsymbol{x_i} = \boldsymbol{m_i} * H \tag{4.25}$$

where $\boldsymbol{m_i}$ is the boxcar model and H is the HRF. In addition to regressors relating to the paradigm, a set of *nuisance* regressors are often included in the design matrix, representing variables such as head movement, which will affect the BOLD signal, but do not directly relate to the neuronal activity of interest. A simulated design matrix is shown in Figure 4.12.

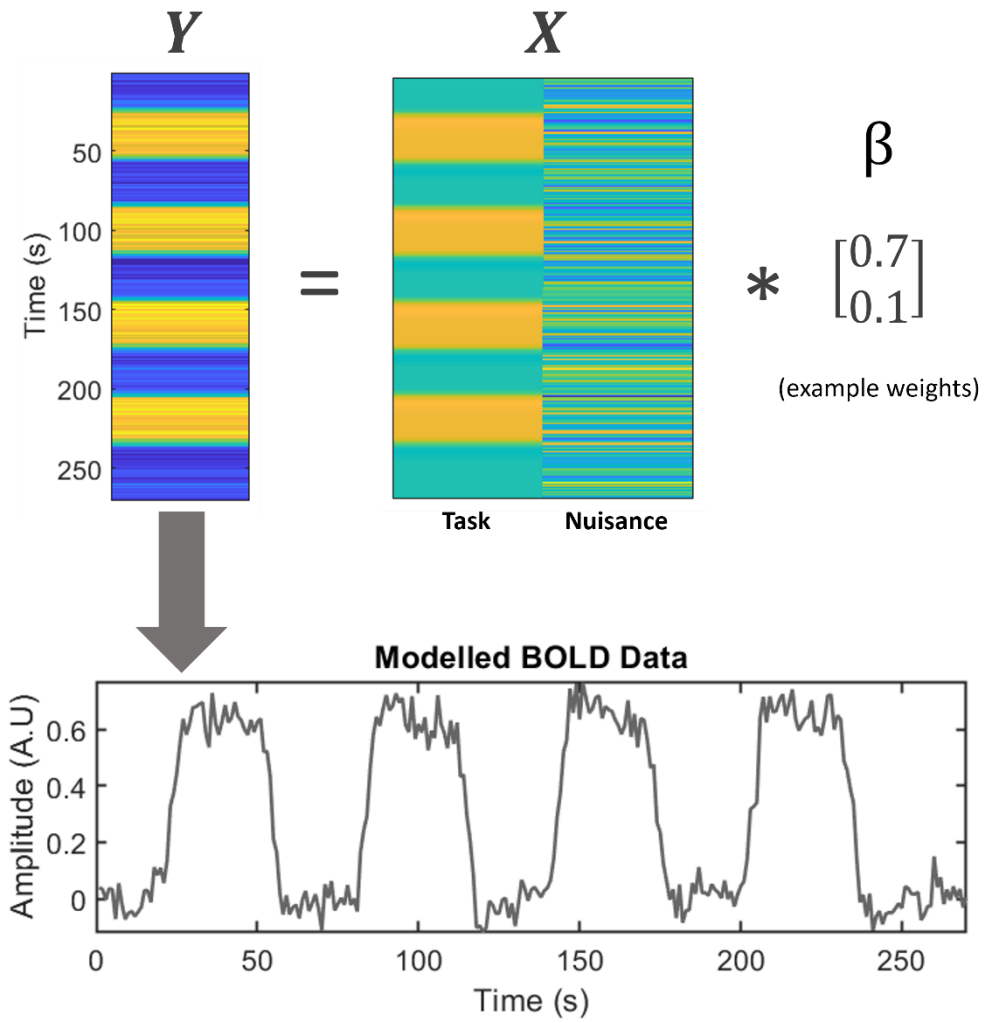


***Figure 4.12**: A schematic showing the process of modelling BOLD fMRI data using a general linear model. The data model Y is the multiplication of a design matrix, X, and a vector of weights, β, which correspond to the contribution of each column in X to the model. The design matrix contains regressors that correspond to task conditions as well as nuisance parameters (e.g. head motion). Here, the task has only two conditions and can therefore be represented in a single column (e.g. eyes-open/eyes-closed). Normally distributed random noise was chosen as an example nuisance parameter, although it is important to note that in real data these will often not behave as random noise.*

The solution to a regression problem such as this is the same no matter the dimensionality of the design matrix, i.e., we can add more independent variables to $\boldsymbol{X}$ without changing the solution. As $\boldsymbol{X}$ is not square, it cannot simply be inverted to find a solution. Instead, it must be multiplied by its transpose before inverting, leading to the following expression:

$$\boldsymbol{\beta} = (\boldsymbol{X}^T\boldsymbol{X})^{-1}\boldsymbol{X}^T\boldsymbol{Y}. \tag{4.26}$$

These weights can now be used to calculate a model of the BOLD data at each voxel in the brain. If the weights corresponding to task-related regressors are large, it suggests that the voxel being modelled is strongly modulated by the task.

It is common to perform statistical tests on the regression coefficients to identify voxels where the effect of a regressor, or combination of regressors, becomes statistically significant (Worsley, 2001). The t-statistic for a particular regression coefficient, or combination of regression coefficients, β, is given by

$$t = \frac{\beta}{\sigma_\varepsilon}, \tag{4.27}$$

where σ_ε is the standard deviation of the model error, adjusted for degrees of freedom (related to number of datapoints and number of regressors in the contrast). The t-statistic is assumed to fall on a t-distribution, which represents the probability that the null hypothesis is correct, i.e., there is no effect of the regressor in the data. The t-distribution is centred around zero, such that a t-statistic close to zero indicates high probability (p) that the null hypothesis is correct ($p \to 1$), while a high t-statistic indicates low probability that the null hypothesis is correct ($p \to 0$). The condition for statistical significance is usually set at $p < 0.05$, meaning there is less than 5% chance that the null hypothesis is correct.

In some GLM implementations, the t-statistic is converted to a z-statistic by finding the value in a z-distribution (normal distribution with mean of 0 and standard deviation of 1) that gives the same p value. This provides a standard measure of the effect of a regressor on the data, which is useful when making comparisons across different voxels, subjects (see section 4.2.3) or studies. Activation maps in fMRI analysis are usually plotted using the t-statistic or z-statistic thresholded at $p < 0.05$.

Despite thresholding activation maps based on p-value, there is still a chance of making false discoveries which increases when repeating the test over multiple voxels (Worsley, 2001). The so-called family-wise error (FWE) corresponds to the chance of making at least one false discovery, i.e., measuring $p < 0.05$ in at least one non-activated voxel. FWE can be mitigated by applying Bonferroni correction, dividing the p threshold for significance by the number of tests performed. Although effective, this method can be overly conservative when performing GLM analysis on a whole-brain with a high number of voxels. An alternative measure to FWE is false discovery rate (FDR), which is the expected proportion of false discoveries amongst all measured effects. Controlling for FDR rather than FWE allows a chosen proportion of the results to be false discoveries, known as the FDR level, often chosen as 5%. From here, all p

values measured (across voxels in the brain in our case) are ranked from smallest to largest, and the new p threshold is the largest p-value that satisfies the expression: $p \leq \frac{rank}{N} * FDR$, where N is the total number of tests performed.

4.2.3 Group Level Analysis

The process of performing a GLM, described above, is initially performed on a single participant dataset, often called a first-level analysis. A higher-level analysis can then be performed, either on multiple runs for the same subject, or across multiple subjects, to analyse effects which are consistent across a set of scans (Beckmann et al., 2003, Leibovici and Smith, 2000).

First-level GLMs are performed in subject-specific functional (EPI) space, while higher-level (specifically group-level) analyses are often performed in a standard space using a template anatomical image. The anatomical template which is generally used is the MNI 152 brain template, which is a standard brain formed of the average of 152 healthy male T1 weighted anatomical MRI scans (Mazziotta et al., 2001). Before moving to standard space, a transformation must first be calculated between the subject-specific functional (EPI) image and a T1-weighted anatomical, often an MPRAGE or PSIR (see section 4.1.11). This requires a rigid body transformation matrix (Challis, 1995), which has six degrees of freedom, allowing only for translations (three degrees) and rotations (three degrees), given the images are of the same brain. Following this, a second transformation matrix is required which transforms the subject-specific anatomical image to a standard anatomical. This transformation requires 12 degrees of freedom (Block, 1974), allowing for scaling and shearing, as the images are of different brains. Once these transformations are calculated, they can be applied to bring functional data from subject-specific functional space to standard space. The process of registration from functional to standard space to perform group-level analyses is shown in Figure 4.13. It should be noted that when performing higher-level analysis on multiple runs of the same subject, the functional data need only be registered between runs using a rigid body transformation, or perhaps transformed to a high resolution anatomical, again with a rigid body transformation, for better visualisation.

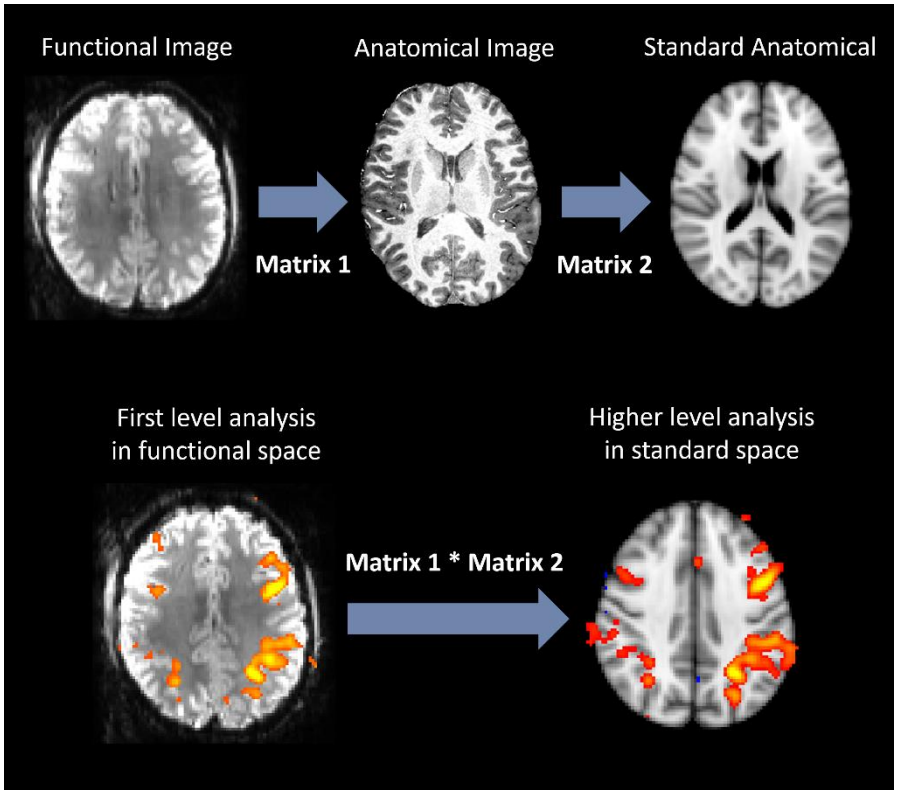


***Figure 4.13**: A schematic showing the process of registration from subject-specific functional space to standard space, for the purpose of higher-level fMRI analysis. Transformation matrices must be calculated which transform function images to subject-specific anatomical images, and anatomical images to a standard anatomical. These matrices are then multiplied together to transform functional images directly to standard space for further analysis.*

Following transformation to the appropriate space, further statistics can be calculated to analyse effects which are consistent over the set of runs, or subjects. The distinction between higher-level analyses performed on multiple runs or multiple subjects is important, as the way the data is combined will differ in each case. If modelling multiple runs of the same subject, a fixed-effects analysis can be used at the higher level, which assumes that any variation between results of the first-level analyses arises entirely from within-subject variance. However, if multiple subjects are being combined in a higher-level analysis, a fixed-effects analysis is insufficient in dealing with variability in the data. A random-effects analysis accounts for heterogeneity across subjects by allowing for random variability between results of the first-level analyses. In practice, this amounts to weighting of the first-level results based on the quality of fit, reducing the impact of outliers and producing a group-level result that should be more representative of a greater population.

4.2.4 Independent Component Analysis

The GLM method discussed previously can be considered a univariate analysis technique, as a separate model is formed for each voxel. However, it is well known that groups of spatially disparate voxels tend to co-activate, during tasks as well as at rest, forming so-called functional networks (see Chapter 2). Multivariate analysis methods such as independent component analysis (ICA) address this by separating the data into a set of spatial maps which tend to co-activate (McKeown and Sejnowski, 1998). This can be written as

$$\boldsymbol{C} = \boldsymbol{W}\boldsymbol{X}, \tag{4.28}$$

Where $\boldsymbol{C}$ is an $n \times v$ matrix of component maps (n is the number of timepoints, v is the number of voxels in the image), $\boldsymbol{X}$ is the $n \times v$ matrix of original images after whitening (each row is a single volume), and $\boldsymbol{W}$ is an $n \times n$ is a matrix which describes the linear combinations of the data which form the components. In ICA, $\boldsymbol{W}$ is chosen such that the rows in $\boldsymbol{C}$ are sufficiently statistically independent. One benefit of this approach is reduced dimensionality of the data, with a single timecourse representing the data from multiple voxels and regions of the brain. Another benefit is the lack of a priori assumptions on the shape of the data. In a GLM, the data is assumed to relate to the experimental paradigm via the HRF, whereas ICA groups the data based on co-activity, allowing for post-hoc analysis of response morphology which is unrestricted by a predetermined HRF.

4.3 Summary

This chapter has provided a description of the semi-classical physics which enables imaging using magnetic resonance, as well as the techniques used to image at high enough temporal resolution to resolve functional changes in the ratio of oxy- and deoxy-haemoglobin, relating to neuronal activity (described in Chapter 2). We have also introduced the basic methodology for analysing functional MRI data, which is explored further in Chapter 7.

5 Post-Task Responses in Oscillatory Activity follow Cessation of Working Memory Processes

5.1 Abstract

Post-task responses (PTRs) are induced oscillatory responses occurring for several seconds between the end of a stimulus/task and a period of rest. The most well-studied of these are beta band (13 – 30 Hz) PTRs in motor networks following movement, often called post-movement beta rebounds, which have both neuroscientific and clinical relevance. It is unknown whether PTRs are specific to sensorimotor and visual systems, or whether they are a more general self-modulatory property of the cortex that occur following cessation of higher cognitive processes as well as movement and visual stimuli. We investigated this by recording MEG responses to a working-memory task in 20 healthy participants using long rest periods to study PTRs following cessation of higher cognitive processes.

Results revealed PTRs in the theta, alpha and beta bands across many regions of the brain, including frontal, parietal and lateral visual regions. These PTRs increased significantly in magnitude with working-memory load, an effect that is independent of oscillatory modulations occurring over the task period as well as those following individual stimuli. Furthermore, we showed that PTRs are functionally related to reaction times in left lateral visual and left parietal regions, while the oscillatory responses measured during the task period are not. Importantly, motor PTRs following button presses did not modulate with task condition, suggesting that PTRs in different networks are driven by non-motor processes involved in working memory.

These findings show that PTRs are not limited to motor networks but are widespread in regions that are recruited during the task. We provide evidence that PTRs have unique properties, scaling with cognitive load and correlating significantly with behaviour. Based on the evidence, we suggest that PTRs act to inhibit task-positive network activity to enable a transition to rest.

5.2 Publication and Contribution Note

This work has been published in NeuroImage as a research article (Coleman et al., 2023). In addition, work from this chapter has been presented as a poster at the

International Conference on Biomagnetism (BIOMAG) 2022, and the Organization for Human Brain Mapping (OHBM) 2023.

All data collection and analysis presented in this chapter was performed by the author. Data analysis was performed using a series of bespoke in-house scripts.

5.3 Introduction

Post-task responses (PTRs) occur in a transition period, starting when a stimulus or task has ended and lasting for up to ten seconds before the brain returns to resting state and the associated oscillatory rhythms. The beta band (13 – 30 Hz) PTR in the motor cortex, often termed the post-movement beta rebound (PMBR), is the most well-studied electrophysiological PTR (Pfurtscheller et al., 1996b, Pfurtscheller, 1981, Stancak and Pfurtscheller, 1995, Cassim et al., 2001). The PMBR is characterised by a rise in beta band power above baseline following cessation of movement, driven by increased probability of beta bursting events (Pfurtscheller, 1981, Pfurtscheller and Lopes da Silva, 1999). These are induced, rather than evoked, effects (see Chapter 2) and are currently *not* thought to be related to other well documented evoked responses such as error-related negativity (ERN) (Falkenstein et al., 1991, Gehring et al., 1995, Gehring et al., 2018) or contingent negative variation (CNV) (Walter, 1968, Babiloni et al., 2005), although explicit relationships are yet to be investigated. As explained in Chapter 2, the PMBR has several interesting characteristics: it modulates with various task parameters, such as force output (Fry et al., 2016) and movement duration (Pakenham et al., 2020), and differs in several patient populations compared to healthy controls (Gascoyne et al., 2021, Liddle et al., 2016, Robson et al., 2016, Gaetz et al., 2020). The response preceding the PMBR, termed the movement-related beta decrease (MRBD), remained unchanged in all of these experiments. Together, these studies showed that the PMBR is modulated independently of the MRBD and can be predictive of symptoms related to disease severity in a way that the MRBD is not. In turn, this suggests that the PMBR can provide unique insight into both healthy and pathological brain function.

The neural mechanisms underlying the PMBR remain unknown, although existing models are outlined in Chapter 2. In short, it has been posited that the PMBR is required to actively inhibit the motor network to prevent further movement from taking place (Chen et al., 1999, Pakenham et al., 2020), potentially reflecting top-down signal propagation in the motor system. Pakenham *et al* suggested that task difficulty drives PMBR amplitude, such that greater cognitive load in the motor network requires greater levels of inhibition (thus larger PMBR) when returning to rest. The direct

relationship between difficulty and the PMRB was not tested directly in this study as there were no differences in behavioural measures of task difficulty that could be related to PMBR amplitude. Another hypothesis is that the PMBR is a marker of certainty in the brain's feed-forward motor model, such that greater uncertainty in the motor action leads to diminished PMBRs (Tan et al., 2014). The two studies above cannot be directly compared, as the study by Pakenham *et al* varied the duration of grip force, which changed the difficulty of the motor action, whereas the study by Tan *et al* varied the degree of mismatch between the internal motor plan and the outcome of the motion, thus modulating motor uncertainty rather than difficulty of execution. In addition, the PMBRs measured by Tan *et al* took place in a very short inter-trial period (< 2 s), rather than a transition to rest, therefore it is likely that there were ongoing cognitive processes (attention towards the task) during the PMBR, possibly confounding the results.

Outside of the motor system, relatively few reports of PTRs have been documented. Alpha band (8 – 13 Hz) PTRs have been reported in the visual cortex (Mullinger et al., 2017), although these are not widely studied. To our knowledge, there have been no reported electrophysiological PTRs outside of the sensory cortex (i.e., outside of motor, visual or auditory cortices). Liddle *et al* reported a "post-stimulus response" in the insula following task-relevant stimuli (Liddle et al., 2016). However, this response began during visual stimulation and took place in a period of active memory maintenance, i.e., not before the brain returns to rest as per our definition of a PTR (Figure 2.10). Thus, it is unclear whether the response reported by Liddle *et al* is a true PTR or an oscillatory response generated for memory maintenance (Jensen et al., 2002, Tuladhar et al., 2007). It is currently unknown whether PTRs are a specific phenomenon of the sensory cortex and associated processes, or whether they are also elicited in higher order areas following executive functions. The distinction is important as it determines whether PTRs are specifically related to sensory processes, or whether they are a ubiquitous cognitive control mechanism of the entire cortex.

To study PTRs following higher cognitive processes we employ an n-back task that: 1) recruits brain regions associated with higher cognitive activity; 2) maintains a relatively constant load in the recruited brain regions during task periods so that the task has definitive on/off periods; 3) modulates cognitive load between task conditions without changing sensory input. Crucially, our n-back task contained long (30 s) rest periods after each task period, allowing for the study of PTRs. We hypothesise that PTRs occur in higher cognitive regions and provide unique information about cognitive processing which is not obtained from the oscillatory task-response (OTR, average MEG response

measured *during* the task period). Furthermore, we aim to corroborate the previously posed hypothesis (Pakenham et al., 2020) that PTRs are driven by perceived task difficulty by relating PTR amplitude to behavioural measures of task performance. This will provide vital new information as to the functional importance of PTRs.

5.4 Methods

20 healthy volunteers (10 female, aged 26 ± 4 [mean ± SD] years) took part in this study, which was approved by the University of Nottingham Medical School Research Ethics Committee and in compliance with all COVID-19 standard operating procedures (as data were collected in 2020). All volunteers gave written, informed consent.

5.4.1 Paradigm

A summary of the n-back paradigm used in the experiment is shown in Figure 5.1. The n-back task conditions were 0-back, 1-back and 2-back (Fig. 5.1), in order of increasing working memory load. Subjects were instructed to use their right index finger to press a button when a target letter was shown. Depending on the block condition, the target letter was either the letter 'x' (0-back), the same letter as the letter before (1-back), or the same letter as two letters before (2-back). At the start of each block, an instruction screen was presented for 2 s which displayed the forthcoming task condition. During a task period, 15 letters (which we term stimuli), 4 of which were targets, were presented for 1 s each in a pseudorandom order, with 1 s interstimulus interval. Each task period was followed by a 30 s rest period, during which a fixation dot was shown. The instruction screen, task period, and rest period formed an experimental block lasting 62 s. The experiment comprised of 2 runs with 8 blocks per condition in each run. Blocks were arranged in a different pseudorandom order for each of the runs. The oscillatory task response (OTR) window was defined as 0.5 – 29.5 s and encompasses slow induced oscillatory changes that span the entire task window, while the post-task response (PTR) window was defined as 31.5 – 33.5 s, positioned at the peak of post-task induced oscillatory changes. The oscillatory stimulus response (OSR) window was defined as 0.3 – 0.5 s following the start of each letter presentation, positioned around the peak of fast induced changes that occur following each new working memory item.

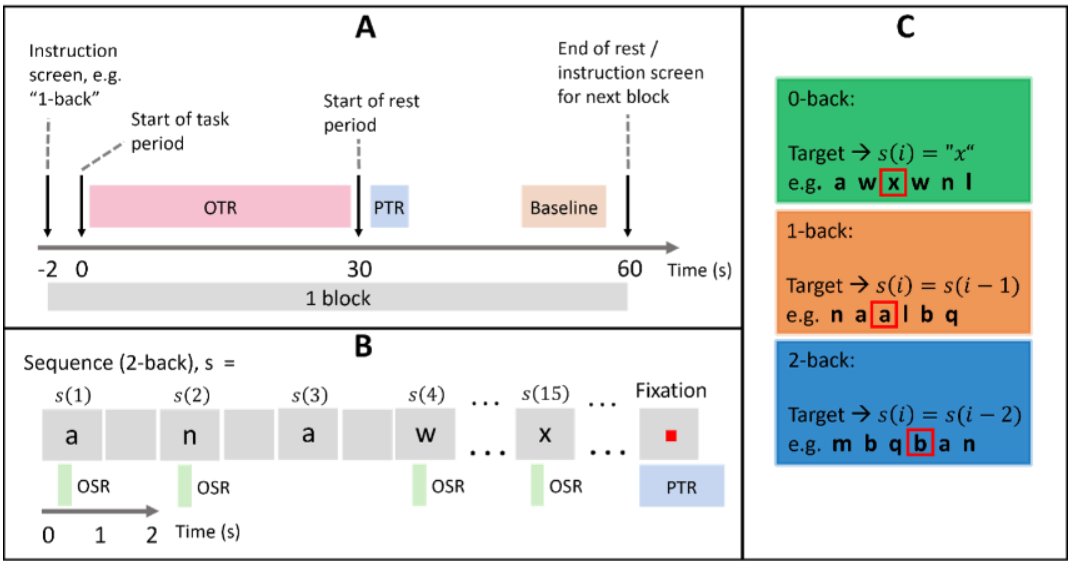


***Figure 5.1**: Panel **A** – each block started with an instruction screen at -2 s, which read either "0-back", "1-back" or "2-back", indicating the condition that would follow. The task period started at 0 s, lasting for 30 s. The rest period started at 30 s and lasted for 30 s. At 60 s, the instruction screen for the next block was shown. The oscillatory task response (OTR) window (0.5 – 29.5 s), the post-task response (PTR) window (31.5 – 33.5 s) and the baseline window (48 – 58 s) are shown. Panel **B** – the timing of the presentation of individual stimuli and indicates oscillatory stimulus response (OSR) window (0.3 – 0.5 s following the start of each stimulus presentation). Panel **C** – the three different task conditions, with the red boxes indicating the target letters. Each subject completed a total of 16 blocks of each condition, in a pseudorandom order, spread over two separate runs.*

5.4.2 Acquisition

Data were collected at a sampling rate of 600 Hz using a 275-channel CTF MEG system (MISL, Coquitlam, BC, Canada) in third order gradiometer configuration (see Chapter 3, section 3.1.3). Head localisation coils were attached to the subjects' nasion and preauricular points prior to scanning to provide fiducial markers for head localisation. The coils were energised before the start and after the end of each run to provide a measure of overall head movement. The subjects were scanned in a seated position in front of a projector screen approximately 80 cm away that displayed the stimuli. An eye-tracker (EyeLink, Ottawa, Canada) was used to monitor the subjects to ensure they remained awake throughout.

In between the two runs, a 3D digital mesh of the head and fiducial coils was acquired using a structure sensor (Occipital, Colorado, USA). Before the head digitisation, subjects were fitted with a swimming cap to flatten down hair, and green stickers were placed on the fiducial coils to enable easy identification of these locations on the head. The digitised head surface and fiducial locations were then co-registered with an anatomical MRI (T_1-weighted MPRAGE sequence acquired on either a 3T or 7T MRI

scanner) to allow the position of the sensors relative to the brain to be determined. It is worth noting that the standard MEG digitisation method, which uses a Polhemus system (Polhemus, Colchester, VT, USA), was not used here due to COVID-19 restrictions.

5.4.3 Behavioural Analysis

Button press responses were used to calculate three primary behavioural metrics relating to n-back task performance: targets hit (TH), false presses (FP) and reaction times (RT). Both TH and FP were calculated using an acceptance threshold of 1.8 s, i.e., a correct button press must have occurred within 1.8 s of the start of presentation of the target, and similarly, a false press must have occurred within 1.8 s of a non-target being presented. RT were only measured for correct button presses. These measures were averaged across runs and subjects to give an overall measure for each condition. The significance of modulations between conditions of each behavioural measure were found using repeated-measures analysis of variance (rm-ANOVA) tests.

5.4.4 MEG Pre-Processing

The sensor-level MEG data were bandpass filtered into 1-150 Hz using a finite impulse response (FIR) filter (Widmann et al., 2015), and DC offset was removed using the entire scan duration, implemented in DataEditor software (CTF systems). Data were segmented into blocks and grouped by task condition. Eye-tracker data were visually inspected to ascertain whether subjects had stayed awake. Each 62 s block was visually inspected and any that contained sensor resets or movement were removed. After removal of noisy data, an average of 46 ± 1 blocks per subject remained across all conditions to be used for all further analysis. Eye-blink and cardiac artifacts were then removed from the remaining data using ICA in Fieldtrip (Oostenveld et al., 2011). All 20 subject datasets remained for further analysis after the pre-processing.

5.4.5 Beamforming

A linearly-constrained minimum-variance beamformer (see Chapter 3.2.2) was applied to transform the sensor-level data into source-space. For each subject, a multiple-spheres head model was used to construct a forward solution, with a source space formed of a regular grid of 4mm cubic voxels. Beamformer weights were calculated using the broadband covariance over all trials (with bad trials removed). Covariance matrices were regularised using the Tikhonov method (Golub et al., 1999, Brookes et al., 2008), with 5% of the maximum eigenvalue.

Source space activation maps were created by a pseudo T-statistic (T-stat) at each location in the brain, following the procedure detailed in Chapter 3.2.2. To identify the regions the OTR and PTR were most strongly modulated by condition, the following time windows were used to create active and control covariance matrices: i) the OTR window (0.5 - 29.5 s); ii) the PTR window, (31.5 - 33.5 s), when the PTR was expected to be the largest. For each of these time windows, the 2-back condition was used to create the active covariance matrix and the 0-back condition was used as the control. This contrast was preferable over contrasting each time window with a section of the rest period, as the PTR window only lasted 2 s, and would therefore be very sensitive to the 2 s control window within the rest period that was chosen. To identify PTR activity which may occur in different frequency bands, T-stat maps were calculated for the theta (4 - 8 Hz), alpha (8 - 13 Hz), and beta (13 - 30 Hz) bands. Narrowband filtering was implemented using FIR filters, which are usually preferrable for electrophysiology analysis as the phase response is linear for all frequency components of the input signal (Widmann et al., 2015). For completeness, additional analysis to create T-stat maps by contrasting the OTR time window (0.5 – 29.5 s) with a conventional rest window (30.5 – 59.5 s) [which includes the PTR period] was performed, akin to previous studies (Brookes et al., 2011b, Luckhoo et al., 2012).

5.4.6 Standard Brain Normalisation

The T-stat maps for each subject and frequency band were moved into a standard space using the MNI 152 brain template, which is a standard brain formed of the average of 152 healthy male T1 weighted anatomicals (Mazziotta et al., 2001), allowing maps to be averaged to create a set of group T-stat maps. This requires a transformation matrix with twelve degrees of freedom (translation, rotation, scaling and shearing) to move from the subject-specific anatomical space to standard space. Transformations were executed using FSL FLIRT (Jenkinson and Smith, 2001, Jenkinson et al., 2002).

In addition, using the inverse of the transformation matrix described above, a set of functional region masks were transformed from standard space to subject-specific space. These are binary masks which are equal to one in a particular functional domain, and zero everywhere else. Once in subject space, these masks can be multiplied by T-stat maps before locating the peak positive or negative voxel, giving the location of peak activation within a particular region. The masks used are listed in Table 5.1.

5.4.7 Time-Frequency Responses

The peak (maxima or minima) T-stat within each masked region was found for each subject, allowing extraction of virtual electrodes (VE). VEs are the beamformer reconstructed MEG data at a particular voxel in the brain, forming an estimate of the data that would be measured by an electrode placed inside a particular region of tissue. Here, the VEs are chosen to contain maximal event-related synchronisation/desynchronisation (ERS/ERD) in 2-back with respect to 0-back. The timecourses from each VE were then used to create time-frequency spectrograms (TFS) to identify whether responses at a given location were broadband or frequency band specific. The TFS were made by taking the power envelope of bandpass filtered data for a range of frequency limits (2 - 4 Hz, 4 - 8 Hz, 8 - 12 Hz, 12 - 16 Hz, 16 - 20 Hz, 20 - 24 Hz, 24 - 28 Hz, 28 - 32 Hz), before averaging over blocks for each frequency so that the time evolution of average spectral data over a block period could be plotted. Then, using the same frequency limits as the corresponding T-stat maps (listed in Table 5.1), the data from each location were bandpass filtered, Hilbert transformed and the resultant power envelopes were averaged over blocks to produce block-averaged timecourses for each subject and condition. A baseline of 48 – 58 s was used for all TFS and timecourses before averaging across subjects to reveal group-level effects for each frequency band and location.

Time-averaged oscillatory power was calculated for each subject during the OTR and PTR at locations of maximal condition-dependent modulation. Average power values during the OTR and PTR were tested for significant modulations between conditions using rm-ANOVA (repeated measures required as measurements in each condition were from the same subjects). Bonferroni correction was used to adjust p-values for multiple comparisons. In regions where a significant effect of condition was observed after Bonferroni correction, post-hoc t-tests were used to establish which condition(s) were driving the measured effects.

To test the hypothesis that PTRs are driven by perceived task difficulty, we tested the correlation between RT and PTR amplitude using ordinary least-squares (OLS) regression. For both the behavioural and oscillatory measures, the difference between 2-back and 1-back was used rather than the absolute measures such that a single regression could be performed between the two metrics. The OTR was also tested to show that any correlations were unique to the PTR. Only regions that displayed a T-stat peak in both the OTR and PTR contrasts were tested to reduce the number of comparisons.

5.4.8 Residual Post-Task Response Modulation

To test whether the PTR modulations between conditions in a given frequency band were independent from the changes in OTR, we performed a regression analysis. For regions and frequency bands where a response was observed in both time windows, trial-wise OTR and PTR average amplitudes were taken for each subject. An OLS regression was calculated between these measures for a given region, frequency band and subject, and the fit between OTR and PTR amplitude was removed from the PTR amplitude to create residual PTR amplitudes. Residual PTR amplitudes were collected across subjects and tested for condition-dependent modulation using rm-ANOVA, again corrected for multiple comparisons.

5.4.9 Post-Movement Beta Rebound

To compare PTRs following higher cognition with the well-studied PMBR, the beta response was taken following successful button presses. The VE location was taken from a ~~T~~-stat map that contrasted the PMBR window (0.5 – 1.5 s following each button press) with the MRBD window (-0.5 – 0.5 s around each button press), which was then used to plot the average peak beta band timecourse with an epoch of -1 – 2 s around the button press. The same baseline was used here as in section 5.4.7 to allow for comparison between the PMBR and the PTRs measured following working memory. The MRBD and PMBR windows were both tested for significant modulation with task condition using rm-ANOVA.

5.4.10 Oscillatory Stimulus Response

We define the oscillatory stimulus response (OSR) as the spectral response following stimulus (letter) presentation (Fig. 5.1). Even though these are technically *post-stimulus* responses, we do not consider these equivalent to the *post-task* response which occurs after completion of the full 30 s task block at the start of rest (as defined in Chapter 1), as the OSR occurs while the participant is still attending to the task (maintaining working memory), while the PTR occurs during the transition to resting state. It should also be noted that the purpose of this analysis was not to measure the evoked potentials (see Chapter 2) relating directly to early stimulus processing, such as ERN, which peaks 100-150 ms following a stimulus and is related to response errors (Bates et al., 2002). Instead, we measure OSRs to directly contrast with PTRs as these are both post-stimulus or post-task induced responses that occur in different phases of the task.

For the following analysis, only the non-targets were considered and any non-targets preceding a false press were excluded in order to remove the confounding response

associated with a button press. Only regions that exhibited both an OTR and PTR (Table 5.1) were included in this analysis to allow for meaningful comparison between OSR and PTR. For each subject, the broadband timecourse from each PTR VE location was extracted and segmented around non-targets using a window of -1 – 2 s relative to stimulus (i.e. each letter) presentation. These were used to produce timecourses and TFS showing the response following stimuli. The TFS and timecourses for OSRs were made as described in section 5.4.7. Baselines were removed from subject timecourses and TFS, using a baseline of -0.3 – 0 s relative to stimulus presentation, before averaging across subjects to produce the group-level stimulus response for each location in the brain. The average timecourse value during the OSR window (0.3 – 0.5 s relative to stimulus presentation) was taken per condition for each subject. Average OSR values were tested for significant modulation using rm-ANOVA across conditions.

To test whether PTRs were dependent on OSRs, we performed a regression analysis (similar to section 5.4.8), producing a set of residual PTRs after removal of the effects of OSR. As there were several OSRs for every single PTR, the OSRs were averaged within a block before being used in the regression. Once the fit between OSRs and PTRs had been removed for every subject, the residual PTRs were tested for significant modulation across conditions using rm-ANOVA.

5.5 Results

5.5.1 Behaviour

Analysis of button presses yielded the group-averaged behavioural results shown in Figure 5.2, including targets hit (TH), false presses (FP) and reaction times (RT). All three behavioural metrics modulated significantly ($p < 0.05$, rm-ANOVA) with task condition. Post-hoc t-tests revealed that RT modulated significantly ($p < 0.05$, t-test) between all pairs of conditions, whereas TH and FP did not show a significant difference between 0-back and 1-back.

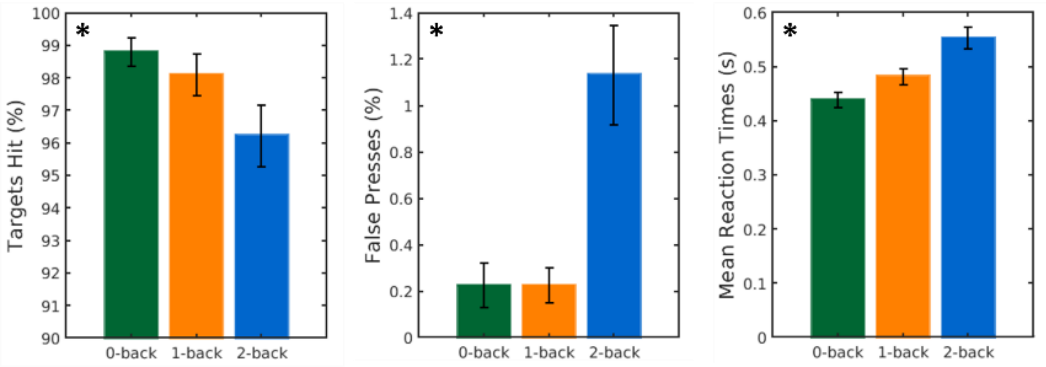


***Figure 5.2**: Behavioural results from the n-back task showing the modulation in targets hit (TH), false presses (FP) and reaction times (RT) with condition, averaged over all subjects. Error bars denote the standard error over subjects. Significant ($p < 0.05$, rm-ANOVA) modulation of measured response with condition is denoted by an asterisk (*). Post-hoc t-tests revealed that RT modulated significantly ($p < 0.05$, t-test) between all pairs of conditions, but TH and FP did not modulate significantly between 0-back and 1-back.*

5.5.2 Activation Maps

T-stat maps showing OTR modulations with condition can be seen in Figure 5.3, for the theta, alpha and beta bands. Additional contrasts of task (0.5 – 29.5 s) vs rest (30.5 – 59.5 s) can be seen in Figure A5.2. Positive values represent an increase in oscillatory power in the 2-back condition compared with the 0-back condition, while negative values represent a decrease in oscillatory power between these conditions. Figure 5.3A shows that: power in the theta band increased in the prefrontal cortex and decreased in parietal and lateral visual regions; power in the alpha band decreased in parietal and lateral visual regions; power in the beta band decreased in the parietal lobe and to a lesser extent, the frontal eye fields, during the 2-back condition compared with the 0-back condition.

Figure 5.3B shows T-stat maps of modulations in the theta, alpha and beta bands during the post-task time-window. When subtracting the 0-back from the 2-back condition, power in the theta band decreased in the prefrontal cortex, the right temporoparietal junction (TPJ), and the left motor cortex, whilst it increased in the left lateral visual and left auditory cortices. Power in the alpha band increased in the left parietal and left lateral visual regions. Power in the beta band increased in the left frontal eye field and left parietal cortex, and to a lesser extent, the right frontal eye field.

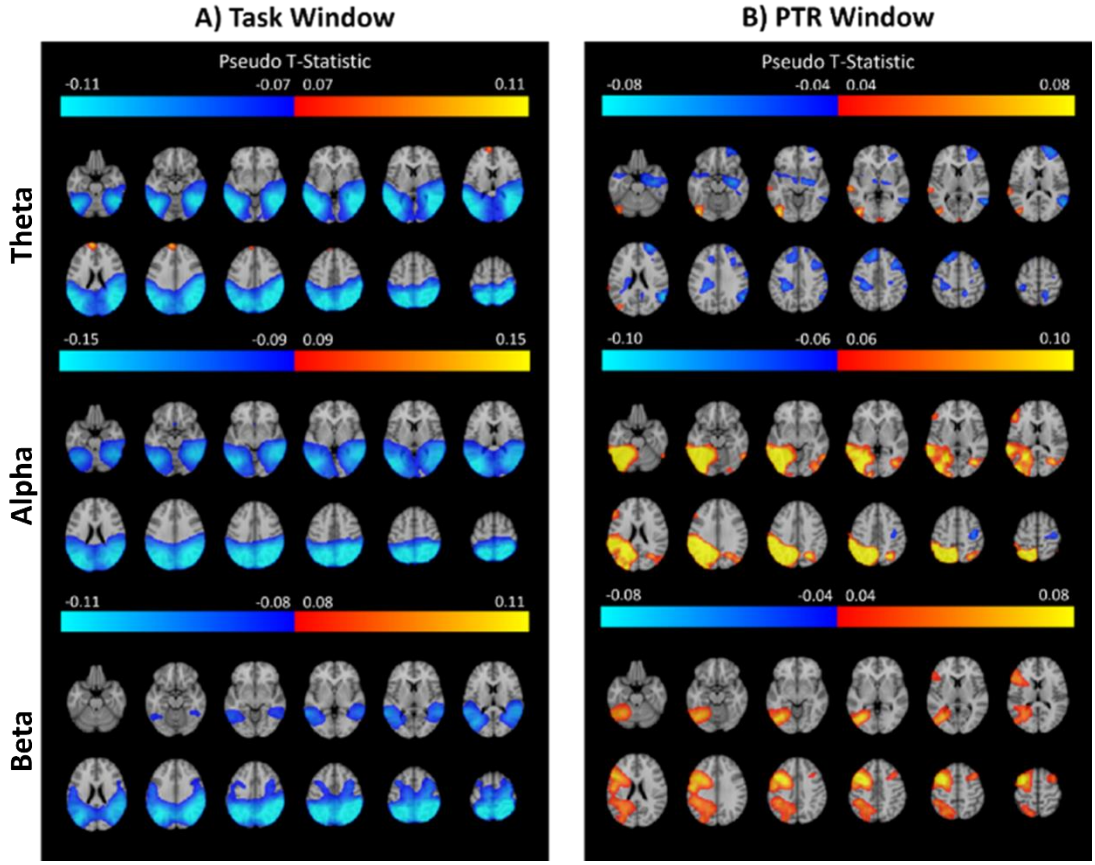


***Figure 5.3**: Group ~~T~~-stat maps for the theta, alpha and beta bands, displayed on the MNI-152 brain, found by contrasting the 2-back condition with 0-back during the task window (column **A**, 0.5 - 29.5 s) and the PTR window (column **B**, 31.5 - 33.5 s). Theta and alpha OTR results mirror previous studies, showing a frontal theta ERS, and posterior theta and alpha ERD. The beta band exhibits a bilateral ERD in the dorsal attention network (DAN) during the OTR, and a left lateralised ERS in the DAN during the PTR, which is mirrored in alpha to some degree.*

5.5.3 Time-Frequency Responses

Mask Name	OTR/PTR Window	Band(s)	Source/Ref
Frontal	OTR, PTR	Theta	Combined AAL regions
Left Parietal	OTR, PTR	Alpha, Beta	Combined AAL regions
Right Parietal	OTR	Alpha, Beta	Combined AAL regions
Left Lateral Visual	OTR, PTR	Alpha	(Przezdzik et al. 2013; Wilson et al. 2015)
Right Lateral Visual	OTR	Alpha	(Przezdzik et al. 2013; Wilson et al. 2015)
Left Frontal Eye Field	PTR	Beta	(Przezdzik et al. 2013; Wilson et al. 2015)
Right TPJ	PTR	Theta	(Mars et al. 2012)
Left Sensorimotor	PTR	Theta	(Przezdzik et al. 2013; Wilson et al. 2015)

***Table 5.1**: Masks used to interrogate the strongest responses during the OTR window (0.5 - 29.5 s) and PTR window (31.5 - 33.5 s).*

The group T-stat maps in Figure 5.3 showed activations that are consistent with previous MEG studies using a similar task, including frontal, parietal, lateral visual, sensorimotor and TPJ activations (Brookes et al., 2011b, Astle et al., 2015, Costers et al., 2020). Masks used to extract VEs are shown in Table 5.1, along with the frequency response that we measured within each of these and the corresponding time-window contrast (OTR or PTR). These anatomical masks were then used to interrogate the strongest responses over the group (Przezdzik et al., 2013, Wilson et al., 2015, Mars et al., 2012, Tzourio-Mazoyer et al., 2002). Parietal and lateral visual theta responses were excluded from the rest of the analysis because TFSs revealed that the effects were likely bleed-through from the alpha band. The frontal eye field beta OTR responses were also excluded as they were relatively weak compared to those in the parietal lobe (Fig. 5.3A).

Group-average TFS are shown in Figure 5.4, with a separate panel for voxels of peak OTR and PTR modulation. Only the 2-back condition is shown in the TFS as this condition exhibited the strongest response in all locations. Most regions exhibit similar behaviour, with sustained ERD during the task, predominantly in the alpha band, with a post-task ERS in the alpha/beta range. The most obvious exception is the frontal theta VE, which shows the opposite behaviour. Equivalent frequency filtered timecourses are shown in Figure A5.1.

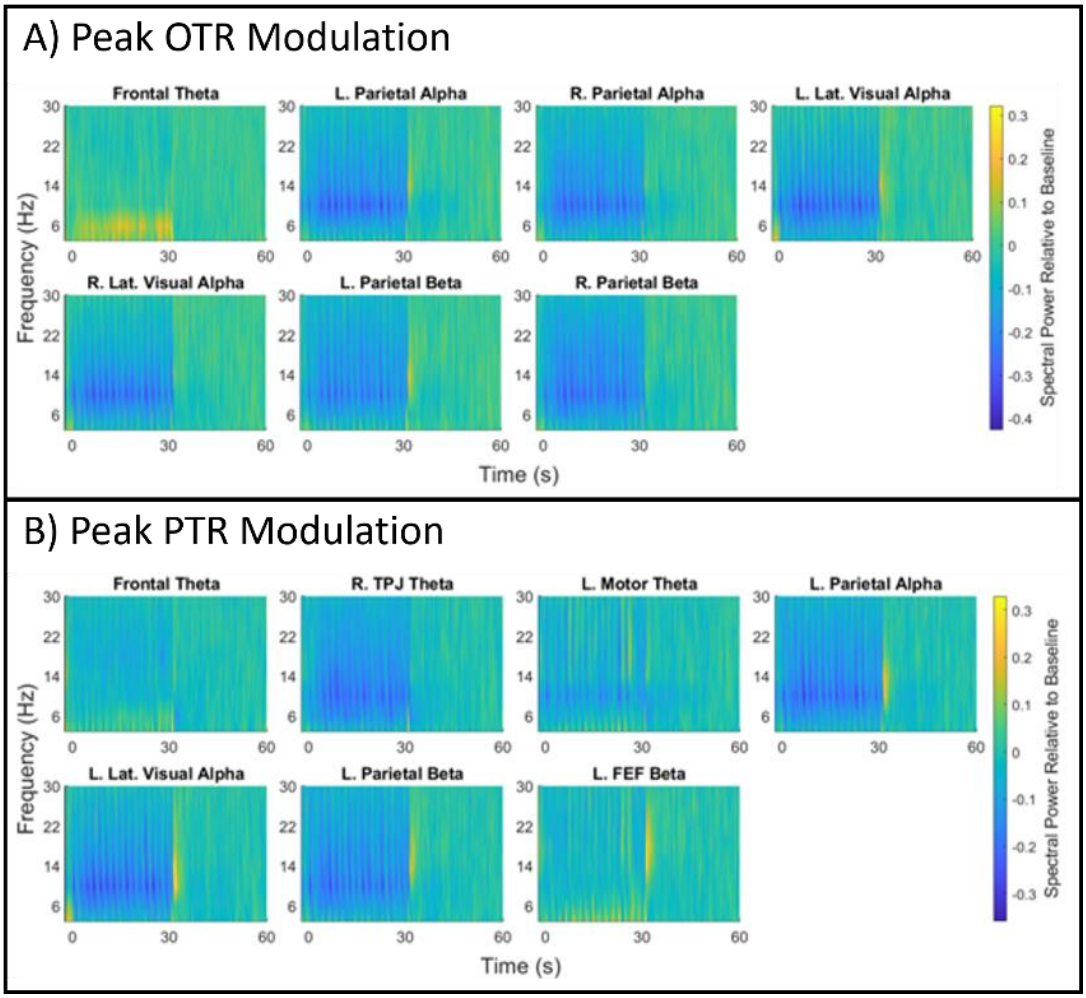


***Figure 5.4**: Time-frequency spectrograms (TFS) for locations that were shown to modulate between 2-back and 0-back during the PTR period (31.5 – 33.5 s). Only the 2-back condition is shown as this condition elicited the strongest response in all cases. A baseline window of 48 – 58 s was used to calculate the relative spectral power at each frequency.*

From the TFS in Figure 5.4A, a set of representative group timecourses are shown in Figure 5.5A, showing trial-dependent OTR modulations in theta, alpha and beta. The timecourses show a large change in OTR power in each of the frequency bands in 2-back compared with the other conditions. The time-averaged OTR for all regions of interest can be seen in Figure 5.5B. When averaging over the OTR time window, all regions interrogated modulated significantly ($p < 0.05$, rm-ANOVA) with task condition after Bonferroni correction, denoted by an asterisk (*) in Figure 5.5B. Post-hoc t-tests showed that for all regions, there were significant ($p < 0.05$) modulations between all pairs of conditions. Interestingly, the change in oscillatory power between 2-back and 1-back was much larger in magnitude than the change between 1-back and 0-back.

The full set of timecourses at locations of peak OTR modulation are shown in Figure A5.1A.

Figure 5.5C shows the equivalent for the PTR window, taking a representative set of timecourses from the TFS in Figure 5.4B. For each of the timecourses in Figure 5.5C, the PTR window is highlighted in an inset. Post-task rebounds in the alpha (Fig. 5.5Cii) and beta bands (Fig. 5.5Ciii), previously only observed in the sensory cortex following movement or visual stimuli, are clearly visible in the left parietal cortex and left frontal eye field, both regions which are associated with higher cognitive activity. The theta band (Fig. 5.5Ci) also shows a clear PTR, although this is an ERD rather than an ERS and is primarily seen in the 2-back condition. The full set of timecourses at locations of peak PTR modulation are shown in Figure A5.1B.

Figure 5.5D shows the average PTR amplitude in all the regions of interest. Apart from theta in the right TPJ, all PTRs modulated significantly ($p < 0.05$, rm-ANOVA) with task condition after Bonferroni correction. As found for the OTR responses, post-hoc t-tests showed that for alpha band activity in left lateral visual and beta band activity in left parietal regions and left frontal eye field, there were significant modulations in the PTRs between all pairs of conditions. However, in contrast to the OTR responses, the PTRs in the theta band activity in frontal and left motor regions and alpha band activity in the left parietal region, there were no significant differences between the 0-back and 1-back conditions, with 2-back condition driving the measured PTR modulations in these regions.

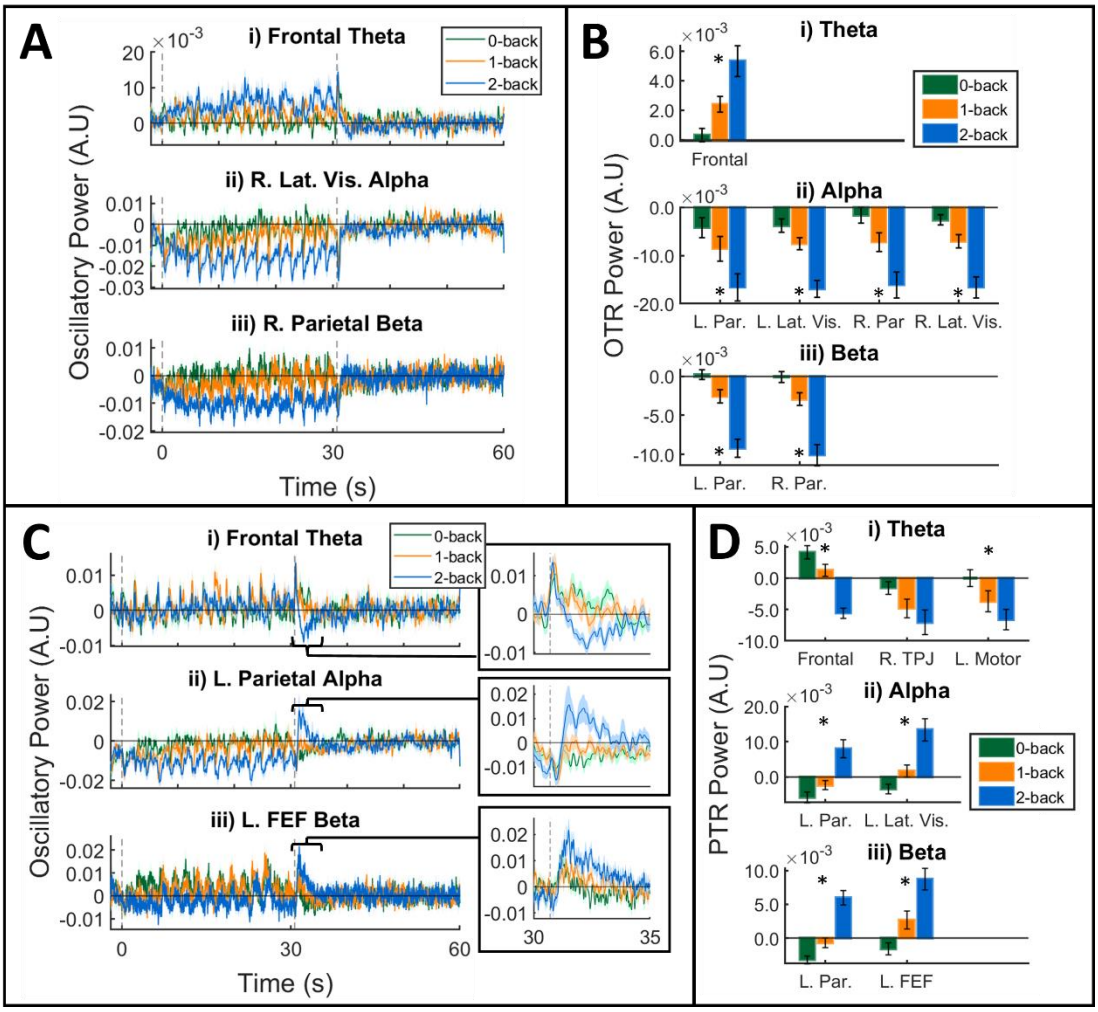


***Figure 5.5**: Timecourses and bar charts from peak ~~T~~-stat locations in each frequency band. Panels A and C show group averaged timecourses from representative OTR and PTR locations in each frequency band (other timecourses can be seen in Fig. A5.1). Timecourses were averaged during the relevant time windows to give the average power over the time windows for each region which is displayed in the bar charts (panels B [OTR] and D [PTR]). Panels A and B show effects during the OTR window (0.5 - 29.5 s), whilst panels C and D show effects during the PTR window (31.5 - 33.5 s). Bar charts that show significant ($p < 0.05$, rm-ANOVA) change across conditions are marked with an asterisk (*). Shading around timecourses (A and C) and error bars (B and D) denote standard error over subjects for each measure.*

5.5.4 Attention Network

In both time-windows, beta band activity was localised to the dorsal attention network (DAN). The group-averaged timecourse for beta activity averaged over all nodes of the DAN (left and right parietal masks, left and right frontal eye field masks) can be seen in Figure 5.6, with maximum OTR modulation shown in Figure 5.6i and maximum PTR modulation shown in Figure 5.6ii. Both the OTR and the PTR of the DAN modulated significantly ($p < 0.05$, rm-ANOVA) between all pairs of conditions.

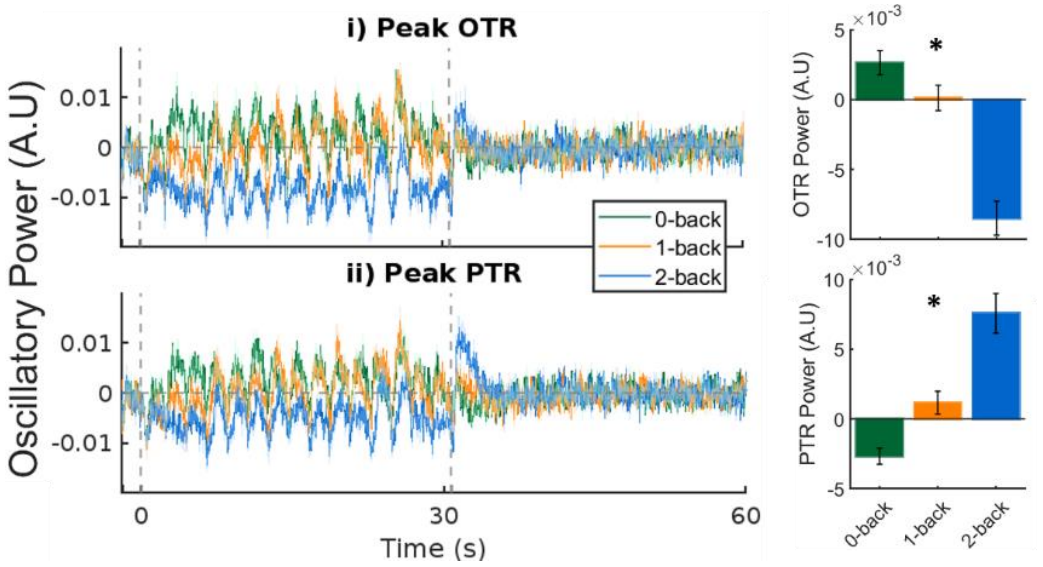


***Figure 5.6**: Group-averaged beta timecourses across the whole DAN, at locations of peak activity during the OTR (**i**, 0.5 - 29.5 s) and PTR (**ii**, 31.5 - 33.5 s) time-windows. Bar charts on the right show average power in the corresponding time windows across conditions. Activity during both time windows modulated significantly ($p < 0.05$, rm-ANOVA) with task condition, denoted with an asterisk (*). Post-hoc t-tests showed that all pairs of conditions varied significantly ($p < 0.05$) in both time-windows. Shading around timecourses and error bars on bar charts represent standard error over subjects for each measure.*

5.5.5 Post-Movement Beta Rebound

Figure 5.7 shows the group-average peak motor response in the beta band when contrasting the PMBR to the MRBD. The peak PMBR location is shown in the ~~T~~-stat map in Figure 5.7A, found by contrasting the PMBR window (0.5 – 1.5 s following each button press) with the MRBD window (-0.5 – 0.5 s around each button press). The group-average timecourse in response to correct button presses is shown in Figure 5.7B for each condition, with the button press occurring at t = 0. The baseline used (48 – 58 s) was the same as the timecourses in Figures 5.5 and 5.6. Using rm-ANOVA, we found no significant modulation between task condition in either the MRBD or PMBR. It should be noted that there was no motor cortex ~~T~~-stat peak when contrasting the PMBR in 2-back with the PMBR in 0-back, confirming that this response is not modulated by task condition here. Regression results are shown in Figure 5.7C, comparing average PMBR following button presses with average PTR in the DAN following task blocks, for each subject. PMBR correlated significantly with PTR in the DAN, despite the PMBR not modulating with task condition, showing that subjects with large PMBRs tend to also have large PTRs in the DAN. However, the two responses differ in that the DAN is functionally modulated by the n-back task, whereas the PMBR is not.

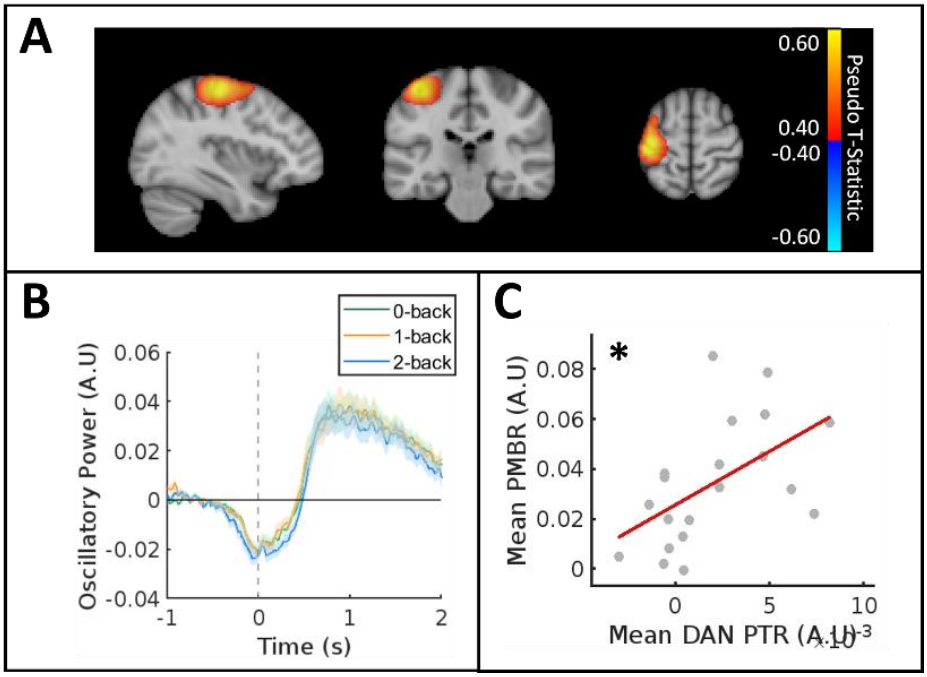


***Figure 5.7**: The well-studied beta response to button press in the motor cortex. Panel A shows a ~~T~~-stat map found by contrasting the PMBR period (0.5 – 1.5 s relative to button press) with the MRBD period (-0.5 – 0.5 s relative to button press) across all conditions. A clear positive peak can be seen in the left (contralateral) motor cortex. Panel B shows the extracted timecourses for each condition, averaged over all correct button presses and over all subjects. The time axis is set such that zero is the time of the button press. The shaded area around each line denoting the standard error over subjects. There were no significant modulations between conditions during the MRBD nor the PMBR. Baselines were removed from timecourses using 48 – 58 s, also used in Figures 5.5 and 5.6. Panel C shows the relationship over subjects between the mean PMBR with the mean DAN PTR over all conditions. * denotes a significant ($p < 0.05$) correlation.*

5.5.6 Residual PTR Modulation

The residual PTR amplitudes after regressing out OTR amplitudes can be seen in Figure 5.8. In all regions where both OTR and PTR effects were observed, the residual PTR signals still showed significant modulation between conditions (Bonferroni corrected), suggesting that the OTR and PTR are largely independent.

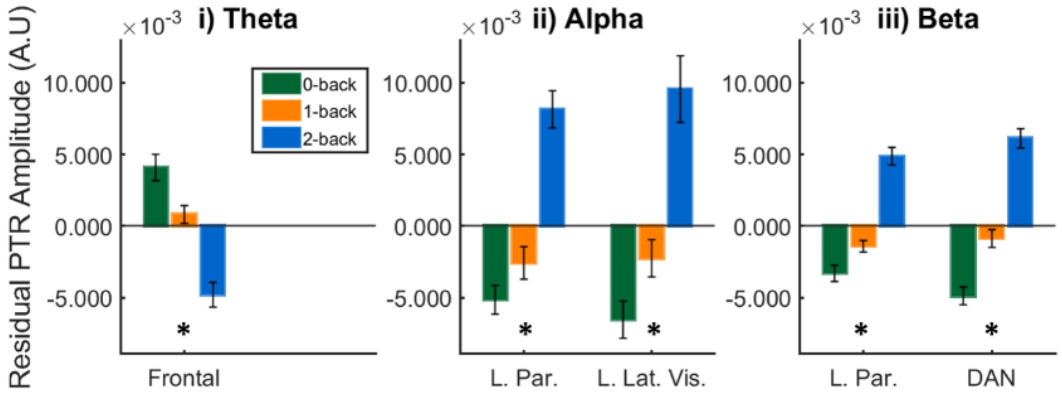


***Figure 5.8**: Average PTR power (as shown in Figure 5.5) after the OTR signals have been regressed out for each subject. Only the regions and frequency bands where both an OTR and PTR modulation were measured were included in these analyses. A significant ($p < 0.05$, RM-ANOVA) change across conditions is marked with an asterisk (*). Error bars denote standard error over subjects.*

5.5.7 Neural-Behaviour Correlations

The results of relating RT to oscillatory activity are shown in Figure 5.9, with OTR against RT in Figure 5.9A and PTR against RT in Figure 5.9B. The analysis showed no significant correlation between oscillatory power in the task window (0.5 – 29.5 s) and RT, for any of the regions. However, the alpha band PTR amplitude in the left lateral visual region showed a significant ($p < 0.05$, OLS) positive correlation with RT, meaning that a subject with greater increase in alpha PTR amplitude also had longer RT in 2-back compared to 1-back condition. Similar correlation was seen for left parietal alpha power and RT, albeit a trend ($p < 0.1$, OLS). These results were not corrected for multiple comparisons, as with only 20 participants, methods such as Bonferroni correction would likely suppress any real effects in the data. These effects are explored further in Chapter 6.

Residual PTRs in the same four regions were correlated with RT, as shown in Figure 5.9C. The left lateral visual alpha band PTR and RT correlation remained the same, however there was no longer a trend between left parietal alpha band PTR and RT. Interestingly, the frontal theta band relationship with the RT became significant. In this region a large change theta ERD in the PTR window was associated with a small change in RT between the two conditions.

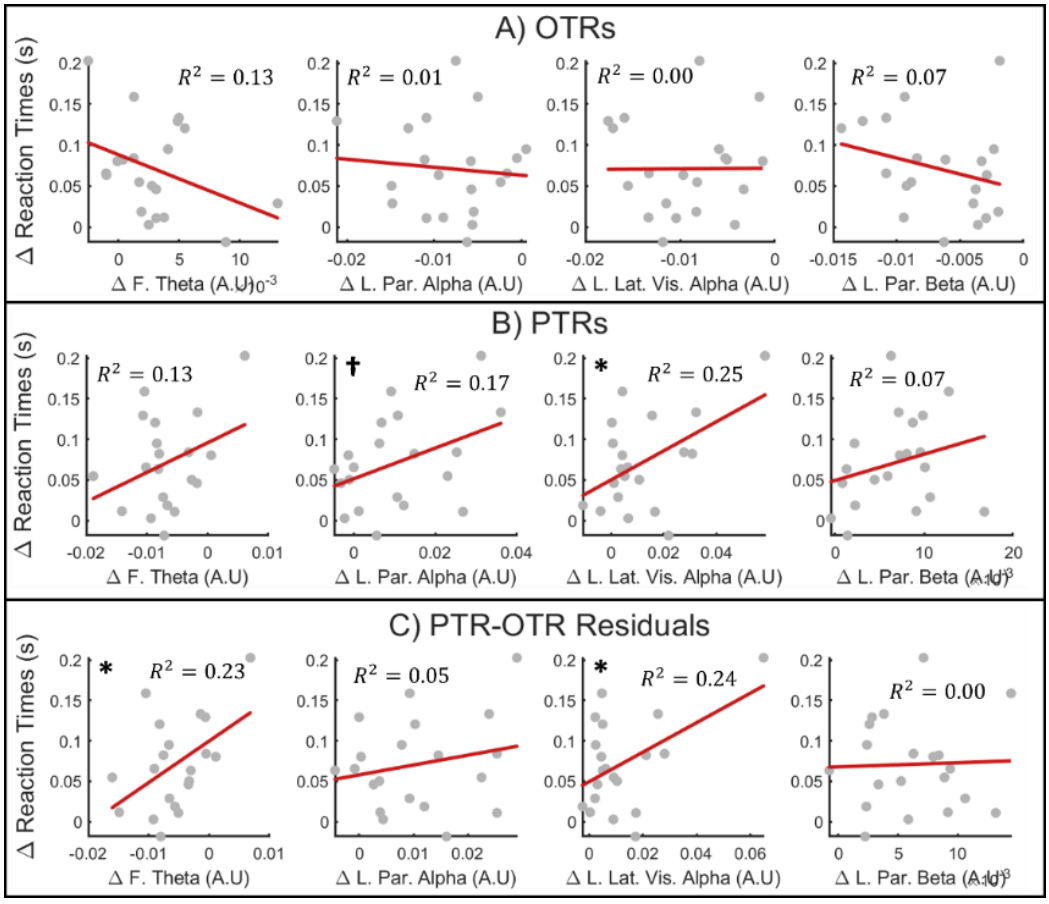


***Figure 5.9**: Least-squares regressions across subjects between the change in reaction time (ΔRT) and change in oscillatory power between 2-back and 1-back conditions, averaged over blocks. Panel A shows the OTR against RT, Panel B shows the PSR against RT and Panel C shows the PTR response after OTR response has been regressed out against RT. Only regions with T-stat peaks associated with both the OTR and PTR time windows were examined. An asterisk (*) denotes a significant ($p < 0.05$) relationship between measures; while a dagger (†) denotes a trend ($p < 0.1$). R^2 is the coefficient of determination denoting goodness of fit.*

5.5.8 Oscillatory Stimulus Response

As expected from the OTR timecourses and TFS in Figures 5.4 and 5.5, when the individual non-target stimuli are interrogated in regions where both OTR and PTR responses were observed, we find oscillatory stimulus response (OSR) consisting of: theta band ERS in the frontal region, and alpha and beta band ERD in the left parietal region along with alpha band ERD in the left lateral visual region occurring between 200 and 500 ms after the letter presentation (Fig. 5.10A). Interestingly, when using -0.3 – 0 s prior to letter presentation for baseline correction (which is standard in analyses of this type), there were no significant modulations between conditions of any of the stimuli responses (Fig. 5.10B). This finding suggests that there is an overall during-task modulation of the responses between conditions, rather than a modulation of individual stimulus response across conditions, which is corroborated by the results

shown in Figures 5.4 and 5.5. Taking the average of the stimulus responses over a block and regressing these responses from the PTR in the corresponding location and frequency band revealed that the PTR is not explained by the responses occurring after each stimulus presentation (Fig. 5.10C), with significant modulation of the PTR between conditions still present after removal of the relationship with the OSR.

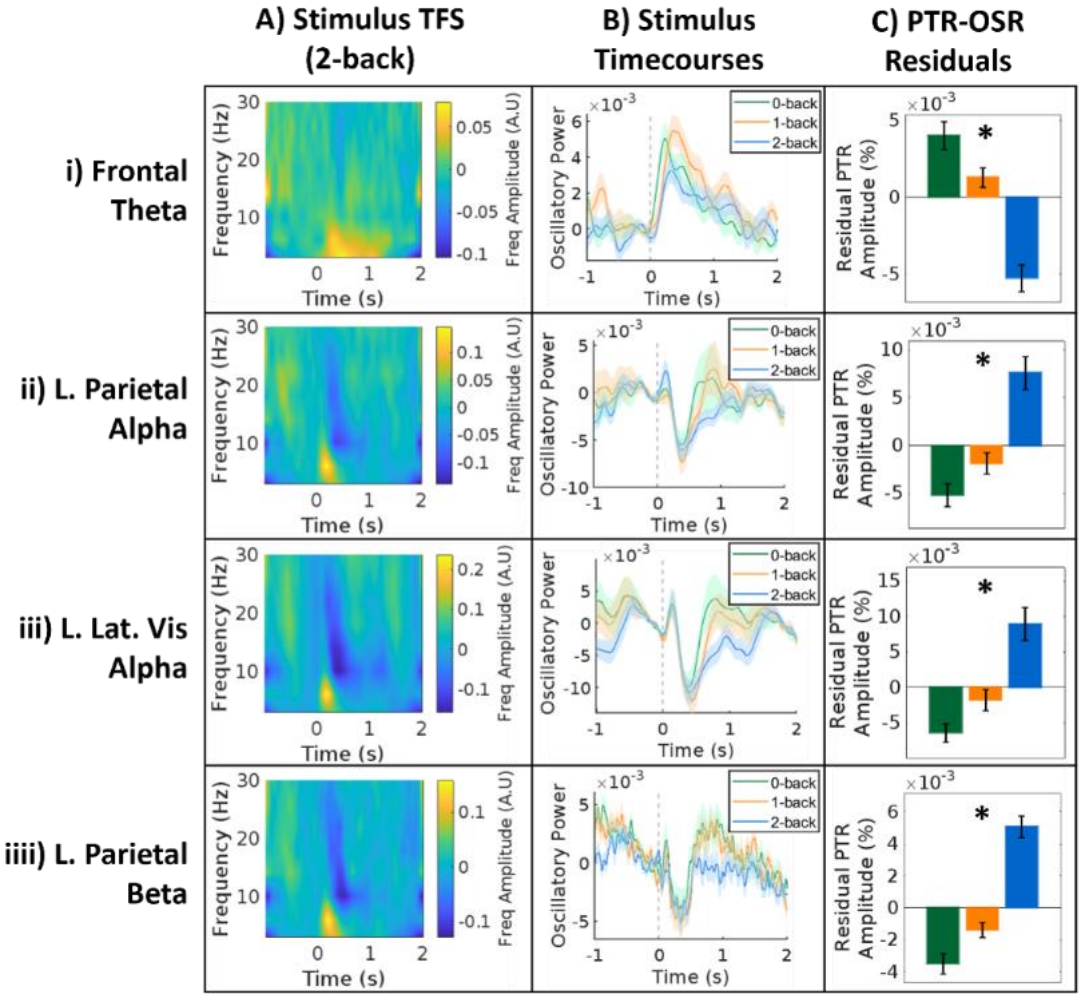


***Figure 5.10**: Panel A shows time-frequency spectrograms (TFS) of the OSR (responses to individual non-target letter presentations) for brain regions where both a PTR and OTR response was found. Locations of maximal activity during the PTR period (31.5 – 33.5 s) were used to extract the VE timecourses. Only the 2-back condition is shown as an exemplar. Panel B shows the average timecourses of oscillatory power across conditions in the frequency bands of primary interest for each location, with shading representing the standard error over subjects. None of these modulated significantly with condition. For Panels A and B, a baseline window of -0.3 – 0 s prior to letter presentation at t = 0 s was used for baseline removal of each frequency response. Panel C shows the PTR average power timecourse responses (as shown in Fig. 5.8) after the individual stimulus oscillatory responses measured in the time window 0.3 – 0.5 s shown in panel B have been regressed out for each subject. Only the regions where a PTR and OTR response were measured were included in these analyses. Error bars denote standard error over subjects. Significant ($p < 0.05$, rm-ANOVA) changes across conditions are marked with an asterisk (*).*

5.6 Discussion

Post-task responses have been studied extensively in the motor cortex (Barratt et al., 2017a, Gascoyne et al., 2021, Hunt et al., 2019, Liddle et al., 2016, Fry et al., 2016, Pakenham et al., 2020, Gaetz et al., 2020, Jurkiewicz et al., 2006b), especially in the beta band. However, despite several standing hypotheses, there is no clear consensus on the functional role of PMBRs, and there has been no evidence that PTRs occur outside of the sensory cortex following higher cognitive processes. We showed that PTRs are a ubiquitous phenomenon, measured in sensory (visual, sensorimotor) and higher cognitive regions (prefrontal, DAN, TPJ) and across the theta, alpha, and beta frequency bands. These PTRs follow cessation of higher cognitive processes such as attention and working memory, as well as sensory processes such as movement or visual stimulation. In several regions, the PTR magnitudes increased significantly with working memory load, suggesting a functional relationship to the task. Furthermore, we show that PTRs are not explained by modulation in the OTR or OSR, i.e., any of the responses occurring during task periods (Fig. 5.8), suggesting distinct cognitive origins. In addition, we also found that the RT of a subject performing the task were predictive of alpha PTR amplitudes in lateral visual ($p < 0.05$) and parietal ($p < 0.1$) regions, whereas RT were not predictive of OTR amplitude in the same regions.

5.6.1 Beta Rebound in Attention and Motor Networks

We observe a decrease in DAN beta power during the task, followed by an increase in beta power above baseline following task cessation, which modulates with working memory load (Fig. 5.3, 5.6). This forms a clear parallel with previous PMBR studies which showed increasing beta PTR amplitude in conditions with greater theoretical load on the motor network (Fry et al., 2016, Solis-Escalante et al., 2012). As with previous studies, we propose that the beta PTR is performing an inhibitory function in networks recruited for the task (Pakenham et al., 2020, Fry et al., 2016, Pfurtscheller et al., 2005), bringing networks back to resting levels of activity. Interestingly, we did not see any PMBR modulation with WM load following correct button presses (Fig. 5.7). We hypothesise that this is because the motor cortex is not specifically recruited for working memory processes during the n-back task, instead being recruited for the button press motor action, which does not change in difficulty across conditions.

Previous fMRI studies have found activations to an n-back task in the DAN that increase with load (Weinberger et al., 1996, Callicott et al., 2003, Blokland et al., 2008, Owen et al., 2005), a phenomenon we explore further in Chapter 7. However, until now, there has been limited identification of this network in electrophysiology studies,

particularly in association with oscillatory responses. Luckhoo *et al* noted that left fronto-parietal network connectivity was modulated in the 8 – 20 Hz frequency band during the task period, but not significantly (Luckhoo et al., 2012). Huang *et al* (Huang et al., 2019) showed there is a change in the alpha and beta bands which appear to overlap with the DAN, but there was considerable spatial blurring of the responses making it difficult to identify the regions recruited. Previous EEG and MEG studies have more often reported modulation of the default mode network (DMN) *during* the task period (Brookes et al., 2011b, Popov et al., 2018), including frontal pole and bilateral parietal regions, which we also observe (Fig. A5.2). Unlike these studies, we observe clear modulations of the DAN in the beta band, predominantly during the PTR, as well as alpha modulations in a more ventral fronto-parietal network during the PTR (Fig. 5.3). Therefore, the reason that previous MEG studies did not observe clear activations in the DAN is likely because they did not interrogate the post-task period.

The general discrepancy between fMRI and MEG n-back studies is likely due to the difference in the sources of each of the signals (see Chapter 2). The positive BOLD response has been shown to relate to increased local neuronal excitation (Logothetis et al., 2001, Logothetis, 2008, Moon et al., 2021), while the negative BOLD response is related to increased inhibition (Shmuel et al., 2006, Devor et al., 2007, Mullinger et al., 2017, Moon et al., 2021). Oscillatory rhythms measured by MEG, however, particularly alpha/beta oscillations, are thought to relate specifically to top-down inhibitory signals in intracortical and thalamo-cortical circuits (Halgren et al., 2019, Van Kerkoerle et al., 2014, Jensen and Mazaheri, 2010, Klimesch et al., 2007). Therefore, while fMRI is sensitive to increased excitation in recruited networks such as the DAN, MEG may be more sensitive to top-down inhibitory signals which should theoretically become stronger following task cessation, required to bring network activity back to resting levels.

Interestingly, we find a significant correlation between the average PMBR response and the average DAN PTR response over subjects (Fig. 5.7), suggesting a link between these two responses, with subjects who exhibit a large PTR in the DAN also exhibiting a greater PMBR. However, it is difficult to determine whether this correlation is driven by a functional relationship between DAN PTRs and the PMBR or simply SNR variation between subjects, i.e., some subjects may have higher measured beta power (or signal in general) which is reflected in both the DAN and motor cortex. We propose that the PTR is not unique to any particular task but is established in the cortical regions or networks most strongly engaged during the task. In the case of the n-back task, the networks which are modulated by task condition are those involved in executive

functions, leading to PTR modulation in these regions. There is no change in the PMBR with task condition as the motor action (button press) remains the same, placing the same load on the motor network despite the changing WM load. Further work is needed to explore the links between PTRs in different regions following different types of activity.

5.6.2 The Role of Alpha Rebounds in Working Memory

In addition to beta band PTRs, we see similar responses in the alpha band. Although alpha PTRs were visible in a fronto-parietal network, there was a far stronger alpha response in parietal than frontal regions, and responses were more inferior. The alpha response was also seen in lateral visual regions during the OTR and PTR time-windows. The difference in the locations of the responses may reflect the locations of the primary sources of alpha and beta, with both bands serving to transition these brain regions to rest. Increases in alpha are now synonymous with the concept of inhibiting task irrelevant information (Roux and Uhlhaas, 2014, Klimesch et al., 2007, Sokoliuk et al., 2019, Jensen and Mazaheri, 2010). Therefore, in the case of the PTR, the rebound in alpha power that we observe most likely represents reduced attention to external stimuli to enable the brain to return to internal processes. Indeed, the idea that alpha and beta band activity are working in concert, and perhaps should not be distinguished, is a well-documented concept within the frameworks that describe oscillations in WM tasks (Hanslmayr et al., 2016, Griffiths et al., 2019), suggesting the need for analysis approaches which do not rely on frequency banding (explored in Chapter 6).

5.6.3 Post-Task Theta Undershoots May Modulate Default Network Activity

A novel observation that we report is a theta ERD following task cessation (Fig. 5.3, 5.4, 5.5), mostly localised to the prefrontal cortex. We see several DMN regions modulate in the theta band, including the medial prefrontal cortex, inferior parietal lobes and temporoparietal junction (Fig. 5.3, A5.2), forming parallels with previous studies that have also seen DMN regions activated in the theta band during an n-back task (Brookes et al., 2011b, Luckhoo et al., 2012, Popov et al., 2018). Given the fMRI studies that show the DMN is suppressed during an n-back task (Pomarol-Clotet et al., 2008, Schneider et al., 2011), and the fact that theta power in DMN regions correlates negatively with BOLD (Meltzer et al., 2007), it is possible that the frontal theta ERD during the PTR window represents reactivation of a network that was suppressed during the task. Similar to alpha/beta PTRs in the DAN and visual network, the theta ERD may act to re-establish resting network activity, but through re-activation rather than inhibition. It follows that the theta undershoot may reflect increased local

excitation, opposite to our proposed function of alpha/beta PTRs, although this remains a tentative speculation due to the novelty of this finding. Chapter 7 explores BOLD overshoots in the DMN that occur following an n-back task, which may form the haemodynamic counterpart of theta PTRs reported here.

5.6.4 Post-Task Responses are Modulated by Behavioural Markers of Task Difficulty

All PTR amplitudes in Figure 5.9B increased with RT, regardless of sign of the PTR. The strongest relationships with RT were seen in the alpha band PTRs in left lateral visual ($p < 0.05$) and left parietal ($p < 0.1$) regions. Crucially, RT were not predictive of OTR amplitudes in the same regions (Fig. 5.9A). Removal of OTR contributions to the PTR amplitudes took away the trend between RT and left parietal alpha band, however the relationship remained in left lateral visual alpha band, and a new significant ($p < 0.05$) correlation was revealed between RT and residual PTR theta band activity in the frontal region (Fig. 5.9C). We did not correct these results for multiple comparisons, as with such a small number of participants, it is likely that this would lead to any real effects being suppressed. It is therefore important that these results are taken as a promising further indication that during-task and post-task oscillatory responses are driven by different cognitive and neuronal processes, rather than proof that PTRs are driven by RT directly. Our results corroborate the hypothesis posed by Pakenham *et al* that task difficulty modulates the PTR (Pakenham et al., 2020), however, we acknowledge that the findings presented require replication in larger cohorts in the future. The fact that the strongest relationships are seen in alpha band PTRs may reflect the unique role that alpha plays in suppressing responses to external stimuli in order to return to rest. It is also possible that we see the strongest relationship in alpha PTRs because this frequency band dominates the oscillatory response to an n-back task (Fig. 5.3, Fig. 5.4), i.e., the relevant frequency band may differ between tasks. In Chapter 6 we explore these relationships further, using bursting characteristics of PTRs rather than average frequency response.

The lack of direct correlation between task performance metrics and OTRs is perhaps unsurprising given that the n-back task involves simultaneous encoding, retention and retrieval processes. In agreement with our findings, similar analysis using EEG showed no direct correlation between any single frequency band and behaviour (Popov et al., 2018). In an alternative approach, Takei *et al* separated the retention and encoding phases of the n-back task and showed that some alpha, beta and gamma oscillatory changes during the task were significantly related to hit rate and RT (Takei et al., 2016). A similar pattern was also observed by Huang *et al* (Huang et al., 2019), although we

note that their behavioural-neuronal relationship is primarily driven by the mild traumatic brain injury patients and in the healthy controls there appears to be no clear correlation. Therefore, we suggest that the lack of correlation between OTRs and behaviour is due to the brain performing multiple overlapping processes simultaneously, whereas in the PTR period the brain is performing a unified function, inhibiting task-related networks to allow the brain to return to idling processes. The level of inhibition required depends on cognitive demand felt by the participant, which is reflected in RT. Repetition of these tests with larger cohorts would confirm that there is no relationship between OTR and RT.

5.6.5 Limitations and Future Work

One clear limitation to this study is the cohort size. At only 20 participants, it is difficult to show statistical effects in the data, increasing the chance of false negatives in the results. This limitation was mainly due to the COVID-19 pandemic, which greatly limited our ability to take data during this project. However, despite this, we still see promising functional modulations of PTRs, as well as relationships between alpha PTRs and RT, which would likely become stronger with a larger cohort size.

With regards to experiment design, our choice of task conditions may have limited the variance that was observed in behaviour and PTR amplitude. As can be seen in Figures 5.2 and 5.5, there was little difference in behaviour and oscillatory amplitudes between the 0-back and 1-back conditions, whereas the 2-back condition creates notably more variance in both. In the case of TH and FP, many “ceiling” or “floor” effects were seen, where participants hit 100% of targets, and had zero false button presses. Anecdotally, participants reported that the 1-back and 0-back conditions were very easy, while the 2-back condition was considerably more difficult, which is likely the reason for these effects in behaviour and oscillatory amplitudes. Removing 0-back and adding a 3-back condition may have created more variance between conditions, which could strengthen our observed relationships between behaviour and PTR amplitude.

Another limitation was the particular structure sensor used to digitise the fiducial locations and shape of the head. At the time of scanning, COVID-19 regulations prevented us from performing a digitisation using a Polhemus FASTRACK digitiser (Polhemus, Colchester, VT, USA), which is the standard approach for head digitisation with cryogenic MEG. We instead used an Occipital Structure Sensor (Occipital Inc., San Francisco, CA, USA), along with green stickers on the fiducial locations so these points could be identified post-hoc. The digitisations produced with this were very susceptible to errors, created by lighting, or movement by the participant or scanner

operator. Therefore, the positions of the fiducials were often uncertain (visibly smeared out), and the shape of the head was lacking detail, which may have led to co-registration errors. A more reliable digitisation method may have improved the beamformer estimates.

Finally, MEG has limited sensitivity to subcortical (deep) brain regions (Hillebrand and Barnes, 2002), which play key roles in information flow to cortical networks (see Chapter 2) such as the DAN. Given the potential relationship between post-task EEG and BOLD data (Mullinger et al., 2017), the addition of fMRI to study PTRs in both cortical and subcortical structures would provide a more complete picture of functional network dynamics when the brain moves between active and resting states. We partially address this limitation in Chapter 7 using 7T fMRI to study a similar task.

Now that we have established the PTR as a potentially brainwide phenomenon that follows both sensory (visual and motor) and higher cognitive tasks, future studies should examine these responses in patient populations to see if PTRs following higher cognitive processes are modulated by illness in the same way as the PMBR.

5.7 Conclusion

We used a bespoke n-back task to investigate PTRs in brain regions and networks associated with higher cognition. Our investigation revealed that PTRs are a ubiquitous phenomenon in the brain, occurring in multiple frequency bands (theta, alpha, beta) and brain regions outside of the sensory cortex, following cessation of higher cognitive processes. We believe we are the first to report post-task beta rebounds in the DAN, which modulate significantly with WM load and likely serve to inhibit network activity to return to rest. We also report negative theta PTRs which may represent re-activation of networks that were suppressed during the task. Alpha PTRs correlated with RT in left lateral visual ($p < 0.05$) and left parietal ($p < 0.1$) regions, while OTRs in the same region showed no correlation with RT, suggesting distinct neuronal or cognitive origins, although replication with larger cohorts is required to confirm this. Together our results suggest that PTRs in different frequency bands work in concert to re-establish resting brain activity, by means of inhibition or re-activation of functional networks. We provide evidence that PTRs may depend on task difficulty, such that greater cognitive demand in active networks requires PTRs of greater amplitude to return to rest.

5.8 APPENDIX A

5.8.1 Peak Modulation Timecourses

To complete the figures presented in the main body, showing TFS (Fig. 5.4) and representative timecourses (Fig. 5.5), the full set of timecourses are shown below in Figure A5.1, including all regions in Table 5.1 filtered into the frequency bands listed on the table. Panel A contains timecourses from VEs of maximal OTR modulation in 2-back compared to 0-back, and panel B shows the equivalent for then PTR time window.

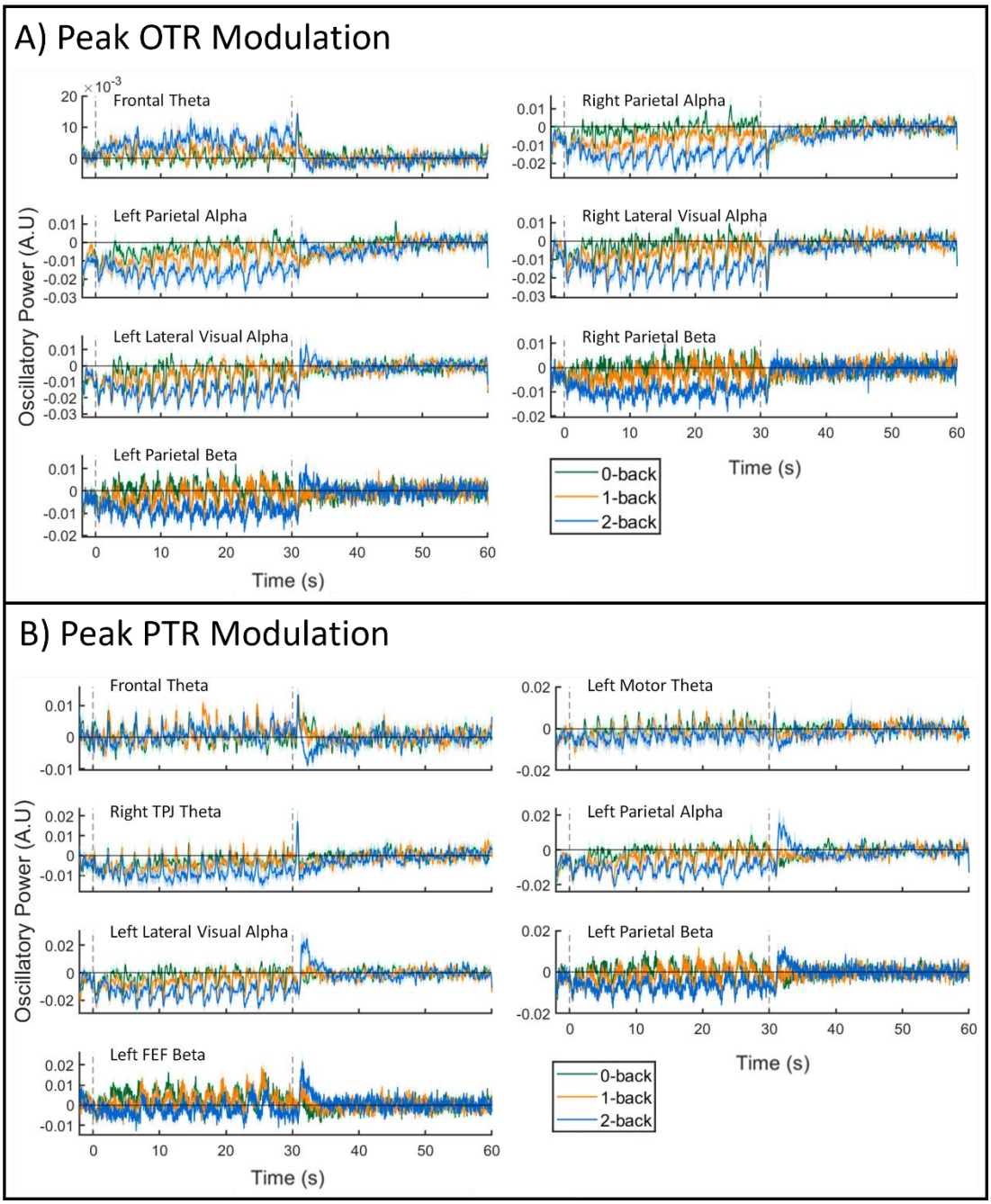


Figure A5.1*: All timecourses for regions and corresponding frequency bands listed in Table 5.1. Panel A shows timecourses from VE locations of maximal OTR modulation, while panel B shows the equivalent for maximal PTR modulation.*

5.8.2 Task vs Rest Contrast

In addition to the results based on modulation of power between task conditions, we also took T-stat maps contrasting task (0.5 – 29.5 s) and rest (30.5 – 59.5 s) windows. The theta frontal ERS and parietal ERD in these maps overlap with superficial DMN regions, although the deeper structures in this network cannot be reliably measured using MEG.

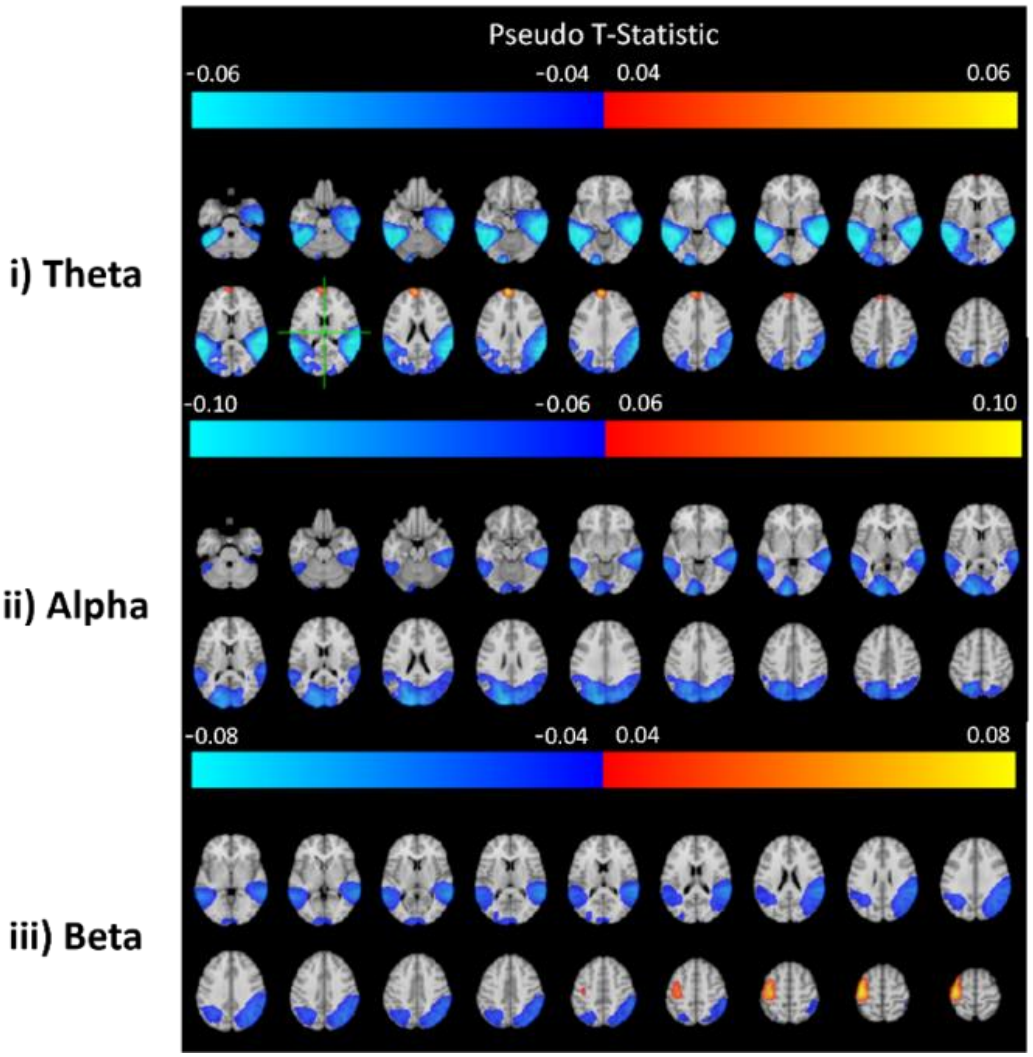


Figure A5.2*: ~~T~~-stat maps created by contrasting the task period (0.5 – 29.5 s) with the rest period (30.5 – 59.5 s) for the theta (row **i**), alpha (row **ii**) and beta (row **iii**) bands. These highlight which regions of the brain were activated by the n-back task, but do not tell us whether there were condition-dependent modulations or activity during the PTR time window.*

6 Characterising Post-Task Responses using Hidden Markov Models

6.1 Abstract

Chapter 5 showed that post-task responses (PTRs) are a ubiquitous phenomenon in the brain, occurring across the cortex in theta, alpha and beta bands, manifesting as rebounds or undershoots in oscillatory power. However, it is currently unknown whether PTRs following working memory are driven by transient bursts, which are moments of short-lived high amplitude oscillatory activity, similar to those that drive the post-movement beta rebound. In addition, due to their cross-frequency nature (uncovered in Chapter 5), it may be more appropriate to study PTRs without the constraints of conventional frequency banding.

Here, we use 3-state univariate hidden Markov models (HMMs), which can segment and characterise events in MEG data without *a priori* knowledge of frequency content or response timings. We use HMMs to compare oscillatory events that drive PTRs in two different MEG datasets: 1) a working memory task (presented in the previous chapter) and 2) a visuomotor task (a pre-existing dataset). Our results show that PTRs across working memory and visuomotor tasks are explained by the timing of transient spectral burst events. These bursts have very similar spectral content variation over the cortex, correlating strongly between the two tasks in the alpha ($R^2 = 0.89$) and beta ($R^2 = 0.53$) bands. The number of oscillations per burst has an almost identical distribution over regions between the two tasks ($R^2 = 0.94$), with a mean burst duration over all regions of around 300 ms in both datasets. In addition, we show that PTRs are supported by concurrent burst events across the majority of the cortex, as well as in task-specific networks. Finally, we demonstrate the ability of HMMs to isolate signals of interest in MEG data, such that the HMM probability timecourse correlates more strongly with reaction times than frequency filtered power envelopes from the same brain regions. Overall, we use HMMs to show that induced PTRs across different tasks are driven by bursts with similar characteristics, suggesting a common underlying neural phenomenon.

6.2 Publication and Contribution Note

This work has been published in Human Brain Mapping (Coleman et al., 2024). In addition, parts of this work were presented as posters at the International Conference

on Biomagnetism (BIOMAG) 2022, the Organization for Human Brain Mapping (OHBM) 2023, and MEG UKI 2023.

The data presented here were partially collected by the author (n-back task, Chapter 5) and partially taken from a previous study (Pakenham et al., 2020). The HMM toolbox was taken from OHBA-analysis GitHub (https://github.com/OHBA-analysis/HMM-MAR), but the post-hoc analysis, which is the primary focus of this experimental chapter, was all performed using a series of bespoke in-house scripts.

6.3 Introduction

As explored in the previous chapter, electrophysiological PTRs, often referred to as rebounds, can be observed in higher cognitive regions following working memory, as well as in sensory regions following motor or visual stimuli (Fry et al., 2016, Robson et al., 2016, Pakenham et al., 2020, Mullinger et al., 2017, Pfurtscheller et al., 2005, Jurkiewicz et al., 2006b, Stevenson et al., 2011). The previous chapter corroborated existing evidence suggesting that rebounds (periods of high amplitude alpha/beta activity) serve an inhibitory function, bringing networks that were involved in stimulus/task processing back to resting levels of activity (Pakenham et al., 2020, Mullinger et al., 2017, Pfurtscheller et al., 2005, Chen et al., 1998, Solis-Escalante et al., 2012). In the previous chapter we also presented evidence that negative PTRs in the theta band may also enable reactivation of task-negative networks. However, it remains unknown whether PTRs following working memory are driven by the same underlying neural phenomenon as those that follow movement or visual stimulus. This chapter uses data-driven techniques to perform an in-depth analysis of PTR characteristics in the human brain in response to visuomotor (Pakenham et al., 2020) and working memory (see Chapter 5) tasks, with the aim of determining whether PTRs in each case are driven by similar transient neural events.

Despite being observed directly more than 40 years ago (Pfurtscheller, 1981), the bursting nature of induced beta band activity in the motor cortex has only recently become recognised and used to model functional data (Seedat et al., 2020, Sherman et al., 2016). Bursts are defined as transient (up to several hundred milliseconds) high amplitude oscillatory events in that become more or less probable to form smooth time-frequency responses when averaged over trials (Pfurtscheller, 1981, Jones, 2016, Vidaurre et al., 2016). These events have been shown to relate to behaviour (Little et al., 2019), neurological illness (Briley et al., 2021), and functional connectivity (Seedat et al., 2020), warranting further study across a range of paradigms and responses. Although these events were classically considered a feature of the beta-band, recent

studies have shown that bursts have a spectral profile that contains peaks in both alpha and beta bands (Seedat et al., 2020, Rier et al., 2021). Hidden Markov Models (HMMs) are becoming a popular tool for identifying and characterising bursting behaviour due to the data-driven nature of state inference (Coquelet et al., 2022, Quinn et al., 2018, Seedat et al., 2020, Baker et al., 2014, Vidaurre et al., 2016, Higgins et al., 2021). Studies that have used HMMs to identify a burst state have shown that the MRBD and PMBR, observed in the beta band, can be explained by changes in probability of burst events, whilst changes in connectivity can be explained by changes in burst coincidence between regions (Seedat et al., 2020, Vidaurre et al., 2018). It is unknown whether PTRs across the cortex following higher cognition are driven by bursts with similar characteristics to those that follow movement. Understanding the trial-level neural events that drive PTRs is key to understanding the relationship between these responses across multiple tasks and functional networks. Building on the established clinical interaction with the PMBR (Gaetz et al., 2020, Barratt et al., 2017b, Gascoyne et al., 2021), the study of burst characteristics driving PTRs could provide a novel set of biomarkers for neurological illness, e.g., burst duration, that may outperform coarser measures such as trial-averaged spectral power in delineating illness type and illness progression.

We hypothesise that: 1) transient trial-level burst events constitute PTRs across the brain irrespective of the particular task or frequency band; 2) if PTRs relate to a similar neuronal process across tasks, they should have similar intrinsic burst properties (spectral and duration) despite being induced by different paradigms; 3) as has been shown in the beta band (Seedat et al., 2020), bursts should drive functional network connectivity across multiple tasks and frequency band responses; 4) HMMs will isolate bursts from other brain activity and noise, strengthening previously reported relationships between PTRs and behaviour (see Chapter 5). To address these hypotheses, we employ a mass-univariate HMM approach to capture PTR activity across the brain, independent of frequency band, across visuomotor and working memory task datasets. We group univariate HMM states across brain regions related to PTRs using k-means clustering based on temporal similarity over the entire scan period. We verify that the PTR states correspond with visible bursting activity in single trial MEG data, which average over trials to form a smooth PTR. We look at spectral content and burst duration to perform a region-wise comparison of bursts that constitute PTRs across the two tasks. We then perform a functional network decomposition using further k-means clustering, finding spatial networks formed from coincidence of bursting activity and interrogate the temporal properties of these

networks for each task. Finally, we explore the utility of HMMs for isolating signals of interest from other neuronal signals and noise by testing whether the HMM PTR state better relates to behaviour of participants than the classic frequency filtered power envelopes that were used in Chapter 5.

6.4 Hidden Markov Modelling

6.4.1 Markov Chains

Traditional event-related analysis is generally based on trial-averaged activity, reflecting average increases or decreases in oscillatory power. Recent years have seen a resurgence of bursting models of oscillatory activity, which describe the transient events that occur on single-trials rather than the average response (Jones, 2016, Quinn et al., 2019, Seedat et al., 2020). A method that is becoming popular for segmenting and characterising transient events in MEG data is the hidden Markov model (HMM).

A Markovian system is defined by a set of discrete states, where the state at time t only depends on the state at time t – 1. A Markov model can be used to characterise systems such as this, with discrete and observable states. This is summarised by the Markov chain (see Fig. 6.1), or equivalently, a transition matrix, showing the probability of transitions between each pair of states.

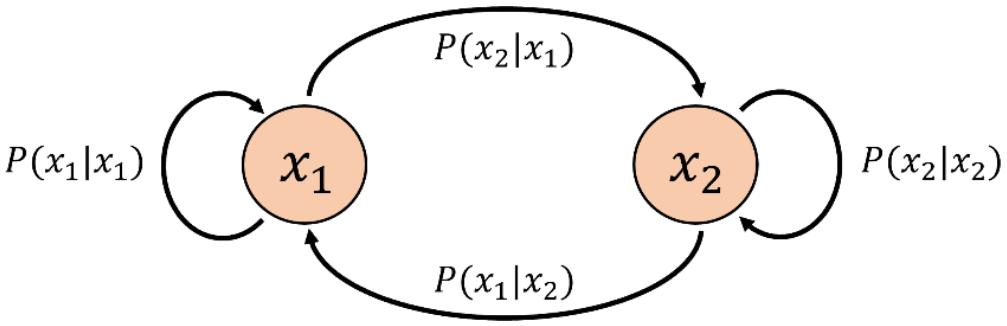


***Figure 6.1**: A simple Markovian system, represented by a Markov chain, containing two discrete, observable states. The probability of observing a state at time t only depends on the state at time t – 1, which can be calculated using a set of transition probabilities.*

In the context of functional neuroimaging, the states would describe the activity of the brain at a given point in time. However, MEG data does not provide a full and discrete description of brain activity, thus, the states are *hidden*, but may be inferred from observable data in a modification of the Markov model, known as a *hidden Markov*

model (see Fig. 6.2) (Woolrich et al., 2013, Vidaurre et al., 2016, Baum and Petrie, 1966). Here, we still have the transition matrix describing the probability of hidden state transitions, but we also have a set of *emission* probabilities which correspond to the probability of measuring an observed value whilst the system is in one of the hidden states.

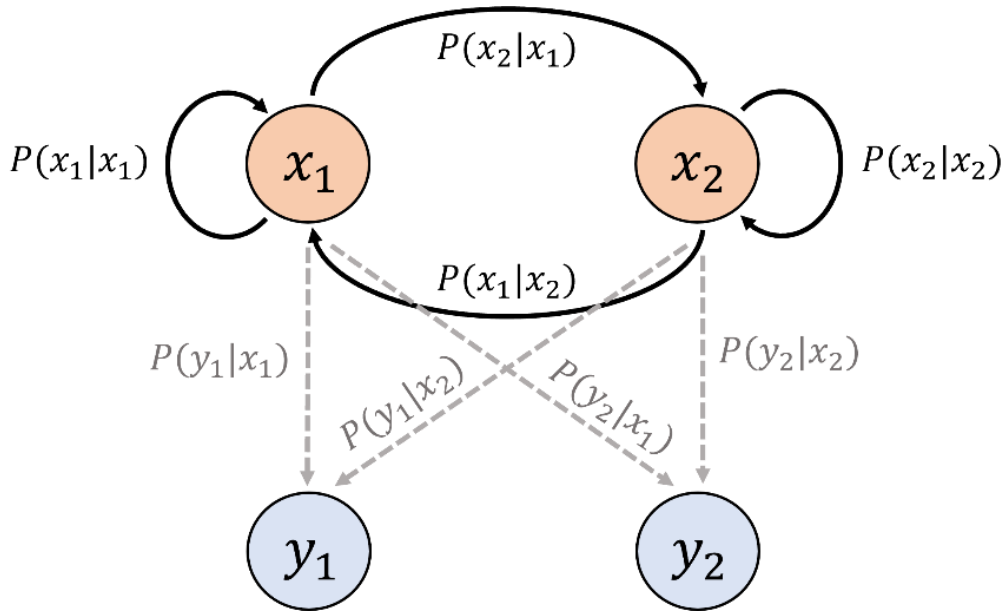


***Figure 6.2**: A modification of the simple Markov model, known as a hidden Markov model. Here, the states x_1 and x_2 are hidden, such that they cannot be observed directly. However, the states are inferred using the observed data, y_1 and y_2. The conditional probabilities marked by the solid black arrows are transition probabilities between hidden states, while the conditional probabilities marked by the dashed grey lines are emission probabilities, connecting the observed data to the hidden states. The probabilities are trained using the observed data.*

6.4.2 The Joint Posterior Probability

Once we know the probability of transitions between hidden states, as well as the emission probabilities of observed values given the current state, we can infer the most likely sequence of hidden states, X, given the set of observed values, Y. This can be written as $P(X|Y)$, which can be calculated using Bayes' theorem (Joyce, 2003)

$$P(X|Y) = \frac{P(Y|X)P(X)}{P(Y)}. \tag{6.1}$$

In practice, the probability of a sequence of data being measured, $P(Y)$, remains fixed, as we can know the measured data with certainty. Because of this, we need only be concerned with the numerator of Bayes' theorem, known as the joint posterior probability,

$$P(X,Y) = P(Y|X)P(X). \tag{6.2}$$

Our goal is to maximise this expression. The Markov property allows us to know the probability of a hidden state occurring at time t, $P(x_t)$, given the previous state in the sequence, $P(x_{t-1})$. Thus, the entire sequence of hidden states, $P(X)$ can be written as

$$P(X) = P(x_0) \prod_{t=1}^{t=n} P(x_t|x_{t-1}), \tag{6.3}$$

where the initial state in the sequence, $P(x_0)$, is the only one that cannot be written via the Markovian condition. Instead, the first term, known as the stationary distribution, is calculated as the first eigenvector of the transition matrix, equivalent to the probability of a state given an infinite sequence. Next, using the emission probabilities, which allow us to know the probability, $P(y_t|x_t)$, of measuring a value whilst the system is in a particular hidden state, we can write

$$P(Y|X) = \prod_{t=0}^{t=n} P(y_t|x_t). \tag{6.4}$$

Equations 6.3 and 6.4 can now be substituted into 6.2 to write an expression for the joint posterior probability,

$$P(X,Y) = P(x_0) \prod_{t=1}^{t=n} P(x_t|x_{t-1}) \prod_{t=0}^{t=n} P(y_t|x_t) \tag{6.5}$$

using only the transition and emission probability matrices.

6.4.3 Free Parameter Optimisation

So far we have assumed that we know the transition matrix between the hidden states, as well as the emission probabilities connecting the hidden states to the observed data. In reality, we know none of these parameters *a priori*, and must learn them from the data (Woolrich et al., 2013). Moreover, for MEG data, the emission probabilities become a probability distribution for each state, such that spatiotemporal variance can be accounted for by a single state assignment. This distribution is known as an observation model. For MEG data, a Gaussian observation model is often chosen, such that each state will have a unique mean and variance. The parameters that define the observation model are denoted by θ. The transition matrix between states is denoted by π. The sequence of hidden states, as before, is given by $X = x_0, \dots, x_n$ while the observed MEG data is given by $Y = y_0, \dots, y_n$. Using this notation (Woolrich et al., 2013), we can re-write the joint posterior probability as

$$P(X,Y,\theta,\pi) = P(x_0|\pi_0) \prod_t P(x_t|x_{t-1},\pi)\ P(y_t|x_t,\theta) P(\theta) P(\pi). \tag{6.6}$$

This expression contains a set of free parameters, X, θ and π, which can be contained within the parameter H, representing the model, or hypothesis about the data. This simplifies equation 6.6 back to 6.2 (where H replaces x), where $P(H|Y)$ is the probability that the model is correct given the measured data, $P(Y|H)$ is the probability of measuring the data given the model, and $P(H)$ is the probability of the model occurring.

Due to the number of free parameters contained in H, and the complexity of the MEG data contained in Y, $P(H|Y)$ can form a complex topology which is difficult to navigate. However, we can make an approximation, $Q(H)$, which resembles $P(H|Y)$, in a process known as variational learning (Rezek and Roberts, 2005). A cost function, which is essentially a distance metric, is minimised between the actual probability distribution, $P(H|Y)$, and the simpler approximation, $Q(H)$. The cost function used here is the Kullback-Leibler divergence, given by

$$F = \int Q(H) \log \frac{Q(H)}{P(H|Y)} dX + \log P(Y) . \tag{6.7}$$

Once a value of $Q(H)$ has been approximated, it can be substituted back into the joint posterior probability,

$$P(H, Y) \approx Q(H)P(H). \tag{6.8}$$

Importantly, due to the mean field assumption (Haft et al., 1999), the hidden variables in the model are independent, meaning that $Q(H)$ can be factorised for each of the variables in H,

$$Q(H) = \prod_i Q_i(H_i) \tag{6.9}$$

where the integral of terms in the product must sum to 1 because Q is a probability distribution,

$$\int Q_i(H_i) dH_i = 1 . \tag{6.10}$$

The consequence of this is that F may be minimised for each of the parameters in H, i.e., the free parameters in the model, separately. Each parameter, Q_i, is optimised separately, whilst keeping the others fixed, progressively improving the estimation of Q. This is shown in the simplified schematic in Figure 6.3, where the complex topology of $P(H|Y)$ is simplified to $Q(H)$ in each dimension separately. Once $Q(H)$ has converged (become optimised), we can take the maximum, which forms an

approximation of the maximum joint posterior probability, from which we can extrapolate the set of model variables contained in H (Rezek and Roberts, 2005).

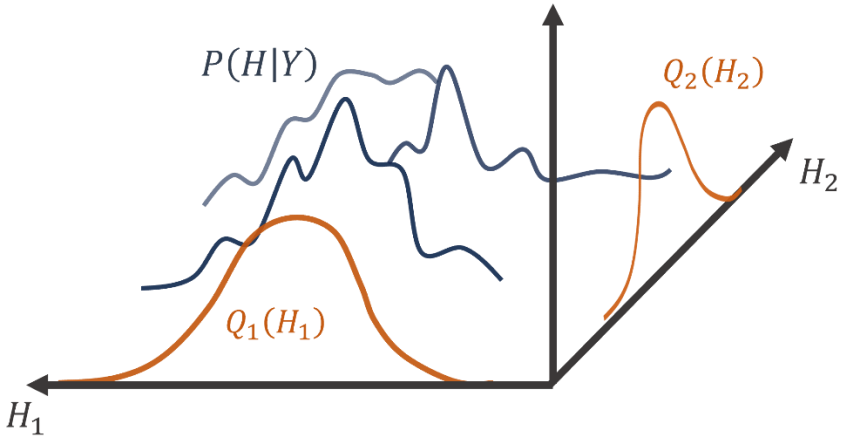


***Figure 6.3**: A simplified schematic showing the variational learning approach used to approximate the joint posterior probability for the set of model parameters. The real joint posterior probability, $P(H|Y)$, can become intractable due to its complexity. However, a simpler approximation of $P(H|Y)$ can be formed for each parameter in H, separately.*

6.4.4 Model Configuration

There are several ways of configuring an HMM, for example, by changing the dimensionality of the input data or the form of the observation model. Each of these configurations will suit different types of data. In the case of MEG data, it is somewhat unrealistic to take an observation as being a single datapoint, as the dynamic timescale of MEG data often spans many datapoints to include features such as evoked responses and spontaneous rhythms. A solution to this is the time-delay embedded (TDE) HMM (Vidaurre et al., 2016), which allows a single observation to contain all datapoints within a specified time-window around a given timepoint. This results in an observation model that describes the autocovariance, or spectral content, of the data observed during a hidden state visit. In this configuration, a time delay must be chosen. For MEG data, a sensible range should be able to contain roughly one entire period of the activity of interest (e.g., alpha oscillations).

Another consideration is the input data. An HMM can be used to model both univariate (single channel/region) and multivariate (many channel/region) data. Modelling of multivariate MEG data means the observation model will contain a spatial component based on the covariance of data from all channels/regions. However, state dynamics of individual regions cannot be deduced from a multivariate HMM, as the states encompass the entire brain. Another consequence of this is that each whole-brain state may only have a single frequency signature, meaning cross-frequency interactions are

difficult to study. Univariate HMMs are generally more flexible as the states inferred in each channel/region may have entirely different dynamics and spectral signatures, although grouping states across regions can be challenging as the states arise from independent models. The choice of HMM, univariate or multivariate, should depend upon the research goal.

The final consideration for configuring the model is the number of states. This must be chosen *a priori* and cannot be learned from the data. The model is able to discard states if they model too little of the data, however, over-fitting is still an issue, and so the number of states must be chosen carefully. A sensible approach is to guide the number of states by the particular phenomenon being studied. For example, if the goal is to study functional network dynamics, the number of states should be limited to the number of large-scale networks that can be feasibly measured with the spatial resolution of MEG (Brookes et al., 2011c), around 10 or fewer. On the other hand, if the goal is to identify spectral bursting events (Rier et al., 2021, Seedat et al., 2020) in single-region data, much fewer states may be needed, as the lower amplitude data is of little interest and can be grouped together into a non-bursting state without impeding the research goal.

We chose to run a separate time-delay embedded HMM on each brain region to allow for region-wise comparison of PTRs, whilst not constraining PTRs to have similar spectral profiles over the whole head or be implicitly part of a functional network, as would be the assumption in a multivariate time-delay embedded HMM. The time-window specified in this study was 230 ms to encompass activity in the canonical frequency bands (Seedat et al., 2020). For both datasets used, we inferred HMMs with three states as we expected: one state to capture PTRs, i.e., high amplitude induced spectral activity; one state to capture other activity that may occur during the task, e.g. evoked responses relating to stimulus processing which are unlikely to hold similar spectral content to PTRs; one state to satisfy the continuity requirement, i.e., a state that becomes active when brain activity encompassed by the other states is *not* happening.

6.5 Methods

6.5.1 Paradigms

Two datasets were analysed, both containing PTRs that modulate with task parameters. The first was the n-back task from the previous chapter, which incorporates elements of working memory, where PTRs modulated with working

memory load (greater PTR amplitude with greater working memory load). The second was a grip-force visuomotor task, previously published by (Pakenham et al., 2020), where PTRs modulated with grip duration (greater PTR amplitude with shorter grip duration).

The n-back task was explained in detail in the previous chapter and is illustrated in Figure 6.1 (A-C). Briefly, during a single 30 s task period of the n-back task, participants were presented with a series of 15 letters, each for 1 s, separated by a 1 s interstimulus interval. Participants were instructed to press a button with their right index finger when a target letter was shown. A target letter was either the letter “x” (0-back), the same as the previous letter (1-back), or the same as the letter before the previous letter (2-back). The three conditions, 0-back, 1-back and 2-back, varied in working memory load, with 2-back being the most demanding. Each task period was preceded by an instruction screen stating the task condition. Task periods were separated by 30 s rest periods. The instruction screen, task period and rest period made up a single experimental block lasting 62 s. Participants completed 16 blocks of each task condition, separated over 2 runs, with conditions arranged in a pseudo-random order.

The grip-force visuomotor task was explained in detail in (Pakenham et al., 2020) and is illustrated in Figure 6.1 (D, E). It required participants to maintain 30% of their maximum voluntary force for either 2 s, 5 s or 10 s. Participants applied this force to a grip bar, attached to the right hand with a glove (to allow the hand to fully relax during rest periods without dropping the bar). Participants were presented with a visual stimulus comprising a target force profile, which appeared 2 s before task onset. During the task, actual force output was plotted over the target profile, giving the participants visual feedback on their performance. Each task period was followed by 30 s rest. During the last 2 s of rest, the target profile for the next task period was shown. The task period and rest period make up a single experimental block. Participants completed 15 blocks of each duration per run, arranged in a pseudo-random order, for two runs.

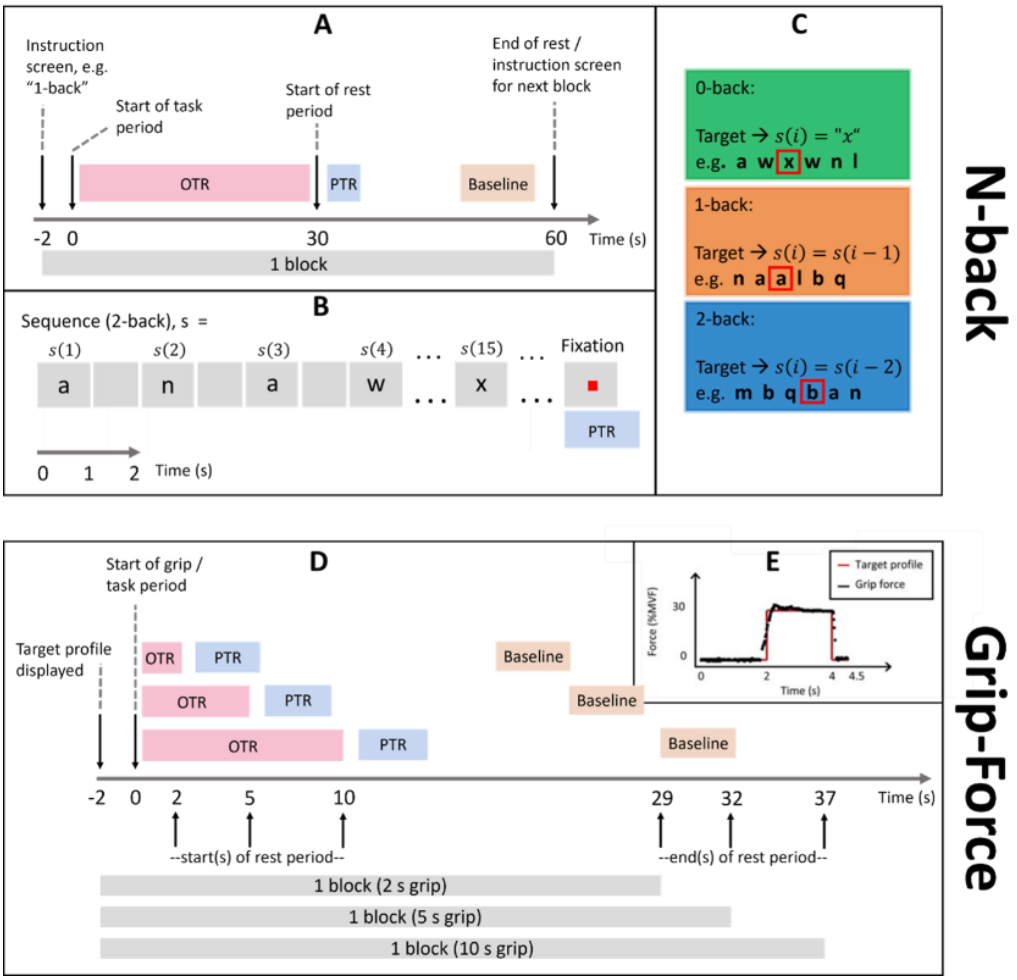


***Figure 6.4**: A schematic summary of the paradigms employed for the two datasets used in this study. The top panel (A-C) shows the n-back task with 0-back, 1-back and 2-back conditions. Panel D shows the grip-force task timings, with 2 s, 5 s and 10 s grip durations, while panel E shows an example of the target profile and visual feedback presented to the participant. Both tasks had 30 s rest periods following each task period to facilitate the study of PTRs. In these figures, the oscillatory task response (OTR) is defined as the oscillatory modulations measured during stimulus/task whilst post task response (PTR) is the oscillatory modulations measured immediately following stimulus/task cessation, defined as 0 – 7 s after task cessation for the n-back task, 2 – 6 s after task cessation for the grip-force task.*

6.5.2 Data Acquisition

20 healthy volunteers (10 female, aged 26 ± 4 (mean ± SD) years) took part in the n-back study, and 15 healthy volunteers (10 female, aged 27 ± 3 (mean ± SD) years) took part in the grip-force study, which were both approved by the University of Nottingham Medical School Research Ethics Committee and, where relevant, in compliance with all COVID-19 standard operating procedures. All volunteers gave written, informed consent.

All data were collected at a sampling rate of 600 Hz using a 275-channel CTF MEG system (MISL, Coquitlam, BC, Canada) in third order gradiometer configuration. Head localisation coils were attached to the participants' nasion and preauricular points prior to recording to provide fiducial markers for head localisation. The coils were energised before the start and after the end of each recording to enable co-registration (see Chapter 3.1.6) and provide a measure of overall head movement. The participants were scanned in a seated position for the n-back task, and supine for the grip-force task, viewing a projector screen that displayed the stimuli. An eye tracker (EyeLink, Ottawa, Canada) was used during the n-back task to monitor the participants to ensure they remained awake throughout.

For the n-back task, a 3D digital mesh of the head and fiducial coils was acquired using a Skanect structure sensor (Occipital, Colorado, USA). For the grip-force task the 3D digitisation was performed using a Polhemus system (Polhemus, Colchester, VT, USA). The digitised head surface and fiducial locations were then co-registered with the individual participant's anatomical MRI (T_1-weighted MPRAGE sequence acquired on either a 3T or 7T MRI scanner) to allow the position of the sensors relative to the brain to be determined.

6.5.3 Pre-Processing

For the n-back task, pre-processing was identical to the steps outlined in Chapter 5.

Pre-processing for the grip-force dataset followed a similar procedure with the additional analysis of electromyography data to define accurately the onset and offset of each grip period. For details, refer to (Pakenham et al., 2020). In this task 14 participants remained for further analysis after the pre-processing.

On average, 46 ± 1 (mean 0-back: 15, mean 1-back: 15, mean 2-back: 15) blocks per participant remained in the n-back dataset after removal of bad/noisy trials, while 75 ± 3 (mean 2 s: 25, mean 5 s: 25, mean 10 s: 24) blocks remained in the grip-force dataset. Inverse solutions were calculated for all data using a linearly constrained minimum variance beamformer (see Chapter 3), using the covariance of the entire participant dataset filtered into broadband (1 – 150 Hz) and a multiple-spheres headmodel.

6.5.4 Parcellation Beamformer

Using the beamformer weights, timecourses were extracted from the centroids of 78 parcellated regions in the automated anatomical labelling (AAL) atlas (Tzourio-Mazoyer et al., 2002), with subcortical regions removed (Hillebrand et al., 2016). This

atlas was constructed manually on a high resolution, T1 weighted anatomical MRI of a single subject, identifying a set of anatomical features such as *gyri* (convex part of fold) and *sulci* (concave part of fold), before being transformed to the MNI-152 brain (Mazziotta et al., 2001). It should be noted that, although this parcellation has been used in a number of MEG functional connectivity studies (Tewarie et al., 2019, Brookes et al., 2016, Seedat et al., 2020), regions are defined by anatomical features rather than function (see Chapter 2). We can therefore assume that functional domains may span several AAL regions, or conversely, more than one functional domain may occupy a single AAL region. The effects of source leakage between reconstructed MEG data in the AAL parcellation were mitigated using symmetric orthogonalization, described in Chapter 3.2.4.

6.5.5 Hidden Markov Modelling

As described in section 6.4.4, we chose to run separate time-delay embedded HMMs on each region in the AAL parcellation, with a time-delay of 230 ms and three states per region. Before HMM inference, the unfiltered source-space data were downsampled from 600 Hz to 100 Hz to reduce computational expense whilst retaining information in the relevant frequency bands (4 – 30 Hz, including theta, alpha and beta bands). For each brain region in turn, data were concatenated across all participants, as well as conditions, so that a single HMM could be applied per brain region, which improves the robustness of the HMM (Seedat et al., 2020) and provides a unified description of the dynamics for each brain region. Z-scoring was applied to the concatenated data to reduce variance between participants in the sequence. For each brain region, the posterior probabilities for each state were thresholded at 2/3 (Seedat et al., 2020) to produce three binary timecourses, each showing when states are “on” and “off”. Power spectral density (PSD) profiles were extracted from the model for each state.

6.5.6 The PTR State

To study single-trial events which lead to PTRs, we first needed to identify an HMM state which captured this activity, which we call the *PTR state*. Despite this naming, we are not suggesting that this state will *only* capture PTRs. Following evidence from previous studies (Seedat et al., 2020, Rier et al., 2021), it is likely that what we are capturing is short-lived, high amplitude oscillatory events, or *bursts*. In the case of sensorimotor beta activity, these events are also known to drive the MRBD (ERD during stimulus) by reducing in probability. We therefore do not assume that PTRs are the only phase of activity captured by the PTR state, generated by oscillatory bursts.

6.5.7 State Grouping with K-Means Clustering

As a univariate HMM was inferred in each brain region separately, the order of inferred states was not consistent between regions. To group PTR states across the brain, we used k-means clustering, which groups univariate HMM states across regions based on temporal similarity over the entire scan. We make the assumption that high amplitude oscillatory events (bursts) across the cortex should be more temporally related than lower amplitude events and noise if these are driving the measured time-frequency response to the tasks (ERD/ERS during task and post-task periods). This assumption is supported by findings of Seedat *et al*, who showed that the MEG functional connectome is driven by the burst state (Seedat et al., 2020).

Our application of k-means clustering partitions a matrix of 234 binary state timecourses ([78 regions * 3 states] * number of timepoints) into *k* optimal clusters by minimising the sum of squared Euclidian distances between state timecourses within each cluster. The number of clusters was chosen to be three, as this is the minimum number of clusters required to assign the three HMM states per region to separate clusters. There are several methods of optimising the number of clusters to properly reflect the dynamics of the underlying system, however, given we were only concerned with the state that captured PTR activity, it served no purpose to infer more clusters than the number of HMM states. A simulation of this process is described in the following section. Once clusters were identified in the HMM state timecourses, the cluster centroid (average of cluster timecourses) which resembled the trial-averaged timecourses in Chapter 5 and (Pakenham et al., 2020) was taken as the PTR state cluster.

6.5.8 Temporal K-Means Clustering Simulation

Our approach to state grouping used k-means clustering in a high dimensionality space. Each timepoint corresponded to a separate axis, such that a single point in the high dimensional space represents the entire time evolution of an HMM state, and therefore temporally similar states are nearby in this clustering space. The algorithm is as follows:

1. The system is initialised with *k* random cluster centroids, each a single point in the clustering space.
2. Each datapoint is assigned to the closest centroid based on Euclidian distance.
3. New cluster centroids are defined which minimise the within-cluster variance, measured as the sum of squared Euclidian distances within-cluster.

4. Points are then re-assigned based on the Euclidian distance to the new cluster centroids.
5. The process is repeated until the clusters become optimised (minimal centroid adjustment with new iterations).

We tested this method using a set of simulated timecourses to ensure that the clusters were meaningful, given the high dimensionality of the clustering space. A set of three ground-truth cluster centroids were simulated using random binary timecourses, each comprising 1000 timepoints (leading to 1000 axes in the clustering space). These were replicated 50 times each, to create three ground-truth clusters of 50 timecourses, where cluster members were identical to their respective cluster centroid. Next, a varying amount of noise was added to each cluster by setting a switching probability (%), which dictated the chance of each timepoint switching value (0 to 1, or 1 to 0). Given that the timecourses were binary, a switching probability of 50% corresponds to complete randomisation of the timecourse (100% noise). Switching probability values tested were 10%, 20%, 30% and 40%. Following the addition of noise (through different switching probabilities), the k-means clustering algorithm was applied to the set of simulated timecourses, and the cluster assignment values were imaged next to the matrix of timecourses to show the clustering accuracy.

As shown in Figure 6.5, we see that timecourses with similar temporal features are clustered effectively until the noise level gets too high (80% noise), at which point the clusters become too poorly defined to reflect the ground truth assignments. This is sufficient in proving that the clustering algorithm is robust in high dimensionality space with binary timecourses.

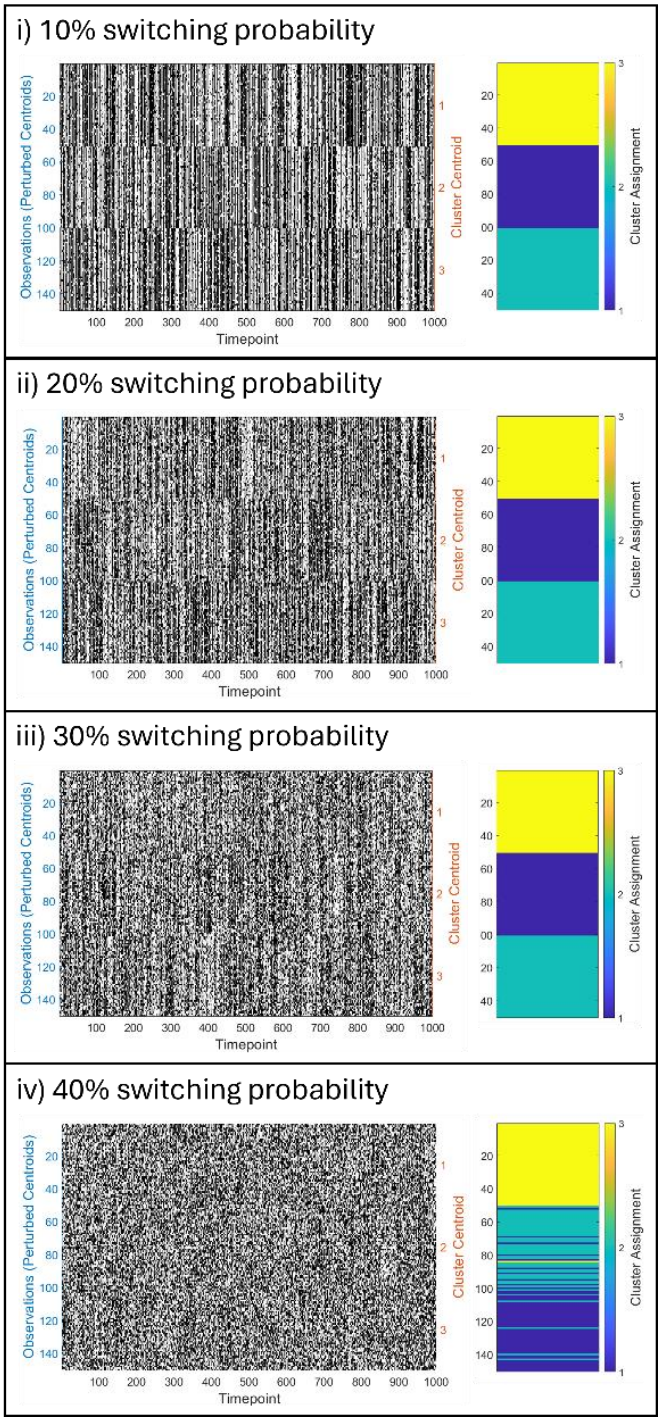


***Figure 6.5**: A simulation demonstrating the ability of the k-means clustering algorithm to group HMM states based on temporal similarity. The matrix on the left of each panel contains three simulated clusters of binary HMM state timecourses, with an amount of noise denoted by the switching probability (% chance for each timepoint to switch value, independently). The result of applying k-means clustering to each matrix is shown by the vector on the right of each panel. For 10%, 20% and 30% switching probability, every single timecourse was assigned correctly. Clustering accuracy broke down at 40%, which is close to complete randomisation of the timecourses (which occurs at 50%). These results show that the k-means clustering approach to grouping HMM state timecourses is robust even when there is a substantial amount of noise present.*

6.5.9 State Probability

After the PTR state was identified for each task from the three whole-brain state clusters, PTR state probability over a single trial/block period was calculated by averaging binary timecourses over all trials/blocks. This was then converted to a percentage change relative to baseline, where the baseline was taken as 40 – 50 s for the n-back task and 18 – 28 s for the grip-force task. The mean relative change during the PTR period[2], taken as 31 – 35 s (2-back condition) for the n-back task and 4 – 8 s (2 s task condition) for the grip-force task, was plotted as a colourmap on a brain to display the regional variation of PTR activity within the whole-brain PTR state. Only the 2-back (n-back) and 2 s (grip-force) conditions were used here as these had the highest amplitude PTRs.

6.5.10 Burst Characteristics

Several measures were taken from the PTR state in each task to determine whether the state represented similar spectral bursting in each case. Firstly, state timings were compared visually to the MEG time-frequency response (TFR) for single data segments lasting 5 s, positioned immediately post-task (when PTRs occur). From these, we were able to visually inspect the events in the MEG data that were encompassed in the HMM PTR state.

The next measure taken from the PTR states across the brain was spectral content. A power-spectral density (PSD) distribution was obtained for the PTR state at each region using the multitaper method (Thomson, 1982). These were clustered using k-means clustering, as described in section 6.5.7-6.5.8, such that PSD curves with similar morphology are clustered – as the purpose of this was simply to visually separate the PSDs, the number of clusters was optimised manually for the best visualisation, set to 6 clusters for both tasks. In addition, using the PSD of the PTR state for each region, we took the power (area under the curve) within three canonical frequency bands: theta (4 – 8 Hz), alpha (8 – 13 Hz) and beta (13 – 30 Hz), to get region-wise spectral content of the PTR state at each AAL region. These power values were plotted on a brain as a colourmap to show the spectral distribution of PTR activity across the brain. We quantitatively compared the spectral content variation across regions between the two tasks using Pearson's correlations.

Next, state lifetimes, equivalent to burst durations, were taken from PTR states in all AAL regions. These were averaged over all participants per region and displayed as a

[2] Compared to Chapter 5, we use a longer PTR period here so that more burst events are contained within the time-window.

colourmap over the brain to compare bursts that drive PTRs in different brain regions. They were also averaged over all regions for each participant to compare variation of average burst duration between the two tasks. Burst durations per region were then compared across tasks using linear regression, akin to the spectral content analyses. Together the spectral content and state lifetimes were used to assess whether PTRs following visuomotor and working memory tasks are driven by bursts with similar intrinsic properties, despite being induced by different tasks.

6.5.11 Burst Connectivity

The connectivity of bursts (captured by the PTR state) was analysed in two different ways:

1) **The Jaccard Index**: This approach has been used in previous studies (Seedat et al., 2020, Rier et al., 2021), it measures the temporal overlap of pairs of binary timecourses, written as

$$J(A,B) = \frac{|A \cap B|}{|A \cup B|}, \tag{6.11}$$

   Where the numerator is the *intersection* of set A and set B, i.e., the number of coincident burst timepoints, and the denominator is the *union* of set A and set B, i.e., the total number of timepoints in the two sets.

2) **Spatial K-Means Clustering**: As with the state grouping approach, we separate the data into *k* clusters by minimising the within-cluster variance based on Euclidian distance. However, this time we find *spatial* clusters that recur in time. An axis in the clustering space represents an AAL region (78 axes), and a single point in the clustering space represents the spatial map at a particular timepoint. Timepoints with similar spatial maps will be more readily clustered. The cluster centroids are the average of the spatial maps at all of the clustered timepoints. A schematic of this process is shown in Figure 6.6. Note that this approach is similar to EEG microstate analysis (Michel and Koenig, 2018), but works on binary timecourses rather than continuous data. The number of clusters is chosen *a priori*, which can alter the results, however, it was found from testing that several robust patterns emerged which remained throughout increasing the number of clusters. We therefore set the number of clusters to six for each task, which was sufficient to demonstrate PTR-related features.

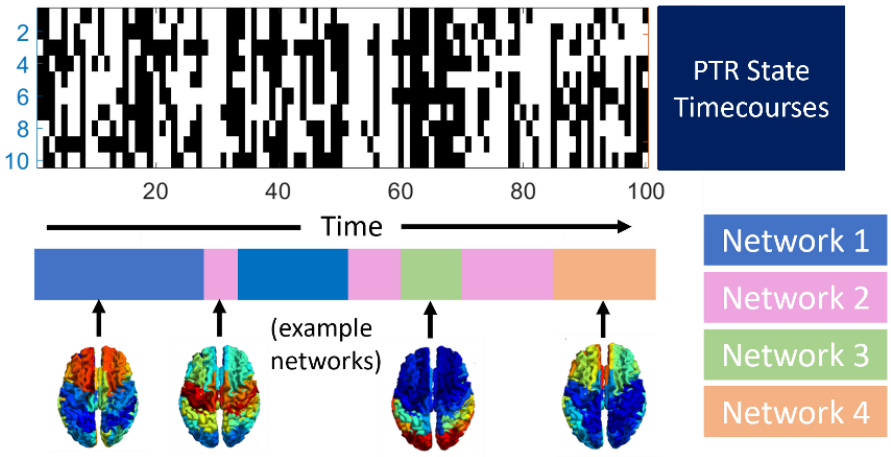


***Figure 6.6**: A schematic of the spatial k-means clustering approach to finding functional connectivity of the PTR state. Clusters are optimised by minimising the within-cluster Euclidian distance between spatial maps. The result is a set of clusters representing the most recurrent functional networks.*

6.5.12 Correlating State Probability with Behaviour

In principle, by capturing activity that drives PTRs, we are isolating the brain signals of interest, separating them from the total MEG signal which contains other neuronal, physiological and environmental signals. This means that correlations between MEG signals and behaviour should be strengthened when using HMM state timecourses as opposed to frequency filtered MEG data from the same region. We tested this by repeating correlations reported in Chapter 5 between oscillatory modulation and RT, for the n-back dataset. Here, as previously, we correlated modulation in PTR state probability with RT modulations, taking the subtraction of 2-back and 1-back. We restrict our analysis to anatomical areas that were examined in the initial analysis – frontal, left parietal, left lateral visual, and the dorsal attention network (DAN), although these were approximated using AAL regions as opposed to taking voxels of peak activity. The correlations between PTR state probability and behaviour were obtained using a Pearson's correlation, and Bonferroni correction was applied to adjust corresponding p values for multiple comparisons.

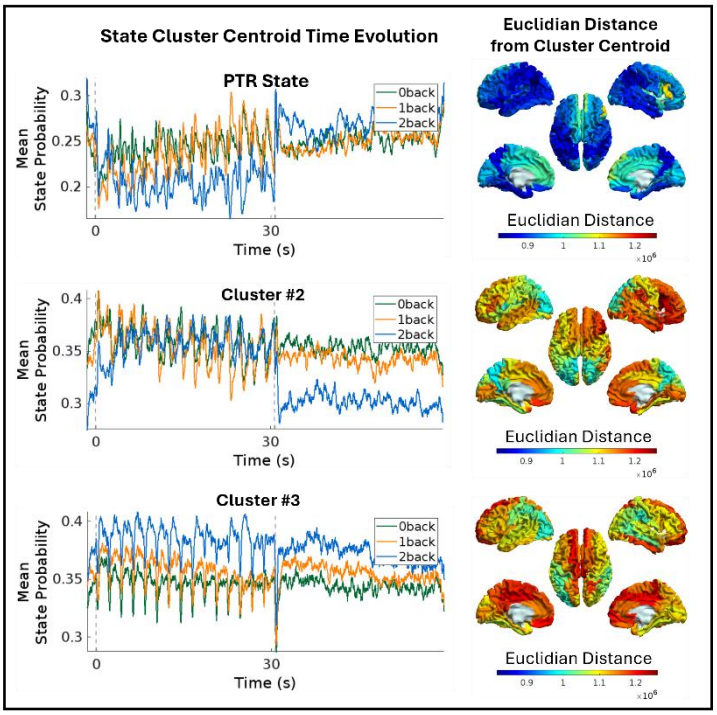
6.6 Results

6.6.1 PTR State Grouping

The HMM successfully modelled activity that drives PTRs in both datasets. The results of applying k-means clustering to group HMM states across anatomical regions are shown in Figure 6.7. This figure shows the cluster centroid timecourses (average timecourse within a cluster across regions, averaged over trials), as well as the Euclidian distances (corresponding to temporal similarity) of each region from the

cluster centroid. The PTR state, visible by the rise in power above baseline after task cessation, is the most well-defined cluster, shown by lower Euclidian distances across all regions compared with the other clusters.

A) N-back



B) Grip-Force

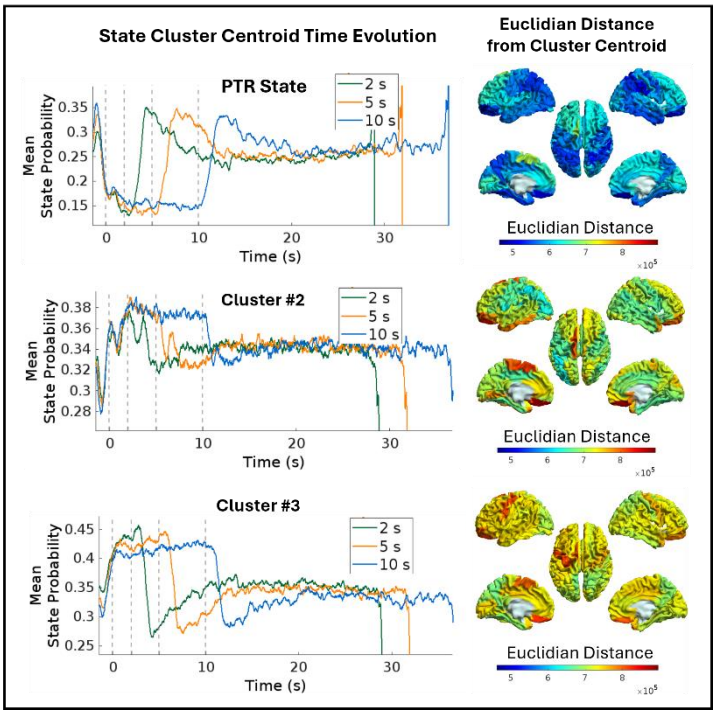


***Figure 6.7**: The result of grouping PTR states across the brain using k-means clustering for the n-back (A) and grip-force (B) task. States are grouped based on temporal similarity of state visits over the entire scan period across all participants. The PTR state is labelled for each task, with each showing a rise in probability above baseline levels after task cessation. The PTR cluster also has the lowest mean Euclidian distance in both datasets, showing that this is the best quality cluster in both cases. Legends in each panel show the three different conditions for each task.*

6.6.2 PTR State Probability

PTR state probability, relative to baseline, during the PTR period, is shown below in brain plots in Figure 6.8. In both datasets, there is strong lateralisation, with PTRs becoming notable on the left-hand side of the brain. Exemplar regions have been plotted, for the 2-back and 2 s conditions only as these had the highest amplitude PTRs. It should be noted that the seemingly negative PTRs on most of the right-hand side of the brain for the n-back task are better described as a slow return to baseline levels of bursting.

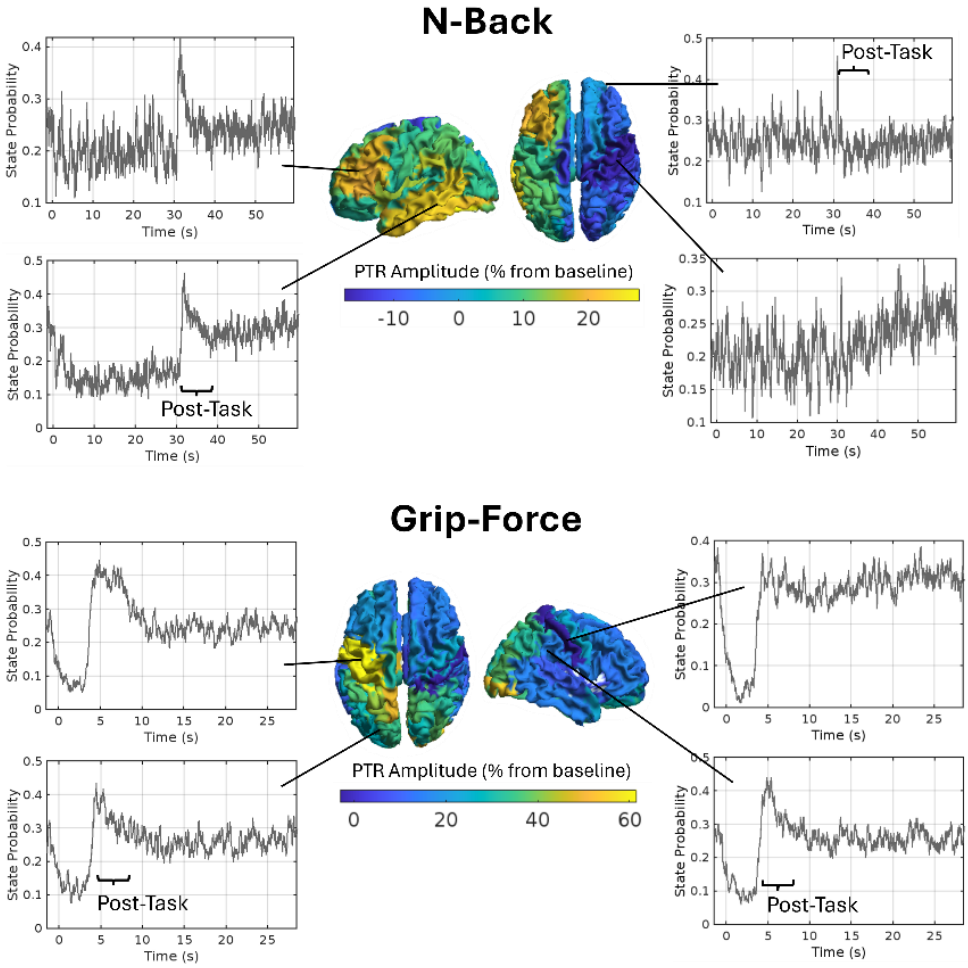


***Figure 6.8**: The brain plots in the centre show PTR amplitudes over the whole head as fractional change of the average PTR response (measured as 31 – 35 s for the n-back task and 4 – 8 s in the grip-force task, for the 2-back and 2 s conditions) relative to baseline (40 – 50 s for the n-back task, and 18 – 28 s for the grip-force task). Group level state probability timecourses are then displayed for regions exhibiting large and small PTRs.*

6.6.3 Single-Trial State Activity

So far, it is clear that the HMM has captured activity which is driving PTRs, grouped across the brain using k-means clustering. Figure 6.9 allows us to see this activity on the single-trial level (trials selected at random), showing a visual comparison between PTR state events, filtered MEG timecourses, and MEG time-frequency response (absolute power) during a 5 s data segment during some example PTR periods (immediately post-task). Each panel shows two AAL regions as exemplars for each task. In both tasks, the PTR state timing corresponds to short periods of high oscillatory power, which can be described as bursts. These transient periods of high power seem to appear mostly within the alpha band although they are also seen in the theta and beta bands.

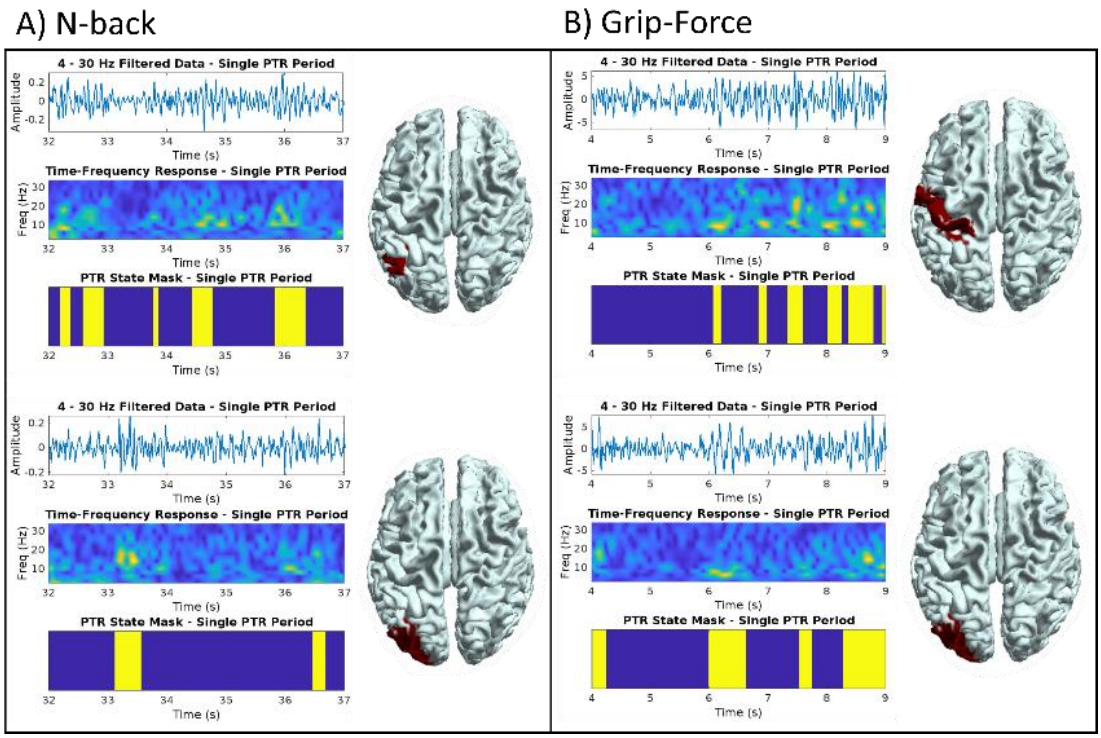


***Figure 6.9**: A qualitative comparison of PTR state events and conventional time-frequency decompositions during example data segments each starting at immediate on task cessation and lasting 5 s, denoted as the PTR period.*

6.6.4 Burst Characteristics

Burst characteristics including duration and spectral content are shown in Figure 6.10 and correlated between tasks. Burst durations were found to be 0.31 ± 0.03 s for the n-back task, and 0.32 ± 0.04 s for the grip-force task (mean over participants ± standard error over participants). Burst durations varied similarly across regions when comparing the two tasks, with $R^2 = 0.56$. The longest durations were seen in the motor

strip, followed by posterior regions, whilst the frontal lobe had notably shorter burst durations in both tasks. When burst durations are normalised to the peak frequency in the same region to get the number of oscillations per burst, the two tasks are almost perfectly correlated, with $R^2 = 0.94$, suggesting a fundamental oscillation stability which depends on emitting region (See top row of Figure 6.10).

Spectral power of the PTR state is shown in theta, alpha and beta bands in the bottom panel of Figure 6.10. This shows that for these two different tasks, the PTR state has the same spectral peak spatial location in each frequency band (theta: temporal, inferior parietal; alpha: visual; beta: sensorimotor), despite variation in relative power across the two tasks. Alpha and beta power are strongly correlated between tasks. Theta power shows more variation between tasks, which is likely due to the fact that regions associated with theta oscillations (inferior parietal, temporal, frontal pole; all associated with the DMN) are more strongly modulated by an n-back task than a grip-force task, whereas alpha and beta emitting regions (visual and motor) were recruited for both tasks more equally due to the shared visuomotor elements.

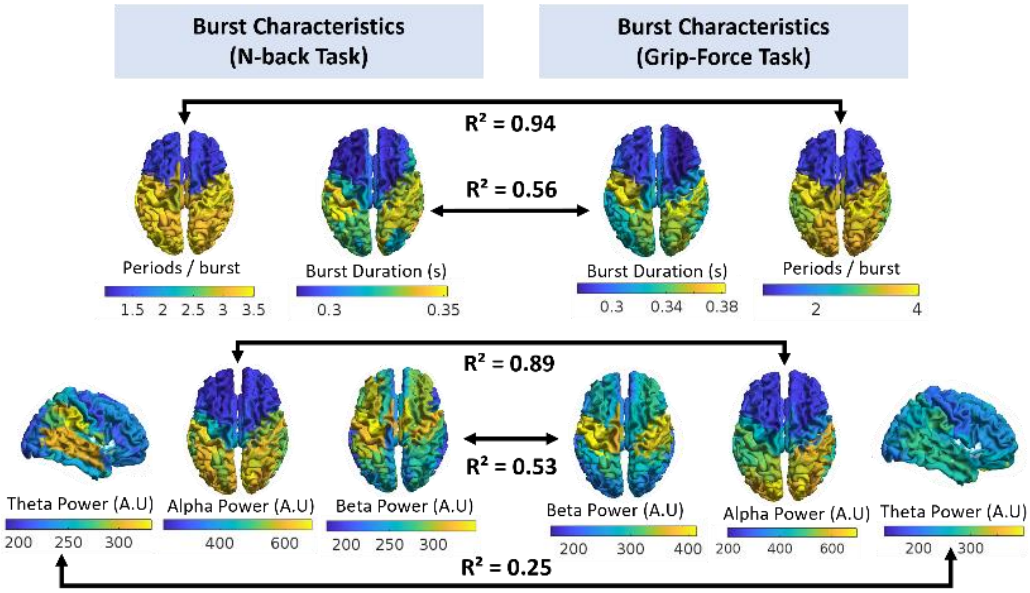


***Figure 6.10**: PTR state burst characteristics for the n-back task (left panel) and grip-force task (right panel). The upper row shows burst durations across the cortex and the number of oscillations per burst (i.e. the burst duration normalised by the peak spectral frequency in the same region). The number of oscillations per burst is almost perfectly correlated between tasks. The lower row shows theta, alpha and beta activity in the PTR state for the n-back and grip-force tasks, distributed over the brain. The two tasks showed high similarity in alpha and beta content across the cortex, whereas theta clearly deviates in relative power between the two tasks.*

Spectral content of bursts is explored further in Figure 6.11, which shows individual PTR state PSDs, clustered into six groups for each task to aid in visualisation. Clearly, bursts that constitute effects such as the PTR occur with distinct frequency profiles depending on the emitting region or network. As would be expected, frontal regions have a more theta dominant profile, sensorimotor regions have relatively greater beta peaks, and alpha, while dominating all PSDs in absolute amplitude, is most prevalent in visual and sensorimotor regions.

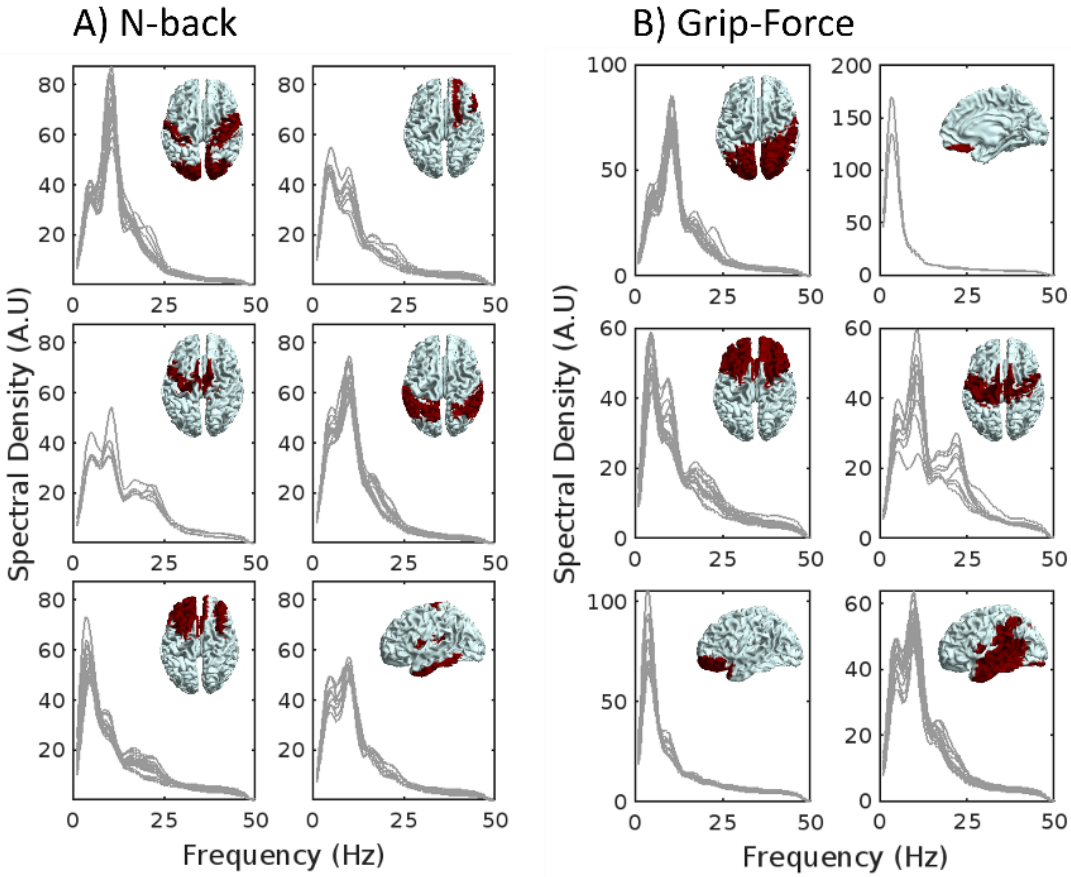


***Figure 6.11**: Individual PSD curves for PTR states across the cortex, clustered into six groups to aid visualisation of spatial patterns of these spectral responses.*

6.6.5 Connectivity

The change in Jaccard index measure of connectivity between the PTR time window and the during-task time window is shown in Figure 6.12. For both tasks, connectivity generally increases during the PTR. For the n-back task, frontal, temporal and inferior parietal regions see the greatest change in connectivity during the PTR as to the task window, with a bias to the left-hand side of the brain. For the grip-force task, bilateral visual, parietal, and left motor regions see the greatest change in connectivity between

PTR and task windows. These results reflect networks known to be modulated by each task.

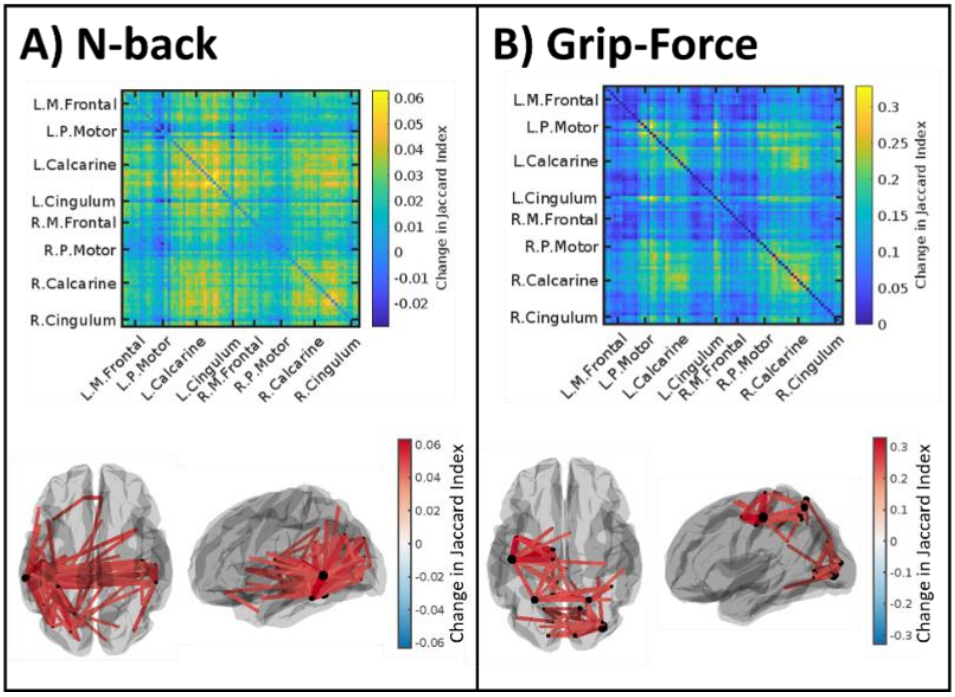


***Figure 6.12**: Functional connectivity, as measured with Jaccard index, representing changes in coincident bursting when moving from the task time window (n-back: 0.5 – 29.5 s, grip-force: -1s – 3s relative to grip start) to the post-task time window (n-back: 30 – 37 s, grip-force: 2s – 6s after grip cessation) for the n-back (A) and grip-force (B) tasks. The top 30% of values in the connectivity matrices are displayed in the glass brain plots.*

We also perform a network decomposition using k-means clustering, shown below in Figure 6.13 for the n-back task, and Figure 6.14 for the grip-force task. Here, the brain colourmaps in panel A show the probability of coincident bursting during the clustered timepoints, while the sum of squared Euclidian distances shows how similar the spatial map is across clustered timepoints, i.e., within-network connectivity. The clusters are ordered to reflect within-network connectivity, such that cluster 1 is the most connected. Networks have been named based on the regions which contribute the most to each network. The least-connected network (most poorly defined cluster) is named “local bursting” as there is very low probability of coincidence across broader regions of the brain, which implies that oscillatory events are occurring on a more local scale. The PSD plots in panel B are the average PSDs of PTR states weighted by the within-cluster coincidence probability. The cluster probability plots in panel C show the average probability of the network appearing over a task block. The plots in panel D show the cluster probability of the networks which capture most of the PTR activity.

The spatial network brain plots with full dynamic range are shown in the Appendix (Fig. A6.1), providing a clearer image of the main contributors to each network.

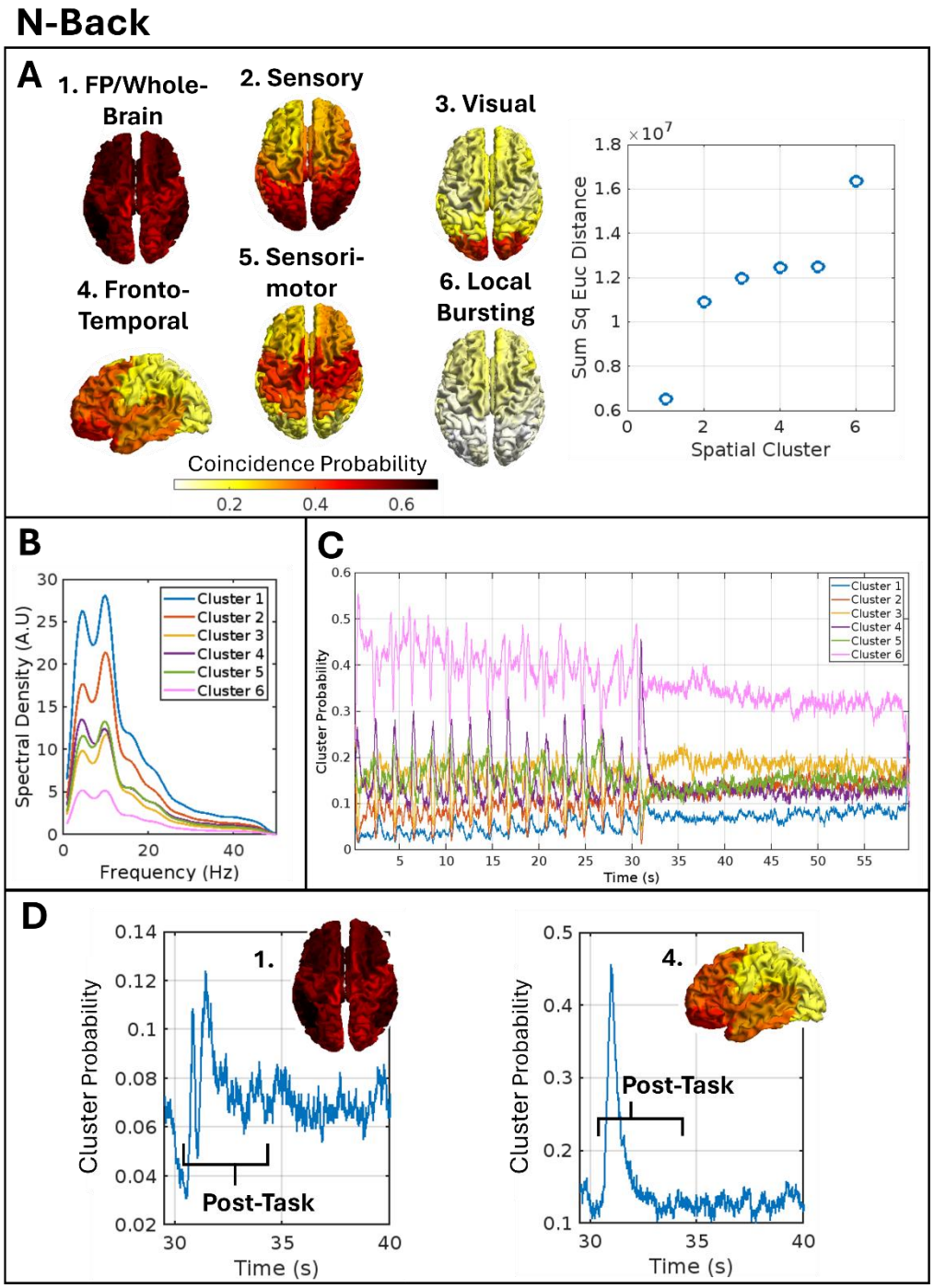


***Figure 6.13**: Network decomposition of the PTR state for the n-back task using k-means clustering. Six networks are shown in panel A in order of within-cluster connectivity, which is also plotted in panel A, measured using the sum of squared Euclidian distance from the cluster centroid. Panel B shows frequency spectra (average of state PSDs weighted by contribution to the cluster). Panel C shows cluster probability (average time spent in a particular network) for all spatial clusters. Panel D shows the post-task segment of cluster probability for spatial clusters that exhibit clear PTR activity.*

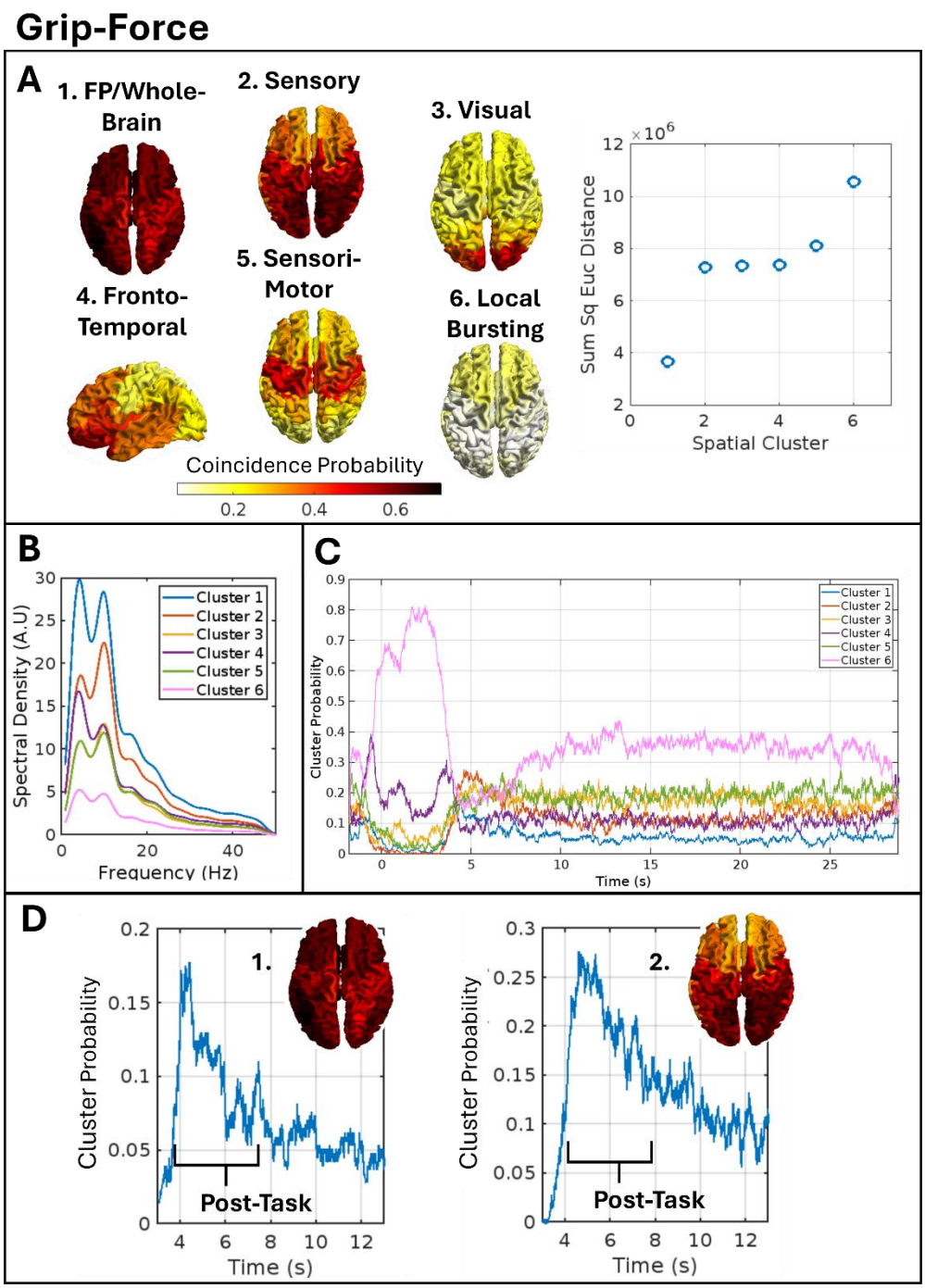


***Figure 6.14**: Network decomposition of the PTR state for the grip-force task using k-means clustering. Six networks are shown in panel A in order of within-cluster connectivity, which is also plotted in panel A, measured using the sum of squared Euclidian distance from the cluster centroid. Panel B shows frequency spectra (average of state PSDs weighted by contribution to the cluster). Panel C shows cluster probability (average time spent in a particular network) for all spatial clusters. Panel D shows the post-task segment of cluster probability for spatial clusters that exhibit clear PTR activity.*

6.6.6 Relating PTRs to Behaviour

Given that the HMM successfully captured high amplitude burst events from the data, the effects of neuronal and physiological signals as well as noise should be reduced in the PTR state. Here, we show that correlations with behaviour are improved by using HMM state burst probability rather than frequency filtered power envelopes. Figure 6.15 A-D shows correlations between PTR state relative probability amplitudes during the PTR period (31 – 35 s) and reaction times, while Figure 6.15 E-H shows the correlations between traditional MEG power envelopes and reaction times, shown earlier in Chapter 5 with the addition of the left DAN. Here we used the HMM PTR state in AAL centroids rather than the MEG power envelopes from peak pseudo-T statistic locations in anatomical regions (shown in Fig. 6.15 E-H). Correlations improved dramatically when using the HMM state rather than the MEG power envelope for all four regions/networks.

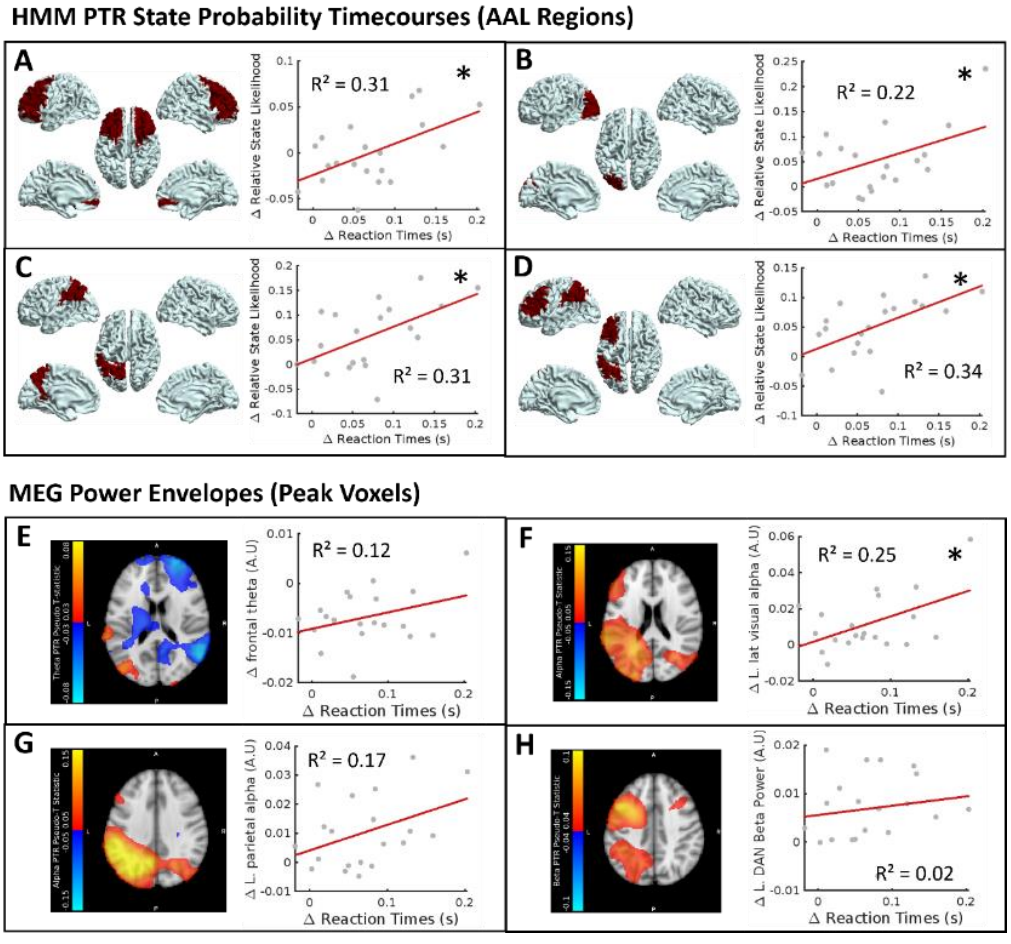


***Figure 6.15**: Panels A-D show correlations between PTR amplitudes in the PTR HMM state, and reaction times, for the n-back task only. Here we use PTR state probability at the centroids of AAL regions, while panels E-H show correlations between MEG power envelopes from locations of peak pseudo T-statistic in specific frequency bands and reaction times, adapted from Chapter 5. * denotes a significant correlation ($p < 0.05$, Pearson's correlation).*

6.7 Discussion

Given the neuroscientific and clinical relevance of the PMBR and beta bursting (Gascoyne et al., 2021, Gaetz et al., 2020, Little et al., 2019, Seedat et al., 2020, Sherman et al., 2016, Briley et al., 2021), it is important that we unify our knowledge of PMBRs with PTRs that occur outside of the motor cortex following higher cognition, which we reported in the Chapter 5. This study takes important steps towards this goal, demonstrating that PTRs following visuomotor and working memory tasks are both explained by the timing of transient high amplitude events in oscillatory MEG data (Fig. 6.9) with similar intrinsic characteristics (Fig. 6.10). We show that PTRs across both tasks are captured by a distinct HMM state, found by running single-region (univariate) HMMs and grouping across regions using k-means clustering (Fig. 6.5, Fig. 6.7). PTR states across both tasks are primarily in the alpha frequency band (Fig. 6.9, Fig. 6.11), with similar lifetimes over participants and regions (Fig. 6.10). In addition, we show that spatial networks are formed by coincidence of oscillatory bursts, with similar structure across the two tasks (Figs. 6.13, 6.14), although the networks that are occupied during the PTR period varies between tasks (panel D of Figs. 6.13, 6.14). Finally, we demonstrated the denoising effects of univariate HMMs on MEG data, showing that PTRs in HMM state timecourses have stronger correlations with reaction times than MEG power envelopes (Fig. 6.15).

6.7.1 The PTR State Captures Transient Oscillatory Bursts

Recent studies have shown that the PMBR, i.e., the post-task ERS in the beta-band in the motor cortex, is explained by changes in timing of transient high amplitude oscillatory events, often referred to as bursts (Brady et al., 2020, Pakenham et al., 2020, Seedat et al., 2020). Interest in bursting is on the rise, with studies attempting to use burst characteristics (such as timing and burst rate) as correlates of behaviour (Little et al., 2019) or pathology (Briley et al., 2021, Tinkhauser et al., 2017a, Tinkhauser et al., 2017b). Some studies have reported burst-like behaviour in alpha (Jaffe and Weiss, 1966) and theta (Hebert and Lehmann, 1977), although these lasted longer (3 – 4 s) than the alpha/theta range oscillatory events that we report (Fig. 6.10), and were considered separate from regular oscillatory activity in the same frequency range. Overall, research into the utility of bursting models for theta and alpha band oscillations is lacking. Our results in Figure 6.9 show that the PTR state cluster corresponds to moments of high amplitude activity, in theta, alpha and beta bands, while our results in Figure 6.10 show that these events are made up of around 1 – 4 oscillations, with variation in burst duration depending on the emitting region. These

burst events make up the induced (see Chapter 2) signals that are observed in trial averaged MEG data, typically referred to as ERD or ERS (Fig. 6.8 and Figs. 5.4, 5.5).

In the motor cortex, the region most rigorously investigated with regards to bursting behaviour, we observe the longest duration of bursts which were 340 ± 20 ms and 390 ± 20 ms (mean ± standard error across subjects) for the n-back and grip-force tasks, respectively. Previous studies that have used HMMs to identify beta bursting events report burst durations of 300 ms (Seedat et al., 2020) [3 state HMM], 200-500 ms (Quinn et al., 2019) [5 state HMM], and 300-400 ms [inferred from duration peaks, 3 state HMM] (Gascoyne et al., 2021). It is difficult to directly compare these values, however the fact that these values all exist in a similar range suggests a common phenomenon was captured by the chosen HMM state in each case. Interestingly, studies using an amplitude thresholding approach for burst detection generally report shorter burst durations, e.g. 238 ms (Zich et al., 2023), 213 ms (Pauls et al., 2022) and 94.2 ms (Little et al., 2019). This discrepancy is possibly due to the thresholds used to detect the bursts.

Overall, in the context of previous work, we demonstrate that PTRs across the cortex following working memory and movement are well-described by a transient bursting model. As with the PMBR case (Pakenham et al., 2020, Seedat et al., 2020), we see that the sustained (after trial-averaging) induced response, where a smooth increase (ERS) in band-specific power is observed, is explained by an increase in frequency of occurrence of the transient bursts (Fig. 6.8). Prior to this study, to our knowledge, burst analysis has been focused on beta-band responses (Shin et al., 2017, Little et al., 2019), which are usually induced by sensorimotor tasks/stimuli. Our results demonstrate that bursting models may be applicable to all induced responses despite variation in induced frequency response and activated regions.

6.7.2 Grouping Whole-Brain Bursting States

The approach proposed here for mass-univariate (multiple single-region) HMM analysis removed the influence of pre-defined frequency borders. This contrasts previous methods which characterised single-region HMM states by correlating them with frequency filtered power envelopes (Seedat et al., 2020, Rier et al., 2021, Khawaldeh et al., 2022, Gascoyne et al., 2021). Given our results, showing that PTRs across multiple frequency bands are all driven by transient bursting, we suggest that it is highly beneficial for univariate HMM states to be grouped without the constraints of the canonical frequency bands. We propose that k-means clustering (or similar clustering algorithms) to group univariate HMM states may be useful in identifying

induced bursting states across a range of tasks, which makes the assumption that high amplitude oscillatory events should be more correlated across the brain than lower amplitude signals and noise. We also recognise that univariate burst states may be grouped by overall spectral density (integral of PSD curve), as, by definition, bursts are of a higher amplitude than other neuronal signals.

6.7.3 Burst Events across Visuomotor and Working Memory Tasks have Similar Region-Wise Characteristics

To determine whether the PTR state in the visuomotor and working memory datasets was capturing a similar neural phenomenon, burst durations and burst frequency content were compared across tasks. The global average burst duration for the PTR state across all regions, for the two tasks, was 310 ms for n-back and 320 ms for grip-force, within one standard error of each other, which is very similar considering the majority of the participants performing each task were different. Regional variation in burst durations was also very similar between tasks, showing high correlation (R^2 = 0.56, Fig. 6.10, top row), with the longest (motor strip) and shortest (frontal lobe) burst durations occurring in the same locations. Once durations were normalised by peak frequency in the same region, the number of oscillations per burst was almost perfectly correlated between tasks (R^2 = 0.94, Fig. 6.10, top row). It must be noted that the absolute duration values may in part be driven by the number of states in the HMM (Seedat et al., 2020). However, as the same number of states were inferred for each region and task, variation of lifetimes across the cortex should be invariant to this effect, and thus high similarity in cortical variation between tasks (Fig. 6.10) still provides indication that the PTR state in both tasks is capturing similar bursting activity.

Spectral content was also used to assess whether the PTR state across the two tasks was capturing the same transient oscillatory events. As is shown in Figure 6.10, there is a high correlation between tasks in the alpha and beta power measured across regions. Alpha contributions are consistently highest in posterior and central regions, particularly in parietal and visual regions, while beta contributions are greater in sensorimotor regions. This clearly agrees with the known predominant generators of these two oscillatory bands during rest (Clayton et al., 2018, Hindriks et al., 2015, Moran et al., 2019, Barone and Rossiter, 2021). Interestingly, theta contributions are the greatest in temporal, inferior parietal and frontal regions for both tasks but the correlation of the theta power over the whole brain for the two tasks is weak. We suggest this difference in theta response between the tasks may be due to a larger modulation of theta-emitting regions (superficial DMN regions) for the n-back task than the grip-force task. We hypothesize that alpha power shows the highest similarity

across the brain over tasks due to both tasks requiring constant visual processing, thus placing relatively equal load on the visual network across tasks (where alpha is strongest). Beta power shows more variation than alpha power, likely due to higher load on motor regions for the grip-force task, where motor output had to be kept constant, as opposed to the n-back task which only required occasional button pressing based on working memory information. In summary, we suggest that variation in the peak frequency of PTRs does not reflect the function of the response, but simply the networks recruited for the task that are being brought to rest. This result supports previous evidence that frequency of induced response depends on network architecture (Pfurtscheller and Lopes da Silva, 1999, Elul, 1971, Lopes da Silva et al., 1976, Pfurtscheller et al., 2000), as well as evidence that different circuits in the brain have natural frequencies (Rosanova et al., 2009). Our results also corroborate speculation that oscillatory activity in the lower frequency bands (theta, alpha, beta) should not be distinguished in their function, but rather, the circuits in which they are active (Hanslmayr et al., 2016, Griffiths et al., 2019, Gratton, 2018).

Together, the results discussed above provide evidence that PTRs following visuomotor and working memory tasks are driven by bursts with similar characteristics, underpinned by a common neural phenomenon. The specific frequency and duration of the bursts appears to be a reflection of the emitting region, while the *probability* of bursts in a particular region is modulated by the processes required to complete the task.

6.7.4 The Role of Bursts in Cortical Network Formation

The Jaccard index results in Figure 6.12 show the pairs of regions that are altered the most in the PTR compared to the task time window, in terms of connectivity. For the n-back task, connections between left inferior parietal, bilateral temporal and frontal regions increase the most during the PTR – domains which are known to be involved in memory and executive functioning (Curtis, 2006, Jeneson and Squire, 2012), i.e., processes which are required during an n-back task. For the grip-force task, connections between visual and left sensorimotor regions increase the most during the PTR, again reflecting regions which must be recruited for the task. It is interesting that connectivity *increases* in regions that are recruited for a task, in a period of time several seconds *after* cessation of the task. Given the well-studied association between oscillatory rhythms (primarily alpha and beta) and inhibition (Jensen et al., 2002, Tuladhar et al., 2007, Chen et al., 1998, Jensen et al., 2005), as well as the putative relationship between these rhythms and neuronal feedback processes (Halgren et al., 2019, Van Kerkoerle et al., 2014, Buschman and Miller, 2007), the increase in burst

connectivity during the PTR may reflect the propagation of top-down inhibitory signals through intracortical networks, i.e., a dampening of network activity guided by recognition of the end of the task period. The effect of burst connectivity during the PTR on thalamo-cortical pathways cannot be inferred here due to the limited depth sensitivity of MEG (Hillebrand and Barnes, 2002). This can be partially addressed with fMRI, as demonstrated in Chapter 7, using haemodynamics as a proxy of brain function.

The Jaccard index gives a single value of temporal similarity between a pair of regions that is proportional to the total number of coincident bursts (Eq. 6.11), meaning that whole brain connectivity maps tend to be biased towards regions with higher signal (more bursts), and any sub-networks that cohere for shorter periods of time may be overlooked. Our alternative approach, using k-means clustering to group timepoints with similar spatial maps, allows us to see entire network structures (Fig. 6.13, 6.14) which are formed of coincident bursts, rather than a single pairwise value. Following the clustering process, the cluster centroids tell us the probability of coincidence in each brain region. The sum of squared Euclidian distances within-cluster tells us how connected each network is, i.e., how similar a spatial network is over the clustered timepoints, with low values representing higher connectivity. Cluster probability tells us how often each network recurs, and in which time windows of the paradigm. The PSD of each network, calculated by averaging PTR state PSDs weighted by the contribution to the cluster, was included to show that networks are formed from cross-frequency interactions, rather than being confined to regions with a similar spectral output, an implicit assumption of traditional connectivity metrics such as amplitude envelope correlation.

For both tasks we infer a very similar set of canonical functional networks, which are expected based on previous literature (Brookes et al., 2011c). It is likely that the similarity between networks across tasks is due to the long rest periods, meaning that we are, to some degree, detecting resting state network architecture. However, the features and dynamics of these networks in relation to phases of the task may provide useful neuroscientific information. Indeed, for both tasks, we see that PTR activity is captured within the most well-connected network (Fig. 6.13D, 6.14D), which occupies most of the brain, but is strongest in frontal and parietal regions (Fig. A6.1). This network, although the most well-connected (the tightest cluster), is the least probable, shown by cluster probability plots in Figure 6.13C and 6.14C. From this we can say oscillatory bursts are sometimes (5 – 10% of the time during rest) coincident across the majority of the cortex, particularly in frontoparietal regions, and these coincident

events increase in probability (to between 12 – 17% probability) during the PTR compared to the task (0 – 5% probability). This suggests that the PTR is associated with long-range connectivity across the cortex, corroborating previous evidence surrounding the PMBR (Tewarie et al., 2019, Seedat et al., 2020). Specifically, given that these whole-brain coincident burst events are suppressed during both tasks, becoming more probably at rest, but overcompensating during the PTR (Fig. 6.13C, 6.14D, cluster 1 in both cases), we can infer that these events support an idling or internal processing brain state, and the PTR acts to re-establish this state following a task period.

We also see PTR activity captured in another spatial network, which is a fronto-temporal network for the n-back task (Fig. 6.13D), and a parietal-sensory network for the grip-force task (Fig. 6.14D). This additional PTR activity may reflect top-down control of networks that are specific to the task, complementing the Jaccard index results and interpretations. For the PTR-related networks identified during both tasks, we observe a left hemisphere bias with both the Jaccard index method (Fig 6.12) and the k-means networks shown in Fig 6.13D and Fig 6.14D (see also Fig. A6.1). This lateralisation does not seem to appear in the other networks derived using k-means clustering, which is likely because we derived networks based on all data, not just the relevant time windows, meaning that the method will tend to detect networks which spontaneously co-activate at rest as well as during tasks. We can therefore infer that within the networks in 6.13D and Fig 6.14D, there may be some short-lived increase in lateralised connectivity during the PTR despite strong bilateral connections which persist throughout the rest of the data. Temporary increases in left lateralised connectivity are accompanied by increased signal in the left hemisphere during the PTR (Fig. 6.8), which likely arise due to the language processing involved in the n-back task and the right hand used for the grip force task.

The least connected network in both tasks was referred to as “local bursting”, as there was very low chance of coincidence between regions of the cortex during these clustered timepoints. It is natural to draw the conclusion that this cluster is purely a mathematical necessity of the k-means algorithm (requiring all points to be assigned to one of the clusters), providing no additional information about network dynamics. However, it should be noted that we formed this network decomposition out of the HMM state in each region containing high amplitude oscillatory events (which we named the PTR state), i.e., excluding lower amplitude oscillatory events and noise. It therefore may be better to ascribe this cluster to oscillatory events which are asynchronous across regions, i.e., local processes which may not be part of a greater

network. Based on this conclusion, it is interesting to note that the brain spends most of the time in this particular “network” during both task and rest periods (Fig. 6.13C, 6.14C), while the broad network events, including those that contain the PTR (Fig. 6.13D, 6.14D) are much less frequent.

6.7.5 HMMs Isolate Functionally Relevant Features in MEG Data

HMMs should, in principle, isolate activity of interest and remove unwanted signals, which may be other neuronal signals or physiological and environmental noise. If PTRs provide a unique insight into inhibitory brain function, as was hypothesized in Chapter 5, they should relate to behavioural measures of cognitive load such as reaction times. We hypothesized that by selecting a PTR state using HMMs, correlations of the PTR response with behaviour should increase compared with using the frequency filtered power envelopes. Figure 6.15 provides evidence to support our hypothesis, with the goodness of fit (R^2 values) increasing dramatically in left parietal (R^2 = 0.17 to 0.31) and frontal (R^2 = 0.12 to 0.31) regions when moving from frequency filtered power envelopes to HMM PTR state probability. In addition, a strong relationship was found in the left DAN (R^2 = 0.34) which had an R^2 = 0.02 when using oscillatory power in the beta band. Here, we clearly show that PTRs across the brain relate to behavioural measures of cognitive load in the preceding task period, which supports the various models of PTRs relating to inhibitory control (Neuper and Pfurtscheller, 2001, Pfurtscheller et al., 2005, Salmelin et al., 1995, Gaetz et al., 2010, Solis-Escalante et al., 2012, Zhang et al., 2008, Engel and Fries, 2010, Chen et al., 1998, Mullinger et al., 2017), expanded in Chapter 5 to include cross-spectral PTRs following working memory. It should be noted that the correlation between RT and left lateral visual PTRs decreased slightly in the HMM states compared to the power envelope (R^2 = 0.25 to 0.22 p = 0.024 to p = 0.038). This may have occurred because the effective location used when averaging AAL parcels in the HMM timecourse was far away from the point of peak activity. From Chapter 5, this seems likely, as the peak activity overlapped with the temporal lobe. Given the structural (rather than functional) basis of the AAL segmentation, this was hard to replicate without including the full temporal lobe, a region which was not studied in Chapter 5. Overall, this finding supports the hypothesis that spectral bursts, that become more probable in the post-task period, serve an inhibitory function to bring active networks to resting levels of activity, and therefore relate to behavioural markers of cognitive load.

6.7.6 Limitations and Future Work

This project provided important steps to understanding the nature of PTRs across multiple task paradigms. A limitation of this study was the use of different participant

groups, taken several years apart. This means that comparisons made between the two tasks were limited to group averages. Testing of the same participant group over multiple paradigms would provide further insight into the nature of PTRs across the cortex, allowing within-subject changes in PTRs and burst characteristics to be examined, as well as between-subject variation which may act as a neural fingerprint (Oswald et al., 2017, Sareen et al., 2021).

In future work, our approach to finding connectivity of bursts through spatial clustering should be tested with different paradigms and participant groups, to potentially provide insight into specific spatial networks which are implicated due to behaviour, age or pathology. For example, studies have shown that functional connectivity is affected in patients with autism (Tsiaras et al., 2011) and mild traumatic brain injury (Rier et al., 2021), using pairwise measures of functional connectivity between sensors or brain regions. Our approach applied to patient and control data could reveal specific network structures which are implicated in illness, shown through differences in within-network connectivity, as well as providing dynamic information in the cluster probability, showing the phase of a paradigm in which differences between patients and controls manifest within the affected networks.

A further aspect of bursting behaviour that could be explored is causality, or *directional* connectivity, which would provide more information about the generation of the PTR and propagation through intracortical networks. This would be particularly useful with concurrent sEEG-EEG/sEEG-MEG data (see Chapter 1), or even EEG-fMRI data, as propagation of the PTR in thalamocortical networks as well as intracortical networks could potentially be studied. Directional connectivity has been explored in existing literature with both MEG (Soleimani et al., 2022) and fMRI data (Zhou et al., 2009). However, it should be noted that one of the most popular methods for analysing these effects is Granger Causality, a technique which has been criticised for its potential to falsely predict a directional relationship between variables (Maziarz, 2015). Therefore, a full exploration of causal modelling would be required to study these effects in PTRs.

6.8 Conclusion

We have shown that PTRs following movement and working memory are driven by transient burst events in oscillatory activity. These bursts, encompassed in a single HMM state for each region, drive induced changes both during-task and post-task. The PTR state cluster showed interesting similarities across tasks. Burst durations across participants are within a standard error of each other between tasks and show highly correlated spatial patterns for both tasks, with the longest durations in the motor strip,

and shortest in the prefrontal cortex. The PTR state showed very similar alpha and beta variation across the brain between tasks, with greater difference in the theta band activity that is likely driven by differences in the network recruitment during the task period. Overall, these results suggest that differences in frequency content of PTRs reflects the emitting regions, and thus the recruited network architecture, rather than variation in PTR function across tasks. We also showed that canonical functional network architecture is supported by concurrent oscillatory bursts across the cortex, with a similar set of networks identified for both tasks. Using this network decomposition, we find that PTRs in both tasks are formed of whole-brain burst coincidence, as well as burst coincidence in different task-specific networks. Finally, for the n-back task, correlations between PTRs and reaction times were improved by using HMM PTR state timecourses rather than frequency filtered power envelopes from the same region, demonstrating the ability of HMMs to isolate signals of interest and corroborating hypotheses relating PTRs to inhibitory control of network activity.

6.9 Appendix

The spatial network results in Figures 6.13 and 6.14 showed all networks on the same colour scale, to show the relative strength of each network. Here, the same results are shown with maximum dynamic range, such that the regions which contribute most to each network are more visible.

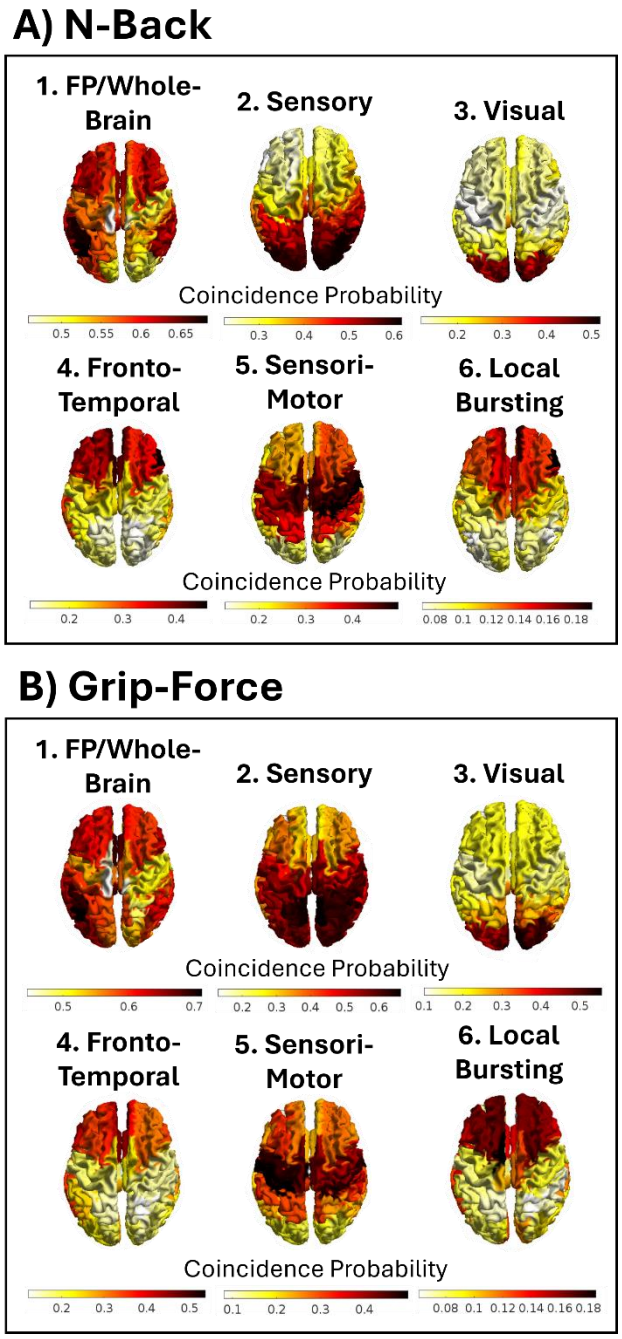


***Figure A6.1**: Spatial networks found using k-means clustering of the PTR state. These are each on a different colour scale, to show maximum contributors to each network despite different network strengths.*

7 Spatial and Dynamic Dissociation of Primary and Post-Stimulus BOLD Responses

7.1 Abstract

The post-stimulus response in BOLD signal is a robust, widely studied component of task-based fMRI data that occurs following stimulus or task cessation. This response has long been thought to be a vascular consequence of the primary BOLD response, holding no excess information about neuronal processes. However, more recent studies have found relationships between the post-stimulus BOLD response and cerebral blood flow, as well as post-stimulus electrophysiological signals, suggesting neuronal origins which may be distinct from responses during stimulation. Here we investigate whether post-stimulus BOLD responses are distinct from primary responses in terms of both spatial location and signal modulation.

We used 7T fMRI and long inter-trial rest periods to optimally resolve post-stimulus BOLD responses to an n-back working memory task (akin to that used in Chapters 5 and 6), with two conditions (1-back: low load, 2-back: high load), in 15 subjects. We used a pseudo T-statistic approach to overcome limitations of general linear models and separately map modulations of the primary and post-stimulus BOLD responses. Condition-dependent modulations of the primary and post-stimulus BOLD response were observed in attention, default and salience networks, as well as the thalamus and hippocampus, with spatial separation of approximately 4 – 10 mm between corresponding primary and post-stimulus peak locations. Normalisation of timecourses from locations of peak post-stimulus modulations revealed that there is modulation of the post-stimulus BOLD response unaccounted for by primary response amplitude modulation. Linear regression analysis also revealed that on a trial-by-trial basis, primary and post-stimulus response modulation is uncoupled. Overall, our results support hypotheses that the post-stimulus BOLD response has neuronal contributors that are distinct from those that drive the primary response. We also provide initial evidence for the involvement of the thalamus and hippocampus in the post-stimulus response, which are difficult to study with MEG alone.

7.2 Publication and Contribution Note

This work has been submitted to Human Brain Mapping as a research article, and is currently in revision.

All data collection and analysis was performed by the author, using a series of bespoke scripts, as well as pre-existing and bespoke analysis packages.

7.3 Introduction

Functional MRI is one of the most widely used methods to study brain function (see Chapters 1 and 4). As discussed in Chapter 4, changes in BOLD signal relating to stimuli or tasks are made of at least two parts – the primary peak and the post-stimulus undershoot, forming the canonical HRF (Glover, 1999). Classically these two phases of the response have been viewed as coupled, with the post-stimulus response considered a by-product of the response during stimulation. Interpreting the BOLD response to tasks can be difficult due to the complex nature of neurovascular coupling (Iadecola, 2017, Rosa et al., 2011, Heeger and Ress, 2002, Logothetis and Wandell, 2004). As outlined in Chapter 2, it is still debated whether the post-stimulus BOLD response has neuronal contributions, and whether these neuronal contributions are distinct from those that drive the primary peak response (Chen and Pike, 2009, Mullinger et al., 2013, Sadaghiani et al., 2009). This study uses 7T fMRI to determine whether post-stimulus BOLD responses show functionally relevant modulations related to changes in cognitive load, and whether these modulations are uncoupled from any modulations of the primary BOLD response.

As discussed in Chapter 2, several studies have suggested that the post-stimulus undershoot may be driven in part by a reduction in CBF (Chen and Pike, 2009, Mullinger et al., 2013, Sadaghiani et al., 2009), which is thought to relate more directly to neuronal activity than CBV (Friston et al., 2000, Sotero and Trujillo-Barreto, 2007). Mullinger *et al* also reported trialwise relationships between post-stimulus BOLD/CBF and alpha power measured with concurrent EEG, suggesting an electrophysiological counterpart to the post-stimulus BOLD response (Mullinger et al., 2017). The post-stimulus BOLD response has also been shown to modulate in clinical populations compared to controls, which is comparative to similar results regarding the electrophysiological PTR. In patients with schizophrenia, the post-stimulus BOLD response was reduced in magnitude (less negative undershoot) compared with controls in the auditory and visual sensory regions for an multisensory detection task (Hanlon et al., 2016). Importantly, there was no effect on the primary response, suggesting that the post-stimulus phase of the response may have a distinct neuronal origin. This is strikingly similar to electrophysiological studies which showed that the PMBR was reduced in patients with schizophrenia, while the MRBD (during-stimulus) response was not (Gascoyne et al., 2021, Hunt et al., 2019). In addition, patients with

autism spectrum disorder (ASD) also showed reduced post-stimulus BOLD response in visual and somatosensory regions following multisensory stimulation, with no reduction of the primary response compare with healthy controls (Murray et al., 2020), forming another parallel with the PMBR (Gaetz et al., 2020). Like the electrophysiological cases, the studies discussed here speculated that the reduced post-stimulus BOLD response was related to reduced inhibitory capability.

In addition to the clinical studies discussed in the previous paragraph, studies have reported variation in HRF shape due to non-clinical factors (Mayhew et al., 2022, Aguirre et al., 1998, Duann et al., 2002, Gonzalez-Castillo et al., 2012). Aguirre *et al* found that there was significant between-subject variability in haemodynamic response in the motor cortex in a simple reaction times task, with some subjects exhibiting little-to-no post-stimulus response, and others exhibiting a post-stimulus response that was comparable in size to the primary response (Aguirre et al., 1998). Handwerker *et al* also observed high levels of between-subject variability in haemodynamic response and investigated the effects of HRF variability on GLMs, noting false negatives caused by deviations in subject-specific HRF away from the standard (Handwerker et al., 2004a). Furthermore, Mayhew *et al* showed that there was a reduction in the post-stimulus BOLD response in ipsilateral motor regions with age, which reduced the sensitivity of GLMs when using a fixed HRF (Mayhew et al., 2022).

Overall, the studies discussed above, both clinical and non-clinical, highlight the limitations of GLMs which use a predetermined HRF. Typically, the HRF has an undershoot set to around 35% of the primary peak, which may not be reflective of all participant groups. As a result of this, GLMs may be biased towards regions, stimuli, and demographics that exhibit a more typical haemodynamic response. A GLM approach with a fixed HRF also ignores the possibility that primary and post-stimulus responses may differ in spatial origin if they are generated by differing neuronal ensembles. Given the spatial disparity of during-task and post-task responses that we report using MEG in Chapter 5, the possibility of spatial disparity in the haemodynamics of these responses cannot be ignored.

Whilst post-stimulus responses in electrophysiology are relatively well studied in cortical grey matter (Pfurtscheller et al., 1996b, Pfurtscheller et al., 2005, Tan et al., 2016, Mullinger et al., 2017, Pakenham et al., 2020), including the PTRs reported in Chapter 5, the role of deep grey matter structures are extremely difficult to interrogate with MEG or scalp EEG due to the distance of these anatomical areas from the sensors on the scalp and the rapid decay of signal with distance (Hillebrand and Barnes, 2002).

MRI signal is invariant to the depth of tissues within the brain, assuming the scanning sequence has been optimised for whole-brain scanning. Therefore, assuming that BOLD post-stimulus responses are a proxy measure for M/EEG PTRs, the role of deep grey matter structures in the generation or propagation of the PTR can feasibly be determined using fMRI. To our knowledge, the role of post-stimulus BOLD responses in deep grey matter regions has not been studied to date, as well as how these relate to post-stimulus BOLD responses in superficial grey matter. Such information could prove important when investigating the role of post-stimulus/post-task responses in healthy and clinical populations, to understand where changes in responses are originating, as well as the affected networks.

Here we aimed to: 1) use an analysis method which did not contain *a priori* assumptions as to the coupling between primary and post-stimulus BOLD responses; 2) use this method to identify regions across the cortex and deep grey matter where each of the responses were observed; 3) Identify whether there was a direct coupling of the primary and post-stimulus responses or whether the post-stimulus response contained variance not explained by the primary response. To address these aims, we performed a 7T fMRI experiment with an n-back task, reflecting the paradigm used in our MEG study presented in Chapter 5 but employing longer (49 s) rest periods between task blocks to maximally resolve the slow post-stimulus BOLD responses. We used two n-back conditions (1-back and 2-back) to contrast high and low working memory load conditions and examine the effects on the primary and post-stimulus BOLD responses, separately. We employed a pseudo t-statistic (~~T~~-stat) approach, similar to the approach used in Chapter 5 as well as many previous MEG studies (Gaetz and Cheyne, 2003, Brookes et al., 2007, Brookes et al., 2011b), to separately identify modulations of primary and post-stimulus responses to the task. This approach removed the assumption that modulations if the primary and post-stimulus response must arise from the same voxel. We extract timecourses from regions of interest (ROIs) and interrogate these timecourses to ascertain if the primary and post-stimulus response are modulated independently by task condition.

Previous evidence links post-stimulus undershoots in BOLD to increased inhibitory neuronal activity (Shmuel et al., 2006, Mullinger et al., 2017). We therefore hypothesise that post-stimulus BOLD responses will become greater in magnitude with working memory load (2-back condition), providing a compensatory response that brings networks from a state that is engaged with the task, to rest. We also hypothesise that these modulations will be decoupled, to some degree, from the primary peak, reflecting different neuronal contributors to each part of the response (Mullinger et al., 2017,

Shmuel et al., 2006, Logothetis et al., 2001, Moon et al., 2021). Finally we hypothesize that if post-stimulus BOLD responses are neuronal in origin, they may be driven by the same circuits that drive PTRs in alpha and theta (Başar et al., 1997, Backus et al., 2016, Soltani Zangbar et al., 2020, Bollimunta et al., 2011), i.e., the responses reported in Chapters 5 and 6. We therefore expect a clear post-stimulus response observed in the thalamus and hippocampus which is uncoupled to the primary response, potentially reflecting the same inhibitory and excitatory processes that are required to re-establish resting levels of task-positive and task-negative networks at the end of a task, as hypothesised in Chapter 5.

7.4 Methods

This study was conducted with approval from the local ethics committee and all subjects gave written informed consent. Data were acquired from 16 participants (age 25.9 ± 0.6 years (mean ± SD), 6 female).

7.4.1 Paradigm

The n-back task used here was, by design, very similar to the one used in Chapter 5. Here, two conditions, 1-back (low load) and 2-back (high load) were used. A reduction in the number of conditions compared with the MEG work was necessary to facilitate the longer rest periods to allow time for the sluggish haemodynamic response to return to baseline. The conditions were chosen because there was little difference in the behaviour and oscillatory responses, particularly the PTR, between 0-back and 1-back, whereas there was a large amount of variance between these two conditions and 2-back (see Fig. 5.2, 5.5, and A5.1).

Similar to Chapter 5, participants were presented with an instruction screen indicating the following task condition, lasting for 2 s. This was followed by the presentation of a block of 15 sequential letters, each presented for 1 s, with 1 s interstimulus interval. During letter presentations, participants were instructed to press a button with their right index finger when the letter shown was the same as the letter shown previously (1-back) or the same as the letter shown before the previous letter (2-back), depending on the task condition. After the last letter of the block was presented, a rest period followed for 49 s (compared with 30 s for the MEG study presented in Chapters 5 and 6), during which a square fixation was shown. The instruction screen, task period and rest period make up a single task block lasting 81 s. A single task block is shown schematically in Figure 7.1. Participants completed a total of 15 blocks of each

condition, arranged pseudorandomly, split over 3 runs. Each run started with a 90s rest period to allow baseline to be captured. Each run lasted 8 minutes and 15 s.

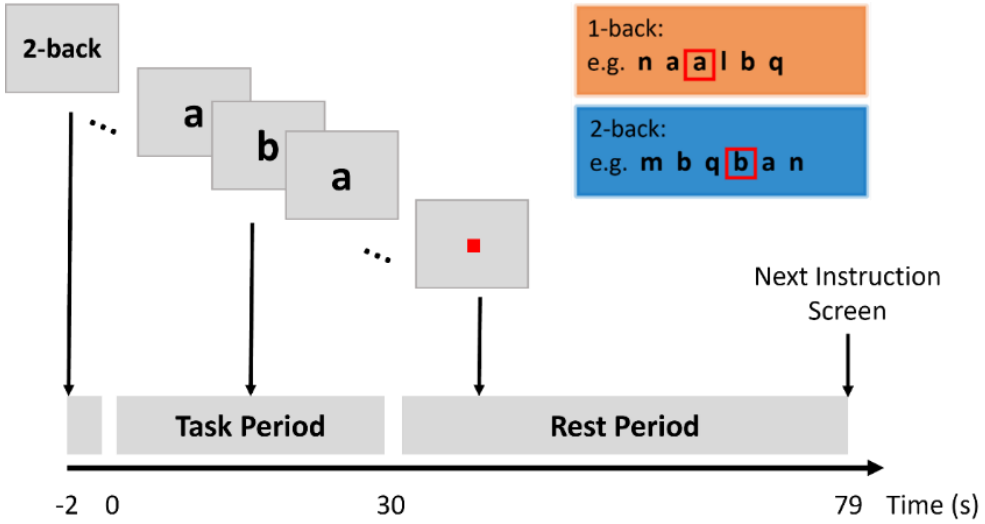


***Figure 7.1**: A schematic of the n-back paradigm used in this Chapter. The task had two conditions: 1-back (low load), where target letters are the same as the previous letter, and 2-back (high load), where target letters are the same as the letter before the previous letter. The instruction screen stating the task condition was shown for 2 s. Each letter stimulus was presented for 1 s, with 1 s of blank screen between sequential letters. A total of 15 letters were presented per task block. A 49 s rest period followed the last letter in the sequence.*

7.4.2 Acquisition

Data were acquired on a 7T Achieva scanner (Philips Medical Systems, The Netherlands) with a head transmit coil and 32 channel head receive coil. Gradient echo EPI data were acquired over the whole head (TR = 1.5 s, TE = 25 ms, 2 mm isotropic resolution, 96 x 96 matrix, multiband factor 2, 70˚ flip angle, SENSE factor 2.4, phase encoding direction: anterior-posterior). 50 axial slices covering the whole cortex were collected in a single TR. 602 volumes were acquired per run. An additional single volume of EPI data was acquired with the phase encoding direction set to posterior-anterior to enable distortion correction to be implemented using TOPUP (Andersson et al., 2003). In addition, a high-resolution whole-brain T1 weighted anatomical was acquired using a PSIR sequence (Mougin et al., 2016) (0.7 mm isotropic resolution, 336 x 336 matrix, 224 slices, TI=785/2685 ms, SENSE factors: 2.2 (right-left, phase encode), 2 (foot-head, slice selection)). Physiological data were collected using a pulse oximeter, fixed to a finger (usually the left index finger), and a pneumatic belt, secured around the participant's diaphragm.

7.4.3 Pre-Processing

All data were pre-processed according to the standard steps outlined in Chapter 4 using functions in FSL (FMRIB Software Library) as well as in-house MATLAB scripts.

Physiological noise (Chapter 4) was corrected using the RETROICOR method (Glover et al., 2000), implemented with an in-house MATLAB script. Susceptibility induced distortions, which EPI sequences are particularly prone to (see Chapter 4), were corrected using the TOPUP function in FSL (Andersson et al., 2003). TOPUP takes paired images with opposite phase-encoding directions and uses the differences of these two images to estimate field inhomogeneity across the image space caused by variations in susceptibility. Following field estimation, the phase at each voxel is adjusted based on the amount of inhomogeneity, creating a distortion-corrected image. Head motion during the scan was corrected using the MCFLIRT function in FSL (Jenkinson et al., 2002). This function derives a rigid (no scaling or warping) transformation matrix between pairs of images in the EPI sequence, which is then applied to correct for movement across the scan period. The reference volume was taken as the middle volume within each run. Runs were then all registered to the second run to correct between-run position changes. Motion parameters were saved from the correction process to check for excessive movement during scanning and be used as nuisance regressors in GLM analysis. Data were highpass filtered using a threshold frequency of $1/n_{block}$, where n_{block} is the length of a single block (81 s in our case). Finally, data were smoothed with a Gaussian smoothing kernel of full-width half maximum (FWHM) 4mm (2 * voxel width). Convolving the smoothing kernel with the data acts to reduce noise. A relatively small FWHM is chosen to limit the loss of spatial specificity of signals.

7.4.4 General Linear Model Analysis

We firstly performed a standard GLM analysis (described in Chapter 4) using FEAT in FSL (Woolrich et al., 2001, Woolrich et al., 2004a) to provide comparative results to our more novel subsequent analysis, as well as previous literature. The two conditions, 1-back and 2-back, were modelled separately by convolving condition timings (boxcars) with a double-gamma canonical HRF (Glover, 1999) (see Chapter 4.2.2). An example design matrix is shown in Figure 7.2.

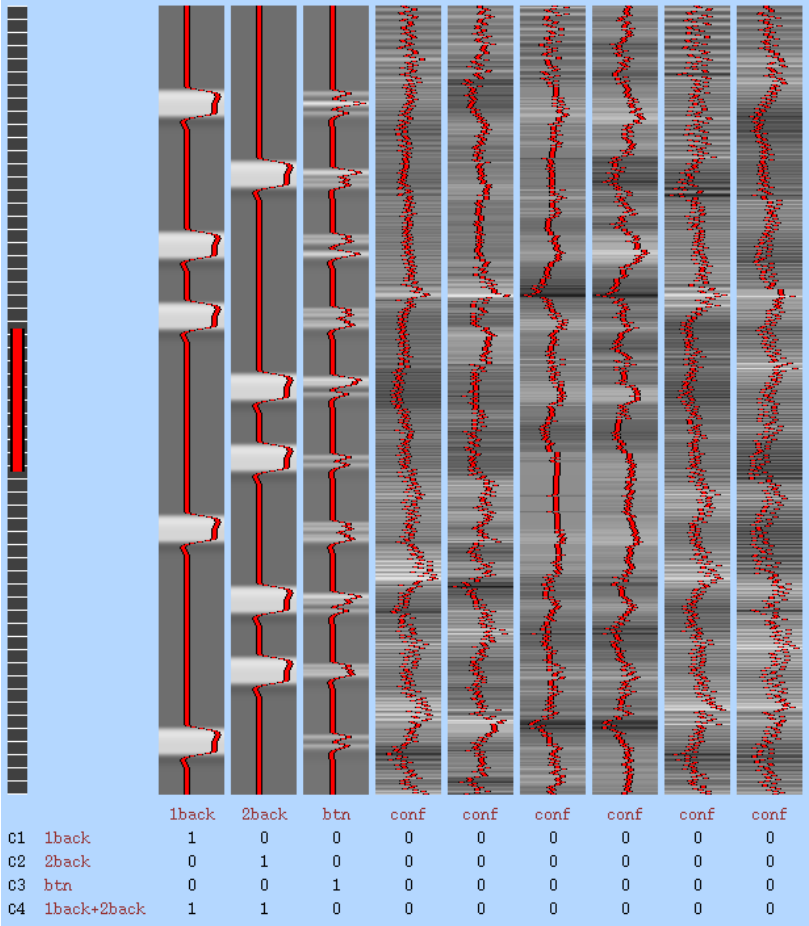


***Figure 7.2**: An example design matrix from the GLM analysis. The two conditions, 1-back and 2-back, are modelled in separate regressors (left two columns). Button presses are also modelled (third column from left). Motion parameters from MCFLIRT were modelled as nuisance regressors. For z-stat maps, separate contrasts were set for each condition and button presses, with an extra contrast which contained both task conditions with equal weighting.*

Although the regressor corresponding to button presses holds some resemblance in timing to the condition regressors, the rank was still equal to the number of regressors, and was therefore not reported deficient by FEAT. The first three eigenvalues of the design matrix were sufficiently high to assume that this did not invalidate the model, with the lowest of these being 0.190 for the design matrix in Figure 7.2, and highest Pearson's r value of 0.49. Both conditions were used in the main analysis contrast to identify regions that responded to the task. First level analysis was performed on each run separately, for each subject. Group level statistical maps (see Chapter 4.2.3) were then formed using mixed effects (FLAME 1). Group level z-statistic maps for each contrast were thresholded at $z > 3.1$ with cluster significance at $p < 0.05$.

7.4.5 Pseudo T-Statistic Analysis

One of our aims with this study was to remove the constraints of classical GLM analysis, by separately interrogating modulations of the primary and post-stimulus

BOLD response. To do this, we adopted a pseudo T-statistic (~~T~~-stat) approach, similar to methods used with electrophysiological data (Gaetz and Cheyne, 2003, Brookes et al., 2007, Brookes et al., 2011b) which were implemented in Chapter 5. The data were pre-processed as described above for the GLM analysis, including physiological noise correction, susceptibility-induced distortion correction, and motion correction, using functions in FSL and in-house MATLAB scripts. The rest of the pre-processing and analysis was performed using an in-house Python package. Data were smoothed and highpass filtered using the same parameters as the GLM analysis. It should be noted that we only performed spatial smoothing for the activation maps, while unsmoothed data were used to find peak voxel locations and extract timecourses (see section 7.4.6). For each voxel and volume, the percentage signal change was then calculated relative to the 90 s baseline taken at the beginning of each run. A ~~T~~-stat value was calculated at each voxel in the brain using the following equation:

$$\mathcal{T} = \frac{P_a - P_c}{N_a + N_c}, \tag{7.1}$$

where P_a and P_c represent mean signal (measured in percentage change) during active and control windows, respectively. N_a and N_c are an approximation of noise during active and control windows, calculated as the standard deviation of the signal during the respective time periods. Two main contrasts were analysed for this study, 1) modulation during the primary peak, where the active window was the mean of the primary peak during the 2-back condition, and the control window was the mean of the primary peak during the 1-back condition; 2) modulation during the post-stimulus response, where the active window was the mean of the post-stimulus response during the 2-back condition, and the control window was the mean of the post-stimulus response during the 1-back condition. In contrasts 1 and 2, the primary peak was taken to be 5.5 – 35.5 s after the start of each task period (Fig. 7.1), while the post-stimulus response was taken to be 38.5 – 53.5 s after the start of each task period (Fig. 7.1). In addition, we took ~~T~~-stat contrasts of primary response (same window as before) versus rest (47.5 – 77.5 s) and post-stimulus response (same window as before) versus rest (62.5 – 77.5 s), for completeness and for comparison with the GLM results (see Appendix A). It should be noted that the additional analyses (Appendix A) used a rest window in the task versus rest contrast that overlapped with the post-stimulus response window in the main analysis. The reason for this was to match the total amount of data in each condition that was put into the ~~$\mathcal{T}$~~-values calculation. Consequently, the "rest" condition of this contrast will contain some of the post-stimulus BOLD response, and should not be considered a proper baseline. In turn, the ~~$\mathcal{T}$~~-values

in those maps should not be considered a quantitative measure as the size of the effects may contain a varying amount of the post-stimulus response.

T-stat maps were averaged across runs for each subject and normalised to MNI space using FSL FLIRT (Jenkinson and Smith, 2001, Jenkinson et al., 2002), which calculates transformation matrices between images. Co-registration was performed according to the steps described in Chapter 4 for group-level GLM analysis. However, unlike GLM analysis, normalised T-stat maps were simply averaged across all subjects to form group T-stat maps, as we did not perform any formal statistics on these.

7.4.6 Functional Network Responses

The data were interrogated in specific regions of interest (ROIs) based on regions/networks known to be recruited by an n-back task (Mencarelli et al., 2019, Luo et al., 2014, Liang et al., 2016). Specifically, we looked at the dorsal attention network (DAN), default mode network (DMN) and salience network (SN). We also analysed data from the thalamus and hippocampus, as both of these regions are known to be recruited in working memory tasks (Peräkylä et al., 2017, Morvan et al., 2022, Hallock et al., 2016, Leszczynski, 2011). We hypothesize that these deep brain regions could hold important information about the propagation of the post-stimulus response due to the known relationships between the thalamus and hippocampus with the alpha and theta rhythms, respectively (see Chapter 2).

Relevant ROI masks (Przezdzik et al., 2013, Wilson et al., 2015) were transformed to subject-space. These masks were used to extract voxels of peak activity using the higher-level T-stat map for each subject (combined over runs), for the primary and post-stimulus contrasts separately. Peak voxel coordinates were transformed to MNI space (using the transformations derived in section 7.4.5) to normalise locations across subjects, and the Euclidian distances between corresponding peaks of the primary and post-stimulus T-stat contrasts were taken to assess whether the two main parts of the BOLD response were spatially distinct.

For each ROI and T-stat contrast, timecourses were taken from 3 x 3 cube of voxels around activation peaks to reduce noise, then averaged over n-back blocks of each condition to produce group-average timecourses for each region over a task block period. Timecourses from separate regions that constitute known functional networks (e.g. DAN) were combined.

7.4.7 Normalised Post-Stimulus Response

To assess whether post-stimulus BOLD activity has a neural contribution that is distinct from the primary response, timecourses from the peak locations in the primary and post-stimulus modulation contrasts were normalised, following a similar method to existing literature (Chen and Pike, 2009). For each region/network, the block-average timecourse for each subject and condition was divided by the mean amplitude of the primary peak (taken between 6 – 29 s), such that the primary peak amplitude had a mean of 1 regardless of condition. This highlights any excess contribution of task condition to post-stimulus BOLD activity that is not explained by primary peak amplitude. A two-way, repeated-measures ANOVA was performed on timecourses from each region/network to check for significant ($p < 0.05$ after Bonferroni correction) interaction between task condition and time, for both the original and normalised timecourses. For timecourses where a significant overall difference between timecourses was seen, post-hoc t-tests were then performed to reveal which timepoints this interaction became significant ($p < 0.05$).

7.4.8 Primary and Post-Stimulus Response Regression

An alternative way to assess distinct contributions of task condition to post-stimulus BOLD amplitude is using linear regressions between primary and post-stimulus components of the response, mirroring analysis that we performed on MEG in Chapter 5. For each network (averaged timecourse from all network nodes) and subject, a linear fit was calculated between trial-wise primary and post-stimulus BOLD amplitudes. The fit was then removed from the set of post-stimulus amplitudes to remove the effect of the primary peak on the post-stimulus response. The mean post-stimulus amplitude was then taken for each condition, per subject, before and after removal of the fit. Following this, a paired t-test was performed between the two conditions to see whether there was a significant effect (after Bonferroni correction for the multiple networks interrogated) of task condition on post-stimulus BOLD response over the group, that was distinct from the primary peak response. An example result using this method is shown below in Figure 7.3, showing the effect of removing the linear fit on mean post-stimulus amplitude for the two task conditions, for a single subject.

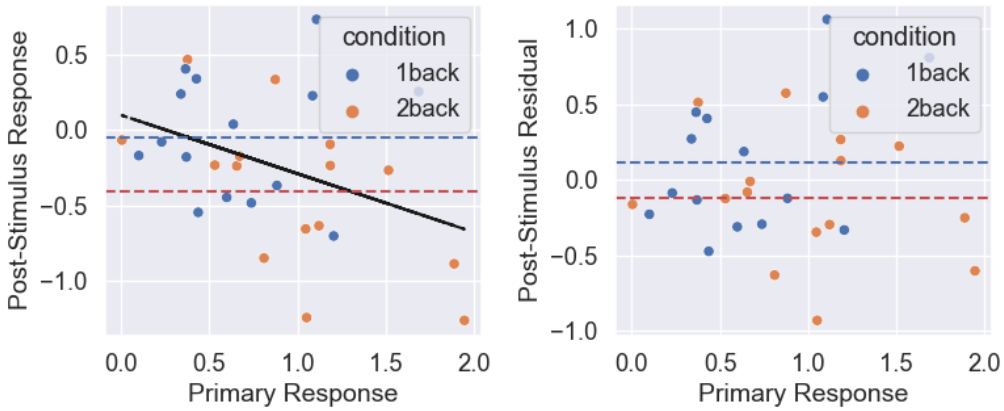


***Figure 7.3**: Demonstration of the regression method applied to assess whether there is modulation in the post-stimulus BOLD response with condition that is not explained by primary response variation. Each dot on the graphs represents the amplitude of the post-stimulus response against the primary response for a single trial of one subject. The black line is the least squares fit between the two. The figure on the right shows the points after having the fit removed. The dotted lines on each graph are the mean post-stimulus amplitudes during each condition.*

7.5 Results

7.5.1 General Linear Model

To allow comparison with previous studies, the results of performing a GLM analysis on the dataset are shown below in Figure 7.4 as a group z-stat map. All conditions (1-back and 2-back) were included in the z-stat contrast. As is commonly observed in the literature (Ceko et al., 2015, Mencarelli et al., 2019, Briley et al., 2021), the DAN and DMN are activated and suppressed, respectively, by the n-back task. As well as these networks, we also see the SN clearly activated, made up of the bilateral insula, dorsolateral prefrontal cortex and anterior cingulate. In addition, we see activation in the bilateral thalamus and deactivation in the bilateral hippocampus. Given the fact that the post-stimulus response is modelled with much lower amplitude than the primary response, these results will mostly be driven by primary peak amplitude and are relatively insensitive to post-stimulus BOLD responses.

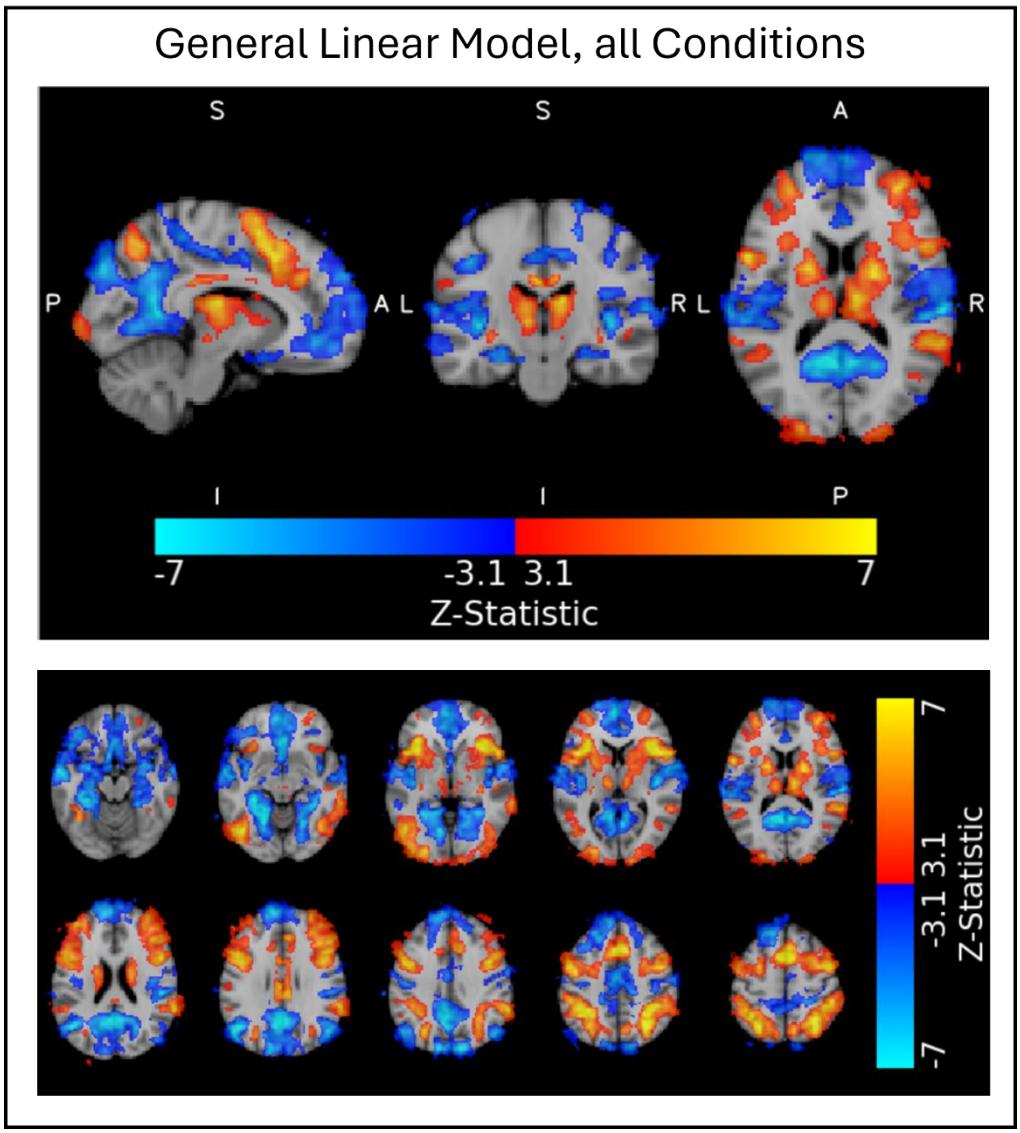


***Figure 7.4**: Group z-stat results from a GLM analysis of the dataset, with both conditions modelled in the contrast. Maps are thresholded at z > 3.1, with p < 0.05. The DAN, SN and thalamus are activated by the task (red-yellow colours), whereas the DMN and hippocampus are suppressed by the task (blue colours).*

The timecourses from the peak response from the GLM analysis in the DAN, DMN, and SN are shown in Figure 7.5. These appear to closely resemble the canonical HRF, with a post-stimulus response that is around 1/3 of the amplitude of the primary response. Figure 7.5A shows that the DAN and SN are significantly modulated by condition ($p < 0.05$, RM-ANOVA), driven by both the primary and post-stimulus phases of the timecourse (post-hoc t-tests). Figure 7.5B shows group timecourses that were normalised to the mean amplitude of the primary peak (normalised per subject before averaging). Here, the amplitude of the post-stimulus response clearly co-modulates (on the subject level) with the primary peak, with no significant modulation with task condition remaining during the post-stimulus response after normalisation for any of

the networks. Although significant effects are seen in the DAN after normalisation, these appear to be driven by differences in primary peak morphology, rather than independent modulation of the primary and post-stimulus response.

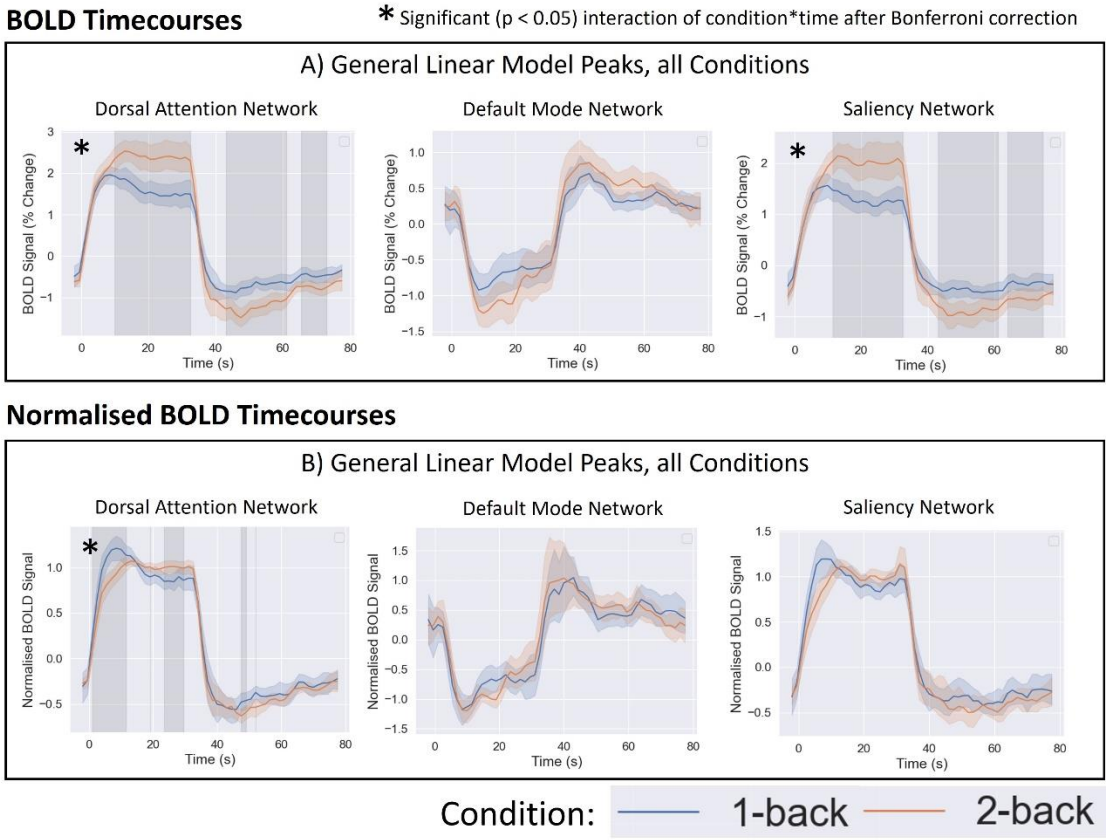


***Figure 7.5**: Panel A shows group average timecourses from three functional networks which are modulated by the n-back task, with peaks taken from the GLM z-stat maps produced for each subject. Panel B shows the same timecourses, normalised for each subject before averaging by dividing each timepoint by the mean during the primary peak (6 – 29 s). An asterisk (*) denotes significant effect of condition*time (p < 0.05, two-way RM ANOVA) after Bonferroni correction. Grey shaded regions mark time periods of significant modulation with condition (p < 0.05, post-hoc T-test).*

In addition to the post-stimulus normalisation in the above figure, we also performed a linear regression analysis, removing the trialwise relationship between the primary and post-stimulus response, and checking for significant modulation with task condition in the residual post-stimulus response. Figure 7.6 shows the results of this analysis. Under each of the network titles, the left boxplot shows the difference in mean amplitude between the two conditions during the post-stimulus window, while the right boxplot shows the same after removal of the linear relationship between the primary and post-stimulus amplitudes. Interestingly, the DMN showed significant modulation in the post-stimulus response after removal of the effects of the primary response,

suggesting that for this network, even using GLM peaks, the primary and post-stimulus response do not co-modulate. Although it should be noted that the DMN appears to have a lower SNR response than the DAN or SN, as can be seen in the trial-level signal plots in Appendix B.

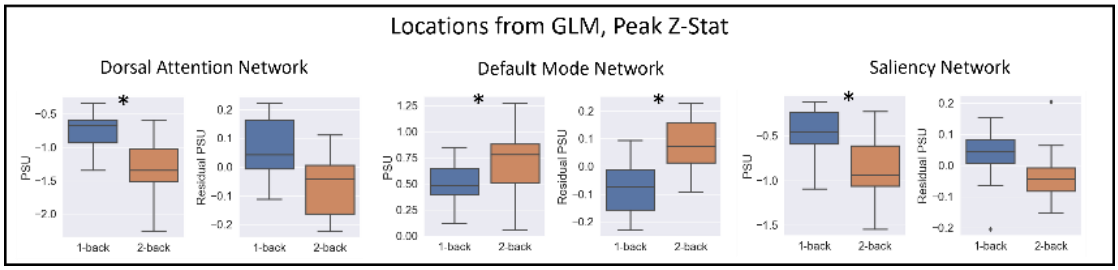


***Figure 7.6**: Regression method, applied to timecourses identified from GLM analysis, to assess whether post-stimulus BOLD response modulates distinctly from the primary response. A paired t-test was performed before and after fit removal to check for excess post-stimulus modulation. An asterisk (*) denotes significant ($p < 0.05$) modulation following Bonferroni correction for the multiple networks tested.*

The GLM also produced significant z-stat peaks in the thalamus and hippocampus. The timecourses for these regions are shown below in Figure 7.7. For these regions, no significant effect of condition with time was observed and therefore no further normalisation analysis was performed.

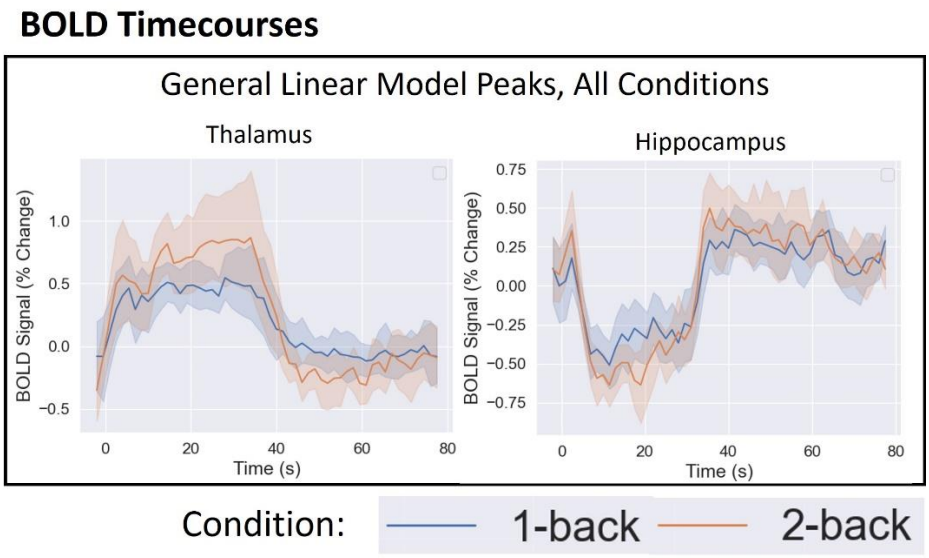


***Figure 7.7**: Group average timecourses from z-stat peaks in the thalamus and hippocampus following GLM analysis. Neither of these regions showed significant interaction of condition with time, for these particular voxel locations.*

7.5.2 Pseudo T-Statistic

Our pseudo T-statistic approach to finding BOLD activations allowed us to separately target activity in the primary and post-stimulus time windows, removing the assumption

that these effects must be spatially alike. Figure 7.8 shows the results of this analysis for the primary response modulation contrast, with a threshold of 20% of the maximum T-stat value. Similar to Figure 7.4, the primary response in the DAN, SN and thalamus are positively modulated in 2-back compared to 1-back, while the DMN and hippocampus are negatively modulated. The post-stimulus contrast, shown in Figure 7.9, reveals the inverse in all these cases, i.e., undershoot in regions that were exhibited a positive primary response, and overshoot in those that exhibited a negative primary response. However, these maps are clearly not the direct inverse of each other. For example, post-stimulus overshoots in the DMN are more widespread than the corresponding negative primary responses, whereas DAN undershoots are more focal than the corresponding positive primary responses. For completeness, we also performed a T-stat analysis comparing the primary and post-stimulus response windows to the rest period (49.5 – 79.5 s for the primary peak contrast, 64.5 – 79.5 s for the post-stimulus contrast). The results for this additional analysis are shown in Appendix A (Fig. A7.1, A7.2).

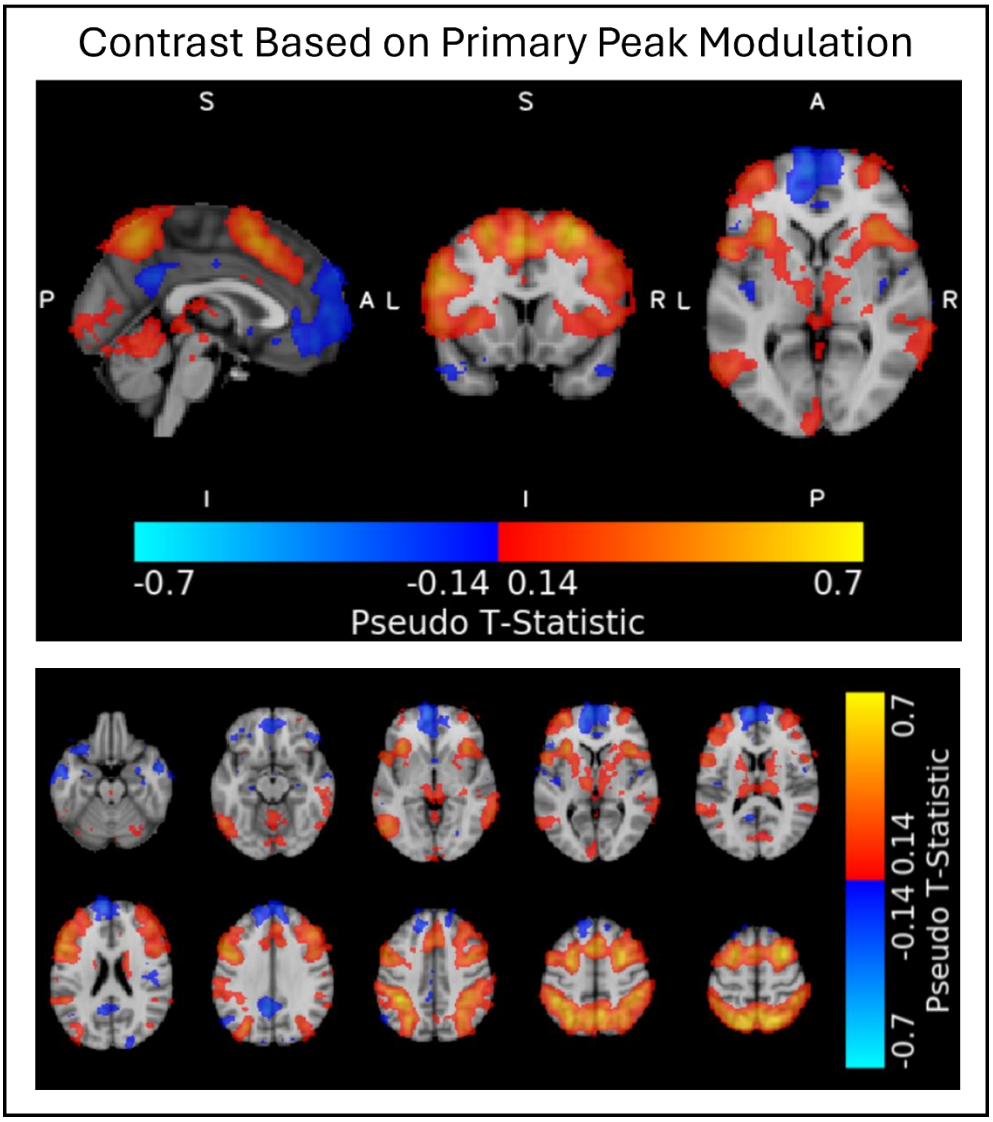


Figure 7.8*: ~~T~~-stat maps, contrasting 2-back and 1-back during: A) primary peak (7 – 37 s) and B) post-stimulus (40 – 55 s). Maps have a threshold of 20% of the maximum ~~T~~-stat value. The DAN, SN and thalamus are activated by the n-back task, whereas the DMN and hippocampus are suppressed. In each of these networks, the inverse sign is seen in the post-stimulus response (Fig. 7.9).*

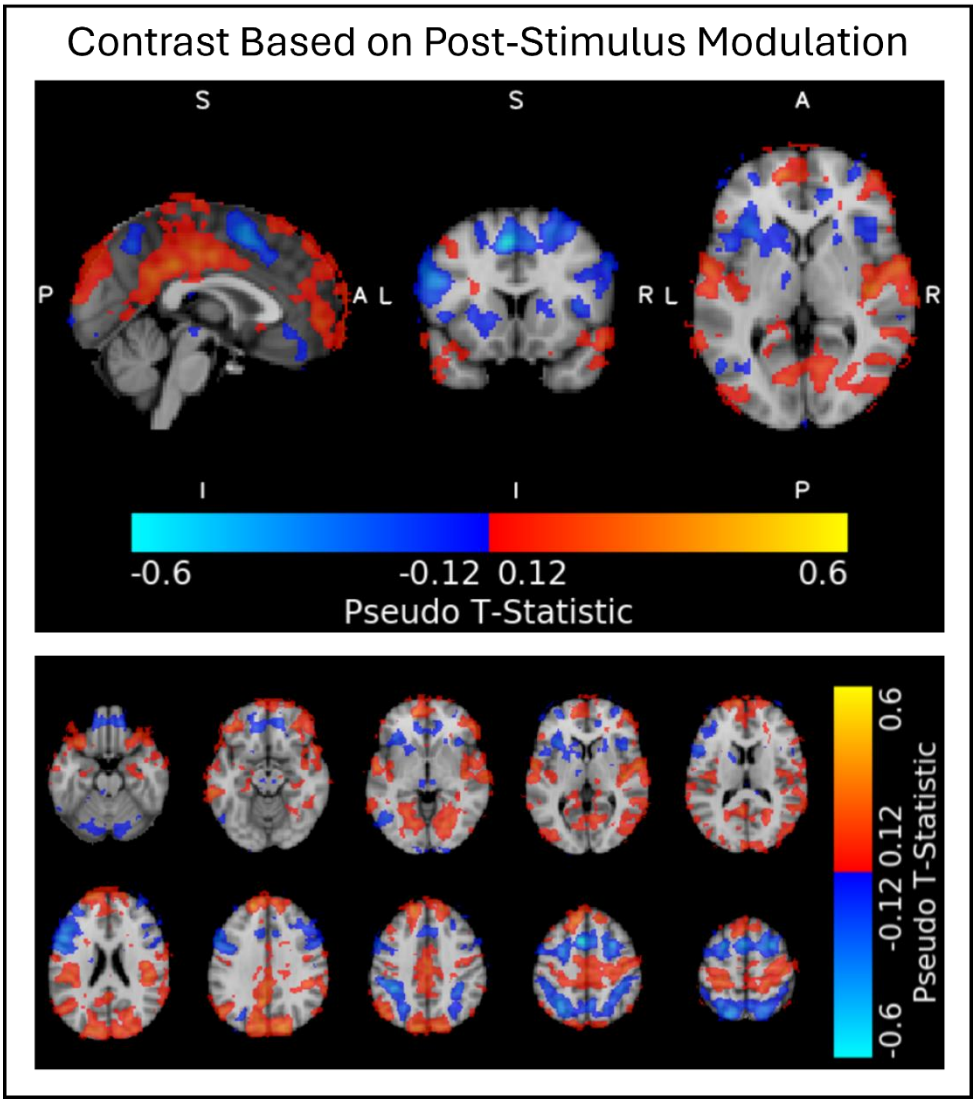


***Figure 7.9**: ~~T~~-stat maps, contrasting 2-back and 1-back during the post-stimulus (40 – 55 s) response. Maps have a threshold of 20% of the maximum ~~T~~-stat value. The DAN, SN and thalamus show a post-stimulus undershoot, while the DMN overshoots.*

To quantify differences between locations of primary and post-stimulus modulation, we took Euclidian distances (mm) between corresponding peaks in subject-specific maps, after averaging over runs and normalising to standard space. Group average Euclidian distances are shown in Table 7.1. Standard error over subjects (mm) is also given. In all cases, distance is greater than the voxel width (2 mm), as well as the error, suggesting that primary and post-stimulus BOLD modulations differ in spatial distribution.

region	distance (mm)	error (mm)
Group_DAN_rIPS	7.86	1.33
Group_DAN_lIPS	8.97	1.66
Group_DAN_rFEF	7.10	1.64
Group_DAN_lFEF	6.78	0.96
Group_DMN_mPFC	10.22	1.18
Group_DMN_PCC	7.92	0.97
Group_DMN_rIPL	5.55	0.71
Group_DMN_lIPL	6.56	0.82
Group_DMN_lMTL	6.36	0.68
Group_DMN_rMTL	6.73	1.00
Group_DMN_rPHG	5.29	0.79
Group_DMN_lPHG	4.70	0.39
Group_Saliency_rDLPFC	6.12	0.75
Group_Saliency_lDLPFC	4.99	0.67
Group_Saliency_lInsula	5.61	0.58
Group_Saliency_rInsula	6.10	0.83
Group_Saliency_ACC	8.20	1.23
Group_leftThalamus	5.96	0.83
Group_rightThalamus	6.87	0.84
Group_leftHippocampus	10.97	1.05
Group_rightHippocampus	10.71	1.24

***Table 7.1**: Euclidian distances between peak T-stat voxels found using primary peak modulation and post-stimulus modulation. Regions listed are all of the ROIs identified in the T-stat maps. Distances are means over all subjects, and errors are the standard error over subjects.*

Peak voxel timecourses were taken for all of the locations in Table 7.1, for each subject. Group BOLD timecourses from regions within strongly modulated networks (DAN, DMN, SN) are shown in Figure 7.10. Timecourses from the locations of maximal primary response modulation are shown in Figure 7.10A whilst timecourses from the locations of maximal post-stimulus modulation are shown in Figure 7.10B. The equivalent normalised timecourses are shown in Figure 7.10C-D. When specifically targeting voxels of maximal post-stimulus modulation, the effect of condition on BOLD responses in the post-stimulus time window is significant in all networks both before and after normalisation (Figure 7.10, panels B and D).

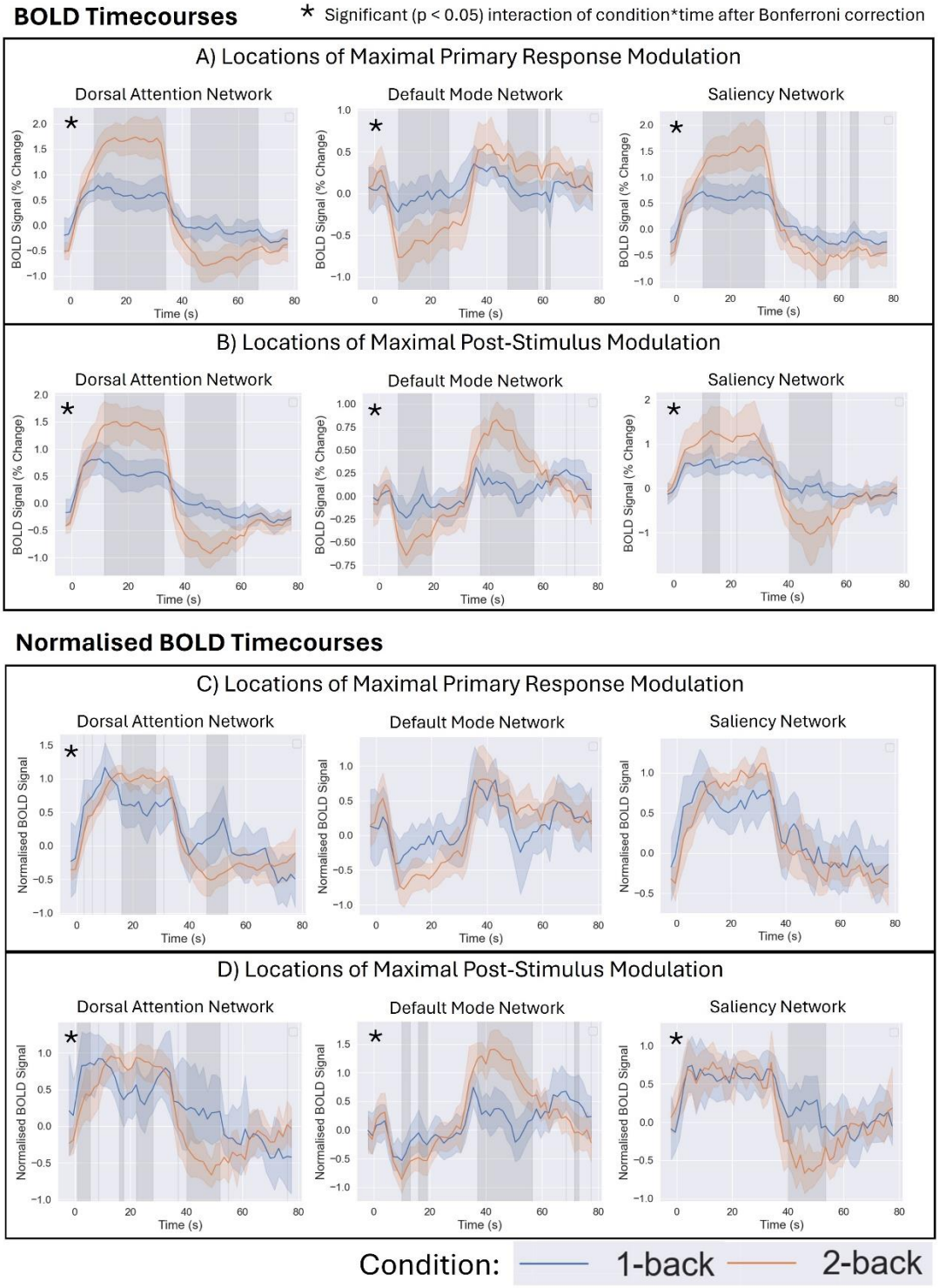


Figure 7.10: *Group average timecourses from three functional networks, clearly modulated by the n-back task. C-D show the same timecourses, normalised by dividing each timepoint by the mean during the primary peak (6 – 29 s). An asterisk (*) denotes significant (after Bonferroni correction) effect of condition*time ($p < 0.05$, two-way repeated measures ANOVA). Grey shaded regions mark time periods of significant modulation with condition ($p < 0.05$, post-hoc t-test).*

Figure 7.11 shows the results of the trialwise linear regression of primary and post-stimulus mean values. When using voxels of peak post-stimulus modulation, all networks showed a significant ($p < 0.05$, paired t-test) difference after Bonferroni correction between the two conditions following removal of the linear fit, in agreement with the results in Figure 7.10.

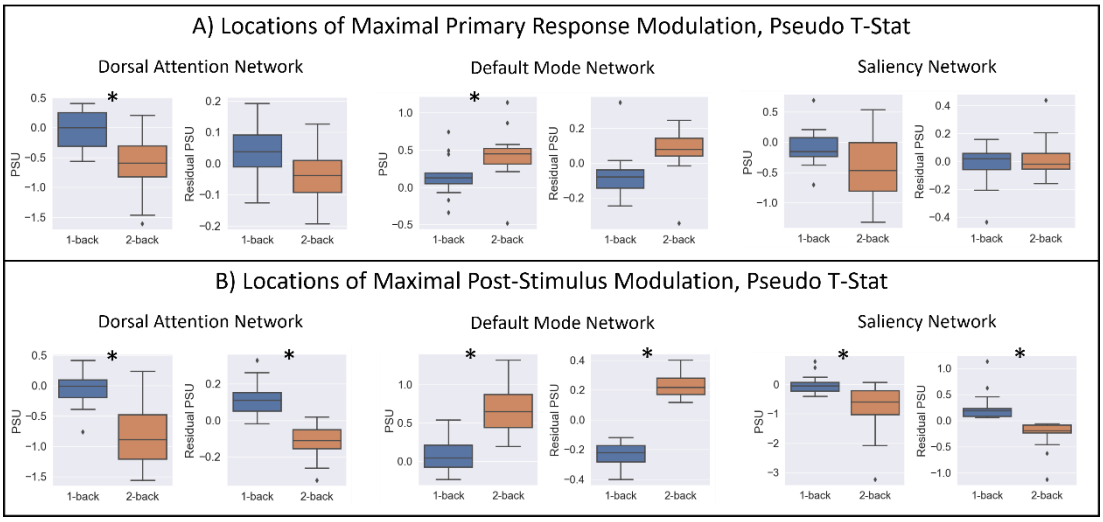


***Figure 7.11**: Regression method, applied to the pseudo T-stat peaks, to assess whether post-stimulus BOLD modulates distinctly to the primary response. The left panel for each network shows the original data measured from each subject. The right panel shows after the removal of the linear fit between trialwise primary and post-stimulus BOLD peak. * denotes significant ($p < 0.05$, paired t-test) difference in post-stimulus amplitude between conditions.*

7.5.3 Peak Pseudo T-Stat in Deep Brain Regions

Our T-stat analysis also identified modulations of both the primary peak and post-stimulus BOLD response in deep brain regions, including both the thalamus and hippocampus. Timecourses for these regions are shown in Figure 7.12, as well as the normalised equivalents to highlight excess post-stimulus modulation that is not explained by the primary peak. The timecourses taken from locations of maximal post-stimulus modulation show relatively large undershoots/overshoots, with hippocampal overshoots showing a greater percentage change in the 2-back condition for the post-stimulus response than the primary negative peak.

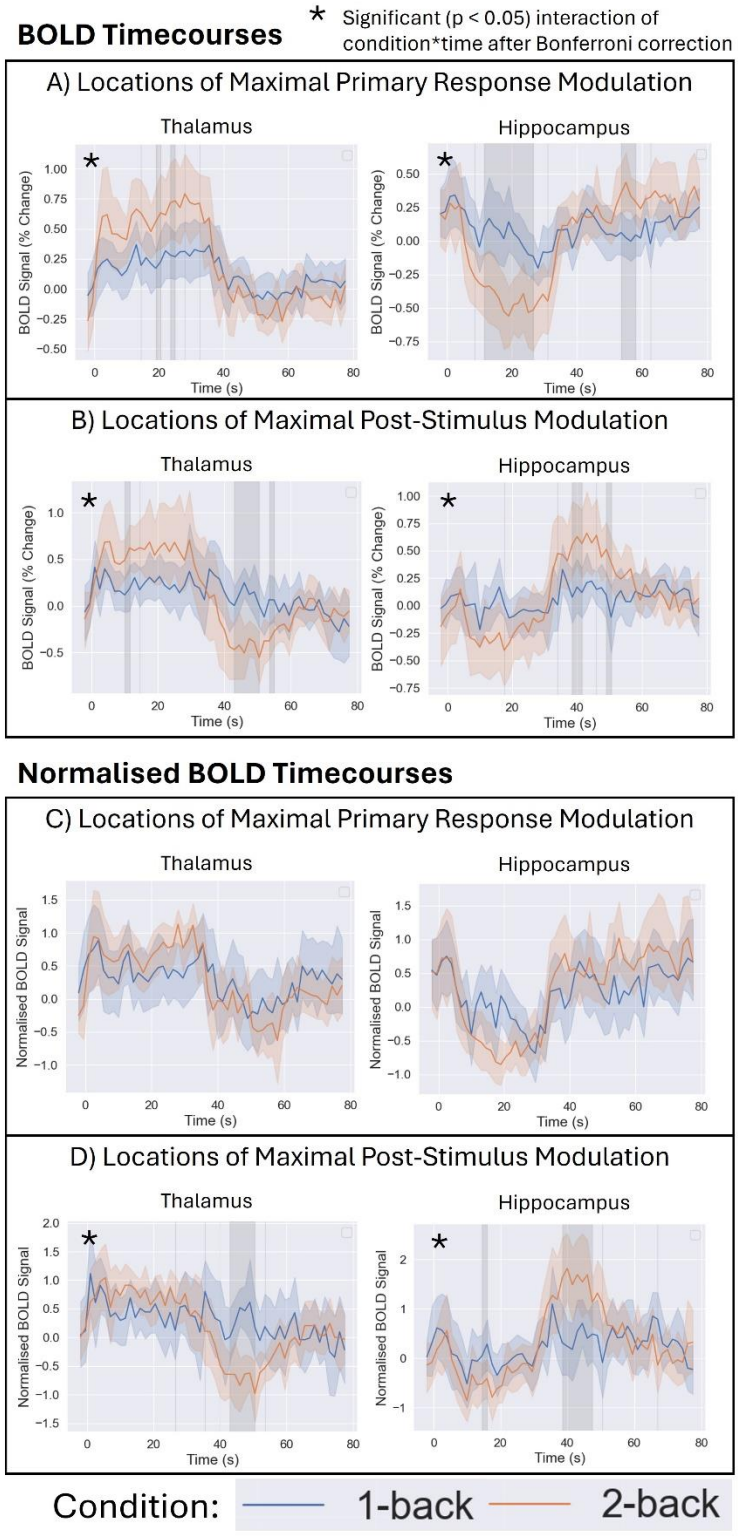


Figure 7.12: *Timecourses from voxels of peak modulation during the primary peak (panel A) and the post-stimulus BOLD response (panel B). The equivalent primary and post-stimulus peak normalised timecourses are shown in panels C and D, respectively. An asterisk (*) denotes significant (after Bonferroni correction) effect of condition*time ($p < 0.05$, two-way repeated measures ANOVA). Grey shaded regions mark time periods of significant modulation with condition ($p < 0.05$, post-hoc t-test).*

As with the GLM and T-stat peaks, we also performed the regression analysis on these deep brain region peaks to assess whether post-stimulus responses contained excess trial-wise variance that was not explained by the primary peak. These results are shown in Figure 7.13. When using the peaks from the post-stimulus modulation T-stat, both the thalamus and hippocampus showed significant excess modulation after removal of the effects of the primary peak.

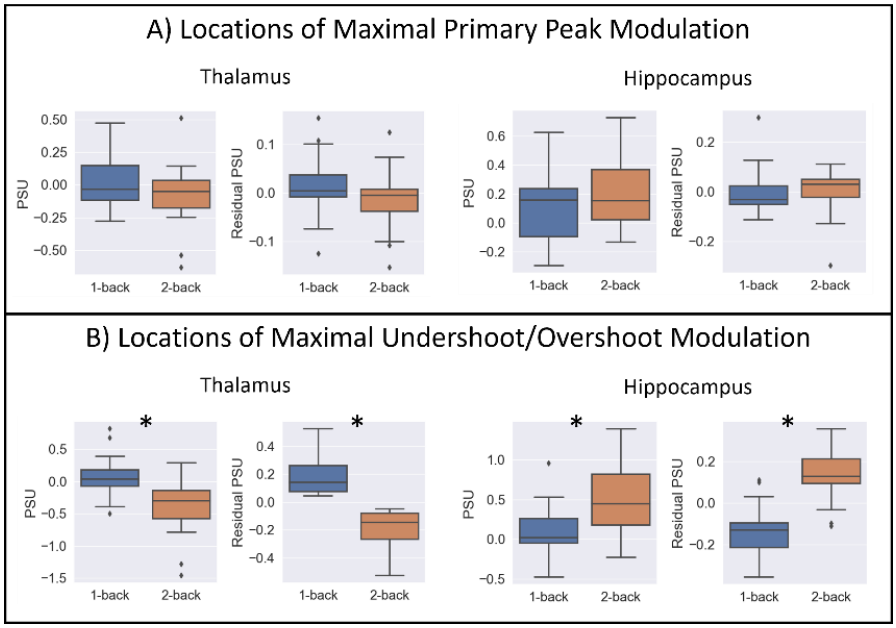


***Figure 7.13**: Regression method, applied to the pseudo T-stat peaks in deep brain regions, to assess whether post-stimulus BOLD modulates distinctly to the primary peak. The left panel for each network shows the original data measured from each subject. The right panel shows after the removal of the linear fit between trialwise primary and post-stimulus BOLD peak. * denotes significant (p< 0.05, paired t-test) difference (after Bonferroni correction) in post-stimulus amplitude between conditions.*

7.6 Discussion

The post-stimulus BOLD response remains poorly understood, and its origins highly debated (van Zijl et al., 2012). This study aimed to contribute to the growing evidence that post-stimulus BOLD has neuronal contributors (Mullinger et al., 2013, Chen and Pike, 2009, Sadaghiani et al., 2009, Mullinger et al., 2017) by determining whether there are functionally relevant modulations of post-stimulus BOLD that are distinct from the primary response. Using both a traditional GLM analysis and T-stat approach, we observed post-stimulus BOLD responses in several functional networks (DAN, DMN, SN) as well as deep grey matter structures (thalamus, hippocampus) which are difficult to study with MEG alone. We showed that locations of maximal primary and post-

stimulus BOLD modulations are spatially distinct using a T-stat approach, separately targeting the two components of the response, and measuring Euclidian distances between the peaks of each contrast, with spatial separation of around 2 – 5 voxels (4 – 10 mm) (Table 7.1). We then showed, by normalising timecourses from these peak locations to the mean height of the primary response, that voxels of greater condition-dependent post-stimulus modulation had a distinct component of the post-stimulus BOLD response that was not explained by primary response amplitude, in all of the activated networks (Figs 7.10, 7.12). This observation was corroborated by an additional analysis which showed that primary and post-stimulus BOLD amplitudes modulate independently on a trial-by-trial basis, when using voxels of peak post-stimulus modulation (Figs 7.11, 7.13).

7.6.1 Spatial Dissociation of Primary and Post-Stimulus BOLD Responses

The use of a fixed HRF remains a limitation of BOLD fMRI analysis, given the between-subject variation of HRF in normal populations (Aguirre et al., 1998, Lu et al., 2007, Handwerker et al., 2004b), as well as variation due to factors such as age (Mayhew et al., 2022, West et al., 2019). Our T-stat approach to detecting BOLD activations (Fig. 7.8 and 7.9) removed the assumption that the primary and post-stimulus components of the BOLD response must be fixed together, both in spatial distribution and relative amplitudes. Methods such as this are not new in fMRI. One of the first methods to analyse activations in fMRI data was a t-test between a set of active images (during stimulation) and baseline images (no stimulation), with each voxel being tested independently (Hathout et al., 1994). Other studies of a similar time, although not explicitly performing a t-test, used subtraction of images taken during an active and baseline state, thus achieving similar results (Turner et al., 1991, Bandettini et al., 1993). The novelty of our method is in the specific spatial targeting of post-stimulus BOLD modulations, which, to our knowledge, has not been investigated in this way previously. Table 7.1 shows that there are substantial differences in the locations of peak modulation during the primary and post-stimulus time windows, supporting existing hypotheses that the primary and post-stimulus BOLD responses have different neuronal contributors (Moon et al., 2021, Mullinger et al., 2017), that may manifest as spatial differences in modulation peaks. This forms a parallel with electrophysiological PTRs, specifically the PMBR, which has been shown to have distinct spatial origins in the motor network compared to the MRBD (during-task response) (Jurkiewicz et al., 2006a, Stancak and Pfurtscheller, 1995, Fry et al., 2016, Pakenham et al., 2020), with the PMBR being generated towards more anterior, higher-order motor-related regions.

7.6.2 Dynamic Decoupling of Primary and Post-Stimulus BOLD Responses

As well as spatial separation of primary and post-stimulus BOLD peaks, we also present dynamic dissociation of these two response components in Figures 7.10 – 7.13. Historical models of post-stimulus BOLD (Buxton et al., 1998, Kruger et al., 1996), involving sustained elevation of either $CMRO_2$ or CBV, imply a post-stimulus undershoot that is proportional to the primary peak (see Chapter 2). Disproportional changes in post-stimulus BOLD response compared to the primary response would imply separate neuronal contributors that are distinct from those that drive the primary peak (Sadaghiani et al., 2009).

The results in Figures 7.10 and 7.12 show that there are areas of the brain, often in known network structures, where the effect of increasing working memory load modulates the post-stimulus BOLD response disproportionately to the primary BOLD response. In these regions, namely the DAN, DMN, SN, thalamus and hippocampus, we observe significant ($p < 0.05$, post-hoc t-test) modulations in excess of the primary response, supporting previous evidence of dissociation of the primary and post-stimulus BOLD responses (Sadaghiani et al., 2009, Mullinger et al., 2013, Mullinger et al., 2017). Figures 7.11 and 7.13 also show that this effect is consistent on a trialwise basis. It must be noted that this is only true in voxels that were targeted based on post-stimulus modulation, although we do not think this detracts from the argument, rather, it supports the case that the post-stimulus response is spatially distinct and provides weight to the need for non-GLM approaches to fMRI analysis which do not bias towards the primary peak.

7.6.3 Vascular Interpretation

The neurovascular coupling of the BOLD response is complex, given that the response is formed by a combination of $CMRO_2$, relating to energy consumption by neuronal ion pumps, CBV, relating to relaxation of smooth muscle and subsequent dilation of blood vessels following neuronal activation, and CBF, reflecting the changes in blood flow that accompany vessel dilation. As discussed in Chapter 2, one of the earliest models of the post-stimulus undershoot was the balloon model, which states that the undershoot is caused by a prolonged increase in CBV following neural activation, after both $CMRO_2$ and CBF have dropped to baseline (Buxton et al., 1998).

One could argue that the post-stimulus undershoots that we report in the DAN and SN are driven by prolonged CBV increase. However, the presence of distinct overshoots that modulate with condition cannot be explained by the balloon model, suggesting that the responses we report must be, at least partially, driven by neuronal activity. In

addition, we report post-stimulus responses that are equivalent (or greater) in magnitude than the preceding primary response (e.g. DMN timecourse in Fig. 7.10B). These large post-stimulus responses, within the framework of the balloon model, would likely require CBV to not decrease at all, or momentarily increase, in the post-task period, which seems biomechanically implausible.

Another explanation is that the large post-stimulus undershoots arise due venous drainage in voxels close to the neuronal activity. Whilst draining vein effects are a well-known confound of BOLD fMRI (Nencka and Rowe, 2007, Krings et al., 1999), it is hard to see the biophysical mechanism by which a positive primary response in one region could cause a negative post-stimulus response in a downstream region. This would likely require an increase in CBV in the downstream region, or alternatively an increase in deoxyhaemoglobin, while a decrease is more likely (due to the primary BOLD response). In addition, cerebral venous flowrates have been measured at 4 – 17 cm/s (Valdueza et al., 1996). The peak undershoots that we observe were a maximum of 10 mm away from peak primary responses, thus the downstream effects would happen on a time scale of 0.06 – 0.25 s, whilst we observe the post-stimulus responses peaking around 10 s after the primary response, and lasting for greater than 15 s in most cases. Despite this, further study must be conducted to delineate the neuronal and vascular contributions to the large post-stimulus responses that we report using the ~~T~~-stat method.

7.6.4 Relationships Between MEG and fMRI Post-Stimulus Responses

Overall, we see some obvious similarities between the MEG PTRs reported in Chapter 5 and the post-stimulus BOLD responses reported here. The most striking of these is in the DAN, where we see a clear positive (ERS) MEG PTR in alpha/beta bands (Fig. 5.3), accompanied by a BOLD undershoot (Fig. 7.9), each modulating with the opposite sign. Given the putative relationship between the BOLD undershoot and neuronal inhibition (Sadaghiani et al., 2009, Mullinger et al., 2013, Mullinger et al., 2017, Moon et al., 2021), the results presented in this chapter support our proposed role of the alpha/beta PTR in the DAN as a marker of increased neuronal inhibition required to bring network activity back to resting levels. However, our BOLD results provide more detailed and widespread topographical information about the post-task period of activity, revealing a more bilateral DAN compared to our MEG results, as well as the SN, and the thalamus, which all see a similar post-stimulus undershoot in BOLD. These additional nodes could provide information about the propagation of the PTR through a wider network, perhaps being generated in the DAN which is directly recruited for task demands and propagating through intracortical and cortico-thalamic

circuits to reestablish resting levels of activity. The reason that MEG only detects alpha/beta PTR activity in the DAN may be the constraints on the sources which MEG can measure, namely, synchronous inputs to pyramidal neurons within grey matter (see Chapter 2 and 3), with limited depth sensitivity (Hillebrand and Barnes, 2002). It is possible that these specific measurable events are more prominent during the generation of the PTR, while the effects of this response on a wider network become too dispersed and asynchronous to be measurable by MEG.

Our results in Figures 7.8 and 7.9 show a considerable number of regions where there are negative primary peaks, followed by positive post-stimulus response, i.e., overshoots. Responses of this type are not properly accounted for in non-CBF models of post-stimulus BOLD (Kruger et al., 1996, Frahm et al., 1996, Buxton et al., 1998, Buxton et al., 2004). Lack of discussion on the origins of post-stimulus overshoots is not surprising given the fact that negative primary peaks are less frequently reported than the positive case. The three main cases where negative primary BOLD peaks are measured are: 1) in regions surrounding those that are activated by a stimulus or task (Devor et al., 2007, Shmuel et al., 2006); 2) in ipsilateral sensory regions during lateralised stimuli (Kastrup et al., 2008, Klingner et al., 2010); 3) in the DMN, negatively tracking attentiveness (Anticevic et al., 2012, Ceko et al., 2015). Unlike many examples in the literature (Sten et al., 2017, Anticevic et al., 2012, Grimm et al., 2009), we see pronounced overshoots in the DMN (Fig. 7.9), which may be attributed to either increased SNR at 7T (compared to more standard 1.5 – 3T) or our prolonged rest period of 49 s which allowed the BOLD signal to fully reach baseline prior to the next trial. In line with evidence that links positive BOLD to increased excitation (Logothetis et al., 2001, Logothetis, 2008, Moon et al., 2021), and negative BOLD to increased inhibition (Shmuel et al., 2006, Devor et al., 2007, Mullinger et al., 2017, Moon et al., 2021), we suggest that the post-stimulus overshoot in the DMN reflects increased excitation required to bring the task-negative DMN back to baseline levels of activity. Following on from evidence presented by Mullinger *et al* that post-stimulus undershoots are in part driven by post-stimulus rebounds in alpha EEG power (Mullinger et al., 2017), we suggest that the overshoot in the DMN may in part be driven by a post-stimulus dip below baseline in oscillatory power. We report a post-stimulus dip in oscillatory power in Chapter 5 (Fig. 5.5) in the theta band (4 – 8 Hz), following an n-back task, which became more negative with working memory load, and spatially overlapped with frontal and temporal nodes of the DMN (Fig. 5.3). This, along with evidence that relates DMN activity in BOLD to concurrently measured frontal EEG (Meltzer et al., 2007, Scheeringa et al., 2008), supports the hypothesis that post-

stimulus haemodynamic and electrophysiological responses are underpinned by the same neuronal contributors. Additionally, it should be noted that in general, theta oscillations are found to modulate in the opposite direction to BOLD (Scheeringa, 2011, Mizuhara et al., 2004).

Another interesting feature of our results, specifically results relating to the post-stimulus ~~T~~-stat contrast (Fig. 7.9 and 7.11), is the presence of voxels that show considerable post-stimulus BOLD responses in 2-back, with little to no post-stimulus effects in the 1-back condition. Our MEG study using the same task found a very similar result, shown in Chapter 5 (Fig. 5.5, A5.1), with many of the activated regions showing substantial PTRs (both above and below baseline) for 2-back, with little-to-no PTR for the 1-back condition, despite the fact that all conditions induced a substantial modulation in oscillatory power during the task. This parallel between the two datasets with the same task supports arguments that post-stimulus BOLD responses may have similar neuronal contributors as post-task M/EEG responses (Mullinger et al., 2013, Mullinger et al., 2017), although direct comparison cannot be made between our two studies as a different participant group was used and data from the two modalities was not taken concurrently.

7.6.5 Post-Stimulus Responses in Deep Grey Matter

The study of neural activity in subcortical structures remains a difficult endeavour, often requiring invasive techniques (see Chapter 1) which are only performed on patients with debilitating neurological illnesses, or animals. The relationship between neuronal and haemodynamic activity makes fMRI a valuable tool for indirectly studying the activity of deep brain regions such as the thalamus and hippocampus. In this study, we have shown that the thalamus and hippocampus exhibit distinct post-stimulus BOLD responses (Fig. 7.12), taking the form of undershoots and overshoots, respectively. Notable undershoots in the thalamus have previously been reported (Yamamoto et al., 2014, Carney et al., 2010), while the presence of an overshoot in hippocampal BOLD is more varied between studies (Nilsson et al., 2013, Schridde et al., 2008). To our knowledge, previous studies have not attempted to spatially or dynamically distinguish primary and post-stimulus BOLD responses in deep grey matter structures.

Multiple lines of evidence suggest that positive BOLD responses relate to local increased excitation (Logothetis et al., 2001, Logothetis, 2008, Moon et al., 2021), while negative BOLD responses relate to local increased inhibition (Shmuel et al., 2006, Devor et al., 2007, Mullinger et al., 2017, Moon et al., 2021). We can therefore

assume that during the post-stimulus BOLD response, there is a shift towards inhibition in the thalamus and a shift towards excitation in the hippocampus. This is in keeping with the results reported in Chapter 5, where we speculated that during the PTR, a shifting of task-positive and task-negative network activity occurs, specifically, suppression of the DAN, reflected in the alpha/beta rebound, and re-activation of the DMN, reflected in the theta undershoot. There are known interactions between the thalamus and the DAN (Rafal and Posner, 1987, Danziger et al., 2004, Saalmann et al., 2012), specifically, temporal coordination of cortical attentional nodes by the pulvinar (Kastner et al., 2020), a posterior thalamic nucleus commonly associated with vision. In addition, the hippocampus is commonly associated with the DMN, with multiple studies showing that long term memory relies on cortico-hippocampal interactions within this network (Rugg and Vilberg, 2013, McCormick et al., 2010). These established relationships suggest that the responses we have observed in each modality, namely, cortical PTRs in MEG, and subcortical post-stimulus BOLD responses, may be related, although further work with concurrent and/or invasive measurements is required to prove this relationship.

We hypothesised in Chapter 6 that coincident bursting in widespread intracortical networks may reflect long range signal transmission, leading to a shift in network activity. Combining our evidence with previous literature which relates the alpha/beta PTR, and alpha/beta oscillations in general, with top-down inhibition (Halgren et al., 2019, Van Kerkoerle et al., 2014, Klimesch et al., 2007, Engel and Fries, 2010, Jensen et al., 2005, Pfurtscheller et al., 2005, Mullinger et al., 2017), it is likely that the thalamus is receiving feedback signals from higher order intracortical networks such as the DAN and SN, reducing the information flow that becomes salient through thalamic relay. Conversely, we see a reduction in midline frontal oscillations during the PTR (Chapter 5, Fig. 5.3, 5.5), accompanied by a BOLD overshoot in the hippocampus (Fig. 7.12), which may indicate feedforward interactions led by the hippocampus to the prefrontal cortex and the rest of the DMN. However, given the novelty of the theta PTR (Chapter 5), it is hard to draw these conclusions with any certainty. Further study is needed, ideally utilising direct measures of electrophysiology, to determine the directionality of interactions between cortical and subcortical domains during the phase of activity that occurs following task cessation.

7.6.6 Limitations and Future Work

The results presented provide a promising indication that post-stimulus BOLD responses have a distinct component that modulates separately to the primary response. However, our results must be considered a preliminary exploration of these

effects rather than conclusive evidence, as we were only able to show that post-stimulus responses were dissociable from primary responses in voxels that were targeted based on peak post-stimulus modulation. This approach was not entirely circular, as a high T-stat based on post-stimulus modulation does not necessarily imply dissociation with the preceding primary response in the same voxel. Future work should build upon these results by repeating the statistics on new data, ideally with techniques that identify voxels without the constraints of HRF shape or windowed modulations.

Although our T-stat approach allowed us to study specific time windows without *a priori* assumptions of the shape of the response, the method was intrinsically more prone to noise than a GLM. This is because our chosen GLM contrast modelled all of the data, for both conditions, thus finding the voxels which followed the boxcar model most closely, over all time. On the other hand, our T-stat approach only required a difference in BOLD activity between two conditions or two time-windows, making the method prone to finding voxels with low signal in the 1-back condition. Despite this limitation, the method was able to pull out BOLD morphologies with dramatic differences to the canonical HRF, highlighting the need for flexible approaches in BOLD analysis. Other studies have used modified GLM approaches with a basis set of HRFs (Woolrich et al., 2004b, Steffener et al., 2010), allowing more flexibility in relative response amplitudes than the standard approach, but still constraining the responses to a particular form. To visualise the difference between the GLM and our various T-stat contrasts, we plotted the trial-level signal for all activated networks, for a single subject, in Appendix B. Figures B7.1 and B7.2 show trial-level signal for the 1-back and 2-back conditions, respectively. These plots also allow visualisation of the trial-by-trial SNR that was achieved by performing the experiment at 7T.

Furthermore, we tentatively discuss the potential relationships between cortical networks and subcortical structures during the PTR, although our data has limited signal quality in deep brain regions (Fig. B7.1 and B7.2). This limitation was primarily due to the relatively small size of these regions, compounded by the effect of employing whole-brain coverage with high spatial resolution – a key requirement of our study to properly characterise post-stimulus responses across the brain. Now that we have characterised these responses across the entire brain, it would be interesting to perform further 7T fMRI experiments which are focussed on only the deep brain structures, including the thalamus and hippocampus. Smaller field of view would allow for smaller voxel sizes, reducing partial voluming effects and potentially allowing the identification of sub-structures such as the thalamic nuclei which are known to play a

role in attentional processes in the cortex (Kastner et al., 2020, Cunningham et al., 2017). This could also be coupled with concurrent EEG recordings, allowing the direct measurement of higher order cortical structures during the post-stimulus BOLD response in subcortical structures.

Finally, despite the promising comparisons that we made here between our MEG and fMRI results, we are fundamentally limited by the use of different participant groups for each study. More definitive comparisons could be made by taking concurrent EEG-fMRI, which would allow us to look at trial-by-trial relationships between cortical EEG PTRs and fMRI network responses which include both cortical and subcortical structures. Alternatively, performing MEG and fMRI in subsequent sessions, for the same subjects, would allow for within-subject comparisons of the two modalities, whilst utilising the full benefits of each technique (see Chapter 1).

7.7 Conclusions

Despite the popularity of task-based fMRI as a method to investigate brain function, the origins of the post-stimulus BOLD response remain unclear. This is in part due to the prevalence of GLMs to analyse fMRI data, which constrain the shape of the haemodynamic response and implicitly bias activation maps to the primary peak. We remove these constraints with a relatively simple pseudo T-statistic approach, allowing us to separately target modulations of the primary and post-stimulus BOLD response in relation to changing working memory load. Our results revealed peak post-stimulus modulations 4 – 10 mm from peak modulations of the primary response within a particular ROI. Timecourses at voxels of peak post-stimulus activity showed large modifications in their dynamics compared to canonical haemodynamic responses. Post-stimulus modulations were shown to modulate disproportionately to the primary response in the same voxel, although this result was only seen in voxels of peak post-stimulus modulation. This was consistent on a trial-by-trial basis, shown using linear regressions between primary and post-stimulus BOLD responses. Additionally, we observed post-stimulus undershoots and overshoots in the thalamus and hippocampus, respectively, suggesting potential cortico-thalamic and cortico-hippocampal network interactions during the post-stimulus response. Together our results show that the primary and post-stimulus BOLD responses can be partially decoupled by separately targeting each part of the response. In general, these results support the hypothesis that post-stimulus BOLD has neuronal contributors that are distinct from those that drive the primary BOLD response, although further work is required for statistical validation and exclusion of alternative vascular interpretations.

7.8 APPENDIX A

7.8.1 Other Pseudo T-Stat Contrasts

For completeness, we took ~~T~~-stat contrasts comparing the primary peak to "rest" (see methods for a description of the confound of this window), and the post-stimulus response to rest (windows stated in methods). The results are shown below in Figure A7.1 for the primary peak contrast, and Figure A7.2 for the post-stimulus contrast. Contrasting the primary peak to rest yields similar spatial pattern to the primary peak modulation contrast, as well as the GLM. The similarity of this ~~T~~-stat analysis to the GLM result is likely because a GLM is mostly sensitive to the primary response and these 2 analyses are the most similar, especially given that part of the post stimulus response is included within the rest window used. Interestingly, the post-stimulus versus rest contrast is clearly different to all other activation maps presented, showing primary visual, superior parietal, temporal and mid-cingulate activations that do not appear in the other maps. Investigating the timecourses from the post-stimulus versus rest contrast revealed that these nodes all behaved similarly and were therefore averaged to form the timecourses in Figure A7.2.

One explanation for this atypical BOLD response is that we are seeing so-called *transient* BOLD effects, without the sustained BOLD response that we observe elsewhere in the brain. Transient responses are known to occur at the beginning and end of task blocks, and are seen as, at least partially, separate from the primary BOLD response and post-stimulus undershoot (Fox et al., 2005, Uludağ, 2008). Fox *et al* showed that transients are a common feature of many types of task, including working memory tasks, and are spatially dissociated from the traditional (HRF) response (Fox et al., 2005). These were posited as a haemodynamic correlate to electrophysiological signals which occur at "state transitions" (onset and offset of task blocks) such as evoked potentials. This interpretation is consistent with our results, as we do not see a modulation with condition in Figure A7.2, meaning this response could be related to early stimulus processing (akin to the OSR in Chapter 5, which did not modulate with condition). Interestingly, the timecourse in Figure A7.2 does not resemble those reported in the study by Fox *et al*, as we see a small *decrease* in BOLD at block onset followed by a gradual rise which peaks just after block offset, rather than an increase in BOLD at block onset and offset, which is more typical. In addition to transients, Harms and Melcher showed that a "train" of stimuli can create a ramp effect in the BOLD (Harms and Melcher, 2002), which seems to resemble the ramp that we observe in Figure A7.2 during a train of letter stimuli. Overall, it is possible that the atypical

timecourse we observe is driven by a combination of multiple effects that are separate from those that drive the standard primary/post-stimulus BOLD response. These effects potentially relate to early neuronal processing, which occurs upon sudden changes in state (block onset, offset) and warrant separate investigation which was not the focus of this thesis.

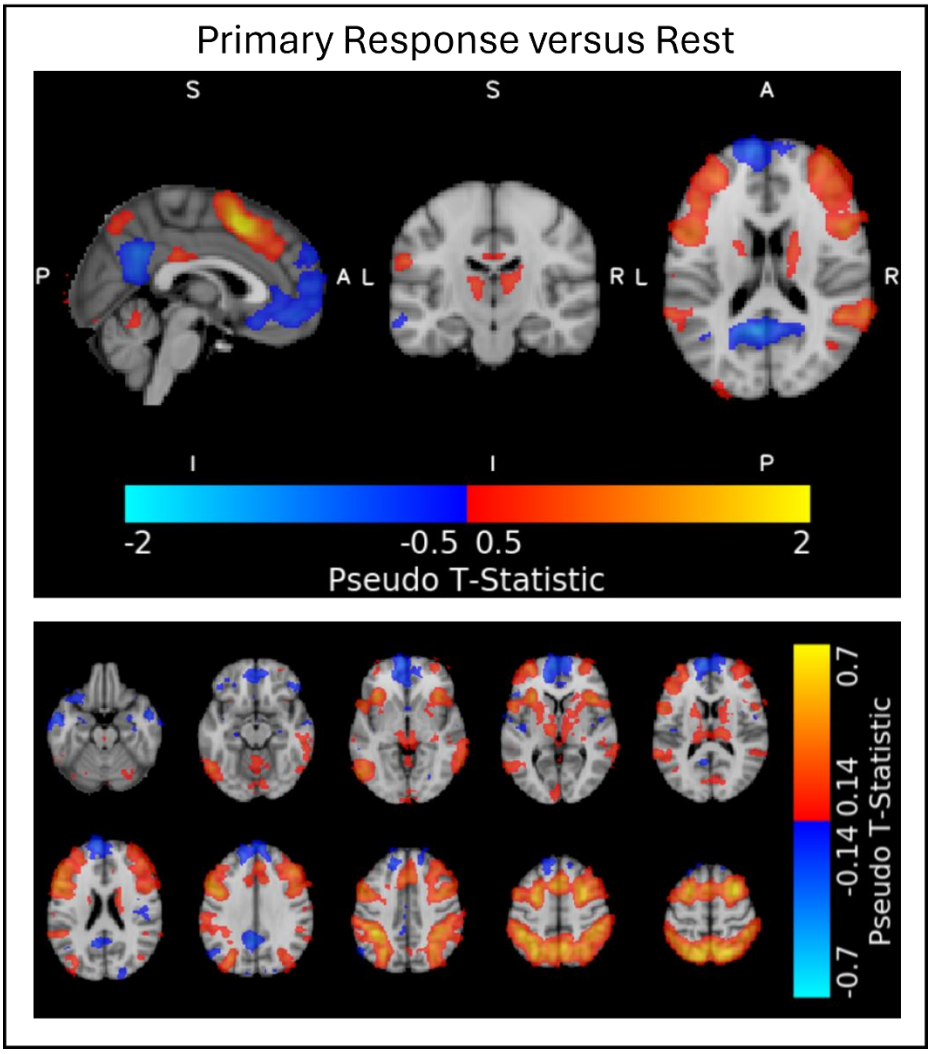


Figure A7.1*: Results from applying a ~~T~~-stat contrast of primary peak versus rest. This contrast closely reflects the GLM results in Figure 7.4.*

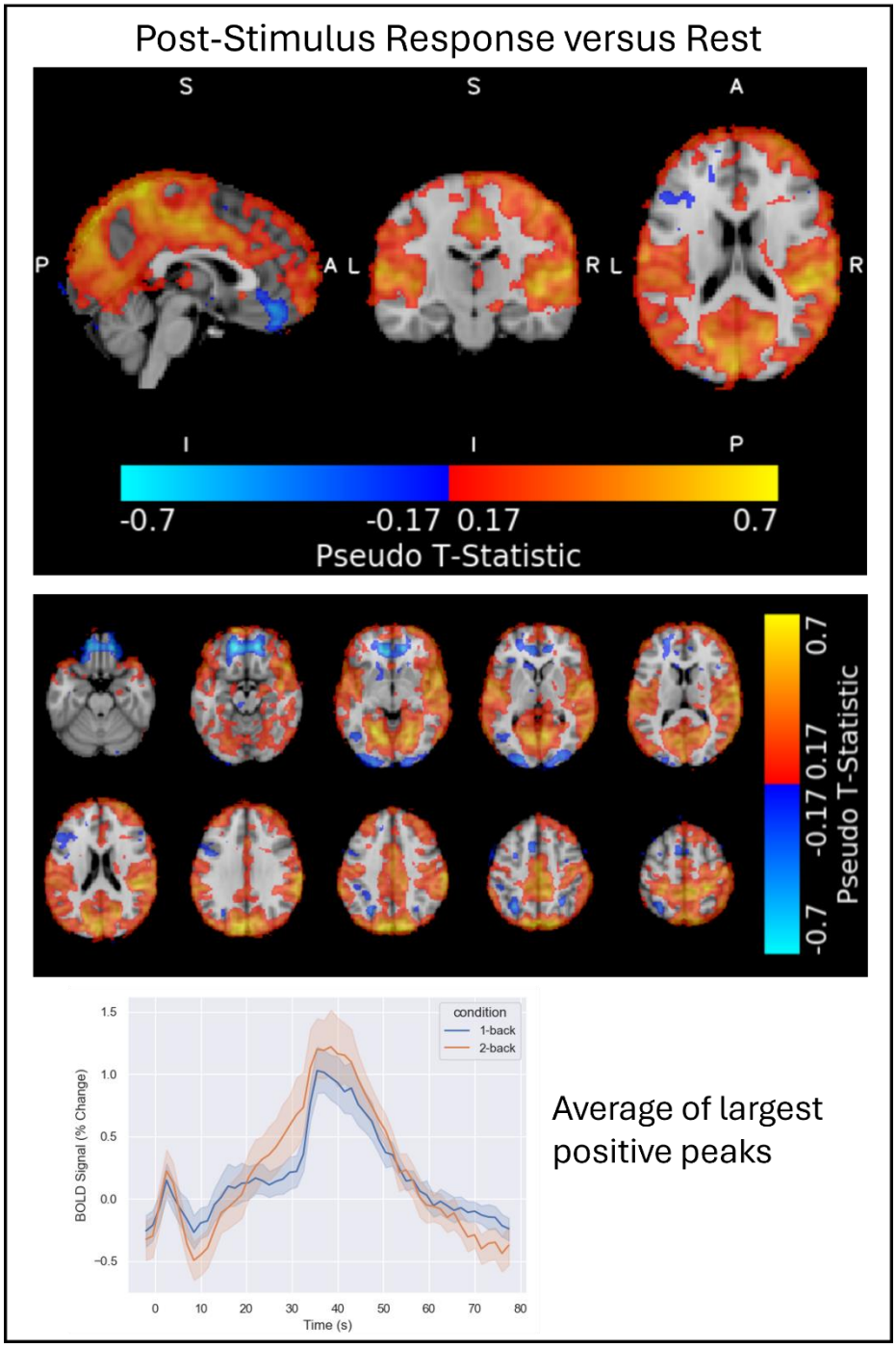


***Figure A7.2**: Results from applying a ~~T~~-stat contrast of post-stimulus response versus rest. The timecourse in at the bottom of the figure is formed from the average of timecourses from positive peaks in the ~~T~~-stat map.*

7.9 Appendix B

7.9.1 Signal to Noise of Different Contrasts

In the main text, it was noted that signal to noise ratio suffers when using a ~~T~~-stat approach compared to a GLM, due to the amount of data being used to select voxels of interest. To examine this effect, the trial-level data are plotted for a single subject,

with each trial stacked vertically, and the percentage change in amplitude at each timepoint represented by the colour. The data are plotted for each of the main networks analysed in the main text, namely the DAN, DMN, SN, thalamus and hippocampus, at peak voxels found using the GLM, as well as the T-stat contrasts relating to primary peak modulation, post-stimulus modulation, and primary peak versus rest. Clearly, 1-back (Fig. B7.1) in the modulation T-stat contrasts has less signal than the GLM, which makes sense as the contrast looks for differences between the conditions rather than modelling all of the data. However, the primary peak versus rest contrast has substantial signal in both conditions, as, similar to the GLM, this contrast finds voxels which are most affected by the block paradigm across both conditions. It should be noted that for the 2-back condition (Fig. B7.2), the post-stimulus T-stat contrast clearly pulls out features from the data which are not visible from the GLM, showing the utility of specifically targeting time windows of interest.

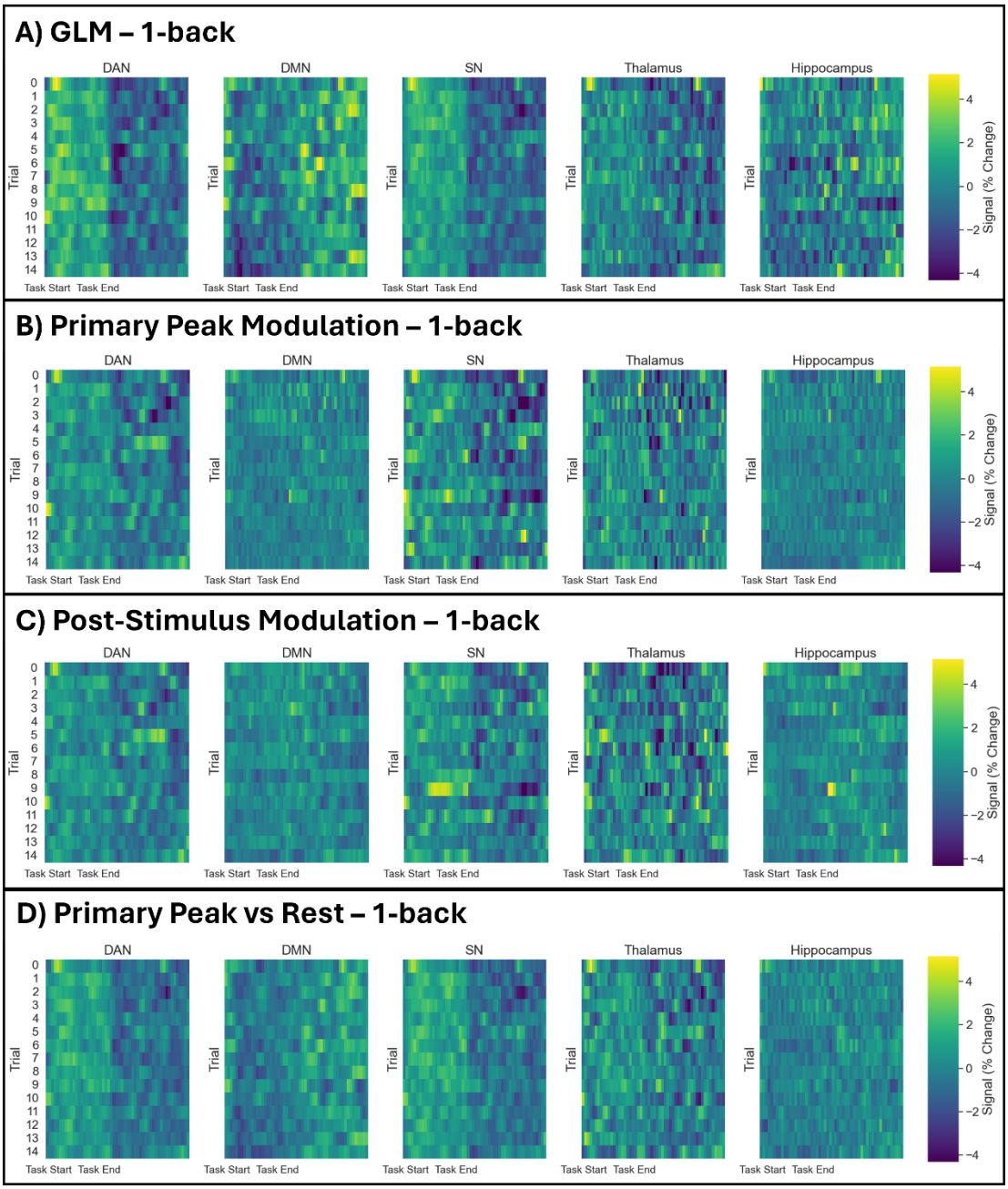


***Figure B7.1**: Trial-level signal for a single subject, at voxels of peak activity, found using the GLM (A), peak primary peak modulation (B), peak post-stimulus modulation (C) and primary versus rest (D), for the 1-back condition only. Colours represent the percentage change in BOLD signal from baseline.*

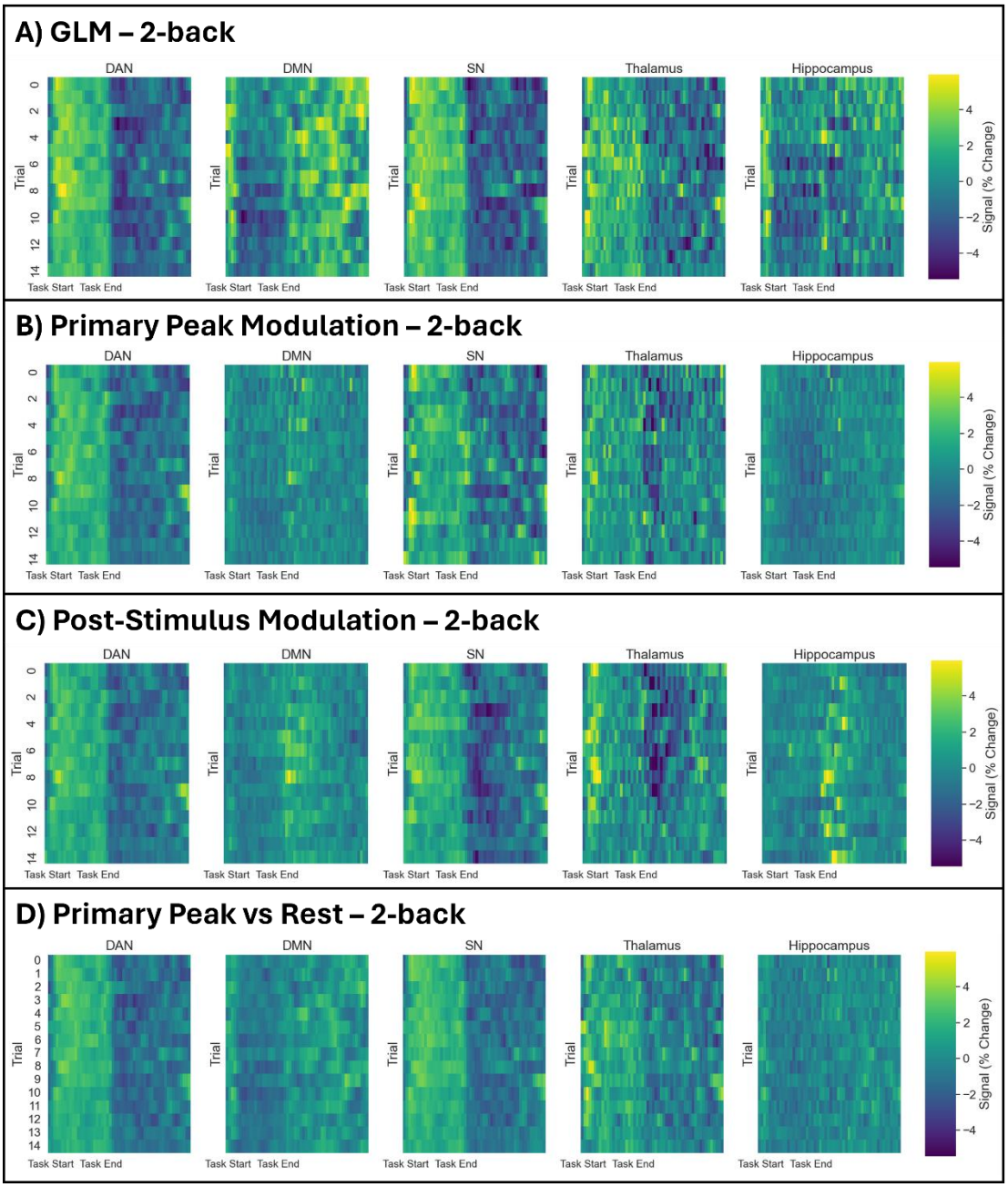


***Figure B7.2**: Trial-level signal for a single subject, at voxels of peak activity, found using the GLM (A), peak primary peak modulation (B), peak post-stimulus modulation (C) and primary versus rest (D), for the 2-back condition only. Colours represent the percentage change in BOLD signal from baseline.*

8 Conclusion

This thesis aimed to investigate the activity in the brain that occurs in the transition period between an engaged state and rest. This was addressed across three experimental chapters, utilising multimodal brain imaging techniques and taking advantage of both traditional and modern analysis approaches.

8.1 Overview of Findings

In Chapter 5, we uncovered a novel set of PTRs in the theta, alpha and beta bands following working memory processes, in both sensory and higher cognitive regions. Responses of this type were previously only studied in the motor and visual cortices following movement and visual stimulation. PTRs following working memory modulated with task condition, increasing in amplitude with working memory load. Corroborating speculations made in previous literature, we found that reaction times, a behavioural marker of task difficulty, are predictive of posterior alpha PTRs, suggesting a link between the cognitive load during the task period and post-task oscillatory power. Importantly, we found that the during-task response was not predictive of PTR amplitude, suggesting that the PTR holds unique information about cognitive processes which occurred during the preceding task. Given the established neuroscientific and clinical relevance of the PMBR, i.e., the beta band PTR following movement, this work takes an important step in broadening our understanding of PTRs as a brain-wide phenomenon, not limited to sensory paradigms or brain regions.

In Chapter 6, PTRs following working memory were compared to PTRs in a visuomotor dataset using hidden Markov models, which successfully captured PTR activity in a single state. A novel application of k-means clustering was used to group univariate states across the brain. Importantly, this approach was entirely independent of response frequency or task timings, a limitation of previous studies that can lead to bias and overlooked information. In both cases, the PTR state corresponded to transient high amplitude oscillatory events which can be described as bursts, which form smooth responses when averaged over trials. These bursts had very similar region-wise characteristics between tasks, including durations and spectral content. Using a spatial network decomposition, we found that PTRs are supported by coincident burst events across vast areas of the cortex, as well as in more focal task-specific networks, suggesting a role in re-establishing long-range connectivity between resting networks. This work provides evidence that PTRs across different tasks are driven by a similar underlying neural phenomenon and demonstrates the utility of

bursting models for looking at novel response characteristics with minimal a priori assumptions.

The final experimental chapter used 7T fMRI to look at the haemodynamic counterparts to the electrophysiological PTRs explored in the previous two chapters, using a similar working memory task to Chapter 5. Our pseudo T-statistic approach revealed modulations of the primary and post-stimulus BOLD responses with working memory load in several known functional networks, including the attention, salience and default networks, along with the thalamus and hippocampus (which are difficult to study with MEG). Post-stimulus responses were shown to modulate separately from the primary response, both spatially, with the location of peak modulation occurring in different voxels, and dynamically, with post-stimulus amplitude containing excess variance not explained by the primary response. These results contribute to evidence that the post-stimulus BOLD response has neuronal contributors that are distinct from those that drive the primary response. We also found non-standard haemodynamic responses to the task by contrasting post-stimulus amplitude with rest in a pseudo T-statistic, which would have been overlooked by traditional analysis methods. Overall, our results support the hypothesis that the post-stimulus BOLD response is driven in part by the same neuronal activity as the electrophysiological PTR, meaning that fMRI provides a valuable tool to study the network dynamics underlying this period of activity at high spatial resolution.

8.2 Future Work

The work presented in this thesis provides a promising step towards understanding the phase of neuronal activity occurring between periods of task and rest. However, further steps can be taken to answer the questions that have arisen from this work.

Firstly, given the known relationship between neurological illness and PMBR amplitude, future studies should investigate whether PTRs following non-motor activity, such as working memory, hold the same relationship. The apparent ubiquity of PTRs across brain regions and cognitive activities suggests that PTRs may provide valuable insight into neuropathology, particularly dysfunction of inhibitory control mechanisms, that could guide future treatment strategies in patient populations. It is conceivable that some illnesses have a greater impact on cognitive control of non-motor networks, meaning PTRs in higher cognitive regions, including the attention and default mode networks, could feasibly provide a set of novel clinical biomarkers. In addition, if post-stimulus BOLD responses are driven in part by the same neuronal mechanisms as the MEG PTR, these could be used to assess cognitive control

mechanisms in deep grey matter structures including the thalamus and hippocampus. As these deep brain regions are heavily involved in most aspects of human cognition, the study of PTRs in these regions is essential to achieving a better mechanistic understanding of cognitive control in both healthy and pathological populations.

Our network decomposition results, using HMM burst timecourses, revealed a canonical network structure formed of coincident bursts, which was very consistent across visuomotor and working memory tasks. Our analysis and discussion were specifically focussed on how PTR activity was supported by these network structures. However, application to patient groups may reveal a connectomic basis for neurological illness (Rier et al., 2021, Gascoyne et al., 2021), allowing us to determine the particular networks that are affected in patients compared to controls, in terms of within-cluster connectivity and cluster probability throughout a task. The same principle could be applied to developmental studies to find connectomic markers of normative brain development (Taylor et al., 2019, Schäfer et al., 2014). In addition, following on from our results that related reaction times to alpha PTRs, future studies should investigate whether cluster probability could explain more of the variance in reaction times than oscillatory power in a particular region.

One of the strengths of our work was the use of particularly long rest periods, allowing us to properly resolve PTRs in both MEG and fMRI. However, an obvious limitation of this approach was the unnatural pause between activity, extending the scan time dramatically and increasing fatigue in participants. In certain populations, including children and patients with neurological illness, it may be impractical to scan for such long periods, and the increase in mind-wandering and movement that could occur during the long rest periods may confound the results. Our work has provided the foundational understanding of PTRs, including implicated regions and characteristic timescales. In addition, we provide a methodology that is free from the need to do baseline correction using burst probability, which is an absolute measure. Theoretically, using these types of methodologies, brain function could be assessed using only a few oscillatory bursts, without needing a large number of trials to separate signal from noise. Burst timings could be analysed in relation to facial monitoring and motion tracking to provide implicit behavioural events and natural rest periods, reducing the reliance on rigid paradigm structures. Overall, these advancements mean that future studies may adopt a more naturalistic approach, with shorter rest periods and more complex paradigms, whilst remaining cognisant of the effects that PTRs may have on oscillatory power whenever there is a step-change in cognitive load.

Although we uncovered several similarities between electrophysiological and haemodynamic PTRs, these relationships cannot be interrogated in depth due to the use of different participant groups and large time lag between studies. Concurrent recording using EEG and fMRI would allow us to measure trial-wise relationships between oscillatory PTRs and functional network activity, across both superficial and deep brain networks. Specifically, this may be able to confirm the relationship between the attention network beta rebound and the corresponding BOLD undershoot, as well as frontal theta undershoots and the default mode network BOLD overshoot. These frequency bands are difficult to study with EEG-fMRI due to MR-induced artefacts, however, recent advancements in EEG artefact correction (Chowdhury et al., 2019, van der Meer et al., 2016) may improve upon some of these issues.

Concurrent EEG-fMRI may also give us clues as to the role that deep brain structures such as the thalamus and hippocampus play in the generation or propagation of the PTR, which could be inferred from trial-wise relationships between BOLD dynamics in deep brain structures and superficial EEG measurements. It is also possible that the newer generation of MEG systems, using optically-pumped magnetometers (Schofield et al., 2022), may provide a means to directly measure thalamic and hippocampal PTRs, as these systems have theoretical advantages in depth sensitivity compared to cryogenic MEG (Boto et al., 2017).

Finally, the addition of functional MRS (Stanley and Raz, 2018), taken concurrently with EEG or in subsequent scanning sessions with other modalities, could elucidate the role of neurotransmitters in the generation of the PTR. We have speculated throughout this thesis the potential relationships between the PTR and top-down inhibition, i.e., the control of feedforward sensory information flow based on recognition of stimuli that signify that a rest period has begun. The use of functional MRS could potentially measure between-subject differences in local glutamate and GABA concentration that could then be correlated with PTR amplitude.

In summary, this thesis has revealed that post-task responses are a brain-wide phenomenon elicited by both sensory and higher cognitive activities. Given the novelty of this finding, and the new questions that have arisen regarding the effect of PTRs in wider brain networks, there remains a huge field of possible exploration, including multi-modal, clinical and lifespan studies.

8.3 Closing Remarks

We are only just beginning to unravel the mechanisms in the brain that lead to the multitude of complex behaviours exhibited in humans. Our ability to investigate brain function *in vivo* has improved rapidly over the past few decades due to the advent of technologies such as fMRI and MEG. In conjunction with this, easier access to high computational power and open-source software has enabled the development of advanced data analysis techniques, such as machine learning models, that can be readily applied to neuroimaging datasets. By leveraging these advancements in hardware and software, we are beginning to understand features in oscillatory phenomena and haemodynamics that contribute to normative brain function, and how disruption of these features may contribute to neurological illness. A multimodal approach is essential to pushing forward this development, as it allows us to observe neuronal phenomena from different perspectives, which, once consolidated, provide a more complete picture of brain function.

References

ADRIAN, E. D. & MATTHEWS, B. H. 1934. The Berger rhythm: potential changes from the occipital lobes in man. *Brain,* 57**,** 355-385.

AGUIRRE, G. K., ZARAHN, E. & D'ESPOSITO, M. 1998. The variability of human, BOLD hemodynamic responses. *Neuroimage,* 8**,** 360-9.

AKSELROD, S., GORDON, D., UBEL, F. A., SHANNON, D. C., BERGER, A. C. & COHEN, R. J. 1981. Power spectrum analysis of heart rate fluctuation: a quantitative probe of beat-to-beat cardiovascular control. *science,* 213**,** 220-222.

ANDERSEN, P. & ANDERSSON, S. A. 1968. Physiological basis of the alpha rhythm. *(No Title)*.

ANDERSSON, J. L., SKARE, S. & ASHBURNER, J. 2003. How to correct susceptibility distortions in spin-echo echo-planar images: application to diffusion tensor imaging. *Neuroimage,* 20**,** 870-888.

ANTICEVIC, A., COLE, M. W., MURRAY, J. D., CORLETT, P. R., WANG, X. J. & KRYSTAL, J. H. 2012. The role of default network deactivation in cognition and disease. *Trends Cogn Sci,* 16**,** 584-92.

ASADA, H., FUKUDA, Y., TSUNODA, S., YAMAGUCHI, M. & TONOIKE, M. 1999. Frontal midline theta rhythms reflect alternative activation of prefrontal cortex and anterior cingulate cortex in humans. *Neuroscience letters,* 274**,** 29-32.

ASTLE, D. E., LUCKHOO, H., WOOLRICH, M., KUO, B.-C., NOBRE, A. C. & SCERIF, G. 2015. The neural dynamics of fronto-parietal networks in childhood revealed using magnetoencephalography. *Cerebral Cortex,* 25**,** 3868-3876.

ATTWELL, D. & LAUGHLIN, S. B. 2001. An energy budget for signaling in the grey matter of the brain. *Journal of Cerebral Blood Flow & Metabolism,* 21**,** 1133-1145.

BABILONI, C., BRANCUCCI, A., CAPOTOSTO, P., ROMANI, G. L., ARENDT-NIELSEN, L., CHEN, A. C. & ROSSINI, P. M. 2005. Slow cortical potential shifts preceding sensorimotor interactions. *Brain research bulletin,* 65**,** 309-316.

BACKUS, A. R., SCHOFFELEN, J.-M., SZEBÉNYI, S., HANSLMAYR, S. & DOELLER, C. F. 2016. Hippocampal-prefrontal theta oscillations support memory integration. *Current Biology,* 26**,** 450-457.

BAILLET, S. 2017. Magnetoencephalography for brain electrophysiology and imaging. *Nature neuroscience,* 20**,** 327-339.

BAKER, A. P., BROOKES, M. J., REZEK, I. A., SMITH, S. M., BEHRENS, T., PROBERT SMITH, P. J. & WOOLRICH, M. 2014. Fast transient networks in spontaneous human brain activity. *elife,* 3**,** e01867.

BANDETTINI, P. A., JESMANOWICZ, A., WONG, E. C. & HYDE, J. S. 1993. Processing strategies for time-course data sets in functional MRI of the human brain. *Magn Reson Med,* 30**,** 161-73.

BARDEEN, J. 1950. Wave functions for superconducting electrons. *Physical Review,* 80**,** 567.

BARDEEN, J., COOPER, L. N. & SCHRIEFFER, J. R. 1957. Theory of superconductivity. *Physical review,* 108**,** 1175.

BARONE, J. & ROSSITER, H. E. 2021. Understanding the Role of Sensorimotor Beta Oscillations. *Front Syst Neurosci,* 15**,** 655886.

BARRATT, E. L., TEWARIE, P. K., CLARKE, M. A., HALL, E. L., GOWLAND, P. A., MORRIS, P. G., FRANCIS, S. T., EVANGELOU, N. & BROOKES, M. J. 2017a. Abnormal task driven neural oscillations in multiple sclerosis: A visuomotor MEG study. *Hum Brain Mapp,* 38**,** 2441-2453.

BARRATT, E. L., TEWARIE, P. K., CLARKE, M. A., HALL, E. L., GOWLAND, P. A., MORRIS, P. G., FRANCIS, S. T., EVANGELOU, N. & BROOKES, M. J. 2017b. Abnormal task driven neural

oscillations in multiple sclerosis: A visuomotor MEG study. *Human brain mapping,* 38**,** 2441-2453.

BARTOLOMEI, F., LAGARDE, S., WENDLING, F., MCGONIGAL, A., JIRSA, V., GUYE, M. & BÉNAR, C. 2017. Defining epileptogenic networks: contribution of SEEG and signal analysis. *Epilepsia,* 58**,** 1131-1147.

BAŞAR, E., SCHÜRMANN, M., BAŞAR-EROGLU, C. & KARAKAŞ, S. 1997. Alpha oscillations in brain functioning: an integrative theory. *International journal of psychophysiology,* 26**,** 5-29.

BATES, A. T., KIEHL, K. A., LAURENS, K. R. & LIDDLE, P. F. 2002. Error-related negativity and correct response negativity in schizophrenia. *Clinical neurophysiology,* 113**,** 1454-1463.

BAUM, L. E. & PETRIE, T. 1966. Statistical inference for probabilistic functions of finite state Markov chains. *The annals of mathematical statistics,* 37**,** 1554-1563.

BECKMANN, C. F., JENKINSON, M. & SMITH, S. M. 2003. General multilevel linear modeling for group analysis in FMRI. *Neuroimage,* 20**,** 1052-1063.

BERGER, H. 1929. Über das elektroenkephalogramm des menschen. *Archiv für psychiatrie und nervenkrankheiten,* 87**,** 527-570.

BERGER, H. 1930. Ueber das Elektrenkephalogramm des Menschen. *Journal für Psychologie und Neurologie*.

BIRN, R. M., DIAMOND, J. B., SMITH, M. A. & BANDETTINI, P. A. 2006. Separating respiratory-variation-related fluctuations from neuronal-activity-related fluctuations in fMRI. *Neuroimage,* 31**,** 1536-1548.

BISWAL, B. B. 2012. Resting state fMRI: a personal history. *Neuroimage,* 62**,** 938-944.

BLAIMER, M., CHOLI, M., JAKOB, P. M., GRISWOLD, M. A. & BREUER, F. A. 2013. Multiband phase-constrained parallel MRI. *Magnetic resonance in medicine,* 69**,** 974-980.

BLOCK, A. A. 1974. Affine transformation. *J. Inst. Telev. Eng. Japan,* 28**,** 251-256.

BLOKLAND, G. A., MCMAHON, K. L., HOFFMAN, J., ZHU, G., MEREDITH, M., MARTIN, N. G., THOMPSON, P. M., DE ZUBICARAY, G. I. & WRIGHT, M. J. 2008. Quantifying the heritability of task-related brain activation and performance during the N-back working memory task: a twin fMRI study. *Biol Psychol,* 79**,** 70-9.

BODURKA, J., YE, F., PETRIDOU, N., MURPHY, K. & BANDETTINI, P. A. 2007. Mapping the MRI voxel volume in which thermal noise matches physiological noise—implications for fMRI. *Neuroimage,* 34**,** 542-549.

BOLLIMUNTA, A., MO, J., SCHROEDER, C. E. & DING, M. 2011. Neuronal mechanisms and attentional modulation of corticothalamic alpha oscillations. *Journal of Neuroscience,* 31**,** 4935-4943.

BOTO, E., MEYER, S. S., SHAH, V., ALEM, O., KNAPPE, S., KRUGER, P., FROMHOLD, T. M., LIM, M., GLOVER, P. M. & MORRIS, P. G. 2017. A new generation of magnetoencephalography: Room temperature measurements using optically-pumped magnetometers. *NeuroImage,* 149**,** 404-414.

BRADY, B., POWER, L. & BARDOUILLE, T. 2020. Age-related trends in neuromagnetic transient beta burst characteristics during a sensorimotor task and rest in the Cam-CAN open-access dataset. *NeuroImage,* 222**,** 117245.

BRILEY, P. M., LIDDLE, E. B., SIMMONITE, M., JANSEN, M., WHITE, T. P., BALAIN, V., PALANIYAPPAN, L., BOWTELL, R., MULLINGER, K. J. & LIDDLE, P. F. 2021. Regional Brain Correlates of Beta Bursts in Health and Psychosis: A Concurrent Electroencephalography and Functional Magnetic Resonance Imaging Study. *Biol Psychiatry Cogn Neurosci Neuroimaging,* 6**,** 1145-1156.

BROOKES, M. J., HALE, J. R., ZUMER, J. M., STEVENSON, C. M., FRANCIS, S. T., BARNES, G. R., OWEN, J. P., MORRIS, P. G. & NAGARAJAN, S. S. 2011a. Measuring functional

connectivity using MEG: methodology and comparison with fcMRI. *Neuroimage,* 56**,** 1082-1104.

BROOKES, M. J., STEVENSON, C. M., BARNES, G. R., HILLEBRAND, A., SIMPSON, M. I., FRANCIS, S. T. & MORRIS, P. G. 2007. Beamformer reconstruction of correlated sources using a modified source model. *Neuroimage,* 34**,** 1454-1465.

BROOKES, M. J., TEWARIE, P. K., HUNT, B. A. E., ROBSON, S. E., GASCOYNE, L. E., LIDDLE, E. B., LIDDLE, P. F. & MORRIS, P. G. 2016. A multi-layer network approach to MEG connectivity analysis. *Neuroimage,* 132**,** 425-438.

BROOKES, M. J., VRBA, J., ROBINSON, S. E., STEVENSON, C. M., PETERS, A. M., BARNES, G. R., HILLEBRAND, A. & MORRIS, P. G. 2008. Optimising experimental design for MEG beamformer imaging. *Neuroimage,* 39**,** 1788-1802.

BROOKES, M. J., WOOD, J. R., STEVENSON, C. M., ZUMER, J. M., WHITE, T. P., LIDDLE, P. F. & MORRIS, P. G. 2011b. Changes in brain network activity during working memory tasks: a magnetoencephalography study. *Neuroimage,* 55**,** 1804-1815.

BROOKES, M. J., WOOLRICH, M., LUCKHOO, H., PRICE, D., HALE, J. R., STEPHENSON, M. C., BARNES, G. R., SMITH, S. M. & MORRIS, P. G. 2011c. Investigating the electrophysiological basis of resting state networks using magnetoencephalography. *Proceedings of the National Academy of Sciences,* 108**,** 16783-16788.

BROSCH, J. R., TALAVAGE, T. M., ULMER, J. L. & NYENHUIS, J. A. 2002. Simulation of human respiration in fMRI with a mechanical model. *IEEE Transactions on Biomedical Engineering,* 49**,** 700-707.

BUSCHMAN, T. J. & MILLER, E. K. 2007. Top-down versus bottom-up control of attention in the prefrontal and posterior parietal cortices. *Science,* 315**,** 1860-2.

BUTLER, R., BERNIER, P.-M., LEFEBVRE, J., GILBERT, G. & WHITTINGSTALL, K. 2017. Decorrelated input dissociates narrow band γ power and BOLD in human visual cortex. *Journal of Neuroscience,* 37**,** 5408-5418.

BUXTON, R. B., ULUDAG, K., DUBOWITZ, D. J. & LIU, T. T. 2004. Modeling the hemodynamic response to brain activation. *Neuroimage,* 23 Suppl 1**,** S220-33.

BUXTON, R. B., WONG, E. C. & FRANK, L. R. 1998. Dynamics of blood flow and oxygenation changes during brain activation: the balloon model. *Magn Reson Med,* 39**,** 855-64.

CALLICOTT, J. H., EGAN, M. F., MATTAY, V. S., BERTOLINO, A., BONE, A. D., VERCHINKSI, B. & WEINBERGER, D. R. 2003. Abnormal fMRI response of the dorsolateral prefrontal cortex in cognitively intact siblings of patients with schizophrenia. *Am J Psychiatry,* 160**,** 709-19.

CARNEY, P. W., MASTERTON, R. A., HARVEY, A. S., SCHEFFER, I. E., BERKOVIC, S. F. & JACKSON, G. D. 2010. The core network in absence epilepsy: differences in cortical and thalamic BOLD response. *Neurology,* 75**,** 904-911.

CARPENTER, T. & WILLIAMS, E. 1999. MRI–From basic knowledge to advanced strategies: Hardware. *European radiology,* 9**,** 1015-1019.

CASILLO, S. M., LUY, D. D. & GOLDSCHMIDT, E. 2020. A history of the lobes of the brain. *World Neurosurgery,* 134**,** 353-360.

CASSIM, F., MONACA, C., SZURHAJ, W., BOURRIEZ, J. L., DEFEBVRE, L., DERAMBURE, P. & GUIEU, J. D. 2001. Does post-movement beta synchronization reflect an idling motor cortex? *Neuroreport,* 12**,** 3859-63.

CATON, R. 1875. Electrical currents of the brain. *The Journal of Nervous and Mental Disease,* 2**,** 610.

CEKO, M., GRACELY, J. L., FITZCHARLES, M. A., SEMINOWICZ, D. A., SCHWEINHARDT, P. & BUSHNELL, M. C. 2015. Is a Responsive Default Mode Network Required for Successful Working Memory Task Performance? *J Neurosci,* 35**,** 11595-605.

CELOZZI, S., ARANEO, R. & LOVAT, G. 2008. Appendix B: Magnetic Shielding. *Electromagnetic Shielding***,** 282-316.

CHALLIS, J. H. 1995. A procedure for determining rigid body transformation parameters. *Journal of biomechanics,* 28**,** 733-737.

CHEN, J. J. & PIKE, G. B. 2009. Origins of the BOLD post-stimulus undershoot. *Neuroimage,* 46**,** 559-68.

CHEN, R., CORWELL, B. & HALLETT, M. 1999. Modulation of motor cortex excitability by median nerve and digit stimulation. *Exp Brain Res,* 129**,** 77-86.

CHEN, R., YASEEN, Z., COHEN, L. G. & HALLETT, M. 1998. Time course of corticospinal excitability in reaction time and self-paced movements. *Ann Neurol,* 44**,** 317-25.

CHOWDHURY, M. E., KHANDAKAR, A., MULLINGER, K., HOSSAIN, B., AL-EMADI, N., ANTUNES, A. & BOWTELL, R. 2019. Reference layer artefact subtraction (RLAS): electromagnetic simulations. *IEEE Access,* 7**,** 17882-17895.

CLARKE, J. 1989. Principles and applications of SQUIDs. *Proceedings of the IEEE,* 77**,** 1208-1223.

CLASSEN, J., GERLOFF, C., HONDA, M. & HALLETT, M. 1998. Integrative visuomotor behavior is associated with interregionally coherent oscillations in the human brain. *J Neurophysiol,* 79**,** 1567-73.

CLAYTON, M. S., YEUNG, N. & COHEN KADOSH, R. 2018. The many characters of visual alpha oscillations. *Eur J Neurosci,* 48**,** 2498-2508.

COHEN, D. 1968. Magnetoencephalography: evidence of magnetic fields produced by alpha-rhythm currents. *Science,* 161**,** 784-6.

COHEN, D. 1972. Magnetoencephalography: detection of the brain's electrical activity with a superconducting magnetometer. *Science,* 175**,** 664-6.

COLCLOUGH, G. L., BROOKES, M. J., SMITH, S. M. & WOOLRICH, M. W. 2015. A symmetric multivariate leakage correction for MEG connectomes. *Neuroimage,* 117**,** 439-448.

COLCLOUGH, G. L., WOOLRICH, M. W., TEWARIE, P., BROOKES, M. J., QUINN, A. J. & SMITH, S. M. 2016. How reliable are MEG resting-state connectivity metrics? *Neuroimage,* 138**,** 284-293.

COLEMAN, S. C., SEEDAT, Z. A., PAKENHAM, D. O., QUINN, A. J., BROOKES, M. J., WOOLRICH, M. W. & MULLINGER, K. J. 2024. Post-task responses following working memory and movement are driven by transient spectral bursts with similar characteristics. *Human Brain Mapping,* 45**,** e26700.

COLEMAN, S. C., SEEDAT, Z. A., WHITTAKER, A. C., LENARTOWICZ, A. & MULLINGER, K. J. 2023. Beyond the Beta Rebound: Post-Task Responses in Oscillatory Activity follow Cessation of Working Memory Processes. *Neuroimage,* 265**,** 119801.

CONNER, C. R., ELLMORE, T. M., PIETERS, T. A., DISANO, M. A. & TANDON, N. 2011. Variability of the relationship between electrophysiology and BOLD-fMRI across cortical regions in humans. *Journal of Neuroscience,* 31**,** 12855-12865.

COQUELET, N., DE TIÈGE, X., ROSHCHUPKINA, L., PEIGNEUX, P., GOLDMAN, S., WOOLRICH, M. & WENS, V. 2022. Microstates and power envelope hidden Markov modeling probe bursting brain activity at different timescales. *NeuroImage,* 247**,** 118850.

COSTERS, L., VAN SCHEPENDOM, J., LATON, J., BAIJOT, J., SJØGÅRD, M., WENS, V., DE TIÈGE, X., GOLDMAN, S., D'HAESELEER, M. & D'HOOGHE, M. B. 2020. Spatiotemporal and spectral dynamics of multi-item working memory as revealed by the n-back task using MEG. *Human Brain Mapping,* 41**,** 2431-2446.

CUNNINGHAM, S. I., TOMASI, D. & VOLKOW, N. D. 2017. Structural and functional connectivity of the precuneus and thalamus to the default mode network. *Human Brain Mapping,* 38**,** 938-956.

CURTIS, C. E. 2006. Prefrontal and parietal contributions to spatial working memory. *Neuroscience,* 139**,** 173-180.

DA SILVA, F. L., HOEKS, A., SMITS, H. & ZETTERBERG, L. 1974. Model of brain rhythmic activity. The alpha-rhythm of the thalamus. *Kybernetik,* 15**,** 27-37.

DA SILVA, F. L. & VAN LEEUWEN, W. S. 1977. The cortical source of the alpha rhythm. *Neuroscience letters,* 6**,** 237-241.

DANZIGER, S., WARD, R., OWEN, V. & RAFAL, R. 2004. Contributions of the human pulvinar to linking vision and action. *Cognitive, Affective, & Behavioral Neuroscience,* 4**,** 89-99.

DEVOR, A., TIAN, P., NISHIMURA, N., TENG, I. C., HILLMAN, E. M., NARAYANAN, S. N., ULBERT, I., BOAS, D. A., KLEINFELD, D. & DALE, A. M. 2007. Suppressed neuronal activity and concurrent arteriolar vasoconstriction may explain negative blood oxygenation level-dependent signal. *J Neurosci,* 27**,** 4452-9.

DEVOR, A., ULBERT, I., DUNN, A. K., NARAYANAN, S. N., JONES, S. R., ANDERMANN, M. L., BOAS, D. A. & DALE, A. M. 2005. Coupling of the cortical hemodynamic response to cortical and thalamic neuronal activity. *Proceedings of the National Academy of Sciences,* 102**,** 3822-3827.

DU, X., CHOA, F.-S., SUMMERFELT, A., ROWLAND, L. M., CHIAPPELLI, J., KOCHUNOV, P. & HONG, L. E. 2017. N100 as a generic cortical electrophysiological marker based on decomposition of TMS-evoked potentials across five anatomic locations. *Experimental brain research,* 235**,** 69-81.

DUANN, J. R., JUNG, T. P., KUO, W. J., YEH, T. C., MAKEIG, S., HSIEH, J. C. & SEJNOWSKI, T. J. 2002. Single-trial variability in event-related BOLD signals. *Neuroimage,* 15**,** 823-35.

DUBBELINK, K. T. O., STOFFERS, D., DEIJEN, J. B., TWISK, J. W., STAM, C. J., HILLEBRAND, A. & BERENDSE, H. W. 2013. Resting-state functional connectivity as a marker of disease progression in Parkinson's disease: A longitudinal MEG study. *NeuroImage: Clinical,* 2**,** 612-619.

DÜHRSEN, L., SAUVIGNY, T., RICKLEFS, F. L., HAMEL, W., KOEPPEN, J. A., HEBEL, J. M., LANZ, M. & MARTENS, T. 2020. Decision-making in temporal lobe epilepsy surgery based on invasive stereo-electroencephalography (sEEG). *Neurosurgical Review,* 43**,** 1403-1408.

EICHENBAUM, H., DUDCHENKO, P., WOOD, E., SHAPIRO, M. & TANILA, H. 1999. The hippocampus, memory, and place cells: is it spatial memory or a memory space? *Neuron,* 23**,** 209-226.

ELUL, R. 1971. The genesis of the EEG. *Int Rev Neurobiol,* 15**,** 227-72.

ENGEL, A. K. & FRIES, P. 2010. Beta-band oscillations--signalling the status quo? *Curr Opin Neurobiol,* 20**,** 156-65.

FALKENSTEIN, M., HOHNSBEIN, J., HOORMANN, J. & BLANKE, L. 1991. Effects of crossmodal divided attention on late ERP components. II. Error processing in choice reaction tasks. *Electroencephalography and clinical neurophysiology,* 78**,** 447-455.

FELDMAN, R. P. & GOODRICH, J. T. 1999. The edwin smith surgical papyrus. *Child's Nervous System,* 15**,** 281-284.

FLANAGAN, F. L., DEHDASHTI, F. & SIEGEL, B. A. PET in breast cancer. Seminars in nuclear medicine, 1998. Elsevier, 290-302.

FOSTER, D. J. & WILSON, M. A. 2007. Hippocampal theta sequences. *Hippocampus,* 17**,** 1093-1099.

FOX, M. D. & GREICIUS, M. 2010. Clinical applications of resting state functional connectivity. *Frontiers in systems neuroscience,* 4**,** 1443.

FOX, M. D., SNYDER, A. Z., BARCH, D. M., GUSNARD, D. A. & RAICHLE, M. E. 2005. Transient BOLD responses at block transitions. *Neuroimage,* 28**,** 956-966.

FRAHM, J., KRUGER, G., MERBOLDT, K. D. & KLEINSCHMIDT, A. 1996. Dynamic uncoupling and recoupling of perfusion and oxidative metabolism during focal brain activation in man. *Magn Reson Med,* 35**,** 143-8.

FRAHM, J., MERBOLDT, K. D., HÄNICKE, W., KLEINSCHMIDT, A. & BOECKER, H. 1994. Brain or vein□ oxygenation or flow? On signal physiology in functional MRI of human brain activation. *NMR in Biomedicine,* 7**,** 45-53.

FRIES, P. 2015. Rhythms for cognition: communication through coherence. *Neuron,* 88**,** 220-235.

FRISTON, K. J. 2002. Dysfunctional connectivity in schizophrenia. *World Psychiatry,* 1**,** 66.

FRISTON, K. J., HOLMES, A. P., POLINE, J., GRASBY, P., WILLIAMS, S., FRACKOWIAK, R. S. & TURNER, R. 1995. Analysis of fMRI time-series revisited. *Neuroimage,* 2**,** 45-53.

FRISTON, K. J., MECHELLI, A., TURNER, R. & PRICE, C. J. 2000. Nonlinear responses in fMRI: the Balloon model, Volterra kernels, and other hemodynamics. *Neuroimage,* 12**,** 466-77.

FRISTON, K. J., WILLIAMS, S., HOWARD, R., FRACKOWIAK, R. S. & TURNER, R. 1996. Movement-related effects in fMRI time-series. *Magnetic resonance in medicine,* 35**,** 346-355.

FRY, A., MULLINGER, K. J., O'NEILL, G. C., BARRATT, E. L., MORRIS, P. G., BAUER, M., FOLLAND, J. P. & BROOKES, M. J. 2016. Modulation of post-movement beta rebound by contraction force and rate of force development. *Hum Brain Mapp,* 37**,** 2493-511.

FUCHS, M., DRENCKHAHN, R., WISCHMANN, H. & WAGNER, M. 1998. An improved boundary element method for realistic volume-conductor modeling. *IEEE Transactions on biomedical engineering,* 45**,** 980-997.

GAETZ, W., MACDONALD, M., CHEYNE, D. & SNEAD, O. 2010. Neuromagnetic imaging of movement-related cortical oscillations in children and adults: age predicts post-movement beta rebound. *Neuroimage,* 51**,** 792-807.

GAETZ, W., RHODES, E., BLOY, L., BLASKEY, L., JACKEL, C. R., BRODKIN, E. S., WALDMAN, A., EMBICK, D., HALL, S. & ROBERTS, T. P. L. 2020. Evaluating motor cortical oscillations and age-related change in autism spectrum disorder. *Neuroimage,* 207**,** 116349.

GAETZ, W. C. & CHEYNE, D. O. 2003. Localization of human somatosensory cortex using spatially filtered magnetoencephalography. *Neuroscience letters,* 340**,** 161-164.

GAGNON, L., SAKADŽIĆ, S., LESAGE, F., MUSACCHIA, J. J., LEFEBVRE, J., FANG, Q., YÜCEL, M. A., EVANS, K. C., MANDEVILLE, E. T. & COHEN-ADAD, J. 2015. Quantifying the microvascular origin of BOLD-fMRI from first principles with two-photon microscopy and an oxygen-sensitive nanoprobe. *Journal of Neuroscience,* 35**,** 3663-3675.

GASCOYNE, L. E., BROOKES, M. J., RATHNAIAH, M., KATSHU, M., KOELEWIJN, L., WILLIAMS, G., KUMAR, J., WALTERS, J. T. R., SEEDAT, Z. A., PALANIYAPPAN, L., DEAKIN, J. F. W., SINGH, K. D., LIDDLE, P. F. & MORRIS, P. G. 2021. Motor-related oscillatory activity in schizophrenia according to phase of illness and clinical symptom severity. *Neuroimage Clin,* 29**,** 102524.

GEHRING, W. J., COLES, M. G., MEYER, D. E. & DONCHIN, E. 1995. A brain potential manifestation of error-related processing. *Electroencephalography and Clinical Neurophysiology-Supplements only,* 44**,** 261-272.

GEHRING, W. J., GOSS, B., COLES, M. G., MEYER, D. E. & DONCHIN, E. 2018. The error-related negativity. *Perspectives on Psychological Science,* 13**,** 200-204.

GESELOWITZ, D. 1970. On the magnetic field generated outside an inhomogeneous volume conductor by internal current sources. *IEEE Transactions on Magnetics,* 6**,** 346-347.

GILBERT, C. D. & LI, W. 2013. Top-down influences on visual processing. *Nature Reviews Neuroscience,* 14**,** 350-363.

GILBERTSON, T., LALO, E., DOYLE, L., DI LAZZARO, V., CIONI, B. & BROWN, P. 2005. Existing motor state is favored at the expense of new movement during 13-35 Hz oscillatory synchrony in the human corticospinal system. *J Neurosci,* 25**,** 7771-9.

GLOVER, G. H. 1999. Deconvolution of impulse response in event-related BOLD fMRI. *Neuroimage,* 9**,** 416-29.

GLOVER, G. H., LI, T. Q. & RESS, D. 2000. Image-based method for retrospective correction of physiological motion effects in fMRI: RETROICOR. *Magn Reson Med,* 44**,** 162-7.

GOENSE, J. B. & LOGOTHETIS, N. K. 2008. Neurophysiology of the BOLD fMRI signal in awake monkeys. *Curr Biol,* 18**,** 631-40.

GOGOLAK, G., STUMPF, C., PETSCHE, H. & STERC, J. 1968. The firing pattern of septal neurons and the form of the hippocampal theta wave. *Brain research,* 7**,** 201-207.

GOLUB, G. H., HANSEN, P. C. & O'LEARY, D. P. 1999. Tikhonov regularization and total least squares. *SIAM journal on matrix analysis and applications,* 21**,** 185-194.

GONZALEZ-CASTILLO, J., SAAD, Z. S., HANDWERKER, D. A., INATI, S. J., BRENOWITZ, N. & BANDETTINI, P. A. 2012. Whole-brain, time-locked activation with simple tasks revealed using massive averaging and model-free analysis. *Proc Natl Acad Sci U S A,* 109**,** 5487-92.

GOULDEN, N., KHUSNULINA, A., DAVIS, N. J., BRACEWELL, R. M., BOKDE, A. L., MCNULTY, J. P. & MULLINS, P. G. 2014. The salience network is responsible for switching between the default mode network and the central executive network: replication from DCM. *Neuroimage,* 99**,** 180-190.

GRAHAM, M. S., DROBNJAK, I., JENKINSON, M. & ZHANG, H. 2017. Quantitative assessment of the susceptibility artefact and its interaction with motion in diffusion MRI. *PloS one,* 12**,** e0185647.

GRATTON, G. 2018. Brain reflections: A circuit-based framework for understanding information processing and cognitive control. *Psychophysiology,* 55**,** e13038.

GRIFFITHS, B. J., PARISH, G., ROUX, F., MICHELMANN, S., VAN DER PLAS, M., KOLIBIUS, L. D., CHELVARAJAH, R., ROLLINGS, D. T., SAWLANI, V., HAMER, H., GOLLWITZER, S., KREISELMEYER, G., STARESINA, B., WIMBER, M. & HANSLMAYR, S. 2019. Directional coupling of slow and fast hippocampal gamma with neocortical alpha/beta oscillations in human episodic memory. *Proc Natl Acad Sci U S A,* 116**,** 21834-21842.

GRIMM, S., BOESIGER, P., BECK, J., SCHUEPBACH, D., BERMPOHL, F., WALTER, M., ERNST, J., HELL, D., BOEKER, H. & NORTHOFF, G. 2009. Altered negative BOLD responses in the default-mode network during emotion processing in depressed subjects. *Neuropsychopharmacology,* 34**,** 932-43.

HAFT, M., HOFMANN, R. & TRESP, V. 1999. Model-independent mean-field theory as a local method for approximate propagation of information. *Network: Computation in Neural Systems,* 10**,** 93-105.

HALGREN, M., ULBERT, I., BASTUJI, H., FABÓ, D., ERŐSS, L., REY, M., DEVINSKY, O., DOYLE, W. K., MAK-MCCULLY, R. & HALGREN, E. 2019. The generation and propagation of the human alpha rhythm. *Proceedings of the National Academy of Sciences,* 116**,** 23772-23782.

HALLIDAY, A., MCDONALD, W. & MUSHIN, J. 1973. Visual evoked response in diagnosis of multiple sclerosis. *British medical journal,* 4**,** 661.

HALLOCK, H. L., WANG, A. & GRIFFIN, A. L. 2016. Ventral midline thalamus is critical for hippocampal–prefrontal synchrony and spatial working memory. *Journal of Neuroscience,* 36**,** 8372-8389.

HÄMÄLÄINEN, M., HARI, R., ILMONIEMI, R. J., KNUUTILA, J. & LOUNASMAA, O. V. 1993. Magnetoencephalography—theory, instrumentation, and applications to noninvasive studies of the working human brain. *Reviews of modern Physics,* 65**,** 413.

HAMZEI, F., DETTMERS, C., RZANNY, R., LIEPERT, J., BÜCHEL, C. & WEILLER, C. 2002. Reduction of excitability ("inhibition") in the ipsilateral primary motor cortex is mirrored by fMRI signal decreases. *Neuroimage,* 17**,** 490-496.

HANDWERKER, D. A., OLLINGER, J. M. & D'ESPOSITO, M. 2004a. Variation of BOLD hemodynamic responses across subjects and brain regions and their effects on statistical analyses. *Neuroimage,* 21**,** 1639-1651.

HANDWERKER, D. A., OLLINGER, J. M. & D'ESPOSITO, M. 2004b. Variation of BOLD hemodynamic responses across subjects and brain regions and their effects on statistical analyses. *Neuroimage,* 21**,** 1639-51.

HANLON, F. M., SHAFF, N. A., DODD, A. B., LING, J. M., BUSTILLO, J. R., ABBOTT, C. C., STROMBERG, S. F., ABRAMS, S., LIN, D. S. & MAYER, A. R. 2016. Hemodynamic response function abnormalities in schizophrenia during a multisensory detection task. *Human brain mapping,* 37**,** 745-755.

HANSLMAYR, S., STARESINA, B. P. & BOWMAN, H. 2016. Oscillations and Episodic Memory: Addressing the Synchronization/Desynchronization Conundrum. *Trends Neurosci,* 39**,** 16-25.

HAREL, N., LEE, S.-P., NAGAOKA, T., KIM, D.-S. & KIM, S.-G. 2002. Origin of negative blood oxygenation level—dependent fMRI signals. *Journal of cerebral blood flow & metabolism,* 22**,** 908-917.

HARMS, M. P. & MELCHER, J. R. 2002. Sound repetition rate in the human auditory pathway: representations in the waveshape and amplitude of fMRI activation. *J Neurophysiol,* 88**,** 1433-50.

HATHOUT, G. M., KIRLEW, K. A., SO, G. J., HAMILTON, D. R., ZHANG, J. X., SINHA, U., SINHA, S., SAYRE, J., GOZAL, D., HARPER, R. M. & ET AL. 1994. MR imaging signal response to sustained stimulation in human visual cortex. *J Magn Reson Imaging,* 4**,** 537-43.

HE, B. J., SNYDER, A. Z., ZEMPEL, J. M., SMYTH, M. D. & RAICHLE, M. E. 2008. Electrophysiological correlates of the brain's intrinsic large-scale functional architecture. *Proceedings of the National Academy of Sciences,* 105**,** 16039-16044.

HEBERT, R. & LEHMANN, D. 1977. Theta bursts: an EEG pattern in normal subjects practising the transcendental meditation technique. *Electroencephalography and clinical neurophysiology,* 42**,** 397-405.

HEEGER, D. J. & RESS, D. 2002. What does fMRI tell us about neuronal activity? *Nat Rev Neurosci,* 3**,** 142-51.

HIGGINS, C., LIU, Y., VIDAURRE, D., KURTH-NELSON, Z., DOLAN, R., BEHRENS, T. & WOOLRICH, M. 2021. Replay bursts in humans coincide with activation of the default mode and parietal alpha networks. *Neuron,* 109**,** 882-893 e7.

HILLEBRAND, A. & BARNES, G. R. 2002. A quantitative assessment of the sensitivity of whole-head MEG to activity in the adult human cortex. *Neuroimage,* 16**,** 638-650.

HILLEBRAND, A., TEWARIE, P., VAN DELLEN, E., YU, M., CARBO, E. W., DOUW, L., GOUW, A. A., VAN STRAATEN, E. C. & STAM, C. J. 2016. Direction of information flow in large-scale resting-state networks is frequency-dependent. *Proceedings of the National Academy of Sciences,* 113**,** 3867-3872.

HILLYARD, S. A. & ANLLO-VENTO, L. 1998. Event-related brain potentials in the study of visual selective attention. *Proceedings of the National Academy of Sciences,* 95**,** 781-787.

HINDRIKS, R. & VAN PUTTEN, M. J. 2013. Thalamo-cortical mechanisms underlying changes in amplitude and frequency of human alpha oscillations. *Neuroimage,* 70**,** 150-163.

HINDRIKS, R., WOOLRICH, M., LUCKHOO, H., JOENSSON, M., MOHSENI, H., KRINGELBACH, M. L. & DECO, G. 2015. Role of white-matter pathways in coordinating alpha oscillations in resting visual cortex. *Neuroimage,* 106**,** 328-39.

HINKLEY, L. B., OWEN, J. P., FISHER, M., FINDLAY, A. M., VINOGRADOV, S. & NAGARAJAN, S. S. 2010. Cognitive impairments in schizophrenia as assessed through activation and connectivity measures of magnetoencephalography (MEG) data. *Frontiers in Human Neuroscience,* 3**,** 73.

HOBURG, J. 1995. Principles of quasistatic magnetic shielding with cylindrical and spherical shields. *IEEE Transactions on electromagnetic compatibility,* 37**,** 574-579.

HOU, P., HASAN, K. M., SITTON, C. W., WOLINSKY, J. S. & NARAYANA, P. A. 2005. Phase-sensitive T1 inversion recovery imaging: a time-efficient interleaved technique for improved tissue contrast in neuroimaging. *American Journal of Neuroradiology,* 26**,** 1432-1438.

HUANG, M., MOSHER, J. C. & LEAHY, R. 1999. A sensor-weighted overlapping-sphere head model and exhaustive head model comparison for MEG. *Physics in Medicine & Biology,* 44**,** 423.

HUANG, M. X., NICHOLS, S., ROBB-SWAN, A., ANGELES-QUINTO, A., HARRINGTON, D. L., DRAKE, A., HUANG, C. W., SONG, T., DIWAKAR, M., RISBROUGH, V. B., MATTHEWS, S., CLIFFORD, R., CHENG, C. K., HUANG, J. W., SINHA, A., YURGIL, K. A., JI, Z., LERMAN, I., LEE, R. R. & BAKER, D. G. 2019. MEG Working Memory N-Back Task Reveals Functional Deficits in Combat-Related Mild Traumatic Brain Injury. *Cereb Cortex,* 29**,** 1953-1968.

HUNT, B. A. E., LIDDLE, E. B., GASCOYNE, L. E., MAGAZZINI, L., ROUTLEY, B. C., SINGH, K. D., MORRIS, P. G., BROOKES, M. J. & LIDDLE, P. F. 2019. Attenuated Post-Movement Beta Rebound Associated With Schizotypal Features in Healthy People. *Schizophr Bull,* 45**,** 883-891.

IADECOLA, C. 2017. The Neurovascular Unit Coming of Age: A Journey through Neurovascular Coupling in Health and Disease. *Neuron,* 96**,** 17-42.

IASEMIDIS, L. D., ZAVERI, H. P., SACKELLARES, J. C. & WILLIAMS, W. J. 1988. Modelling of ECoG in temporal lobe epilepsy. *Biomed Sci Instrum,* 24**,** 187-193.

INANAGA, K. 1998. Frontal midline theta rhythm and mental activity. *Psychiatry Clin Neurosci,* 52**,** 555-66.

JAFFE, R. & WEISS, A. H. 1966. THE SIGNIFICANCE OF UNILATERAL ALPHA-RANGE BURSTS IN THE EEG. *Acta Neurologica Scandinavica,* 42**,** 257-267.

JENESON, A. & SQUIRE, L. R. 2012. Working memory, long-term memory, and medial temporal lobe function. *Learning & memory,* 19**,** 15-25.

JENKINSON, M., BANNISTER, P., BRADY, M. & SMITH, S. 2002. Improved optimization for the robust and accurate linear registration and motion correction of brain images. *Neuroimage,* 17**,** 825-841.

JENKINSON, M. & SMITH, S. 2001. A global optimisation method for robust affine registration of brain images. *Medical image analysis,* 5**,** 143-156.

JENSEN, O., GELFAND, J., KOUNIOS, J. & LISMAN, J. E. 2002. Oscillations in the alpha band (9-12 Hz) increase with memory load during retention in a short-term memory task. *Cereb Cortex,* 12**,** 877-82.

JENSEN, O., GOEL, P., KOPELL, N., POHJA, M., HARI, R. & ERMENTROUT, B. 2005. On the human sensorimotor-cortex beta rhythm: sources and modeling. *Neuroimage,* 26**,** 347-55.

JENSEN, O. & MAZAHERI, A. 2010. Shaping functional architecture by oscillatory alpha activity: gating by inhibition. *Front Hum Neurosci,* 4**,** 186.

JÖBSIS, F. F. 1977. Noninvasive, infrared monitoring of cerebral and myocardial oxygen sufficiency and circulatory parameters. *Science,* 198**,** 1264-1267.

JONES, S. R. 2016. When brain rhythms aren't 'rhythmic': implication for their mechanisms and meaning. *Current opinion in neurobiology,* 40**,** 72-80.

JOSEPHSON, B. D. 1962. Possible new effects in superconductive tunnelling. *Physics letters,* 1**,** 251-253.

JOYCE, J. 2003. Bayes' theorem.

JURKIEWICZ, M. T., GAETZ, W. C., BOSTAN, A. C. & CHEYNE, D. 2006a. Post-movement beta rebound is generated in motor cortex: evidence from neuromagnetic recordings. *Neuroimage,* 32**,** 1281-1289.

JURKIEWICZ, M. T., GAETZ, W. C., BOSTAN, A. C. & CHEYNE, D. 2006b. Post-movement beta rebound is generated in motor cortex: evidence from neuromagnetic recordings. *Neuroimage,* 32**,** 1281-9.

KANA, R. K., KELLER, T. A., MINSHEW, N. J. & JUST, M. A. 2007. Inhibitory control in high-functioning autism: decreased activation and underconnectivity in inhibition networks. *Biological psychiatry,* 62**,** 198-206.

KANDEL, E. R., SCHWARTZ, J. H., JESSELL, T. M., SIEGELBAUM, S., HUDSPETH, A. J. & MACK, S. 2000. *Principles of neural science*, McGraw-hill New York.

KASTNER, S., FIEBELKORN, I. C. & ERADATH, M. K. 2020. Dynamic pulvino-cortical interactions in the primate attention network. *Current opinion in neurobiology,* 65**,** 10-19.

KASTRUP, A., BAUDEWIG, J., SCHNAUDIGEL, S., HUONKER, R., BECKER, L., SOHNS, J. M., DECHENT, P., KLINGNER, C. & WITTE, O. W. 2008. Behavioral correlates of negative BOLD signal changes in the primary somatosensory cortex. *Neuroimage,* 41**,** 1364-71.

KHAWALDEH, S., TINKHAUSER, G., TORRECILLOS, F., HE, S., FOLTYNIE, T., LIMOUSIN, P., ZRINZO, L., OSWAL, A., QUINN, A. J., VIDAURRE, D., TAN, H., LITVAK, V., KUHN, A., WOOLRICH, M. & BROWN, P. 2022. Balance between competing spectral states in subthalamic nucleus is linked to motor impairment in Parkinson's disease. *Brain,* 145**,** 237-250.

KLIMESCH, W. 1999. EEG alpha and theta oscillations reflect cognitive and memory performance: a review and analysis. *Brain Res Brain Res Rev,* 29**,** 169-95.

KLIMESCH, W., SAUSENG, P. & HANSLMAYR, S. 2007. EEG alpha oscillations: the inhibition-timing hypothesis. *Brain Res Rev,* 53**,** 63-88.

KLINGNER, C. M., HASLER, C., BRODOEHL, S. & WITTE, O. W. 2010. Dependence of the negative BOLD response on somatosensory stimulus intensity. *Neuroimage,* 53**,** 189-95.

KOENIGS, M., BARBEY, A. K., POSTLE, B. R. & GRAFMAN, J. 2009. Superior parietal cortex is critical for the manipulation of information in working memory. *Journal of Neuroscience,* 29**,** 14980-14986.

KRINGS, T., ERBERICH, S. G., ROESSLER, F., REUL, J. & THRON, A. 1999. MR blood oxygenation level–dependent signal differences in parenchymal and large draining vessels: implications for functional MR imaging. *American journal of neuroradiology,* 20**,** 1907-1914.

KRUGER, G., KLEINSCHMIDT, A. & FRAHM, J. 1996. Dynamic MRI sensitized to cerebral blood oxygenation and flow during sustained activation of human visual cortex. *Magn Reson Med,* 35**,** 797-800.

KWONG, K. K., BELLIVEAU, J. W., CHESLER, D. A., GOLDBERG, I. E., WEISSKOFF, R. M., PONCELET, B. P., KENNEDY, D. N., HOPPEL, B. E., COHEN, M. S. & TURNER, R. 1992. Dynamic magnetic resonance imaging of human brain activity during primary sensory stimulation. *Proceedings of the National Academy of Sciences,* 89**,** 5675-5679.

LACHAUX, J. P., FONLUPT, P., KAHANE, P., MINOTTI, L., HOFFMANN, D., BERTRAND, O. & BACIU, M. 2007. Relationship between task-related gamma oscillations and BOLD signal: New insights from combined fMRI and intracranial EEG. *Human brain mapping,* 28**,** 1368-1375.

LARKMAN, D. J., HAJNAL, J. V., HERLIHY, A. H., COUTTS, G. A., YOUNG, I. R. & EHNHOLM, G. 2001. Use of multicoil arrays for separation of signal from multiple slices simultaneously excited. *Journal of Magnetic Resonance Imaging: An Official Journal of the International Society for Magnetic Resonance in Medicine,* 13**,** 313-317.

LEE, M. H., SMYSER, C. D. & SHIMONY, J. S. 2013. Resting-state fMRI: a review of methods and clinical applications. *American Journal of neuroradiology,* 34**,** 1866-1872.

LEIBOVICI, D. G. & SMITH, S. 2000. Comparing groups of subjects in fMRI studies: a review of the GLM approach. *Oxford). Available at www. fmrib. ox. ac. uk/analysis/techrep/tr00dl1/tr00dl1/index. html. Accessed September,* 4**,** 2014.

LESZCZYNSKI, M. 2011. How does hippocampus contribute to working memory processing? *Frontiers in Human Neuroscience,* 5**,** 168.

LIANG, X., ZOU, Q., HE, Y. & YANG, Y. 2016. Topologically reorganized connectivity architecture of default-mode, executive-control, and salience networks across working memory task loads. *Cerebral cortex,* 26**,** 1501-1511.

LIDDLE, E. B., PRICE, D., PALANIYAPPAN, L., BROOKES, M. J., ROBSON, S. E., HALL, E. L., MORRIS, P. G. & LIDDLE, P. F. 2016. Abnormal salience signaling in schizophrenia: The role of integrative beta oscillations. *Hum Brain Mapp,* 37**,** 1361-74.

LIN, P., HASSON, U., JOVICICH, J. & ROBINSON, S. 2011. A neuronal basis for task-negative responses in the human brain. *Cerebral Cortex,* 21**,** 821-830.

LITTLE, S., BONAIUTO, J., BARNES, G. & BESTMANN, S. 2019. Human motor cortical beta bursts relate to movement planning and response errors. *PLoS Biol,* 17**,** e3000479.

LITVA, J. & LO, T. K. 1996. *Digital beamforming in wireless communications*, Artech House, Inc.

LIU, T. T. 2016. Noise contributions to the fMRI signal: An overview. *NeuroImage,* 143**,** 141-151.

LIU, Y.-W. 2012. Hilbert transform and applications. *Fourier Transform Applications***,** 291-300.

LOGOTHETIS, N. K. 2008. What we can do and what we cannot do with fMRI. *Nature,* 453**,** 869-78.

LOGOTHETIS, N. K., PAULS, J., AUGATH, M., TRINATH, T. & OELTERMANN, A. 2001. Neurophysiological investigation of the basis of the fMRI signal. *Nature,* 412**,** 150-7.

LOGOTHETIS, N. K. & WANDELL, B. A. 2004. Interpreting the BOLD signal. *Annu Rev Physiol,* 66**,** 735-69.

LOPES DA SILVA, F. H., VAN ROTTERDAM, A., BARTS, P., VAN HEUSDEN, E. & BURR, W. 1976. Models of neuronal populations: the basic mechanisms of rhythmicity. *Prog Brain Res,* 45**,** 281-308.

LU, Y., GROVA, C., KOBAYASHI, E., DUBEAU, F. & GOTMAN, J. 2007. Using voxel-specific hemodynamic response function in EEG-fMRI data analysis: An estimation and detection model. *Neuroimage,* 34**,** 195-203.

LUCKHOO, H., HALE, J. R., STOKES, M. G., NOBRE, A. C., MORRIS, P. G., BROOKES, M. J. & WOOLRICH, M. W. 2012. Inferring task-related networks using independent component analysis in magnetoencephalography. *Neuroimage,* 62**,** 530-41.

LUNDQVIST, M., MILLER, E. K., NORDMARK, J., LILJEFORS, J. & HERMAN, P. 2024. Beta: bursts of cognition. *Trends in Cognitive Sciences*.

LUO, Y., QIN, S., FERNANDEZ, G., ZHANG, Y., KLUMPERS, F. & LI, H. 2014. Emotion perception and executive control interact in the salience network during emotionally charged working memory processing. *Human Brain Mapping,* 35**,** 5606-5616.

MACHADO, S., ARIAS-CARRIÓN, O., SAMPAIO, I., BITTENCOURT, J., VELASQUES, B., TEIXEIRA, S., NARDI, A. E., PIEDADE, R. & RIBEIRO, P. 2014. Source imaging of P300 visual evoked potentials and cognitive functions in healthy subjects. *Clinical EEG and neuroscience,* 45**,** 262-268.

MAKEIG, S., WESTERFIELD, M., JUNG, T.-P., ENGHOFF, S., TOWNSEND, J., COURCHESNE, E. & SEJNOWSKI, T. J. 2002. Dynamic brain sources of visual evoked responses. *Science,* 295**,** 690-694.

MANSFIELD, P. 1977. Multi-planar image formation using NMR spin echoes. *Journal of Physics C: Solid State Physics,* 10**,** L55.

MARS, R. B., SALLET, J., SCHUFFELGEN, U., JBABDI, S., TONI, I. & RUSHWORTH, M. F. 2012. Connectivity-based subdivisions of the human right "temporoparietal junction area": evidence for different areas participating in different cortical networks. *Cereb Cortex,* 22**,** 1894-903.

MATTHEWS, P. M., HONEY, G. D. & BULLMORE, E. T. 2006. Applications of fMRI in translational medicine and clinical practice. *Nature Reviews Neuroscience,* 7**,** 732-744.

MAYHEW, S. D., COLEMAN, S. C., MULLINGER, K. J. & CAN, C. 2022. Across the adult lifespan the ipsilateral sensorimotor cortex negative BOLD response exhibits decreases in magnitude and spatial extent suggesting declining inhibitory control. *Neuroimage,* 253**,** 119081.

MAZIARZ, M. 2015. A review of the Granger-causality fallacy. *The journal of philosophical economics: Reflections on economic and social issues,* 8**,** 86-105.

MAZZIOTTA, J., TOGA, A., EVANS, A., FOX, P., LANCASTER, J., ZILLES, K., WOODS, R., PAUS, T., SIMPSON, G. & PIKE, B. 2001. A probabilistic atlas and reference system for the human brain: International Consortium for Brain Mapping (ICBM). *Philosophical Transactions of the Royal Society of London. Series B: Biological Sciences,* 356**,** 1293-1322.

MCCORMICK, C., MOSCOVITCH, M., PROTZNER, A. B., HUBER, C. G. & MCANDREWS, M. P. 2010. Hippocampal–neocortical networks differ during encoding and retrieval of relational memory: functional and effective connectivity analyses. *Neuropsychologia,* 48**,** 3272-3281.

MCKEOWN, M. J. & SEJNOWSKI, T. J. 1998. Independent component analysis of fMRI data: examining the assumptions. *Human brain mapping,* 6**,** 368-372.

MELTZER, J. A., NEGISHI, M., MAYES, L. C. & CONSTABLE, R. T. 2007. Individual differences in EEG theta and alpha dynamics during working memory correlate with fMRI responses across subjects. *Clin Neurophysiol,* 118**,** 2419-36.

MENCARELLI, L., NERI, F., MOMI, D., MENARDI, A., ROSSI, S., ROSSI, A. & SANTARNECCHI, E. 2019. Stimuli, presentation modality, and load-specific brain activity patterns during n-back task. *Hum Brain Mapp,* 40**,** 3810-3831.

MERCADANTE, A. A. & TADI, P. 2023. Neuroanatomy, Gray Matter. *StatPearls.* Treasure Island (FL).

MICHALAREAS, G., VEZOLI, J., VAN PELT, S., SCHOFFELEN, J.-M., KENNEDY, H. & FRIES, P. 2016. Alpha-beta and gamma rhythms subserve feedback and feedforward influences among human visual cortical areas. *Neuron,* 89**,** 384-397.

MICHEL, C. M. & KOENIG, T. 2018. EEG microstates as a tool for studying the temporal dynamics of whole-brain neuronal networks: a review. *Neuroimage,* 180**,** 577-593.

MITCHELL, D. J., MCNAUGHTON, N., FLANAGAN, D. & KIRK, I. J. 2008. Frontal-midline theta from the perspective of hippocampal "theta". *Progress in neurobiology,* 86**,** 156-185.

MIZUHARA, H., WANG, L.-Q., KOBAYASHI, K. & YAMAGUCHI, Y. 2004. A long-range cortical network emerging with theta oscillation in a mental task. *Neuroreport,* 15**,** 1233-1238.

MOON, H. S., JIANG, H., VO, T. T., JUNG, W. B., VAZQUEZ, A. L. & KIM, S. G. 2021. Contribution of Excitatory and Inhibitory Neuronal Activity to BOLD fMRI. *Cereb Cortex,* 31**,** 4053-4067.

MORAN, J. K., MICHAIL, G., HEINZ, A., KEIL, J. & SENKOWSKI, D. 2019. Long-Range Temporal Correlations in Resting State Beta Oscillations are Reduced in Schizophrenia. *Front Psychiatry,* 10**,** 517.

MORGAN, S., HANSEN, J. & HILLYARD, S. 1996. Selective attention to stimulus location modulates the steady-state visual evoked potential. *Proceedings of the National Academy of Sciences,* 93**,** 4770-4774.

MORUZZI, G. 1996. The electrophysiological work of Carlo Matteucci. *Brain research bulletin,* 40**,** 69-91.

MORVAN, T., BOCH, L., MIKHINA, E., COSQUER, B., STÉPHAN, A., DE VASCONCELOS, A. P. & CASSEL, J.-C. 2022. Ventral midline thalamus activation is correlated with memory performance in a delayed spatial matching-to-sample task: A c-Fos imaging approach in the rat. *Behavioural Brain Research,* 418**,** 113670.

MOUGIN, O., ABDEL-FAHIM, R., DINEEN, R., PITIOT, A., EVANGELOU, N. & GOWLAND, P. 2016. Imaging gray matter with concomitant null point imaging from the phase sensitive inversion recovery sequence. *Magn Reson Med,* 76**,** 1512-1516.

MUGLER III, J. P. & BROOKEMAN, J. R. 1990. Three-dimensional magnetization-prepared rapid gradient-echo imaging (3D MP RAGE). *Magnetic resonance in medicine,* 15**,** 152-157.

MULLINGER, K. J., CHERUKARA, M. T., BUXTON, R. B., FRANCIS, S. T. & MAYHEW, S. D. 2017. Post-stimulus fMRI and EEG responses: Evidence for a neuronal origin hypothesised to be inhibitory. *Neuroimage,* 157**,** 388-399.

MULLINGER, K. J., MAYHEW, S. D., BAGSHAW, A. P., BOWTELL, R. & FRANCIS, S. T. 2013. Poststimulus undershoots in cerebral blood flow and BOLD fMRI responses are modulated by poststimulus neuronal activity. *Proc Natl Acad Sci U S A,* 110**,** 13636-41.

MURPHY, K., BIRN, R. M. & BANDETTINI, P. A. 2013. Resting-state fMRI confounds and cleanup. *Neuroimage,* 80**,** 349-359.

MURRAY, S. O., KOLODNY, T., SCHALLMO, M.-P., GERDTS, J. & BERNIER, R. A. 2020. Late fMRI response components are altered in autism spectrum disorder. *Frontiers in Human Neuroscience,* 14**,** 241.

MUTHUKUMARASWAMY, S. D. & SINGH, K. D. 2009. Functional decoupling of BOLD and gamma-band amplitudes in human primary visual cortex. *Human brain mapping,* 30**,** 2000-2007.

MUTHUKUMARASWAMY, S. D. & SINGH, K. D. 2013. Visual gamma oscillations: the effects of stimulus type, visual field coverage and stimulus motion on MEG and EEG recordings. *Neuroimage,* 69**,** 223-230.

NENCKA, A. S. & ROWE, D. B. 2007. Reducing the unwanted draining vein BOLD contribution in fMRI with statistical post-processing methods. *Neuroimage,* 37**,** 177-188.

NEUPER, C. & PFURTSCHELLER, G. 2001. Event-related dynamics of cortical rhythms: frequency-specific features and functional correlates. *Int J Psychophysiol,* 43**,** 41-58.

NILSSON, J., FERRIER, I. N., COVENTRY, K., BESTER, A. & FINKELMEYER, A. 2013. Negative BOLD response in the hippocampus during short-term spatial memory retrieval. *Journal of cognitive neuroscience,* 25**,** 1358-1371.

NUÑEZ, A. & BUÑO, W. 2021. The theta rhythm of the hippocampus: from neuronal and circuit mechanisms to behavior. *Frontiers in cellular neuroscience,* 15**,** 649262.

NUSSBAUMER, H. J. & NUSSBAUMER, H. J. 1982. *The fast Fourier transform*, Springer.

O'NEILL, G. C., BARRATT, E. L., HUNT, B. A., TEWARIE, P. K. & BROOKES, M. J. 2015. Measuring electrophysiological connectivity by power envelope correlation: a technical review on MEG methods. *Physics in Medicine & Biology,* 60**,** R271.

OGAWA, S., LEE, T. & BARRERE, B. 1993a. The sensitivity of magnetic resonance image signals of a rat brain to changes in the cerebral venous blood oxygenation. *Magnetic resonance in medicine,* 29**,** 205-210.

OGAWA, S. & LEE, T. M. 1990. Magnetic resonance imaging of blood vessels at high fields: in vivo and in vitro measurements and image simulation. *Magnetic resonance in medicine,* 16**,** 9-18.

OGAWA, S., LEE, T. M., KAY, A. R. & TANK, D. W. 1990. Brain magnetic resonance imaging with contrast dependent on blood oxygenation. *Proc Natl Acad Sci U S A,* 87**,** 9868-72.

OGAWA, S., MENON, R., TANK, D. W., KIM, S., MERKLE, H., ELLERMANN, J. & UGURBIL, K. 1993b. Functional brain mapping by blood oxygenation level-dependent contrast magnetic resonance imaging. A comparison of signal characteristics with a biophysical model. *Biophysical journal,* 64**,** 803-812.

ÖHMAN, A. 2005. The role of the amygdala in human fear: automatic detection of threat. *Psychoneuroendocrinology,* 30**,** 953-958.

OOSTENVELD, R., FRIES, P., MARIS, E. & SCHOFFELEN, J.-M. 2011. FieldTrip: open source software for advanced analysis of MEG, EEG, and invasive electrophysiological data. *Computational intelligence and neuroscience,* 2011**,** 1-9.

OSWALD, V., ZEROUALI, Y., BOULET-CRAIG, A., KRAJINOVIC, M., LAVERDIERE, C., SINNETT, D., JOLICOEUR, P., LIPPÉ, S., JERBI, K. & ROBAEY, P. 2017. Spontaneous brain oscillations as neural fingerprints of working memory capacities: A resting-state MEG study. *Cortex,* 97**,** 109-124.

OWEN, A. M., MCMILLAN, K. M., LAIRD, A. R. & BULLMORE, E. 2005. N-back working memory paradigm: a meta-analysis of normative functional neuroimaging studies. *Hum Brain Mapp,* 25**,** 46-59.

PAKENHAM, D. O., QUINN, A. J., FRY, A., FRANCIS, S. T., WOOLRICH, M. W., BROOKES, M. J. & MULLINGER, K. J. 2020. Post-stimulus beta responses are modulated by task duration. *Neuroimage,* 206**,** 116288.

PANG, J. C. & ROBINSON, P. A. 2018. Neural mechanisms of the EEG alpha-BOLD anticorrelation. *Neuroimage,* 181**,** 461-470.

PARVIZI, J. & KASTNER, S. 2018. Human intracranial EEG: promises and limitations. *Nature neuroscience,* 21**,** 474.

PASANTA, D., HE, J. L., FORD, T., OELTZSCHNER, G., LYTHGOE, D. J. & PUTS, N. A. 2023. Functional MRS studies of GABA and glutamate/Glx–A systematic review and meta-analysis. *Neuroscience & Biobehavioral Reviews,* 144**,** 104940.

PAULS, K. A. M., KORSUN, O., NENONEN, J., NURMINEN, J., LILJESTROM, M., KUJALA, J., PEKKONEN, E. & RENVALL, H. 2022. Cortical beta burst dynamics are altered in Parkinson's disease but normalized by deep brain stimulation. *Neuroimage,* 257**,** 119308.

PERÄKYLÄ, J., SUN, L., LEHTIMÄKI, K., PELTOLA, J., ÖHMAN, J., MÖTTÖNEN, T., OGAWA, K. H. & HARTIKAINEN, K. M. 2017. Causal evidence from humans for the role of mediodorsal nucleus of the thalamus in working memory. *Journal of cognitive neuroscience,* 29**,** 2090-2102.

PFURTSCHELLER, G. 1981. Central beta rhythm during sensorimotor activities in man. *Electroencephalogr Clin Neurophysiol,* 51**,** 253-64.

PFURTSCHELLER, G. & LOPES DA SILVA, F. H. 1999. Event-related EEG/MEG synchronization and desynchronization: basic principles. *Clin Neurophysiol,* 110**,** 1842-57.

PFURTSCHELLER, G. & NEUPER, C. 2001. Motor imagery and direct brain-computer communication. *Proceedings of the IEEE,* 89**,** 1123-1134.

PFURTSCHELLER, G., NEUPER, C., BRUNNER, C. & DA SILVA, F. L. 2005. Beta rebound after different types of motor imagery in man. *Neurosci Lett,* 378**,** 156-9.

PFURTSCHELLER, G., NEUPER, C. & KRAUSZ, G. 2000. Functional dissociation of lower and upper frequency mu rhythms in relation to voluntary limb movement. *Clin Neurophysiol,* 111**,** 1873-9.

PFURTSCHELLER, G., STANCAK, A., JR. & NEUPER, C. 1996a. Event-related synchronization (ERS) in the alpha band--an electrophysiological correlate of cortical idling: a review. *Int J Psychophysiol,* 24**,** 39-46.

PFURTSCHELLER, G., STANCAK, A., JR. & NEUPER, C. 1996b. Post-movement beta synchronization. A correlate of an idling motor area? *Electroencephalogr Clin Neurophysiol,* 98**,** 281-93.

POGOSYAN, A., GAYNOR, L. D., EUSEBIO, A. & BROWN, P. 2009. Boosting cortical activity at Beta-band frequencies slows movement in humans. *Curr Biol,* 19**,** 1637-41.

POMAROL-CLOTET, E., SALVADOR, R., SARRO, S., GOMAR, J., VILA, F., MARTINEZ, A., GUERRERO, A., ORTIZ-GIL, J., SANS-SANSA, B., CAPDEVILA, A., CEBAMANOS, J. M. & MCKENNA, P. J. 2008. Failure to deactivate in the prefrontal cortex in schizophrenia: dysfunction of the default mode network? *Psychol Med,* 38**,** 1185-93.

POPOV, T., POPOVA, P., HARKOTTE, M., AWISZUS, B., ROCKSTROH, B. & MILLER, G. A. 2018. Cross-frequency interactions between frontal theta and posterior alpha control mechanisms foster working memory. *Neuroimage,* 181**,** 728-733.

PRUESSMANN, K. P., WEIGER, M., SCHEIDEGGER, M. B. & BOESIGER, P. 1999. SENSE: sensitivity encoding for fast MRI. *Magnetic Resonance in Medicine: An Official Journal of the International Society for Magnetic Resonance in Medicine,* 42**,** 952-962.

PRZEZDZIK, I., BAGSHAW, A. P. & MAYHEW, S. D. Some brains are more strongly functionally connected than others: a resting-state fMRI study of inter and intra network coherence. Proc ISMRM, 2013. 603-610.

QUINN, A. J., VAN EDE, F., BROOKES, M. J., HEIDEMAN, S. G., NOWAK, M., SEEDAT, Z. A., VIDAURRE, D., ZICH, C., NOBRE, A. C. & WOOLRICH, M. W. 2019. Unpacking Transient Event Dynamics in Electrophysiological Power Spectra. *Brain Topogr,* 32**,** 1020-1034.

QUINN, A. J., VIDAURRE, D., ABEYSURIYA, R., BECKER, R., NOBRE, A. C. & WOOLRICH, M. W. 2018. Task-Evoked Dynamic Network Analysis Through Hidden Markov Modeling. *Front Neurosci,* 12**,** 603.

RAFAL, R. D. & POSNER, M. I. 1987. Deficits in human visual spatial attention following thalamic lesions. *Proceedings of the National Academy of Sciences,* 84**,** 7349-7353.

RAICHLE, M. E. 2015. The brain's default mode network. *Annual review of neuroscience,* 38**,** 433-447.

RAJU, V. R. 2020. Efficacy of lead point using MER with DBS in accurate targeting for persevering subthalamic-nuclei neurons-geometry of the electrode and its implantation in Parkinson‘s. *IP Indian J Neurosci,* 6**,** 301-16.

REZEK, I. & ROBERTS, S. 2005. Ensemble hidden Markov models with extended observation densities for biosignal analysis. *Probabilistic modeling in bioinformatics and medical informatics.* Springer.

RIER, L., ZAMYADI, R., ZHANG, J., EMAMI, Z., SEEDAT, Z. A., MOCANU, S., GASCOYNE, L. E., ALLEN, C. M., SCADDING, J. W., FURLONG, P. L., GOODING-WILLIAMS, G., WOOLRICH, M. W., EVANGELOU, N., BROOKES, M. J. & DUNKLEY, B. T. 2021. Mild traumatic brain injury impairs the coordination of intrinsic and motor-related neural dynamics. *Neuroimage Clin,* 32**,** 102841.

RITTER, P., MOOSMANN, M. & VILLRINGER, A. 2009. Rolandic alpha and beta EEG rhythms' strengths are inversely related to fMRI-BOLD signal in primary somatosensory and motor cortex. *Human brain mapping,* 30**,** 1168-1187.

ROBINSON, P. A., DRYSDALE, P. M., VAN DER MERWE, H., KYRIAKOU, E., RIGOZZI, M., GERMANOSKA, B. & RENNIE, C. J. 2006. BOLD responses to stimuli: dependence on frequency, stimulus form, amplitude, and repetition rate. *Neuroimage,* 31**,** 585-599.

ROBSON, S. E., BROOKES, M. J., HALL, E. L., PALANIYAPPAN, L., KUMAR, J., SKELTON, M., CHRISTODOULOU, N. G., QURESHI, A., JAN, F., KATSHU, M. Z., LIDDLE, E. B., LIDDLE, P. F. & MORRIS, P. G. 2016. Abnormal visuomotor processing in schizophrenia. *Neuroimage Clin,* 12**,** 869-878.

ROELFSEMA, P. R., ENGEL, A. K., KONIG, P. & SINGER, W. 1997. Visuomotor integration is associated with zero time-lag synchronization among cortical areas. *Nature,* 385**,** 157-61.

ROLAND, P. E. & ZILLES, K. 1998. Structural divisions and functional fields in the human cerebral cortex. *Brain research reviews,* 26**,** 87-105.

ROSA, M. J., KILNER, J. M. & PENNY, W. D. 2011. Bayesian comparison of neurovascular coupling models using EEG-fMRI. *PLoS Comput Biol,* 7**,** e1002070.

ROSANOVA, M., CASALI, A., BELLINA, V., RESTA, F., MARIOTTI, M. & MASSIMINI, M. 2009. Natural frequencies of human corticothalamic circuits. *J Neurosci,* 29**,** 7679-85.

ROUX, F. & UHLHAAS, P. J. 2014. Working memory and neural oscillations: alpha-gamma versus theta-gamma codes for distinct WM information? *Trends Cogn Sci,* 18**,** 16-25.

RUGG, M. D. & VILBERG, K. L. 2013. Brain networks underlying episodic memory retrieval. *Current opinion in neurobiology,* 23**,** 255-260.

RUSINKIEWICZ, S. & LEVOY, M. Efficient variants of the ICP algorithm. Proceedings third international conference on 3-D digital imaging and modeling, 2001. IEEE, 145-152.

SAALMANN, Y. B., PINSK, M. A., WANG, L., LI, X. & KASTNER, S. 2012. The pulvinar regulates information transmission between cortical areas based on attention demands. *science,* 337**,** 753-756.

SADAGHIANI, S., UGURBIL, K. & ULUDAG, K. 2009. Neural activity-induced modulation of BOLD poststimulus undershoot independent of the positive signal. *Magn Reson Imaging,* 27**,** 1030-8.

SALMELIN, R., HÁMÁALÁINEN, M., KAJOLA, M. & HARI, R. 1995. Functional segregation of movement-related rhythmic activity in the human brain. *Neuroimage,* 2**,** 237-243.

SAREEN, E., ZAHAR, S., VAN DE VILLE, D., GUPTA, A., GRIFFA, A. & AMICO, E. 2021. Exploring MEG brain fingerprints: Evaluation, pitfalls, and interpretations. *NeuroImage,* 240**,** 118331.

SARVAS, J. 1987. Basic mathematical and electromagnetic concepts of the biomagnetic inverse problem. *Physics in Medicine & Biology,* 32**,** 11.

SAUSENG, P., GRIESMAYR, B., FREUNBERGER, R. & KLIMESCH, W. 2010. Control mechanisms in working memory: a possible function of EEG theta oscillations. *Neurosci Biobehav Rev,* 34**,** 1015-22.

SAUSENG, P., KLIMESCH, W., SCHABUS, M. & DOPPELMAYR, M. 2005. Fronto-parietal EEG coherence in theta and upper alpha reflect central executive functions of working memory. *Int J Psychophysiol,* 57**,** 97-103.

SCHÄFER, C. B., MORGAN, B. R., YE, A. X., TAYLOR, M. J. & DOESBURG, S. M. 2014. Oscillations, networks, and their development: MEG connectivity changes with age. *Human brain mapping,* 35**,** 5249-5261.

SCHALL, J. D. 2004. On the role of frontal eye field in guiding attention and saccades. *Vision research,* 44**,** 1453-1467.

SCHEERINGA, R. 2011. *On the relation between oscillatory EEG activity and the BOLD signal.* Radboud University Nijmegen Nijmegen.

SCHEERINGA, R., BASTIAANSEN, M. C., PETERSSON, K. M., OOSTENVELD, R., NORRIS, D. G. & HAGOORT, P. 2008. Frontal theta EEG activity correlates negatively with the default mode network in resting state. *International journal of psychophysiology,* 67**,** 242-251.

SCHNEIDER, F. C., ROYER, A., GROSSELIN, A., PELLET, J., BARRAL, F. G., LAURENT, B., BROUILLET, D. & LANG, F. 2011. Modulation of the default mode network is task-dependant in chronic schizophrenia patients. *Schizophr Res,* 125**,** 110-7.

SCHÖDER, H. & GÖNEN, M. 2007. Screening for cancer with PET and PET/CT: potential and limitations. *Journal of Nuclear Medicine,* 48**,** 4S-18S.

SCHOFFELEN, J. M. & GROSS, J. 2009. Source connectivity analysis with MEG and EEG. *Human brain mapping,* 30**,** 1857-1865.

SCHOFIELD, H., BOTO, E., SHAH, V., HILL, R. M., OSBORNE, J., REA, M., DOYLE, C., HOLMES, N., BOWTELL, R. & WOOLGER, D. 2022. Quantum enabled functional neuroimaging: the why and how of magnetoencephalography using optically pumped magnetometers. *Contemporary Physics,* 63**,** 161-179.

SCHOONHEIM, M. M., MEIJER, K. A. & GEURTS, J. J. 2015. Network collapse and cognitive impairment in multiple sclerosis. *Frontiers in neurology,* 6**,** 82.

SCHRIDDE, U., KHUBCHANDANI, M., MOTELOW, J. E., SANGANAHALLI, B. G., HYDER, F. & BLUMENFELD, H. 2008. Negative BOLD with large increases in neuronal activity. *Cerebral cortex,* 18**,** 1814-1827.

SEEDAT, Z. A., QUINN, A. J., VIDAURRE, D., LIUZZI, L., GASCOYNE, L. E., HUNT, B. A. E., O'NEILL, G. C., PAKENHAM, D. O., MULLINGER, K. J., MORRIS, P. G., WOOLRICH, M. W. & BROOKES, M. J. 2020. The role of transient spectral 'bursts' in functional connectivity: A magnetoencephalography study. *Neuroimage,* 209**,** 116537.

SEELEY, W. W. 2019. The salience network: a neural system for perceiving and responding to homeostatic demands. *Journal of Neuroscience,* 39**,** 9878-9882.
SHERMAN, M. A., LEE, S., LAW, R., HAEGENS, S., THORN, C. A., HAMALAINEN, M. S., MOORE, C. I. & JONES, S. R. 2016. Neural mechanisms of transient neocortical beta rhythms: Converging evidence from humans, computational modeling, monkeys, and mice. *Proc Natl Acad Sci U S A,* 113**,** E4885-94.
SHIGETO, H., TOBIMATSU, S., YAMAMOTO, T., KOBAYASHI, T. & KATO, M. 1998. Visual evoked cortical magnetic responses to checkerboard pattern reversal stimulation: a study on the neural generators of N75, P100 and N145. *Journal of the neurological sciences,* 156**,** 186-194.
SHIN, H., LAW, R., TSUTSUI, S., MOORE, C. I. & JONES, S. R. 2017. The rate of transient beta frequency events predicts behavior across tasks and species. *Elife,* 6.
SHIPP, S. 2007. Structure and function of the cerebral cortex. *Current Biology,* 17**,** R443-R449.
SHMUEL, A., AUGATH, M., OELTERMANN, A. & LOGOTHETIS, N. K. 2006. Negative functional MRI response correlates with decreases in neuronal activity in monkey visual area V1. *Nat Neurosci,* 9**,** 569-77.
SIAPAS, A. G., LUBENOV, E. V. & WILSON, M. A. 2005. Prefrontal phase locking to hippocampal theta oscillations. *Neuron,* 46**,** 141-151.
SINGER, W. 1993. Synchronization of cortical activity and its putative role in information processing and learning. *Annual review of physiology,* 55**,** 349-374.
SOKOLIUK, R., MAYHEW, S. D., AQUINO, K. M., WILSON, R., BROOKES, M. J., FRANCIS, S. T., HANSLMAYR, S. & MULLINGER, K. J. 2019. Two Spatially Distinct Posterior Alpha Sources Fulfill Different Functional Roles in Attention. *J Neurosci,* 39**,** 7183-7194.
SOLEIMANI, B., DAS, P., KARUNATHILAKE, I. D., KUCHINSKY, S. E., SIMON, J. Z. & BABADI, B. 2022. NLGC: Network localized granger causality with application to MEG directional functional connectivity analysis. *Neuroimage,* 260**,** 119496.
SOLIS-ESCALANTE, T., MULLER-PUTZ, G. R., PFURTSCHELLER, G. & NEUPER, C. 2012. Cue-induced beta rebound during withholding of overt and covert foot movement. *Clin Neurophysiol,* 123**,** 1182-90.
SOLTANI ZANGBAR, H., GHADIRI, T., SEYEDI VAFAEE, M., EBRAHIMI KALAN, A., FALLAHI, S., GHORBANI, M. & SHAHABI, P. 2020. Theta oscillations through hippocampal/prefrontal pathway: importance in cognitive performances. *Brain connectivity,* 10**,** 157-169.
SOMMER, M. A. & WURTZ, R. H. 2006. Influence of the thalamus on spatial visual processing in frontal cortex. *Nature,* 444**,** 374-377.
SOTERO, R. C. & TRUJILLO-BARRETO, N. J. 2007. Modelling the role of excitatory and inhibitory neuronal activity in the generation of the BOLD signal. *Neuroimage,* 35**,** 149-65.
SOUFINEYESTANI, M., DOWLING, D. & KHAN, A. 2020. Electroencephalography (EEG) technology applications and available devices. *Applied Sciences,* 10**,** 7453.
SPEHLMANN, R. 1965. The averaged electrical responses to diffuse and to patterned light in the human. *Electroencephalography and clinical neurophysiology,* 19**,** 560-569.
STANCAK, A., JR. & PFURTSCHELLER, G. 1995. Desynchronization and recovery of beta rhythms during brisk and slow self-paced finger movements in man. *Neurosci Lett,* 196**,** 21-4.
STANLEY, J. A. & RAZ, N. 2018. Functional magnetic resonance spectroscopy: the "new" MRS for cognitive neuroscience and psychiatry research. *Frontiers in psychiatry,* 9**,** 76.
STEFFENER, J., TABERT, M., REUBEN, A. & STERN, Y. 2010. Investigating hemodynamic response variability at the group level using basis functions. *Neuroimage,* 49**,** 2113-2122.
STEHLING, M. K., TURNER, R. & MANSFIELD, P. 1991. Echo-planar imaging: magnetic resonance imaging in a fraction of a second. *Science,* 254**,** 43-50.

STEN, S., LUNDENGARD, K., WITT, S. T., CEDERSUND, G., ELINDER, F. & ENGSTROM, M. 2017. Neural inhibition can explain negative BOLD responses: A mechanistic modelling and fMRI study. *Neuroimage,* 158**,** 219-231.

STERIADE, M., GLOOR, P., LLINAS, R. R., DA SILVA, F. L. & MESULAM, M.-M. 1990. Basic mechanisms of cerebral rhythmic activities. *Electroencephalography and clinical neurophysiology,* 76**,** 481-508.

STEVENSON, C. M., BROOKES, M. J. & MORRIS, P. G. 2011. beta-Band correlates of the fMRI BOLD response. *Hum Brain Mapp,* 32**,** 182-97.

STRICSEK, G., LANG, M. J. & WU, C. 2018. Stereoelectroencephalography (sEEG) versus grids and strips. *Functional neurosurgery and neuromodulation.* Elsevier.

STROBER, L., ENGLERT, J., MUNSCHAUER, F., WEINSTOCK-GUTTMAN, B., RAO, S. & BENEDICT, R. 2009. Sensitivity of conventional memory tests in multiple sclerosis: comparing the Rao Brief Repeatable Neuropsychological Battery and the Minimal Assessment of Cognitive Function in MS. *Multiple Sclerosis Journal,* 15**,** 1077-1084.

SUTTON, S., BRAREN, M., ZUBIN, J. & JOHN, E. 1965. Evoked-potential correlates of stimulus uncertainty. *Science,* 150**,** 1187-1188.

SZCZEPANSKI, S. M., PINSK, M. A., DOUGLAS, M. M., KASTNER, S. & SAALMANN, Y. B. 2013. Functional and structural architecture of the human dorsal frontoparietal attention network. *Proceedings of the National Academy of Sciences,* 110**,** 15806-15811.

TAKEI, Y., FUJIHARA, K., TAGAWA, M., HIRONAGA, N., NEAR, J., KASAGI, M., TAKAHASHI, Y., MOTEGI, T., SUZUKI, Y., AOYAMA, Y., SAKURAI, N., YAMAGUCHI, M., TOBIMATSU, S., UJITA, K., TSUSHIMA, Y., NARITA, K. & FUKUDA, M. 2016. The inhibition/excitation ratio related to task-induced oscillatory modulations during a working memory task: A multtimodal-imaging study using MEG and MRS. *Neuroimage,* 128**,** 302-315.

TAN, H., JENKINSON, N. & BROWN, P. 2014. Dynamic neural correlates of motor error monitoring and adaptation during trial-to-trial learning. *J Neurosci,* 34**,** 5678-88.

TAN, H., WADE, C. & BROWN, P. 2016. Post-Movement Beta Activity in Sensorimotor Cortex Indexes Confidence in the Estimations from Internal Models. *J Neurosci,* 36**,** 1516-28.

TAYLOR, M. J., URBAIN, C. & PANG, E. W. 2019. Application of MEG in understanding the development of executive and social cognitive functions. *Magnetoencephalography: From Signals to Dynamic Cortical Networks***,** 769-798.

TER-POGOSSIAN, M. M., PHELPS, M. E., HOFFMAN, E. J. & MULLANI, N. A. 1975. A positron-emission transaxial tomograph for nuclear imaging (PETT). *Radiology,* 114**,** 89-98.

TEWARIE, P., LIUZZI, L., O'NEILL, G. C., QUINN, A. J., GRIFFA, A., WOOLRICH, M. W., STAM, C. J., HILLEBRAND, A. & BROOKES, M. J. 2019. Tracking dynamic brain networks using high temporal resolution MEG measures of functional connectivity. *Neuroimage,* 200**,** 38-50.

THOMSON, D. J. 1982. Spectrum estimation and harmonic analysis. *Proceedings of the IEEE,* 70**,** 1055-1096.

TINKHAUSER, G., POGOSYAN, A., LITTLE, S., BEUDEL, M., HERZ, D. M., TAN, H. & BROWN, P. 2017a. The modulatory effect of adaptive deep brain stimulation on beta bursts in Parkinson's disease. *Brain,* 140**,** 1053-1067.

TINKHAUSER, G., POGOSYAN, A., TAN, H., HERZ, D. M., KUHN, A. A. & BROWN, P. 2017b. Beta burst dynamics in Parkinson's disease OFF and ON dopaminergic medication. *Brain,* 140**,** 2968-2981.

TRIANTAFYLLOU, C., HOGE, R. D., KRUEGER, G., WIGGINS, C. J., POTTHAST, A., WIGGINS, G. C. & WALD, L. L. 2005. Comparison of physiological noise at 1.5 T, 3 T and 7 T and optimization of fMRI acquisition parameters. *Neuroimage,* 26**,** 243-250.

TSIARAS, V., SIMOS, P. G., REZAIE, R., SHETH, B. R., GARYFALLIDIS, E., CASTILLO, E. M. & PAPANICOLAOU, A. C. 2011. Extracting biomarkers of autism from MEG resting-state functional connectivity networks. *Computers in biology and medicine,* 41**,** 1166-1177.

TULADHAR, A. M., TER HUURNE, N., SCHOFFELEN, J. M., MARIS, E., OOSTENVELD, R. & JENSEN, O. 2007. Parieto-occipital sources account for the increase in alpha activity with working memory load. *Hum Brain Mapp,* 28**,** 785-92.

TURNER, R., LE BIHAN, D., MOONEN, C. T., DESPRES, D. & FRANK, J. 1991. Echo-planar time course MRI of cat brain oxygenation changes. *Magn Reson Med,* 22**,** 159-66.

TYVAERT, L., LEVAN, P., GROVA, C., DUBEAU, F. & GOTMAN, J. 2008. Effects of fluctuating physiological rhythms during prolonged EEG-fMRI studies. *Clinical neurophysiology,* 119**,** 2762-2774.

TZOURIO-MAZOYER, N., LANDEAU, B., PAPATHANASSIOU, D., CRIVELLO, F., ETARD, O., DELCROIX, N., MAZOYER, B. & JOLIOT, M. 2002. Automated anatomical labeling of activations in SPM using a macroscopic anatomical parcellation of the MNI MRI single-subject brain. *Neuroimage,* 15**,** 273-289.

ULLSPERGER, M. & DEBENER, S. 2010. *Simultaneous EEG and fMRI: recording, analysis, and application*, Oxford University Press.

ULUDAĞ, K. 2008. Transient and sustained BOLD responses to sustained visual stimulation. *Magnetic resonance imaging,* 26**,** 863-869.

VALDUEZA, J. M., SCHMIERER, K., MEHRAEIN, S. & EINHAÜPL, K. M. 1996. Assessment of normal flow velocity in basal cerebral veins: a transcranial Doppler ultrasound study. *Stroke,* 27**,** 1221-1225.

VAN DE MOORTELE, P.-F., AUERBACH, E. J., OLMAN, C., YACOUB, E., UĞURBIL, K. & MOELLER, S. 2009. T1 weighted brain images at 7 Tesla unbiased for Proton Density, T2$*$ contrast and RF coil receive B1 sensitivity with simultaneous vessel visualization. *Neuroimage,* 46**,** 432-446.

VAN DER MEER, J. N., PAMPEL, A., VAN SOMEREN, E. J., RAMAUTAR, J. R., VAN DER WERF, Y. D., GOMEZ-HERRERO, G., LEPSIEN, J., HELLRUNG, L., HINRICHS, H. & MÖLLER, H. E. 2016. Carbon-wire loop based artifact correction outperforms post-processing EEG/fMRI corrections—A validation of a real-time simultaneous EEG/fMRI correction method. *Neuroimage,* 125**,** 880-894.

VAN KERKOERLE, T., SELF, M. W., DAGNINO, B., GARIEL-MATHIS, M.-A., POORT, J., VAN DER TOGT, C. & ROELFSEMA, P. R. 2014. Alpha and gamma oscillations characterize feedback and feedforward processing in monkey visual cortex. *Proceedings of the National Academy of Sciences,* 111**,** 14332-14341.

VAN VEEN, B. D. & BUCKLEY, K. M. 1988. Beamforming: A versatile approach to spatial filtering. *IEEE assp magazine,* 5**,** 4-24.

VAN ZIJL, P. C., HUA, J. & LU, H. 2012. The BOLD post-stimulus undershoot, one of the most debated issues in fMRI. *Neuroimage,* 62**,** 1092-102.

VERTES, R. P. 2005. Hippocampal theta rhythm: A tag for short-term memory. *Hippocampus,* 15**,** 923-935.

VIDAURRE, D., HUNT, L. T., QUINN, A. J., HUNT, B. A., BROOKES, M. J., NOBRE, A. C. & WOOLRICH, M. W. 2018. Spontaneous cortical activity transiently organises into frequency specific phase-coupling networks. *Nature communications,* 9**,** 2987.

VIDAURRE, D., QUINN, A. J., BAKER, A. P., DUPRET, D., TEJERO-CANTERO, A. & WOOLRICH, M. W. 2016. Spectrally resolved fast transient brain states in electrophysiological data. *Neuroimage,* 126**,** 81-95.

VRBA, J. 2002. Magnetoencephalography: the art of finding a needle in a haystack. *Physica C: Superconductivity,* 368**,** 1-9.

VRBA, J. & ROBINSON, S. E. 2001. Signal processing in magnetoencephalography. *Methods,* 25**,** 249-71.

WALTER, W. G. 1968. The contingent negative variation: an electro-cortical sign of sensori-motor reflex association in man. *Progress in brain research,* 22**,** 364-377.

WARD, L. M. 2013. The thalamus: gateway to the mind. *Wiley Interdisciplinary Reviews: Cognitive Science,* 4**,** 609-622.

WEINBERGER, D. R., MATTAY, V., CALLICOTT, J., KOTRLA, K., SANTHA, A., VAN GELDEREN, P., DUYN, J., MOONEN, C. & FRANK, J. 1996. fMRI applications in schizophrenia research. *Neuroimage,* 4**,** S118-26.

WEST, K. L., ZUPPICHINI, M. D., TURNER, M. P., SIVAKOLUNDU, D. K., ZHAO, Y., ABDELKARIM, D., SPENCE, J. S. & RYPMA, B. 2019. BOLD hemodynamic response function changes significantly with healthy aging. *Neuroimage,* 188**,** 198-207.

WESTNER, B. U., DALAL, S. S., GRAMFORT, A., LITVAK, V., MOSHER, J. C., OOSTENVELD, R. & SCHOFFELEN, J.-M. 2022. A unified view on beamformers for M/EEG source reconstruction. *Neuroimage,* 246**,** 118789.

WHEELER, A. L. & VOINESKOS, A. N. 2014. A review of structural neuroimaging in schizophrenia: from connectivity to connectomics. *Frontiers in human neuroscience,* 8**,** 653.

WIDMANN, A., SCHRÖGER, E. & MAESS, B. 2015. Digital filter design for electrophysiological data–a practical approach. *Journal of neuroscience methods,* 250**,** 34-46.

WIERENGA, H. J. 1993. *MEG, EEG and the integration with magnetic resonance images*, HJ Wieringa.

WILSON, R. S., MAYHEW, S. D., ROLLINGS, D. T., GOLDSTONE, A., PRZEZDZIK, I., ARVANITIS, T. N. & BAGSHAW, A. P. 2015. Influence of epoch length on measurement of dynamic functional connectivity in wakefulness and behavioural validation in sleep. *Neuroimage,* 112**,** 169-179.

WISE, R. G., IDE, K., POULIN, M. J. & TRACEY, I. 2004. Resting fluctuations in arterial carbon dioxide induce significant low frequency variations in BOLD signal. *Neuroimage,* 21**,** 1652-1664.

WOLINSKI, N., COOPER, N. R., SAUSENG, P. & ROMEI, V. 2018. The speed of parietal theta frequency drives visuospatial working memory capacity. *PLoS Biol,* 16**,** e2005348.

WOOLRICH, M. W., BAKER, A., LUCKHOO, H., MOHSENI, H., BARNES, G., BROOKES, M. & REZEK, I. 2013. Dynamic state allocation for MEG source reconstruction. *Neuroimage,* 77**,** 77-92.

WOOLRICH, M. W., BEHRENS, T. E., BECKMANN, C. F., JENKINSON, M. & SMITH, S. M. 2004a. Multilevel linear modelling for FMRI group analysis using Bayesian inference. *Neuroimage,* 21**,** 1732-1747.

WOOLRICH, M. W., BEHRENS, T. E. & SMITH, S. M. 2004b. Constrained linear basis sets for HRF modelling using Variational Bayes. *NeuroImage,* 21**,** 1748-1761.

WOOLRICH, M. W., RIPLEY, B. D., BRADY, M. & SMITH, S. M. 2001. Temporal autocorrelation in univariate linear modeling of FMRI data. *Neuroimage,* 14**,** 1370-1386.

WORSLEY, K. J. 2001. Statistical analysis of activation images. *Functional MRI: An introduction to methods,* 14**,** 251-270.

WURTZ, R. H. & KANDEL, E. R. 2000. Central visual pathways. *Principles of neural science,* 4**,** 523-545.

XU, F., GE, Y. & LU, H. 2009. Noninvasive quantification of whole-brain cerebral metabolic rate of oxygen (CMRO2) by MRI. *Magnetic Resonance in Medicine: An Official Journal of the International Society for Magnetic Resonance in Medicine,* 62**,** 141-148.

YABLONSKIY, D. A. & HAACKE, E. M. 1994. Theory of NMR signal behavior in magnetically inhomogeneous tissues: the static dephasing regime. *Magnetic resonance in medicine,* 32**,** 749-763.

YAMAMOTO, D. J., REYNOLDS, J., KRMPOTICH, T., BANICH, M. T., THOMPSON, L. & TANABE, J. 2014. Temporal profile of fronto-striatal-limbic activity during implicit decisions in drug dependence. *Drug and alcohol dependence,* 136**,** 108-114.

YANG, T., HAKIMIAN, S. & SCHWARTZ, T. H. 2014. Intraoperative ElectroCorticoGraphy (ECog): indications, techniques, and utility in epilepsy surgery. *Epileptic Disorders,* 16**,** 271-279.

YEN, C.-T. & LU, P.-L. 2013. Thalamus and pain. *Acta Anaesthesiologica Taiwanica,* 51**,** 73-80.

YUAN, H., LIU, T., SZARKOWSKI, R., RIOS, C., ASHE, J. & HE, B. 2010. Negative covariation between task-related responses in alpha/beta-band activity and BOLD in human sensorimotor cortex: an EEG and fMRI study of motor imagery and movements. *Neuroimage,* 49**,** 2596-2606.

YUK, V., DUNKLEY, B. T., ANAGNOSTOU, E. & TAYLOR, M. J. 2020. Alpha connectivity and inhibitory control in adults with autism spectrum disorder. *Molecular autism,* 11**,** 1-13.

ZARAHN, E., AGUIRRE, G. K. & D'ESPOSITO, M. 1997. Empirical analyses of BOLD fMRI statistics. *NeuroImage,* 5**,** 179-197.

ZHANG, Y., CHEN, Y., BRESSLER, S. L. & DING, M. 2008. Response preparation and inhibition: the role of the cortical sensorimotor beta rhythm. *Neuroscience,* 156**,** 238-46.

ZHOU, Z., DING, M., CHEN, Y., WRIGHT, P., LU, Z. & LIU, Y. 2009. Detecting directional influence in fMRI connectivity analysis using PCA based Granger causality. *Brain research,* 1289**,** 22-29.

ZICH, C., QUINN, A. J., BONAIUTO, J. J., O'NEILL, G., MARDELL, L. C., WARD, N. S. & BESTMANN, S. 2023. Spatiotemporal organisation of human sensorimotor beta burst activity. *Elife,* 12.